Methods in Molecular Biology 915

Springer Protocols

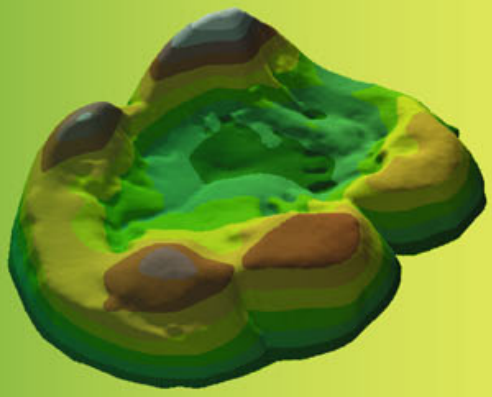

Lynne S. Bell *Editor*

Forensic Microscopy for Skeletal Tissues

Methods and Protocols

Humana Press

METHODS IN MOLECULAR BIOLOGY™

Series Editor
John M. Walker
School of Life Sciences
University of Hertfordshire
Hatfield, Hertfordshire, AL10 9AB, UK

For further volumes:
http://www.springer.com/series/7651

Forensic Microscopy for Skeletal Tissues

Methods and Protocols

Edited by

Lynne S. Bell

School of Criminology, Simon Fraser University, Burnaby, BC, Canada

Humana Press

Editor
Lynne S. Bell
School of Criminology
Simon Fraser University
Burnaby, BC, Canada

ISSN 1064-3745 ISSN 1940-6029 (electronic)
ISBN 978-1-61779-976-1 ISBN 978-1-61779-977-8 (eBook)
DOI 10.1007/978-1-61779-977-8
Springer New York Heidelberg Dordrecht London

Library of Congress Control Number: 2012942798

Printed on acid-free paper

Humana Press is a brand of Springer
Springer is part of Springer Science+Business Media (www.springer.com)

Preface

Forensic anthropology is concerned with human remains usually in the skeletonized form. The tissues of interest are therefore bone and teeth. The application of microscopy to skeletal tissues is well established and used routinely in biomedical science. Its adaptation to forensic questions is an increasing area of interest, and publications utilizing microscopy have increased in the scientific literature.

The aim of this book is to bring together differing forms of microscopy that are used in association with forensic anthropology, or have relevance to questions concerning forensic anthropology. This has brought together a number of authors from forensic, archaeological, and paleontological disciplines, who have developed or applied microscopic methods to address questions that intersect, or usefully inform, forensic anthropology. The methods themselves utilize differing forms of light, confocal, scanning electron, and transmission electron microscopy. Embedding protocols for wax and plastic embedding are provided and a review article on the state of the art for SEM analysis gives a useful backdrop to more developments in backscattered and environmental SEM hardware and application. In addition, interpretative chapters provide a user approach to image recognition of either surface or internal changes to bone and teeth, either for mapping or for identification purposes.

It is rare in any paper, even a methodological one, that the entire microscopic method and the sample preparation that precedes it will provide sufficient detail to accurately and exactly reproduce it. The aim of this book is to articulate these methods in long-form, and to provide interpretative chapters to aid assessment of pre- or postmortem changes to skeletal material.

Burnaby, BC, Canada *Lynne S. Bell*

Acknowledgements

I wish to thank Springer Humana for generously providing the color production of micrographs for this book. I am particularly indebted to Aleisha Best for her patience and expert editorial assistance. And finally, an enormous thanks to Nadine Schuurman for her support and endless encouragement.

Contents

Contributors

Peter Andrews • *Department of Paleontology, Natural History Museum, London, UK*
Lynne S. Bell • *School of Criminology, Simon Fraser University, Burnaby, BC, Canada*
Christian Crowder • *Office of Chief Medical Examiner, New York, NY, USA*
M. Christopher Dean • *Department of Cell and Developmental Biology, University College London, London, UK*
John C. Dennis • *Department of Anthropology, University of Arkansas, Fayetteville, AR, USA*
Yolanda Fernández-Jalvo • *Department of Paleobiologia, Museo Nacional de Ciencias Naturales, Madrid, Spain*
Jarred Heinrich • *Department of Anthropology, University of Toronto, Toronto, ON, Canada*
Chris G. Jones • *Department of Mineralogy, The Natural History Museum, London, UK*
Zachary S. Klukkert • *Department of Anthropology, The Graduate Center, City University of New York, New York, NY; New York Consortium in Evolutionary Primatology (NYCEP)*
Hannah E.C. Koon • *BioArch, Department of Biology, University of York, York, UK*
Randell Leifheit • *Solarius Development Inc., Columbia, TN, USA*
Francis M'Kirera • *Ross University School of Medicine, North Brunswick, NJ*
Christopher R. Moore • *Department of Physics and Earth/Space Sciences, University of Indianapolis, Indianapolis, IN, USA*
Kim Piper • *Department of Cellular Pathology, Bartshealth NHS Trust, London, UK*
Christopher W. Schmidt • *Indiana Prehistory Laboratory, Department of Anthropology, University of Indianapolis, Indianapolis, IN, USA*
Mary Higby Schweitzer • *North Carolina State Museum of Natural Sciences, Raleigh, NC, USA*
Sam D. Stout • *Department of Anthropology, The Ohio State University, Columbus, OH, USA*
Margaret Streeter • *Department of Anthropology, Boise State University, Boise, ID, USA*
Rose Uhlig • *Ridge Trail, Carol Stream, IL, USA*
Peter S. Ungar • *Department of Anthropology, University of Arkansas, Fayetteville, AR, USA*
Gail Valentine • *Department of Cellular Pathology, Barts and the London NHS Trust, London, UK*

A.H.J. Wighton • *Department of Mineralogy, The Natural History Museum, London, UK*
Ursula Wittwer-Backofen • *Anthropologie, Medizische Fakultat der Albert Ludwigs—Universitat Frieberg, Freiburg, Germany*
Wenxia Zheng • *Department of Marine, Earth and Atmospheric Sciences, North Carolina State University, Raleigh, NC, USA; North Carolina State Museum of Natural Sciences, Raleigh, NC, USA*

Chapter 1

Scanning Electron Microscopy: Preparation and Imaging for SEM

Chris G. Jones

Abstract

Scanning electron microscopy (SEM) has been almost universally applied for the surface examination and characterization of both natural and man-made objects. Although an invasive technique, developments in electron microscopy over the years has given the microscopist a much clearer choice in how invasive the technique will be. With the advent of low vacuum SEM in the 1970s (The environmental cold stage, 1970) and environmental SEM in the late 1980s (J Microsc 160(pt. 1):9–19, 1989), it is now possible in some circumstances to examine samples without preparation. However, for the examination of biological tissue and cells it is still advisable to chemically fix, dehydrate, and coat samples for SEM imaging and analysis. This chapter aims to provide an overview of SEM as an imaging tool, and a general introduction to some of the methods applied for the preparation of samples.

Key words: Scanning electron microscope (SEM), Electron, Secondary electron (SE), Back scattered electron (BSE), Detector, Fixation, Critical point drying, Coating

1. Introduction

Scanning electron microscopy (SEM) was developed from transmission electron microscopy (TEM), with the earliest instruments developed experimentally in the late 1930s by attaching scan coils to a TEM (1–4). The first commercial SEM was introduced in 1965 by the Cambridge Instrument Company as the "Stereoscan." The first instrument was delivered to DuPont in USA for the examination of nylon fibers.

Since that time SEM has developed into a range of imaging, analytical and research tools, with capabilities ranging from simply imaging surface topography through to resolving structures at the subnanometre scale.

SEM is usually applied because of its ability to resolve smaller structures at a higher magnification than light microscopy, while

Lynne S. Bell (ed.), *Forensic Microscopy for Skeletal Tissues: Methods and Protocols*, Methods in Molecular Biology, vol. 915,
DOI 10.1007/978-1-61779-977-8_1,

also retaining good depth of field. The resolution of the human eye (unaided) is in the region of 100 μm, which is around the diameter of a human hair. Observing anything smaller than this requires some assistance. A light microscope will resolve structures less than 1 μm in size, but with limited contrast and depth of field. This is simply due to the wavelength of light and our ability to "squeeze" it into a small enough space to resolve an object. As SEMs use electrons rather than light as their source of illumination it is possible to resolve structures as small as 0.4 nm with the latest generation of in-lens field emission scanning electron microscopes.

Current SEMs can be divided into three basic categories:

Standard high vacuum SEMs using a tungsten or LaB_6 electron source.

Low vacuum and environmental SEMs (ESEM), allowing the operator the choice of imaging in high or low vacuum, and ESEM for the additional ability to image at water vapor pressure.

Field emission SEM for high resolution imaging and analysis.

A modern standard high vacuum standard SEM using a tungsten filament will typically achieve a resolution of around 3 nm, assuming a conductive sample with high electron yield. Low vacuum and ESEM instruments may achieve similar performance but at the expense of some resolution with increasing chamber pressure.

As SEM chamber pressure increases, the primary electron beam is scattered by the gas molecules in the sample chamber (5), resulting in a broadening of the beam diameter (6), and a corresponding reduction in resolution. Although there are some mechanisms for dealing with this it is always good practice to use the minimum gas pressure necessary to counteract charging at the sample surface. If 10 Pa is sufficient to control the charging there is little point in using 50 Pa chamber pressure as the primary beam will be scattered unnecessarily, with a consequential reduction in resolution.

As an imaging technique, the primary beam from an electron microscope has the potential to excite many different signals from the surface of a sample (Fig. 1).

As the electron beam scans across the sample in a raster pattern, signals of different energies are excited from the sample surface and may be detected. These signals include secondary electrons, backscattered electrons, X-rays, photons, and electron beam-induced current. Other signals may also be detected, but for the purposes of this study the secondary and backscattered electrons will be considered.

Because the passage of electrons is readily scattered or even stopped in a gaseous environment, an electron microscope column and sample chamber operate in a vacuum, typically at a pressure of 10^{-3}–10^{-5} Pa or better, depending on the type of microscope.

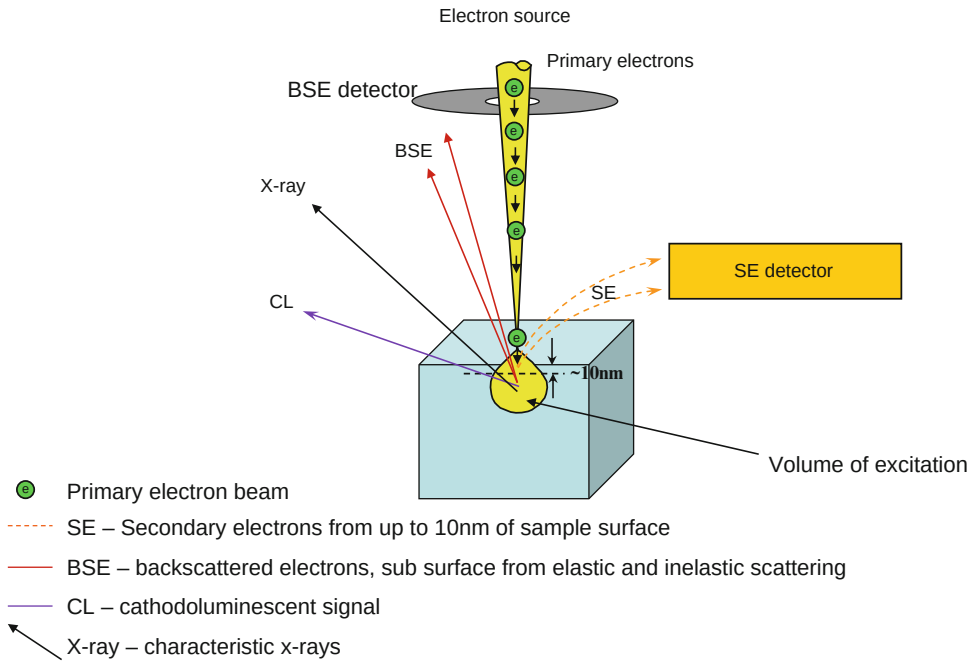

Fig. 1. Illustration of the interaction of the primary electron beam with a specimen surface, and the resulting excitation of signals.

Field emission microscopes, for example, operate with a gun vacuum better than 10^{-8} Pa.

The high vacuum of the electron gun and column allow for the efficient acceleration and focus of the primary electron beam through the column, condenser lenses, and objective lens. A scan generator rasters the electrons across the surface of the sample. The x, y area (size) of the raster also determines the on-screen magnification. A magnification module scales the size of the raster to fit the SEM imaging monitor; making the raster smaller gives a corresponding increase in magnification, and vice versa. A scale, usually calibrated to show mm, microns, or nanometres is displayed on the SEM screen and is usually accurate to ± 5%.

The beam is focused on to the sample surface by the final or objective lens, sometimes referred to as the pole piece. By changing focus, the current in the objective lens changes and controls the position at which the raster interfaces with the sample surface. When the raster is at the sample surface the sample is in focus.

Apart from the greater magnification range offered by the electron microscope when compared to light microscopy, the other great benefit of the technique is depth of field, the extent to which a topographic area on a sample is all in focus at the same time. Because electrons have a much shorter wavelength than visible light, the depth of field or focus achieved by the electron microscope is greatly improved. At low magnifications (< ×100) an SEM

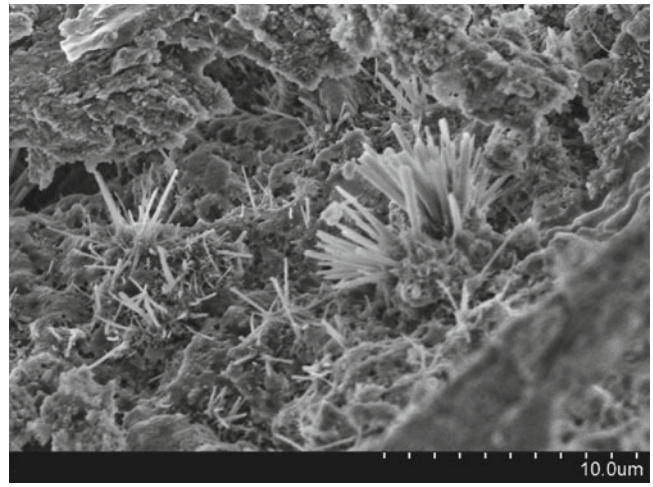

Fig. 2. Gypsum crystals in sample of plaster show the depth of field capability of the SEM. Scale bar = 10 μm. Original magnification ×5K.

can achieve a depth of focus of a few millimeters. Although this depth of focus reduces as magnification increases, it is still possible to image complex surfaces and keep the majority of the imaged area in focus. Apertures associated with the objective lens can also be employed to change the angle of divergence of the electron beam to the sample surface, thus helping to control the depth of focus achieved; a 50 μm aperture will give a better depth of focus than a 100 μm aperture (Fig. 2).

When an electron beam is rastered or scanned across a sample, the beam forms a scanning spot or point of interaction with the sample surface, usually 0.4–5 nm in size. This spot of electrons is moved across the sample in a raster pattern, forming a three dimensional teardrop-shaped area of excitation. The size of the excitation area will be dependent on accelerating voltage (kV), the spot size of the electron beam (specimen current) and density of the sample material (Fig. 3). The larger the spot size/higher the beam current, the larger the area of excitation and interactive volume of the electron beam to the sample surface. A dense conducting material, such as a metal, will have a smaller interactive volume than a less dense sample such as plant tissue.

This teardrop-shaped area of excitation forms an interactive volume of primary electrons having inelastic and elastic scattering events with orbiting electrons and atomic nuclei in the sample surface. (7). Inelastic scattering describes both a change in trajectory and energy of the electron beam, resulting in the transfer of energy from the primary electron beam to the specimen after collision events with nuclei and orbiting electrons, culminating in the emission of secondary electrons (Fig. 4), characteristic X-rays and other energies.

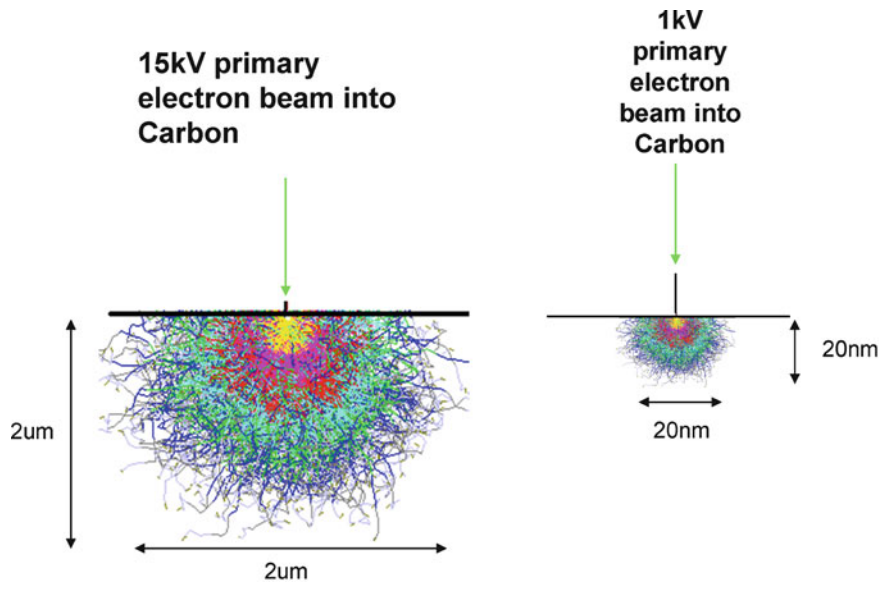

Fig. 3. Monte Carlo simulations to illustrate beam:sample interaction volumes. The volume of excitation is dependent on sample density and thickness, accelerating voltage of the primary beam and beam current. Here it can be seen that at 15 kV the resulting interactive volume in the sample surface is in the region of 2 μm^3, where a beam of only 1 kV will excite an area of around 20 nm^3.

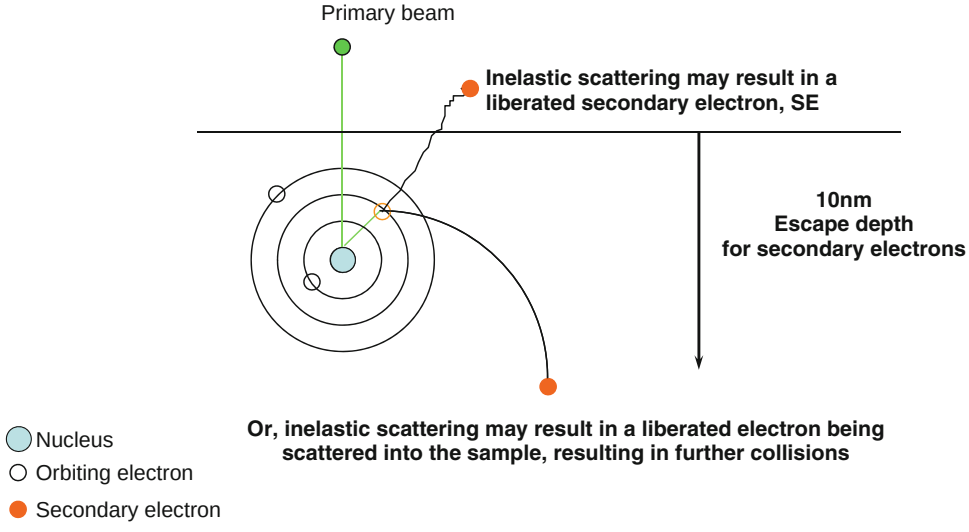

Fig. 4. Secondary electrons. Some electrons from the primary beam may collide with orbiting electrons in the sample, becoming inelastically scattered.

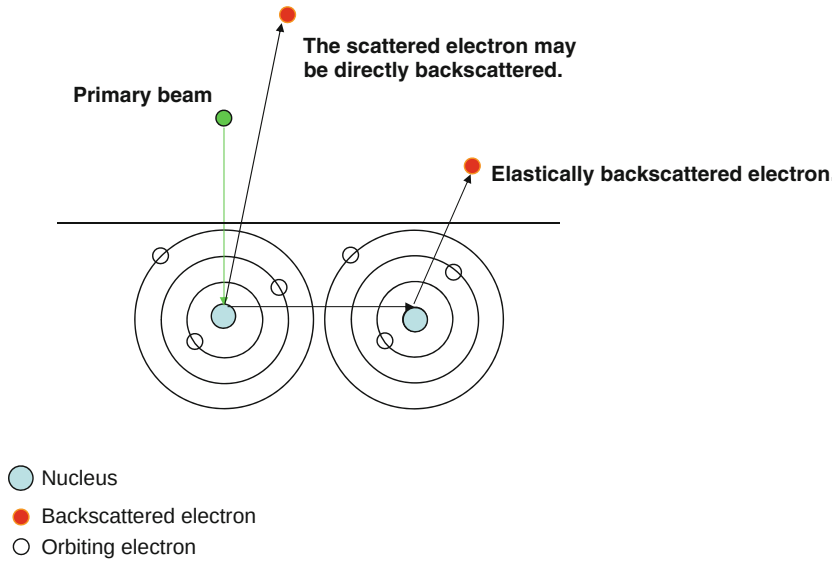

Fig. 5. Backscattered electrons. The nucleus of an atom retards the primary electron beam energy and deflects the beam. The deflected beam will have many additional collisions with other nuclei or orbiting electrons, resulting in backscattered electrons some distance from the point of primary beam excitation.

Elastic scattering occurs due to the deflection of the primary electron beam by the positive charge of the nucleus of an atom in the specimen, resulting in a change of trajectory for the electron but its energy remains the same. The derived interactive volume of energy formed in the specimen gives rise to backscattered electrons (Fig. 5).

Depending on the accelerating voltage (usually in a range from 0.1 kV to 30 kV) and density of the sample, an electron beam may penetrate the surface of a sample by just a few nm to a few microns. Remember, the beam will form a three dimensional area of excitation. Inelastic interactions with nuclei and electrons within the surface of the sample may remove an orbiting electron from the sample. This liberated electron (a secondary electron) may escape from the surface of the sample without any further collisions or interactions, and be detected by a secondary electron detector.

These secondary electrons (SEs) are low-energy electrons, with energies <50 eV. As a result any secondary electrons excited at the sample surface may only have sufficient energy to escape from the upper 10 nm of the sample surface, if its trajectory is correct. Any SEs with a different trajectory or from more than 10 nm below the surface may not have sufficient energy to escape from the sample, and will not be detected. Secondary electrons show absolute surface contrast (Fig. 6) as a result of surface topography in the sample; areas of the sample with topography facing the SE detector will be brighter than areas where SEs have been generated from areas in apparent shadow, due to topography between the point of electron generation and the SE detector itself (Figs. 7 and 8).

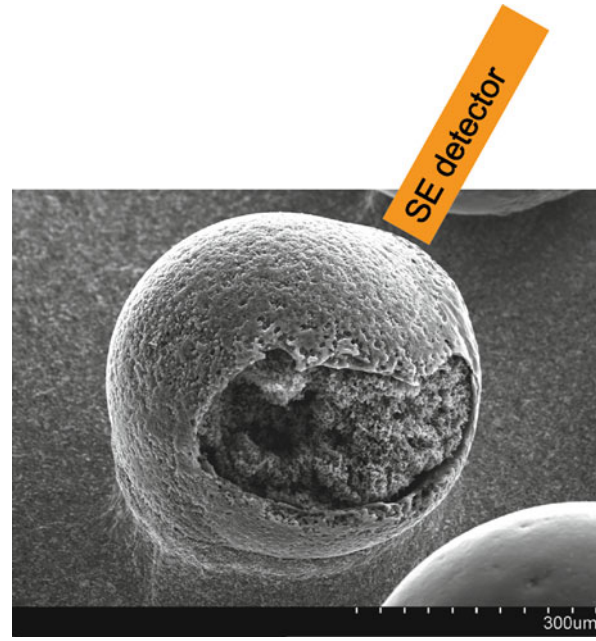

Fig. 6. Secondary electron (SE) image of a nano powder bound within a bead, to show surface contrast and shadowing. The SE detector in this case is positioned in the NE area. The sample surface facing, and close to the detector shows high brightness and contrast levels. The fractured area of the sample facing away from the detector shows shadowing. Scale bar = 300 μm.

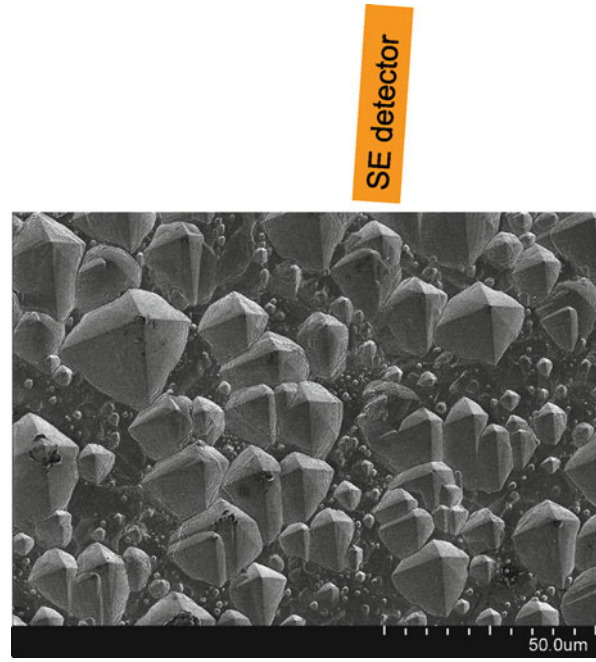

Fig. 7. SE image of a solar cell surface to show directional shadowing related to surface relief in the sample. Scale bar = 50 μm.

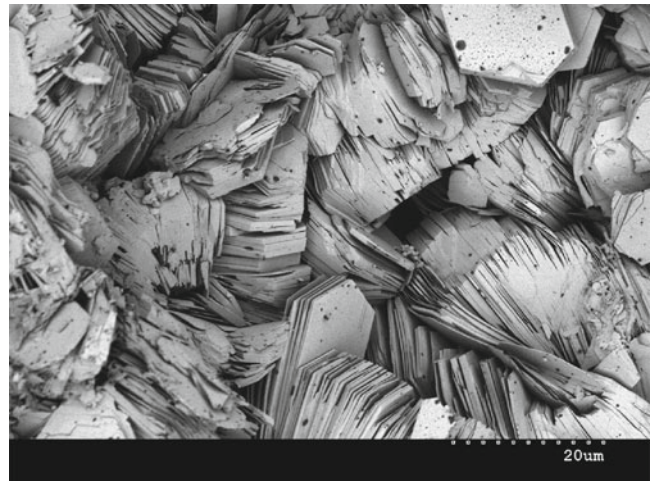

Fig. 8. Topographic contrast in clay minerals. Scale bar = 20 μm.

The SE detector is normally of the Everhart–Thornley type (8), consisting of a biased grid or collection ring, a coated scintillator (for example, coated with phosphor), photo multiplier tube and finally the microscope's display mechanism or viewing monitor. SEs are attracted to the detector by a positive bias voltage on a grid or ring close to the detector. As the attracted electrons collide with a scintillator surface at the front of the detector, photons are generated for each electron collision. Each photon is photo-multiplied and is finally displayed as a gray level per pixel on the microscope's imaging screen. A proportion of the backscattered electrons will also be attracted to the SE detector and contribute to the final image, although most of the backscattered electrons will be traveling too fast to be attracted by the bias of the SE detector.

Backscattered electrons (BSEs) are much more highly energetic, with energies from >50 eV up to the energy of the primary electron beam, for example, 20 kV. Most backscattered electrons are generated when a primary electron has an elastic scattering event with a nucleus, resulting in the electron either being directly backscattered from the nucleus and out of the sample surface, or being deflected by the collision with the nucleus by >90° and going on to have further collisions with either orbiting electrons or other nuclei. Elastically backscattered electrons may have energies up to 80% of the primary electron beam energy.

A cascade of inelastic scattering events will generate both secondary and backscattered electrons, which continues as the primary electron beam scans across the sample surface.

As BSEs have much higher energies than SEs, their trajectory and speed requires a detector to be placed between the sample surface and objective lens. Most high energy BSEs are traveling too fast to be influenced by the bias of the SE detector, mounted on

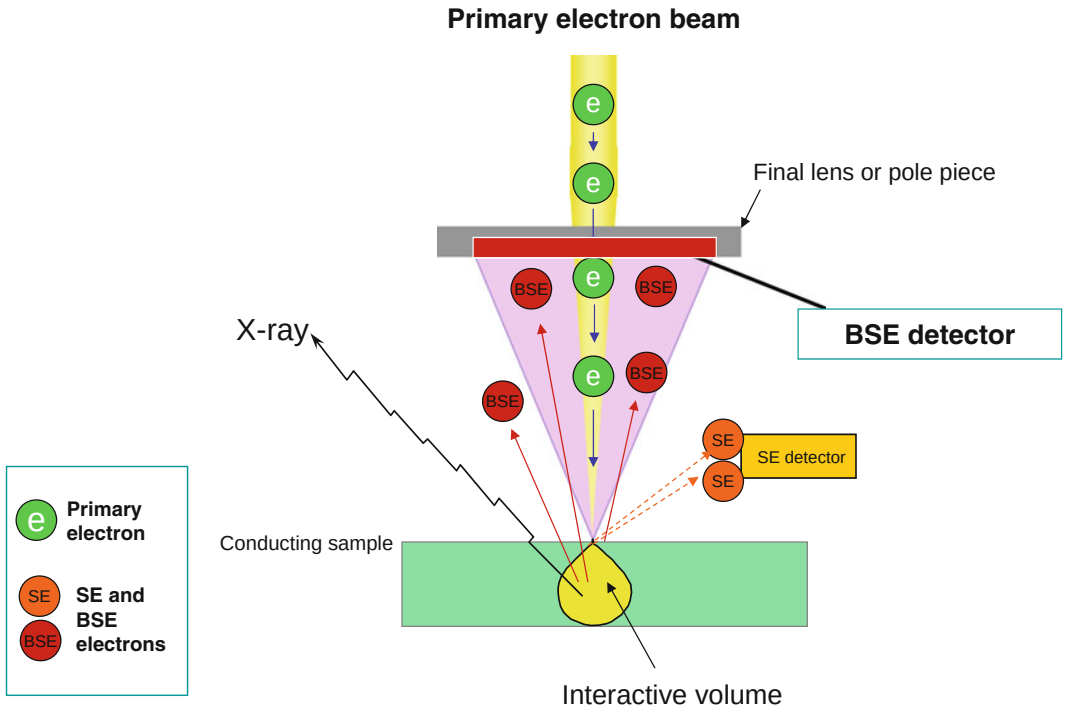

Fig. 9. Collection of elastically backscattered electrons. The backscattered electron (BSE) detector is positioned directly below the final lens or pole piece.

one side of the SEM chamber. Consequently a BSE detector will normally be positioned directly below the objective lens, as an efficient position to collect the highly energetic BSE signal (Fig. 9).

BSE detectors may be one of two types; a scintillator using a doped collection surface, light pipe and photomultiplier tube, such as the Robinson detector. Alternatively, and more commonly, the BSE detector will be a solid-state device, using p–n junctions across a detecting surface to generate an image (Figs. 10 and 11).

High energy electrons associated with the primary beam will have a collision event with a nucleus and be elastically reflected or backscattered from the nucleus, and out of the sample surface. Heavier elements (higher atomic number) backscatter electrons more strongly than lighter elements, so a heavier element will contribute more signal to an image and form a brighter area than the signal from an adjacent lighter element. A BSE detector will show differences in elemental contrast in a sample (Fig. 12).

Solid-state detectors may have a surface of just two diodes, four evenly sized quadrants or even five segments (Fig. 13), where a fifth segment is positioned off-axis from the primary beam, allowing collection of high energy BSEs to the regular four quadrants, and lower energy/trajectory BSEs to the fifth segment.

Fig. 10. SE image (*left*) showing topographic contrast and BSE image (*right*) showing elemental contrast. Scale bar = 500 μm.

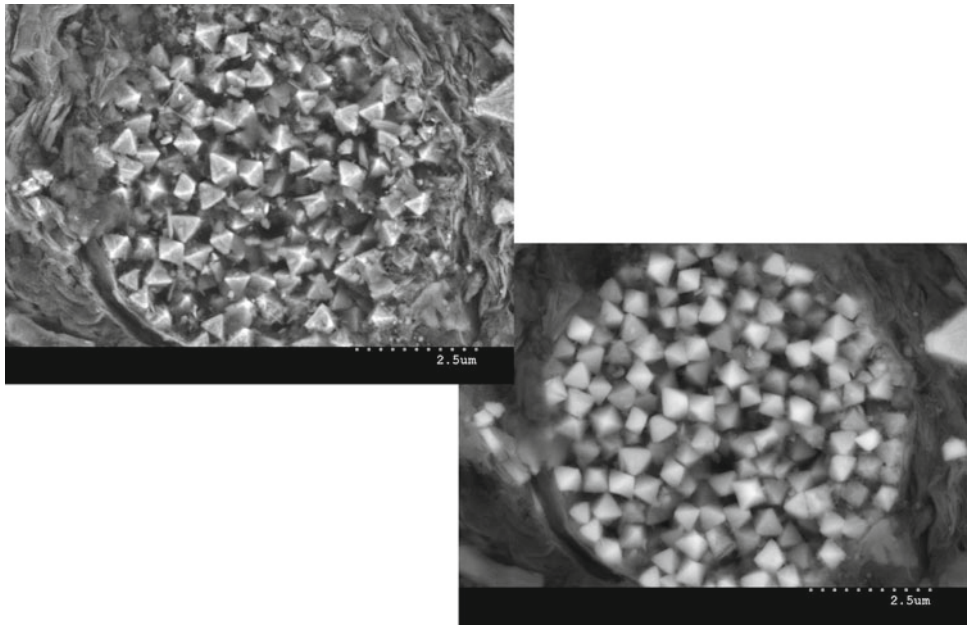

Fig. 11. SE image (*left*) of iron pyrite grains within a clay matrix. BSE image (*right*) of the same field of view showing the difference in elemental contrast and brightness between the pyrite (*bright*) and clay (*darker*) matrix. Scale bars = 2.5 μm.

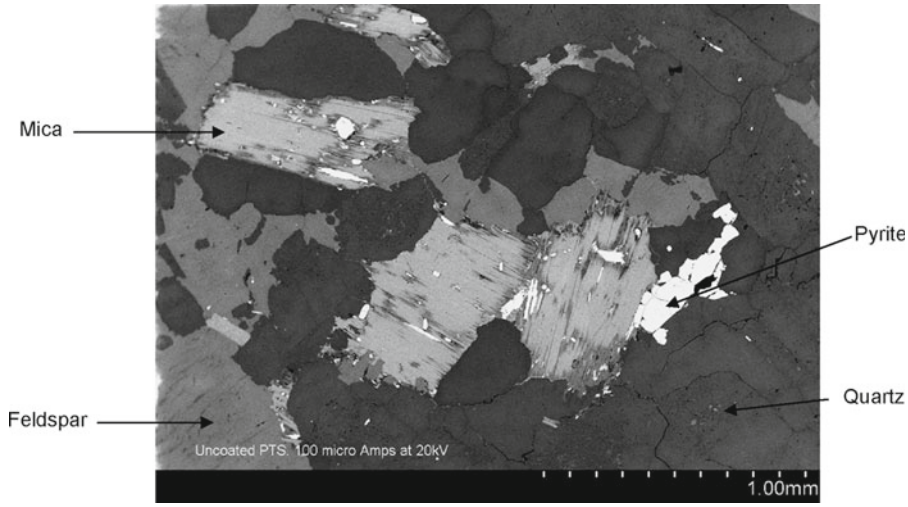

Fig. 12. Backscattered electron image of a geological thin section showing differences in elemental contrast. The brighter the area the heavier the element. Scale bar = 1 mm.

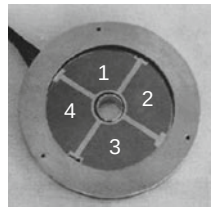

4-quadrant solid state backscattered electron detector

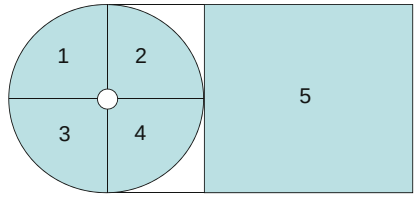

5-segment solid state backscattered electron detector layout

Fig. 13. Typical solid-state detectors utilizing either four equally sized quadrants for BSE collection or 4 + 1, with the fifth segment positioned off-axis from the electron beam, for the capture of lower angle and trajectory backscattered electrons.

The advantage of the five segment detector is its ability to image both elemental contrast and topography.

With the BSE detector placed in an annular collection position below the objective lens, the detector may collect symmetrically to all its surfaces and produce an image of elemental contrast. However, it is also possible to switch the bias voltage to each individual segment to allow preferential collection to one side of the detector only, resulting in topographic contrast at the expense of elemental contrast.

Most SEMs will have some standard "auto" collection settings for the BSE detector, but may also offer the operator the ability to set things up manually, depending on the image information required, for example, topographic or shadow modes.

Because BSEs are more highly energetic than SEs and are generated from a larger region of excitation, likely to be >10 nm below the sample surface, the resolution of BSEs is less than that achieved by SEs.

2. Materials and Methods

Much has been published on the subject of preparation techniques for biological SEM, including volumes already within this series of Methods in Molecular Biology (9).

As this chapter forms a review of current and established techniques relating to electron microscopy for the study of bone material, a number of key references have been considered which should provide the researcher with the relevant information relating to techniques such as specimen fixation, dehydration, and coating.

2.1. Preparing the Sample

Preparation of biological material for SEM follows many of the initial procedures and protocols used for TEM sample handling. A suitable sample must be processed using techniques suitable to:

Preserve a representative part of the sample for examination.

Ensure the sample has retained its original three dimensional morphological characteristics.

The sample is prepared in such a way to be robust enough for examination in the high vacuum or variable pressure environment of the SEM chamber.

In order to achieve this a specimen will be cleaned, trimmed or dissected, chemically fixed, dehydrated or dried, mounted, coated (if appropriate), and examined in the SEM.

2.2. Sampling and Chemical Fixation

Before preparation begins it is important to ensure the specimen selected for examination is representative. Bearing in mind SEM is a surface examination technique, the specimen must be clean and prepared in such a way to thoroughly and robustly preserve the tissue and its associated structure. The specimen will have to be adequately prepared to withstand examination in a high vacuum environment, without any degradation such as shrinkage.

Samples will normally be dissected as appropriate, before fixation in a suitable chemical aldehyde. The fixation stage is used to preserve the structure of the cells and tissue, usually through a process of cross-linking the labile organic molecules. It is essential that correct health and safety protocols are adhered to as the

chemical fixatives cannot distinguish between the sample tissue and those of the preparatory. Therefore, appropriate personal protection and laboratory equipment must be used, such as suitable gloves and a fume cupboard with adequate extraction for the purpose. A standard glutaraldehyde-osmium tetroxide protocol was developed (10), using primary fixation of 4% glutaraldehyde followed by a secondary or post fixation process using osmium tetroxide. This post fixation reacts with lipids, oxidizing the fatty acids and adds both density and contrast to the tissue. Solutions must also be correctly buffered according to tissue type to reduce the possibility of introducing artifacts. Buffers can be toxic and, in some cases, may be carcinogenic so always follow appropriate laboratory procedures and check MSDS data. Many current laboratory protocols are variations on Sabatini's method, with adjustments made to suit the particular tissue or cell type, or adjustment to the pH of the solutions suitable to the sample. Again, osmium tetroxide is a dangerous chemical, readily reacting with any living tissue so must be used with extreme caution and appropriate equipment, such as nonporous gloves and a fume cupboard.

Hayat (11) details many methods for the preparation of cells and tissue for electron microscopy, including methods to ensure the fixative solution used is approximately isotonic with the cell or tissue fluids. Nowell and Pawley (12) give additional information relating to suitable methods for specific tissue types.

As a general rule, the two-stage fixation protocol briefly described above will adequately prepare samples up to 1 mm in size. Anything larger is unlikely to be fully infiltrated by the fixatives before they start to chemically fix the cells.

Once a specimen has been chemically fixed, it is washed several times to remove any remaining residue from the fixatives and rinsed in a pH-balanced buffer, suitable for the specimen cells or tissue.

2.3. Dehydration

Following the fixation process, the specimen must be dehydrated using a controlled procedure. This is to ensure all remaining water is replaced and removed to prevent the collapse of tissues or any shrinkage during a dehydration process. In most instances air drying is not possible because of the resultant surface tension of the water/air interface causing such a great localized force, sufficient to cause tissue collapse and shrinkage of up to 80%. A surface tension of as much as 2000 PSI (13) can be applied to the specimen surface during air drying, so it is generally avoided.

However, the use of chemical dehydration at standard room temperatures and pressures (14, 15) has been used with some degree of success in more recent years.

Specimens can be dried using one of a number of methods, including critical point drying and freeze drying.

Critical point drying is commonly used for biological tissue, cells, and bacteria. It is a routine procedure carried out in the

Fig. 14. Typical sample baskets for retaining specimens during critical point drying process.

Fig. 15. A typical bench to Critical point drier, connected to a liquid withdrawal CO_2 cylinder.

laboratory, using a dehydrating fluid such as an acetone or ethanol series. Specimens are placed in a sample holder or basket (Fig. 14) and subjected to a dehydration process using a graded series of solutions of acetone, methyl, or ethyl alcohols in concentrations typically from 15, 30, 50, 70, 90, 95, and 100% to gradually replace the water in the sample. As 100% alcohol and acetone solutions are hygroscopic it is good practice to store the solutions over a drying agent before use, to ensure no further introduction of water is allowed to take place during the dehydration process.

Once the sample is in 100% solution (and a number of solution changes have been cycled) the sample and its dehydrating fluid is transferred to the critical point dryer (Fig. 15) chamber (sometimes

also called a "bomb!"). The dehydrating fluid is then gradually replaced with a transitional fluid, such as liquid CO_2 in a closed chamber. Once the dehydration fluid has been replaced with a number of changes of the transitional fluid (in this case liquid CO_2), and the sample is immersed in only the transitional fluid, the chamber of the critical point dryer is heated. As the liquid CO_2 heats in the closed vessel, the pressure of the vessel increases. At a temperature of 31.1 °C, and a chamber pressure of 1073 PSI the critical point for liquid CO_2 is reached, the liquid CO_2 passes directly from the liquid to gaseous phase, without boiling, leaving the sample in a dense gaseous environment of CO_2 vapor. At this critical point, the liquid and gas phases of the transitional fluid are in equilibrium without any phase boundary, so the specimen has no surface tension. As a result the specimen is not subjected to any surface tension pressures. The sample is now dry, and the vessel can be gradually vented to atmospheric pressure to allow removal of the specimen, maintaining the heat in the vessel to prevent formation of condensation. The dry samples are ready to be mounted to a suitable substrate and coated, if necessary, prior to imaging and analysis.

Critical point drying is not without its problems and can cause shrinkage in some types of tissue (16, 17).

Alternatively, freeze drying requires the specimen to be frozen rapidly from its postfixed and washed aqueous and buffered state, followed by rapid evacuation in a suitable vacuum chamber. By maintaining the sample at <–80 °C under vacuum prevents crystalline ice formation, which may damage cell structure, although cryo protectants such as glycerol can be utilized. (16). The low temperature and vacuum condition will slowly sublime the amorphous ice from the specimen, allowing the frozen water to move directly to the gaseous phase and be pumped away, leaving a dry specimen. However, this can be very slow process, depending on the size of the specimen.

2.4. Specimen Mounting

Before a specimen can be mounted it is worth considering a number of points:

What type of substrate to use?

How to attach the specimen to the substrate?

Orientation of the specimen.

Whether a conducting coat needs to be applied.

2.5. Substrates

Different substrates serve different purposes. A standard aluminum mount or stub may be suitable for many specimens, forming a conductive base to be attached to the SEM stage. Stubs are available in a number of sizes and formats and provide a suitable flat substrate for imaging the specimen. However, if the specimen is also going to be analyzed it is likely that the resulting analytical results will

also have a contribution from the composition of the substrate, for example, Al X-ray lines from the aluminum stub. To avoid such contributions from the substrate, samples and substrates can be carbon coated, or the sample can be mounted using a carbon-based adhesive. Alternatively the sample can be attached to the stub using a double-sided self-adhesive carbon tab.

Specimens embedded in resin blocks may be mounted in a suitable block holder, but may also need coating to ensure good electrical continuity to the microscope stage. However, samples can be imaged and analyzed uncoated if the SEM can be operated in variable pressure or environmental mode.

It is also possible to use a variety of accessories to help position specimens on the substrate, perhaps to assist in achieving a specific orientation or holding an area of the sample back to avoid obscuring an area of interest. Metal clips, pins, sprung clamps can all be utilized for such tasks. These accessories can also be painted with colloidal carbon to prevent too much signal contribution in the image from the clips, pins, etc., for example, when imaging pin-mounted insects.

2.6. Attaching the Specimen to the Substrate

Many materials are available for this purpose but those most commonly used include self-adhesive carbon tabs and tape, self-adhesive aluminum or copper tape, conducting silver paint (dag), conducting epoxy resin, carbon paint, or colloidal graphite. Each has its own advantages and disadvantages. For example, silver dag is effective for attaching bulk samples to a stub but may flow over smaller samples and obscure useful information. Self-adhesive carbon tabs are readily available and cheap to buy but can cause out gassing in the SEM chamber and, if used for high resolution imaging, samples may be seen to be drifting under the beam as the adhesive on the tab surface moves in the high vacuum of the microscope. Try to plan ahead to ensure mounting is done in a timely manner, especially after taking time to prepare a sample correctly. It is also important to ensure the glue is suitable to use both with the specimen but also in the vacuum environment of the SEM, and the electron beam. Where possible, place mounted specimens in a warm drying oven <40 °C for a few hours to ensure adhesives have cured thoroughly and to reduce the amount of out gassing in the SEM chamber.

Some adhesives are only temporary, allowing removal of the specimen after study either for archiving, further examination at a later date or for remounting in a new orientation. Other adhesives form a permanent bond, such as some of the two part epoxy resins. These can be very effective but must be given adequate time to cure thoroughly to achieve their full strength. It is best to avoid the rapid-curing epoxy resins as cure exothermically, giving off heat that may have an adverse effect on the specimen. In addition, some of the rapid-cure epoxies also shrink as they cure, causing damage to the specimen.

Fig. 16. Sputter coater.

Many of the epoxy resins are nonconductive so the sample and adhesive surface may also need to be coated to form a conductive surface for the electron beam. Witcomb (18) made a comprehensive study of many of the commonly used mounting media.

2.7. Orientation of the Specimen

Consider the shape or morphology of the specimen and the orientation(s) required to image the areas of interest. Although a modern SEM will have the flexibility of 5-axis stage movement it can still be useful to mount a specimen in such a way to assist in the imaging result, for example, on a pretilted stub to orientate a specimen toward a detector or to mount a specimen to ensure part of its anatomy does not obscure the area of interest. Look at the geometry of the SEM chamber and the position of the detectors with respect to the stage and the stage movement. An understanding of the sample to detector position can ensure samples are correctly orientated for both morphological illustration and correct illumination and shadowing. A secondary electron detector positioned to the North East side of the sample will show shadowing on the South East side of the sample, whereas a solid-state backscattered electron detector will give more of a top-down, evenly illuminated view with less directional shadowing.

2.8. Coating

Metal coating is applied to a specimen surface to aid signal generation but also to prevent the buildup of a charge on a nonconducting surface. Charging can cause displacement of the primary beam, resulting in some unsightly imaging artifacts. Samples may be coated in a sputter coater (Fig. 16) or evaporative coater, preferably with an attachment to monitor the coating process to determine

the thickness of coating being deposited. Sputter coaters fitted with a Peltier-cooled sample holder will deposit a surface of finer-grained coating, as well as thinner film thickness than that achieved by a coater without the benefit of Peltier-cooled stage or holder.

Typical coating materials include carbon, gold, gold-palladium, platinum-palladium, platinum, and chromium. A coating thickness of up to a few nm is usually sufficient to form a sufficiently conducting surface; 1–3 nm for high resolution imaging, up to 10 nm for other applications.

For irregular-shaped samples a coating unit with a tilting and rotating stage can be a more efficient method of ensuring good distribution of metallic particles across the whole specimen surface. Coating thickness will, of course, vary with topography and orientation of the sample to the metal target. A coater fitted with a motorized tilt and rotate stage will apply a more evenly distributed coating than one with a static stage.

The type of coating material selected is determined by how the specimen will be examined. Of course, by coating a specimen you are introducing an artifact which, for all intents and purposes, is permanent. Although there are some chemical techniques available for the removal of coating surfaces from samples, they are difficult to use and not particularly effective.

Samples for imaging only can be coated with any of the metals listed above. However, each has its own advantages. For example, gold coating alone will lay down an even thickness of highly conductive metal but does tend to form "islands" of gold, separated by surface cracking. None of this texture is visible at magnifications below something in the region of ×30K. However, if higher magnifications are required it is worth considering using something like Gold-palladium as the coating metal. This will deposit a much finer texture than gold alone, so is suited for high resolution imaging. Platinum is also suited to high resolution imaging, but gives less contrast in the image when compared to samples coated with gold-palladium. Chromium is another good choice for high resolution imaging, but samples must be examined in the SEM immediately after coating as the chromium will quickly oxidize in air, causing a deterioration of the coated surface.

If samples are going to be imaged and analyzed then a different choice of coating metal may be required. The selected coating surface should not mask any X-ray energy peak positions for elements being analyzed, or form any peak overlaps which may be problematical during peak de-convolution methods. Carbon is the most common choice of coating media for samples requiring X-ray microanalysis in the SEM. It is easily applied either using carbon rods in an evaporative coater or from carbon string/fiber in a sputter-type coater (using an appropriate high tension head). A thickness of just a few nm of carbon can be deposited on the sample

surface, giving both a conducting surface but also one suitable for light element analysis if required.

It is also possible to image and analyze samples without applying any surface conductive coating, either by using variable pressure SEM (VPSEM) or ESEM.

VPSEM has been available commercially since the 1970s but has benefited from the development of detectors capable of working in gaseous or partly hydrated environments. ESEM has been available since the late 1980s and can be used for imaging and analysis of samples in a hydrated condition at (if required) atmospheric pressure. There are of course limitations to both techniques, such as beam skirting and a reduction in resolution. Stokes (19) has published a useful book detailing the differences between the techniques and their development. Tang & Joy (20) describe an experimental model to investigate beam broadening in the VPSEM chamber.

Jirak et al. (21) has described the mechanisms for collection of the gas-amplified secondary electron signal.

References

1. LaneWC (1970) The environmental cold stage. Proceedings of the Third Scanning Electron Microscopy Symposium, IIT Research Institute, Chicago, IL, 60616
2. Danilatos G (1989) Mechanisms of detection and imaging in the ESEM. J Microsc 160(pt. 1):9–19
3. Von Ardenne M (1938) Das Elektronen-Raster Mikroskop (The scanning electron microscope). Z Tech Phys 19:407–416
4. Von Ardenne M (1938b) Das Elektronenmikroskop; Theoretische Grundlagen (The scanning electron microscope: theoretical fundamentals). Z Phys 109:553–572. Z Techn Phys 19, 407
5. Moncrieff DA, Barker PR, Robinson VNE (1979) Electron scattering by gas in the scanning electron microscope. J Phys D Appl Phys 12(4):481–488
6. Craven JP, Baker FS, Thiel BL, Donald AM (2002) Consequences of positive ions upon imaging in low vacuum SEM. J Microsc 205(1):96–105
7. Newbury DE et al (1987) Advanced scanning electron microscopy and X-ray microanalysis. Plenum Press, New York
8. Everhart TE, Thornley RFM (1960) Wideband detector for micro-microampere low-energy electron currents. J Sci Inst 37:246–248
9. Nasser Hajbagheeri MA (Ed) (1999) Electron microscopy methods and protocols. Methods in Mol Biol Vol 117. Humana Press
10. Sabatini DD, Bensch K, Barrnett RJ (1963) Cytochemistry and electron microscopy. The preservation of cellular ultrastructure and enzymatic activity by aldehyde fixation. J Cell Biol 17:19–58
11. Hayat MA (1982) Fixation for electron microscopy. Academic, New York
12. Nowell JA, Pawley JB (1980) Preparation of experimental animal tissue for SEM. Scan Electron Microsc Pt 2:1–19
13. Anderson TF (1951) Techniques for the preservation of three dimensional structure in preparing specimens for the electron microscope. Trans NY Acad Sci, Series 2 131: 130–134
14. Conway K, Kieman JA (1999) Chemical dehydration of specimens with 2,2-dimethoxypropane (DMP) for paraffin processing of animal tissues: practical and economic advantages over dehydration in ethanol. Biotech Histochem 74(1):20–26
15. Carr JH, Anderson RL, Favero MS (1996) Comparison of chemical dehydration and critical point drying for the stabilization and visualization of aging biofilm present on interior surfaces of PVC distribution pipe. J Appl Microbiol 80(2):225–232

16. Boyde A (1978) Pros and cons of critical point drying and freeze drying for SEM. SEM/1978/II, SEM Inc., AMF O'Hare, IL, pp 303–314
17. Boyde A, Macoonachie E (1979) Volume changes during preparation of mouse embryonic tissue for scanning electron microscopy. Scanning 2, 149. Witzstrock Verlag Baden-Baden
18. Witcomb MJ (1981) The suitability of various adhesives as mounting media for scanning electron microscopy. J Microsc 121:289
19. Stokes DJ Principles and Practice of Variable Pressure/Environmental SEM (VP-ESEM). Royal Microscopical Society. ISBN 978-0-470-06540-2
20. Tang X, Joy DC (2005) An experimental model of beam broadening in the variable pressure scanning electron microscope. Scanning 27(6):293–297
21. Jirak J et al (2010) Scintillation SE detector for VP SEM. J Microsc 239(3):233–238

Chapter 2

Plastic Embedding and Polishing of Bone for Reflected Light and Electron Microscopy

A.H.J. Wighton, Chris G. Jones, and Lynne S. Bell

Abstract

The successful embedding of bone or any sample for reflected light or electron microscopy is crucial to the success of any analysis that might follow. Different materials present different embedding challenges, and here we discuss bone. Embedding is developed often as an adapted in-house protocol, and will vary from one institution to another, and is barely referenced in any detail in scientific papers. This chapter provides the protocol for bone that has proved successful at the Natural History Museum, both for reflected light and particularly for scanning electron microscopic examination.

Key words: Bone, Resin, Plastic, Mould, Abrasive, Scanning electron microscopy, Light microscopy, Polish

1. Introduction

Plastic embedding of bone is a basic and critical first step toward microscopic examination either by reflected light or a form of scanning electron microscopy (SEM). The protocols to achieve this are often given in short form in scientific papers and the necessary skill set cannot be developed without a certain amount of trial and error, and differing laboratories will have their own approach. The embedding of a range of materials at the Natural History Museum (NHM) has been ongoing for a good number of years, and we felt that it would be useful to provide the NHM protocol in long form as a guide to those who may wish to embark or adapt their own embedding protocols.

Lynne S. Bell (ed.), *Forensic Microscopy for Skeletal Tissues: Methods and Protocols*, Methods in Molecular Biology, vol. 915, DOI 10.1007/978-1-61779-977-8_2,

2. Materials

2.1. Polishing Materials and Embedding Resins

Loctite 358 UV curing resin (250 mL).

1000 grit silicon carbide paper (18 μm). Cat no. 30-5218-010.

2500 grit silicon carbide paper (10 μm). Cat no. 30-5218-025.

Texmet 1500 polishing cloths. Cat no. 40-7618.

Diamond suspension, 6 μm polycrystalline. Cat no. 40-6632-032.

Diamond suspension, 3 μm polycrystalline. Cat no. 40-6631F-032.

Diamond suspension, 1 μm polycrystalline. Cat no. 40-6630F-032.

Samplkup moulds. For mounting samples. Cat no. 20-9178.

All the above are available from: Buehler UK/USA/Germany, metsales@buehler.co.uk

Specifix-20 Kit (see Note 1). Available from: Struers Ltd, www.struers.co.uk, info@struers.co.uk.

0.3 μm Ultra Fine Aluminum Oxide Powder (see Note 2). Cat no: 0CON-015. Available from: Logitech Ltd., info@logitech.uk.com, www.logitech.uk.com.

2.2. Equipment

1. Logitech GTS1 cut-off saw (see Note 3). The blade is a 12″ continuous rimmed blade.
2. Logitech LP50 Lapping machine (see Note 4).
3. 10″ Metaserv 2000 Twin Lap Grinder Polisher (see Note 5). Variable speed control 50–500 rpm.
4. Logitech PM5 Polishing machine. This polishing machine has a 12″ lap and is capable of holding six samples at one time.
5. Logitech model 15 Saw (see Note 6).
6. Technomat low pressure impregnation chamber (see Note 7); requires an external source of compressed air.
7. Petro-thin (see Note 8).
8. Low power reflected light binocular microscope.

3. Method

The method outlined is specific to the plastic embedding of bone that has been rendered into a dry state and does not have any soft tissue or fat adhering to the sample.

3.1. Separating Bone as a Block

Cut the selected bone sample using a water-irrigated rock cutting diamond edged saw or dental drill (see Note 6) to the required size. Cut the specimen to obtain a straight edge and make the

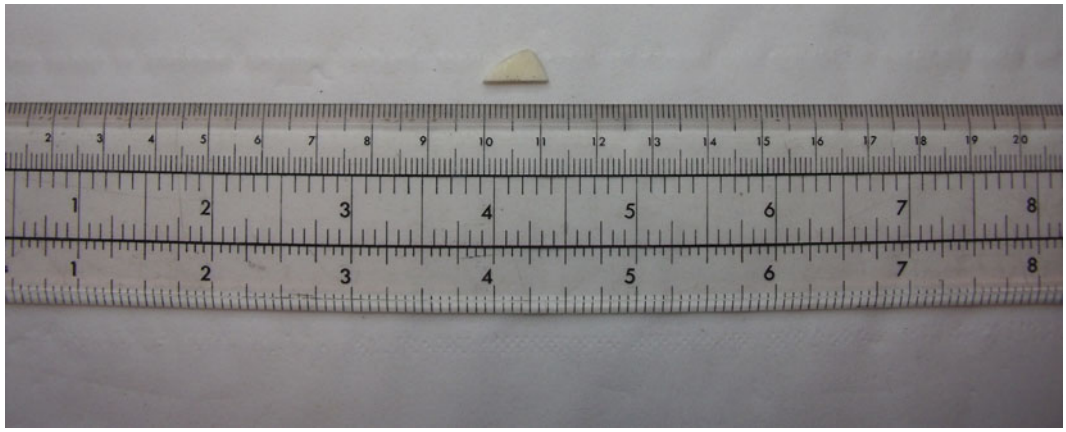

Fig. 1. Bone sample after cutting with diamond saw.

parallel cut immediately afterwards in order to make the top and bottom of bone perfectly plane parallel (see Note 9) (Fig. 1). The thickness of the bone sample is determined by the type of analysis to be undertaken.

3.2. Drying Block

Dry the sample thoroughly to ensure any water/fluids from the cutting/grinding process have been removed. Sample may be dried at room temperature or at an appropriate elevated temperature in an incubator or drying oven over an extended period. Do not attempt to speed dry as this may cause the bone to crack or distort.

3.3. Grinding Prior to Embedding

Once a suitable surface has been cut to expose the relevant structures, the bone sample must be ground flat using the LP50 rotary lap with a fixed abrasive diamond wheel/cloth of 125 μm grade or using the silicon carbide papers given at the beginning of Subheading 2. This initial polishing step is necessary to remove some of the damage left by the cutting tool on the bone surfaces, and to ensure the surface for preparation is reasonably flat.

3.4. Mould Preparation and Labeling

Ensure the sample has been clearly labeled, either on the back face of the sample or by inserting a paper label and number into the Metset mould (see Note 10) (Figs. 2, 3, and 4). Wipe the inside of the mould with a suitable releasing agent such as silicon grease.
The sample should be placed face down (the surface that will be examined microscopically) in the mould and the resin gradually poured from one side, slowly filling the mould (Figs. 5, 6, and 7). Try to avoid trapping air between the sample and the resin.

Once the resin is above the height of the sample by 5–10 mm tap the mould firmly on the laboratory bench a number of times to help dislodge any trapped air bubbles. The sample and resin can be left on the bench or in a fume cupboard (follow the MSDS information for the product) for the resin to cure overnight (see Note 11).

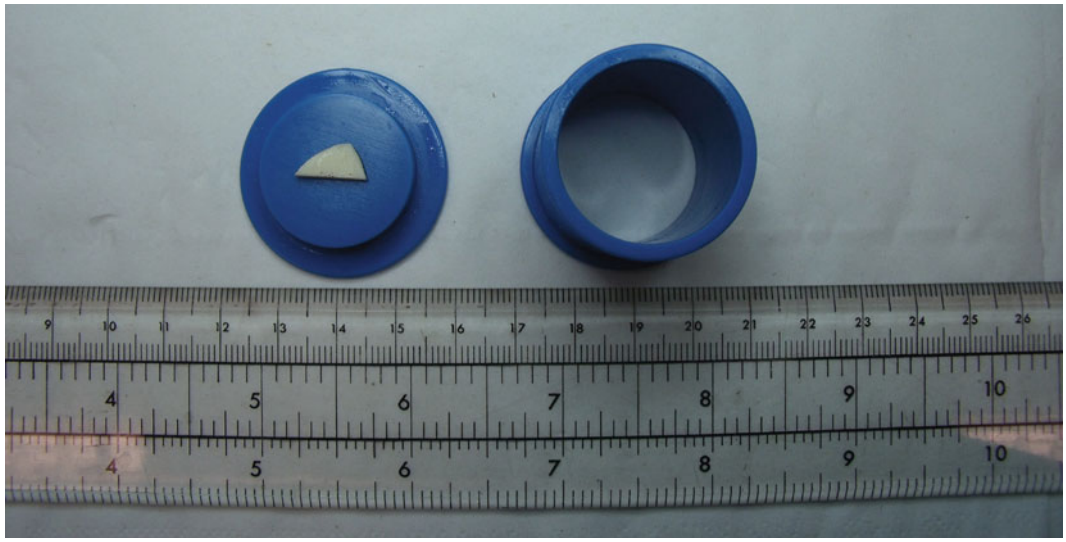

Fig. 2. Mould (25 mm) containing the cut bone sample. The mould and its backing have been wiped with releasing agent, e.g., silicon grease.

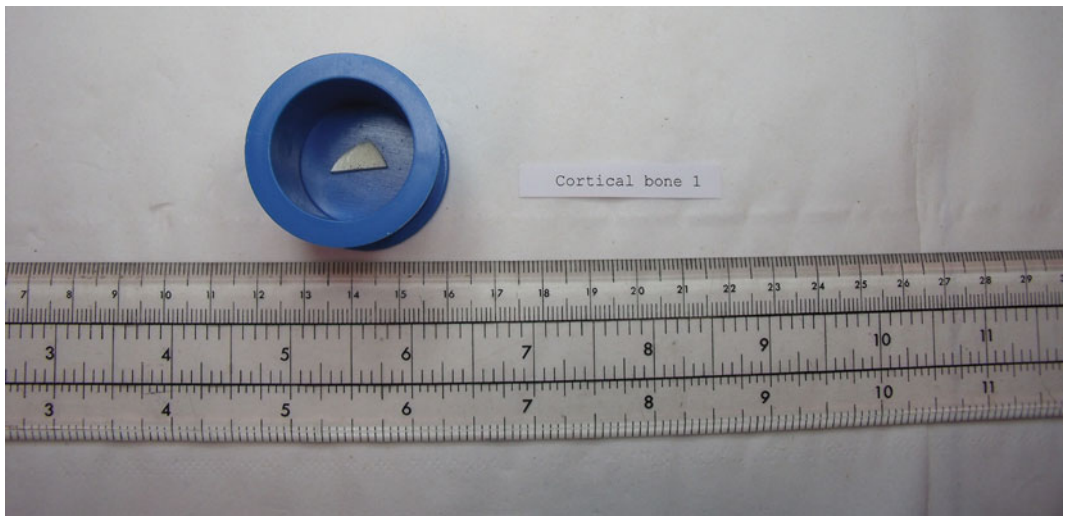

Fig. 3. The sample label has been printed and will be embedded with the sample.

Once the resin has cured it can still be worthwhile standing the sample in an incubator or oven at 30 °C for an hour to ensure the resin has fully cured and the top-most surface layer is not tacky.

3.5. Pressure Vessel Embedding Alternative Step

Alternatively, the resin-encapsulated sample and mould can be placed in a pressure vessel to facilitate infiltration of the sample with resin.

Place the resin filled mould in a pressure vessel (e.g. a Kulzer Technomat) at an air pressure of 2 Mbar overnight. This will help ensure thorough impregnation of the bone by the resin (see Note 12).

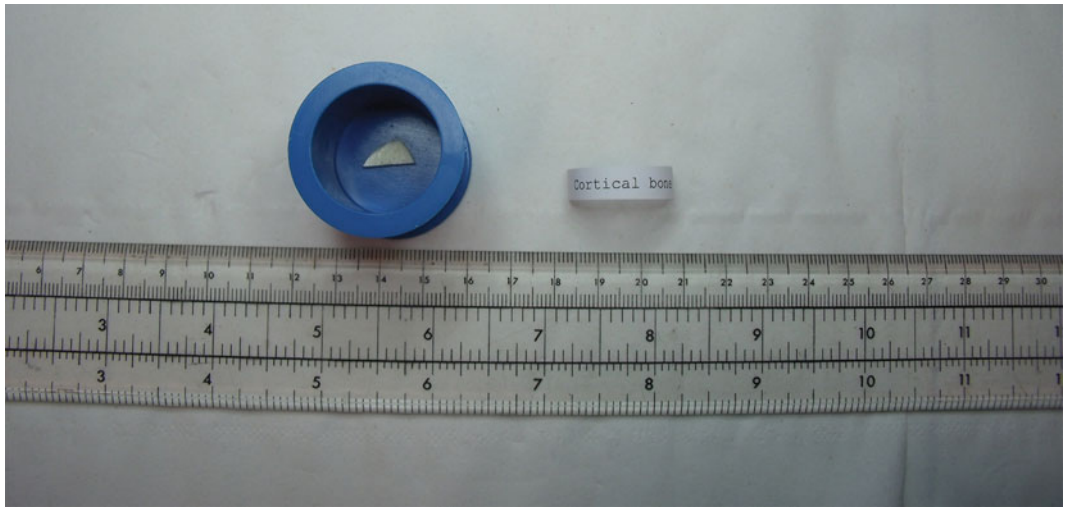

Fig. 4. As previous image, except the label has been drawn along the edge of a blade to curl it allowing it to fit snuggly inside the circular mould.

Fig. 5. The sample will be embedded in an epoxy resin suitable for examination using light or electron microscopy. In this case, SpeciFix 20 Resin has been used.

3.6. Removal from Mould

Once the resin has hardened (overnight) the resin block containing the sample can be removed from the mould. Remove the backing to the mould and press the sample out (Fig. 8). A new mould may take considerable force to release the sample.

Fig. 6. Mix the two-part epoxy (resin and hardner) following manufacturers' guidelines. Wait for air bubbles to dissipate in the resin before pouring slowly down one side of the mould until resin has submerged sample. Fill to a depth a few mm above the back of the sample.

Fig. 7. The resin has been poured leaving the sample in the center of the mould and the label wrapped around the inside of the mould surface. Tap the mould firmly on the bench to dislodge any trapped air between the mould, sample, and resin interfaces.

3.7. Coarse Block Preparation

The cut surface and back face of the resin block can now be prepared to ensure front and back faces are parallel. This can be done by hand using a rotating grinding wheel or a machine such as a Buehler Petrothin (see Note 8) (Fig. 9). In the example case, a diamond saw can be used to remove excess resin from the back of the resin block, before grinding flat with a diamond wheel. Leave a thickness of a few mm plain resin on the back face of the block (Figs. 10 and 11). Grind the front face of the block, containing the bone sample, on a

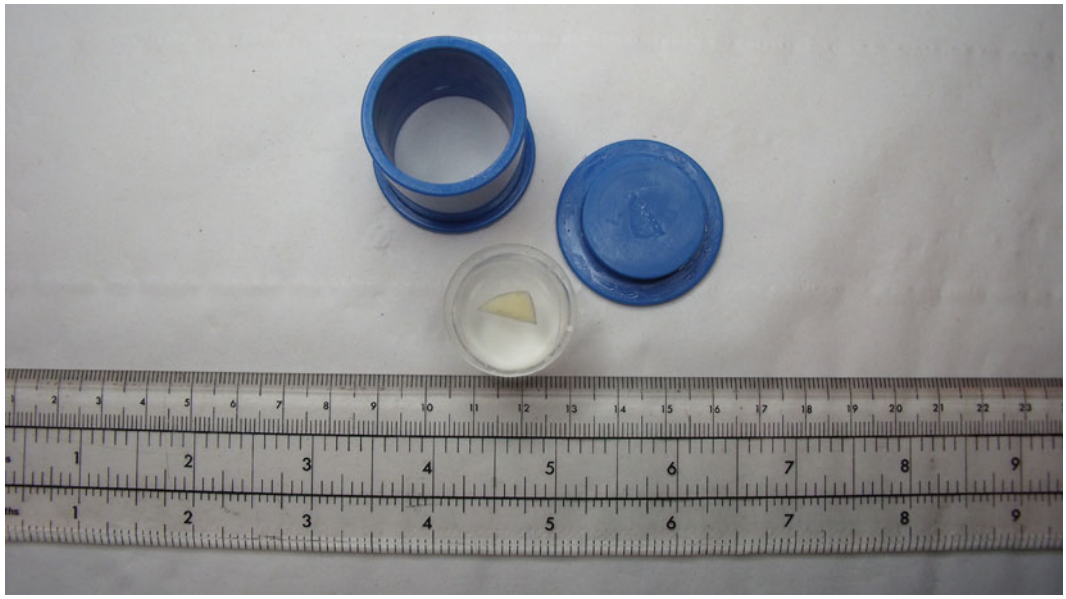

Fig. 8. Once the resin has been allowed to cure (usually overnight at room temperature), the resin block can be removed from the mould by removing the base and pressing out the block.

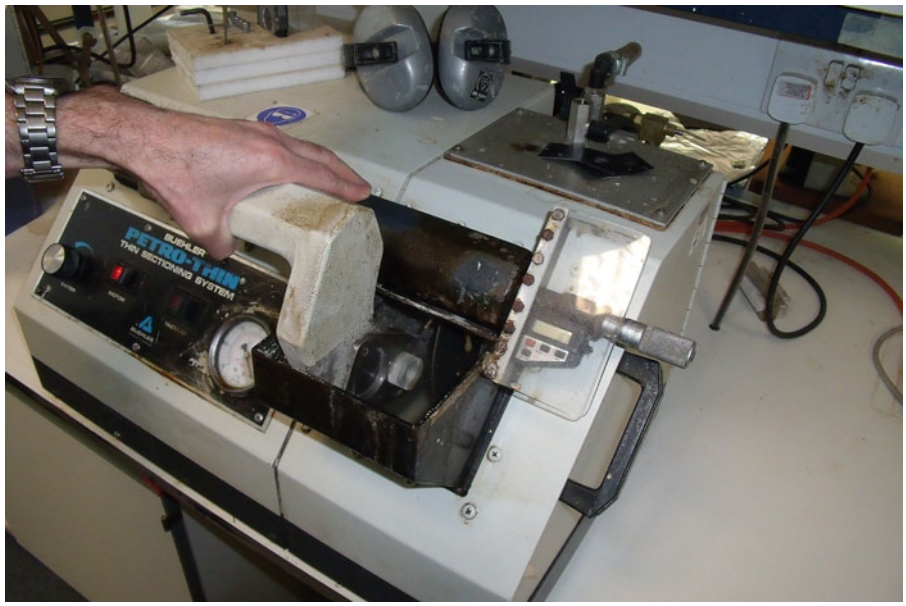

Fig. 9. The resin block is held in a chuck and excess resin is removed from the back of the block by using a diamond saw blade, cooled by water. A few mm of resin is retained at the back of the block.

rotary lap diamond grinding wheel to remove the initial surface of resin from the front face of the bone sample (Fig. 12).

Once the sample has been evenly exposed and a flat parallel surface prepared on the grind wheel, the sample can be transferred to a suitable machine for further grinding, prior to polishing.

Fig. 10. The diamond saw removing the excess resin from the back of the block, leaving a few mm of resin behind the bone sample.

Fig. 11. The block has now been reversed in the chuck, allowing the front face with the bone sample to be exposed for grinding.

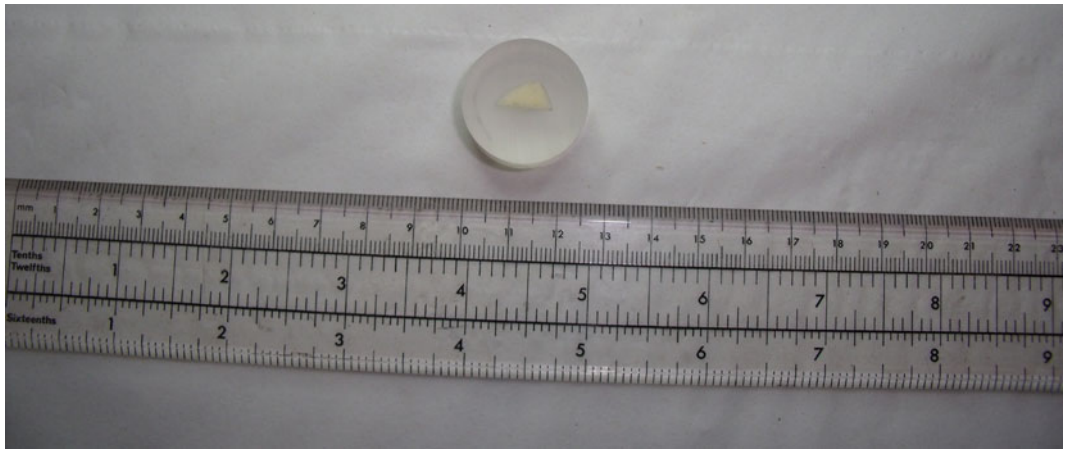

Fig. 12. The embedded sample following impregnation where the cutting has ensured the front and back surfaces are parallel and the bone surface has been exposed for grinding.

3.8. Staged Abrasion of Block

The authors used either a Struers Rotopol V or Metaserv 2000.

Both machines are twin-wheeled rotary grinding/polishing machines. For the following grinding stage, the machines were run at a speed of up to 150 rpm, with plain water running across the cloths for cooling/lubrication.

Fixed abrasive diamond discs on a metal (magnetic) back plate are used for gradual removal of bone material, reducing the abrasive size of disc until a suitable surface has been prepared for polishing. Use of the magnetic-backed cloths makes changes between abrasive grades very quick. Diamond cloths with a grain size of 125 μm followed by 74 μm should be used for the initial grinding process, changing to the finer grade once the initial cutting damage has been removed. Check the surface frequently to ensure flatness and a parallel surface, by reflecting the ground surface of the sample in a strong light source, at a low angle.

The aim of each stage of abrasive is to remove any surface damage/depth of damage left by the previous abrasive grade (seen as scratches) (see Note 13).

Once the initial grinding has been completed to a grade of 74 μm or less, move to a series of silicon carbide abrasive papers for finer grinding. Again, attach the papers to a suitable base to be used on a rotating wheel at a speed of up to 150 rpm.

Step through abrasive grades, moving to silicon carbide papers rotating at 150 rpm, still using plenty of water for cooling and lubricating the surface of the bone where it contacts with the grinding media. A basic rule of thumb is to use a paper with half the grit size of the proceeding step.

Clean the surface of the sample between each abrasive step using a soft brush under running water.

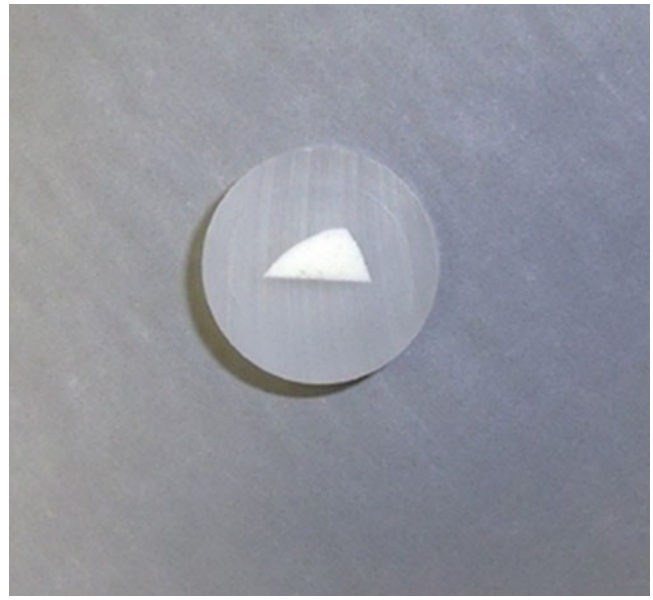

Fig. 13. Surface of bone after grinding to fully expose impregnated bone surface.

A suggested range of silicon carbide abrasive papers is:

P600 grit

P1000 grit

P2400 grit

P4000 grit

Check the surface of the sample and resin block to ensure all grind marks have been removed and the face is flat. Do this repeatedly (Figs. 13, 14, 15, 16, 17, and 18).

Chamfer (remove sharpness) the edges of the front face of the block to help prevent the block sticking to, or snatching against the polishing cloth.

3.9. Polishing the Block Face

First, drill a small hole a few mm deep into the center of the back of the block (Fig. 14). Do not drill into the sample itself. Proceed to clean surface of bone using a soft brush under running water.

Now that the surface of the bone has been ground to remove any damage from previous cutting and grinding steps it is ready to polish.

Polishing should be carried out on a rotating wheel using a suitable cloth, such as Texmet 1500. The cloths are available with adhesive backing or magnetic bases, for ease of changing. The polishing wheel is run at a speed of up to 150 rpm, preferably with the sample attached to an oscillating arm. A weight is attached to the back of the sample (see Note 14) (Fig. 19).

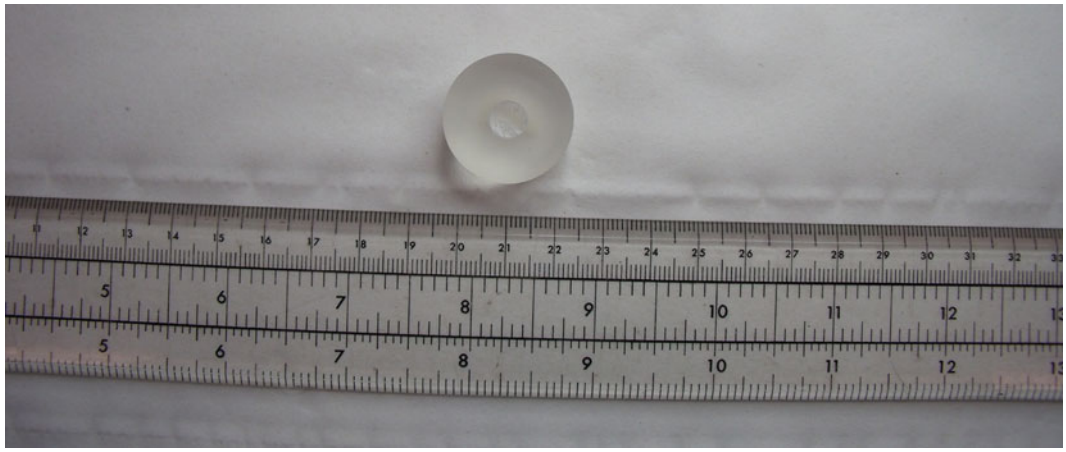

Fig. 14. A hole has been drilled into the resin at the back of the block. This hole is necessary to attach to the polisher arm.

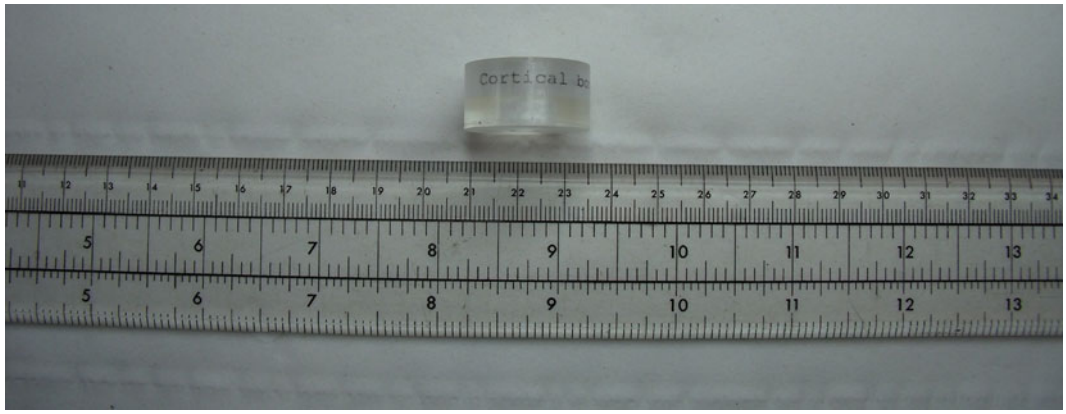

Fig. 15. The sample label can be clearly seen through the embedding resin.

The oscillating motion of the sample on the rotating polishing cloth allows the surface of the block to rotate freely to take up an evenly polished surface.

Just two polishing steps are likely to be necessary:

1. 0.3 μm Aluminum oxide (Al_2O_3) 50:50 by volume with water. Before starting the machine, charge the cloth with some of the aluminum oxide media. The polishing media has a hexagonal crystalline morphology, providing many abrasive facets and corners for the initial polishing stage. Allow the sample to polish on a rotating cloth at up to 150 rpm for around a minute before introducing a drip feed of distilled water for cooling/lubrication. The drip feed should be set for one drop of water every few seconds, or faster for soft samples. As the polishing process proceeds the abrasive gradually becomes worn, reducing the initial cutting nature of the grains and becoming finer over time.

Fig. 16. The surface of the embedded bone is ground flat using a series of abrasive diamond and/or silicon carbide papers. A continuous stream of water is used to keep the cloth and sample lubricated. The wheel is rotating at approximately 80 rpm.

Fig. 17. Inspecting the ground surface for flatness.

An initial polishing time of around 3 min may be sufficient to remove the damage from the P4000 silicon carbide grinding stage. Check the polished surface under a suitable reflected light microscope for any surface damage and scratching. If there is still a lot of damage or scratching, re-charge the cloth with polishing media and repeat the polishing stage for a further 3 min. Prolonged polishing with Al_2O_3 will cause

Fig. 18. Closer image of block face revealing no obvious imperfection in the flatness of the face.

Fig. 19. Once the sample is flat and has been ground to a suitable standard (P4000 grit paper) it can be transferred to a polisher. Initial polishing is carried out using a Texmet/Pellon cloth and a 0.3 mm Al_2O_3 in water, followed by 1 μm polycrystalline diamond paste. Another approach is to have staged polycrystalline pastes at 6, 3, and 1 μm polishing steps.

surface relief in the sample, due to differential polishing hardness of materials in the sample.

Once a satisfactory polish has been achieved, clean the surface of the sample with a soft brush under running water and proceed to the final polishing step.

2. 1 μm Polycrystalline liquid diamond in suspension. Use a Verdutex or RAM type polishing cloth. Charge the cloth with the diamond media and polish on a rotating wheel at up to

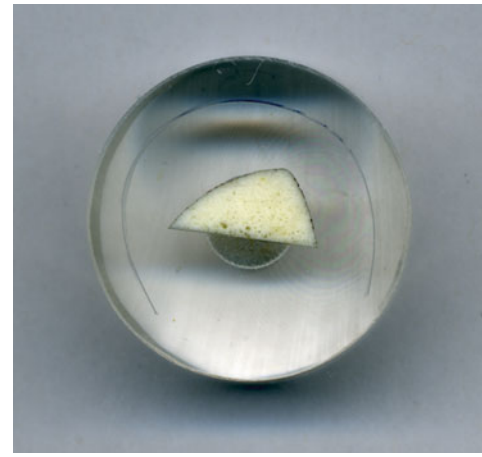

Fig. 20. The surface of the bone sample following the polishing process should have a clear glassy look with no scratches on the block surface when inspected under low power reflected light. The sample face has been cleaned using a soft brush and running water to remove any remnants of the polishing media (with robust specimens the sample may have been immersed in an ultrasonic bath for a few seconds).

150 rpm using an appropriate weight (150 g to 1 kg, depending on the hardness of the sample) behind the sample. Polish for around 1.5 min before cleaning and checking the surface of the sample under a reflected light microscope. Repeat this polishing stage until a suitable scratch and relief-free surface has been achieved, before final cleaning with a soft brush under running water (see Note 15).

The bone sample is now ready for reflected light microscopy and electron microscopy (Fig. 20).

4. Notes

1. Two part epoxy resin used to vacuum/pressure impregnate the sample prior to thin sectioning or preparing a polished block.
2. This polishing powder is used with distilled water (or non-aqueous liquids, for water-soluble material) on all samples where the use of aluminum oxide does not cause a problem with the analysis.
3. A general purpose cut-off saw for average sized samples.
4. This machine is mainly used for the production of thin sections, but is sometimes used to lap polished blocks prior to polishing. However, on bone material or porous/friable samples fixed silicon carbide abrasive papers are preferable, as they

minimize the effects of undercut and avoid the take up of loose abrasive into the sample.

5. Used mainly with silicon carbide papers for hand grinding samples, can also be used as a polishing machine.
6. A saw used to cut small samples either by hand or using a vice before mounting in resin, or cutting the impregnated sample prior to setting the sample in the resin block at the required orientation.
7. Works in the opposite way to vacuum. Pushes resin into the sample displacing the air in the process. A technique used in the Mineral Prep Lab is to vacuum impregnate the sample first, then before the resin cures transfer the sample to the pressure chamber to help force the resin further into the sample. It exerts a small amount of pressure 1–2 Mbar.
8. This is a thin section system, comprising a cut-off blade and a diamond cup wheel housed in a bench top unit. It is used to cut and grind the impregnated sample to expose the impregnated bone (or mineral/rock), and also to ensure the top and bottom of the block are parallel. The sample holder has been adapted to allow it to hold polished blocks, as this machine is designed primarily for the production of petrographic thin sections mounted on glass slides.
9. The type of blade and its thickness determines how much material will be lost as a result of the cutting process. This is an important point to consider if handling forensic or archaeological samples, or samples from museum or reference collections. As a general rule, the amount of material lost during the cutting process will be at least 1.5× the thickness of the cutting blade itself.

   When cutting bone, particularly if cutting dry, wear suitable personal protective equipment (PPE) and use appropriate extraction for air borne bone dust and particulates.

   In general, because of the brittle nature of dry bone it may be necessary to impregnate or embed the sample prior to cutting, to avoid any unnecessary splintering and proximal damage. The same applies to any grinding process that may be considered necessary. The decision to embed or not will largely depend on the sample, its context, what procedures will be used for its examination and whether the sample will be archived.
10. Metset moulds come in a variety of sizes. Choose the mould that most closely fits your sample but allows for all the edges of your sample to be fully encased by the resin.
11. Bear in mind the volume of resin required to embed the sample. Many epoxy resins have a greater exothermic reaction when resin and hardener components are mixed together if the volume mixed is too large. To overcome this problem when

embedding a large sample it may be necessary to introduce the resin in a number of stages, pouring a small volume at a time and letting the resin cure before the next stage.

12. This is preferable to using a vacuum vessel or vacuum oven as the epoxy resin can boil as the vapor pressure is reduced, or the resin may cure exothermally causing boiling of the resin and introduction of air.
13. Grinding is the mechanical process of abrading the surface of the sample against an abrasive that is fixed/attached to a substrate, such as a grind wheel or embedded in a cloth. By using a grinding process the risk of uptake of grinding compound into the bone surface is minimized. Lapping, on the other hand, is the process of abrading a sample against a free-moving abrasive and the risk of uptake of lapping compound is much higher for a porous material such as bone.
14. As a general rule, the softer the sample the smaller the weight used, and heavier weights for harder samples. A weight between 150 g and 1 kg will be sufficient, depending on the hardness of the sample and its components. Prolonged polishing with a lot of weight may produce a degree of polishing relief in the sample, either seen as hardness differences between the phases in the sample or polishing hardness differences between the sample and resin.
15. Diamond suspension abrasives 6, 3, and 1 μm may be used in stages if the surface proves difficult to clear of scratches.

Chapter 3

Preparation of Mineralized Tissue for Light Microscopy

Gail Valentine and Kim Piper

Abstract

Production of stained tissue sections for examination by light microscopy is a step-wise process which begins with preservation of tissue (fixation), then dehydration and clearing of the tissue, and finally impregnation with wax (processing). Mineralized tissues such as bone and teeth are subject to a further step (decalcification). Thin sections are then attached to a glass slide for staining and light microscopy.

In the UK, it is usual for a preliminary diagnosis to be made using hematoxylin and eosin (H&E) staining. A definitive diagnosis may need further investigation with immunocytochemistry. All of these procedures must allow morphology and tissue structure to remain in tact, as any pathology present must not be compromised.

Key words: Fixation, Decalcification, Processing, H&E staining, Immunocytochemistry

1. Introduction

1.1. Fixation

The aim of fixation is to produce a snapshot of the tissue as it is when still functioning in the body. Therefore fixation must prevent autolysis and putrification but also ensure retention of tissue components and structure. In practice, no fixative is perfect; the user must determine his/her own needs and select the appropriate method.

In our laboratory, the most common general fixative contains an aldehyde, formaldehyde (trade name Formalin). Tissue shrinkage and distortion are inevitable; however with the addition of salt and water this can be kept to a minimum, the resulting fixative is 10% formal saline.

Fixatives can be classified into several classes as below; however, this chapter will concentrate on aldehydes.

1. Aldehydes.
2. Oxidizing agents.
3. Coagulant (protein precipitating).

Lynne S. Bell (ed.), *Forensic Microscopy for Skeletal Tissues: Methods and Protocols*, Methods in Molecular Biology, vol. 915,
DOI 10.1007/978-1-61779-977-8_3,

4. Other cross-linking agents.
5. Physical.
6. Miscellaneous.

1.2. Aldehydes

This is a short mild reaction. Covalent bonds are formed between proteins especially lysine residues found on the exterior of the protein molecule (1).

The vast majority of skeletal specimens received in the laboratory are subject to routine investigation requiring fixation.

Small biopsies may be ready in 12–24 h; larger specimens may be up to 48 h or more. Adult teeth may take 4 days; younger teeth with a more open pulp cavity may only require 24 h. Teeth are fixed whole.

1.3. Undecalcified Bone

If sections are required prior to decalcification, the specimen can be fixed and then impregnated with methyl methacrylate (MMA) plastic; once set, these can be ground down to produce sections as thin as 3 μm according to the cutting/grinding system used or cut on a microtome. Ideally thin even slices of bone should be used. This can be achieved with a manual/automated band saw or more easily using a diamond saw. Any bone cut with a saw will have scratches and irregularities which must be ground down or sliced off with a fine toothed saw before examination under the microscope (2–6).

1.4. Decalcification

Bone consists of heavily mineralized collagen; the mineral (hydroxyapatite) consists of calcium, phosphate. and hydroxyl ions. In order to cut thin bone sections this mineral must be decalcified.

It is essential that fixation is complete as this will protect the bone and surrounding tissues from the effect of the decalcifying solution.

This can be achieved by use of reagents which react with calcium to form soluble calcium salts, such as strong acids (nitric and hydrochloric), weak acids (formic, acetic and picric), or chelating agents (EDTA) which take up calcium ions.

Retaining tissue morphology and antigenicity is essential for accurate diagnosis, so care must be taken to choose the correct form of decalcification and to ensure that over decalcification does not take place. This can be achieved by regularly monitoring the tissue using a decalcification endpoint test such as the calcium oxalate method or if available a radiographic method (e.g., Faxitron) (Fig. 1) (6, 7).

1.5. Processing

The aim of tissue processing is to enable thin sections to be cut; this is achieved by embedding in a solid medium. The most satisfactory embedding material for routine histology is paraffin wax. Most fixatives are aqueous based and these are not miscible with hydrophobic paraffin wax. The tissue must be processed in stages to enable impregnation with this medium. The first stage is dehydration

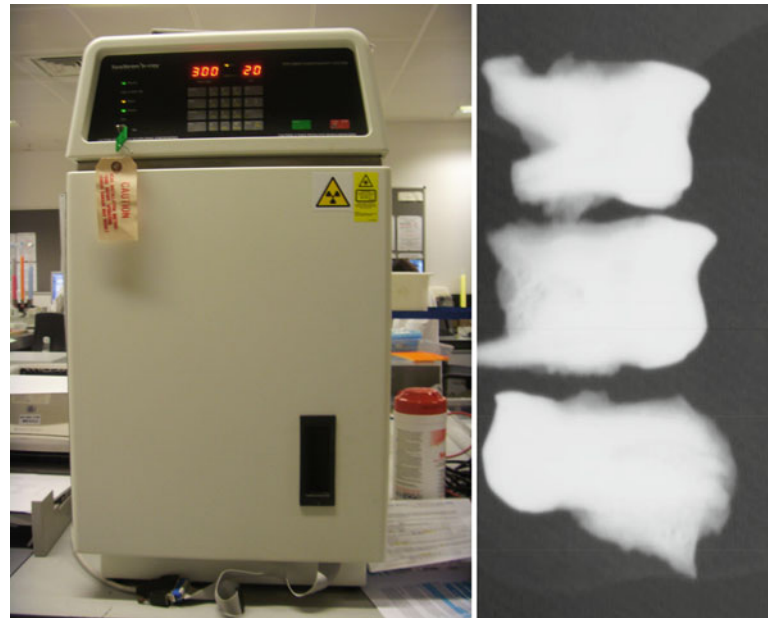

Fig. 1. Bench-top X-ray machine (Faxitron®), used to ensure optimal decalcification without having to transport specimens out of the laboratory. Radiograph of teeth demonstrating even and optimal decalcification. Regular radiographs can be taken at specific time points to ensure over decalcification does not occur.

using alcohol to remove excess fixative and water, followed by clearing with an intermediate reagent (xylene) designed to make the tissue miscible with the embedding medium. The final stage is impregnation with the embedding medium. Busy diagnostic laboratories have now automated processing which is usually run overnight. However hand processing and staining are still practiced.

1.6. Microtomy

The most common type of microtome is the rotary (Fig. 2) but sledge microtomes are also used.

Using disposable blades, thin sections can be accurately cut by setting the microtome to the required thickness. It is common practice to cut routine sections at 4 μm.

1.7. Staining

In order to visualize the tissue and any abnormalities present, the tissue must be stained. The routine stain in the UK is the hematoxylin & eosin (H&E). Hematoxylin is extracted from the tree *Haematoxylon campechianum*. The main oxidization component of this is hematein and it is this which colors the tissue. Hematoxylin is weakly anionic and has a poor affinity for tissue, so it must therefore be used in conjunction with a mordant (polyvalent metal cation) such as aluminum, iron, or tungsten salts. The mordant gives an overall positive charge to the dye-mordant complex and allows binding to anionic tissue sites such as nuclear chromatin.

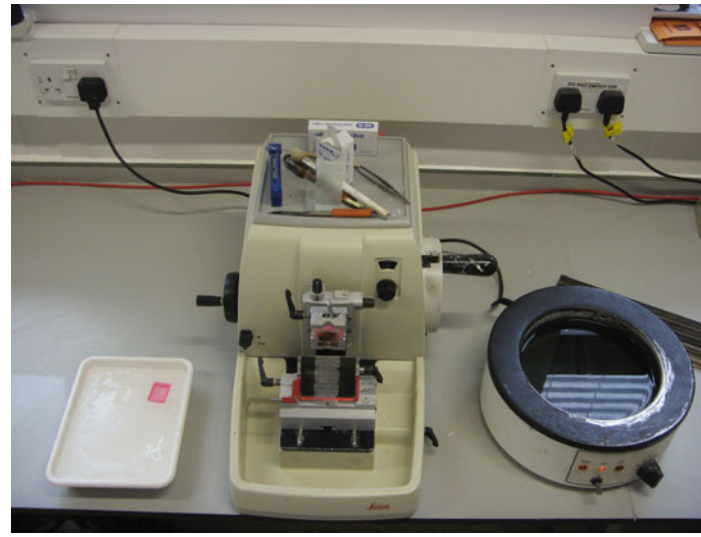

Fig. 2. Rotary microtome for cutting the decalcified and embedded specimens together with adjacent water bath to float the sections out.

In our laboratory H&E staining is used regressively, i.e., the tissue is overstained with hematoxylin which is then differentiated using acid alcohol to leave only the cell nucleus stained. After "blueing" in tap water (a process of using alkaline tap water to form a blue 1:1 non-ionic dye:mordant:tissue coordination complex), the tissue section is then immersed into eosin, a cationic xanthene dye which stains the anionic cytoplasmic cellular components, such as connective tissues.

Essentially the whole process to which the tissue has been subjected to when processing to wax is reversed in order to rehydrate the tissue to allow staining with aqueous dye solutions. In most diagnostic laboratories this is now virtually a universally automated process.

1.8. Immunocytochemistry

Immunocytochemistry is an extremely useful tool in the immunophenotyping and grading of tumors. In recent times it has also proven to be very useful in prognosis and has also found a role in targeted cancer treatment response prediction.

Visualization of antigen/antibody reaction can be achieved using a number of methods. In recent years supersensitive polymer kits have been introduced which have improved the sensitivity and specificity of reactions. Due to formaldehyde fixation many antibodies require antigen retrieval of tissue before they will bind to their antigenic site. There are several ways to break the formalin-induced bonds including enzymatic digestion, heat, and pressure. Several enzymes may be used including trypsin and, as here, protease. Pressure cookers and microwaves used in conjunction with antigen retrieval solutions also give excellent results (8).

1.9. Microscopy

It is important to set up a microscope correctly in order to achieve the optimum resolution and to avoid optical artifacts. It is particularly important when performing polarizing, fluorescence, or phase contrast microscopy and is absolutely essential when performing microphotography. The best way to do this is to set Kohler illumination.

2. Materials

2.1. Fixation (See Note 1)

Formal saline.

Formaldehyde (37–40% w/v) trade name Formalin is a respiratory irritant, toxic and carcinogenic; this must be used with some form of extraction either a downdraught table or fume hood.

For 10 L:

1. Weigh out 85 g of sodium chloride and add to a 10 L plastic container.
2. Measure 1 L of concentrated formalin (40% W/V). Add the formalin to the container (the specimen container should be more than 20× the volume of specimen).
3. Fill the reservoir with tap water to the 10 L mark.
4. Mix well.

2.2. Sodium Undecalcified Bone (See Notes 2 and 3)

Use a downdraught table or fume hood.

1. 50, 70, 90% ethanol.
2. 15 mL methyl methacrylate monomer (unwashed).
3. 15 mL dibutyl phthalate.
4. 1 g dried benzoyl peroxide (potentially explosive if exposed to heat or direct sunlight).

2.3. Decalcification (See Notes 2, 3, and 4)

Use a downdraught table or fume hood.

5 or 10% Formic acid (VWR 98%).

Calcium oxalate test (see Note 5)

1. Conc. Ammonia (VWR).
2. Litmus indicator solution (VWR).
3. Saturated aqueous ammonium oxalate (VWR).

2.4. Processing (See Note 5)

Use a downdraught table or fume hood.

1. Xylene.
2. 70, 95, and 100% Industrial methylated spirit/alcohol 99% 74 OP (IMS).

3. Histology wax (Leica).

2.5. Staining (See Note 6)

Use a downdraught table or fume hood.

1. Xylene.
2. 70, 95, and 100% IMS.
3. Gills 2 Hematoxylin: Leica.
4. 1% aqueous eosin: Leica.
5. 1% Acid Alcohol: 1% conc. Hydrochloric acid in 70% IMS/water.
6. Scott's Tap Water Substitute (S.T.W.S.):
   (a) Sodium hydrogen carbonate: 17.5 g.
   (b) Magnesium Sulphate (Hydrated): 100 g.
   (c) Tap Water: 5,000 mL.

2.6. Immunocytochemistry (See Note 7)

Antigen retrieval: Enzyme

Protease XIV (Sigma P-5147).

Phosphate buffered saline Instamed 9.55 g/L (Biochrom).

Antigen retrieval: pressure cooker

Antigen Unmasking Solution pH 6.0/8.0 (Vector H—3300/3301)

Peroxidase block

50 mL IMS.

750 µL concentrated Hydrogen peroxide (VWR 30%).

Antibody diluent (ZYTOMED Systems).

Supersensitive wash buffer (Biogenix HK583).

Biogenix Kit (Leica Bio systems).

Biogenix DAB:

20 mL Stable DAB buffer.

680 µL liquid DAB.

Gills 2 Hematoxylin (Leica).

3. Methods

The following standard operating procedures (SOPs) are adapted from those used within the Cellular Pathology, The Royal London Hospital (9).

3.1. Fixation (See Note 1)

Formal saline (10%).

The volume needed will vary from laboratory to laboratory.

1. Immerse trimmed tissue in fixative for 12–24 h.

3.2. Undecalcified Bone (See Notes 2 and 3)

1. Dehydrate through 50, 70, 90% ethanol 1 h in each (blocks $10 \times 5 \times 2$ mm).
2. Place in 100% ethanol for 1 h.
3. Repeat step 2.
4. Infiltrate in two changes of infiltration solution for 1 h.
5. Infiltrate in a further change overnight.
6. Embed in 10 mL aliquots of infiltration solution to which 125 mL of *N-N* dimethylaniline is added. Polymerization will occur in 2–3 h.

Hand grinding usually involves two glass plates, one of which is abrasive on one surface. The bone section is ground between the two surfaces.

3.3. Decalcification (See Note 4)

1. After fixation, discard the formalin and replace with 5 or 10% formic acid.
2. 5% for smaller specimens (for example BMT).
3. Large Oral Pathology specimens (e.g., larynx, mandible, and maxilla) are placed in 10% formic acid after cutting with a band saw.
4. The specimen container should be more than 20× the volume of specimen.
5. Write the start date of decalcification on the lid of the specimen pot using a permanent marker pen.
6. Ensure the specimen pot's lid is securely fastened.
7. Place the specimen pot on the orbital shaker table (IKA Laboratechnik digital KS501) (Fig. 3).
8. Ensure that the timer control dial is set for continuous movement.
9. Small specimens less than 1 cm maximum dimension can be removed from decal after 48 h.
10. Formic acid should be changed each day.

Calcium oxalate test (see Note 5)

1. Take 5 mL of the used decalcifying fluid from the specimen pot and place into a labeled test tube.
2. Add one drop of litmus indicator solution to the test tube and mix. Avoid too much indicator as it masks the test results.
3. Add concentrated ammonia solution drop by drop whilst swirling the test tube until the solution turns from red to blue (approximately pH 7.0).

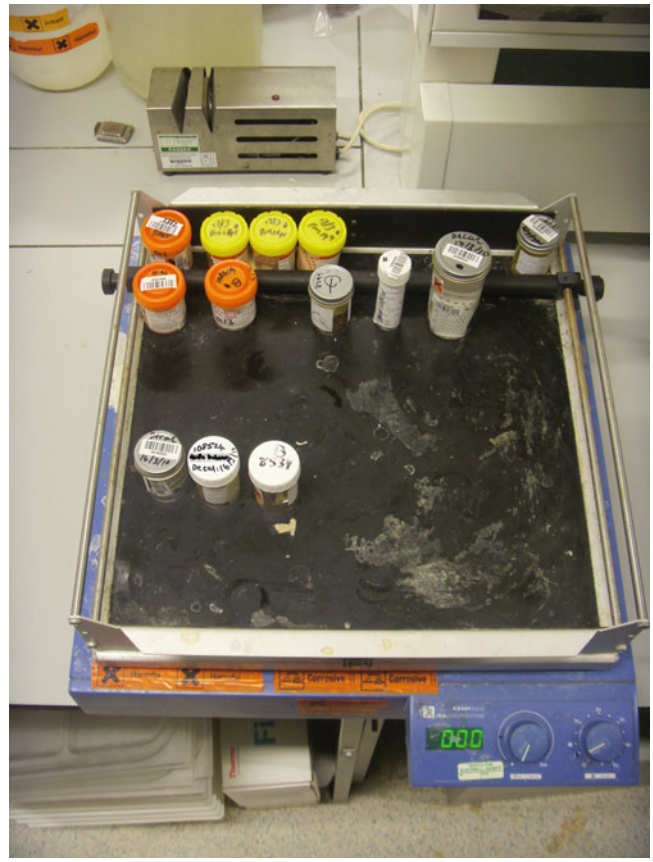

Fig. 3. The orbital shaker provides a more rapid decalcification process than using decalcification fluid within static pots.

4. Using a disposable Pasteur pipette measure out 0.5 mL of saturated ammonium oxalate and add. Shake well.
5. Allow the solution to stand for 30 min.

Results

A cloudy solution shows that there are still calcium ions in solution and therefore calcium is still present in the specimen. Change the formic acid decal solution in the specimen pot and replace onto the orbital shaker.

A clear solution shows that all calcium ions have been removed from the specimen and it can therefore be processed.

3.4. Processing (See Note 2)

1. Use 500 mL glass jars (xylene will melt unprotected plastic).
2. Add tissue, allowing 20 times the volume of fluid to tissue.
3. For identification purposes each tissue should have an individual labeled jar.

4. Add 70% IMS.
5. Place on a roller mixer for 1 h.
6. Discard and replace with 95% IMS for 1 h.
7. Repeat step 6.
8. Discard and replace with 100%IMS for 1.5 h.
9. Repeat three times.
10. Discard and replace with 100% IMS and leave overnight.
11. Discard and replace with Xylene for 2 h.
12. Repeat for 1.5 h.
13. Discard and remove tissue.
14. Immerse in molten paraffin wax under vacuum for 1 h (Paraffin wax impregnation should be carried out under vacuum. If this is not possible, length of immersion must be extended if using only a 60 °C oven).
15. Discard wax and repeat for 1.5 h.
16. Discard and repeat for 2 h.
17. The specimen can now be embedded.
18. Larger/denser specimens can be hand processed but times will be greatly extended (i.e., all day in 70% alcohol).
19. Best practice recommends automation of processing.

3.5. Staining (See Note 6)

Use a downdraught table or extraction system

1. Dewax tissue sections in xylene.
2. Place slides in 100% IMS for 2 min.
3. Repeat step 2.
4. Place slides in 70% IMS for 2 min.
5. Place in running tap water and allow to rinse.
6. Place slides in Gills 2 Hematoxylin for 5 min.
7. Blue—differentiate—blue (BD.B, Blue in tap water then steps 8–13).
8. Differentiate in 1% acid alcohol for 30 s.
9. Rinse in tap water.
10. Check staining under a staining microscope.
11. Repeat step 8 if necessary.
12. Blue in running tap water.
13. Recheck nuclear staining under the microscope.
14. Place slides in 1% aqueous eosin Y for 5 min.
15. Rinse in running tap water.

16. D.C.M (Dehydrate, Clear, and Mount. Take slides up through increasing concentrations of IMS, clear in Xylene, and mount in a xylene-based mountant and coverslip).

3.6. Immunocytochemistry (See Note 7)

1. Dewax sections and take to alcohol.
2. Block endogenous peroxidase.
3. Wash in tap water.
4. Use appropriate Antigen Retrieval Method.
5. Transfer to tap water and wash.
6. Wipe around sections and ring section with a hydrophobic pen.
7. Apply primary antibody at correct dilution.
8. Wash off primary antibody with supersensitive wash buffer.
9. Apply Super Enhancer ready-to-use reagent.
10. Wash in supersensitive wash buffer.
11. Apply SS Label ready-to-use reagent.
12. Wash in supersensitive wash buffer.
13. Apply DAB.
14. Wash in deionized water.
15. Counterstain cell nuclei with Gills 2 Hematoxylin.
16. B.D.B.
17. D.C.M.

Results

Antigenic sites: Brown

Nuclei: Blue

Antigen retrieval: Enzyme

1. Allow a 37 °C water bath to come up to temperature.
2. Fill coplin jars with 50 mL phosphate buffer and place in the water bath to pre-warm.
3. Weigh out 50 mg Protease for each coplin jar needed.
4. Place sections in pre-warmed 37 °C PBS for 5 min.
5. Add the protease to pre-warmed buffer, mix, and digest for 20 min.
6. Place slides into tap water.
7. Wash for 5 min.

Antigen retrieval: Pressure cooker

1. Set Hotplate to full heat.
2. Place at least 2 L Vector Antigen Unmasking Solution pH 6.0 into Teflon Pressure Cooker (slides must be well covered).
3. Replace lid but do not lock.

4. Allow solution to warm until boiling.
5. Remove from heat source.
6. Place slides into solution using long forceps.
7. Close lid.
8. Replace pressure cooker onto heat source, close pressure selector.
9. Set timer for 10 min and allow solution to reheat, the pressure indicator should rise and a steady flow of steam should be produced from the outlet valve.
10. Once steam is being produced from the outlet valve start timing for a further 10 min.
11. Switch off hotplate and remove pressure cooker.
12. Release pressure selector.
13. When pressure indicator drops, carefully remove lid.
14. Add cold running tap water to pressure cooker for 5 min.
15. Remove slides with long forceps and place in tap water.
16. Slides are now ready for primary antibody to be applied.

3.7. Microscopy

1. Switch the microscope on.
2. Adjust the binocular eyepieces to suit your inter-ocular distance.
3. Look at the scale between the eyepieces and note the number.
4. Adjust the eyepiece focus rings to the inter-ocular reading.
5. Put a slide on the stage, select the ×10 objective and place the swing—in top lens in the light path, then, viewing through the left eyepiece only, focus on the specimen using the main focus control.
6. Refocus the right eyepiece using the eyepiece focus ring and without touching the main focus controls.
7. Without altering the primary focus, move the slide to a clear area and then close down the field iris until you can see its edges in the field of view.
8. Focus the edges of the field iris using the condenser rack and pinion.
9. Check that the image of the iris is central; if it is not then center it using the two screws provided for this on the condenser.
10. Open the field iris until its image just disappears from your field of view.
11. Close the condenser iris until you can see the light intensity drop. You can also do this by removing an eyepiece, then closing this iris until you can see its image in the tube and then reopening it until it is no longer visible.
12. Your microscope should now be perfectly set up.

4. Notes

1. Good fixation is the cornerstone of routine Histopathology. This can be achieved by following a list of simple rules.
   (a) Correct fixative selection/concentration.
   (b) Immersion into fixative as soon as possible after resection.
   (c) Adequate container size.
   (d) Adequate specimen to fixative ratio (ideally 20× the volume of fixative to specimen).
   (e) Transport to histopathology laboratory as soon as possible.
   (f) On receipt in the laboratory large specimens should be sliced to allow adequate penetration of fixative.
   (g) Change the fixative regularly to prevent deposition of formalin pigment.
   (h) Specimens should be left to fix for an adequate time.
   (i) Avoid overfixation.
2. Bone should be cut into slices to allow the fixative solution to penetrate a larger surface area. This can be done by using an electric/hand band saw. Blocks put through for processing after decalcification may need further trimming with a scalpel as optimal results will depend on allowing the processing reagents to penetrate and surround the tissue. Blocks which completely fill or spill out of processing cassettes will be poorly processed and subsequent sectioning/staining will be compromised.
3. A robust microtome is needed to cut bone in this instance and solid knives are recommended over the disposable blade.
4. Strong acids should only be employed for urgent cases requiring fast results, because prolonged exposure to these reagents will result in loss of tissue architecture and subsequent staining may be impaired.

   Rapid commercial decalcifying solutions can also be used, although evaluation of these must be robust due to a more rapid decrease in tissue antigenicity.

   Chelating agents (e.g., EDTA) offer the best decalcification as morphology and antigenicity are retained. However due to their slow action, busy routine diagnostic laboratories rarely employ these.

   Incomplete decalcification will lead to poor section quality as chattering of the tissue will occur when the microtome blade comes into contact with the harder parts of the tissue (Fig. 4).

   If decalcification is incomplete or sections are difficult to cut, surface decalcification can be employed; the trimmed block can be placed into a solution of 5% formic acid for up to

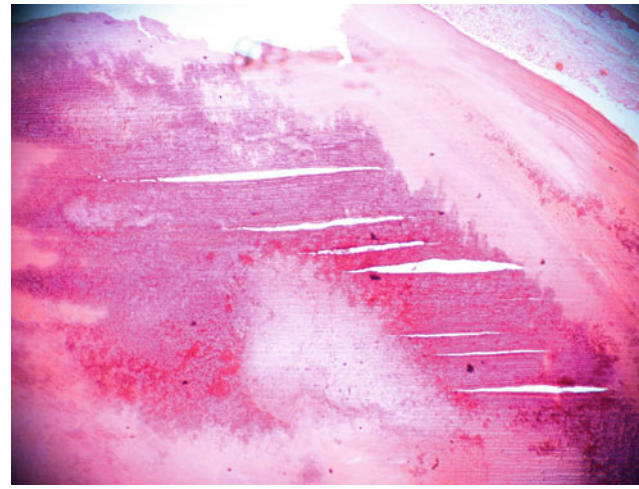

Fig. 4. A hematoxylin and eosin (H&E) section showing a poorly decalcified specimen. This leads to chattering of the section when the blade comes into more densely calcified areas within the section.

24 h. The acid will only penetrate superficially into the tissue and therefore sections should be taken as soon as possible. Commercial tissue softeners can be used in the same way (7).

5. The calcium oxalate test has a major drawback in that if fatty tissues are tested it will give a false cloudy result even if the specimen is completely decalcified. It is then essential that the specimen is properly trimmed and cut to size.
6. Overexposure of tissue to decalcification fluid can lead to loss of nuclear detail as the hematoxylin fails to form a bond with the cell nucleus and staining is almost totally eosinophilic (Fig. 5). If a definite diagnosis cannot be made it may be necessary to return to the original undecalcified specimen and take further blocks or to re-biopsy the patient.
7. Tissues which need further investigation with immunocytochemistry are subject to stringent pretreatments, it is therefore essential that coated or preferably charged slides are used for this purpose. Bone sections especially are apt to fall off uncoated slides after the decalcification process itself.
   Pressure cooking:

   We have found that allowing the cooker to fill with running water prevents any flash drying that may occur when removing the slides from the hot solution. Flash drying will produce areas within the tissue which will not stain.

   Digital pressure cookers are now available which standardize the retrieval process. Buffer solutions can be bought which are pre-diluted and will dewax and block your tissue sections. The cost of this can be prohibitive however.

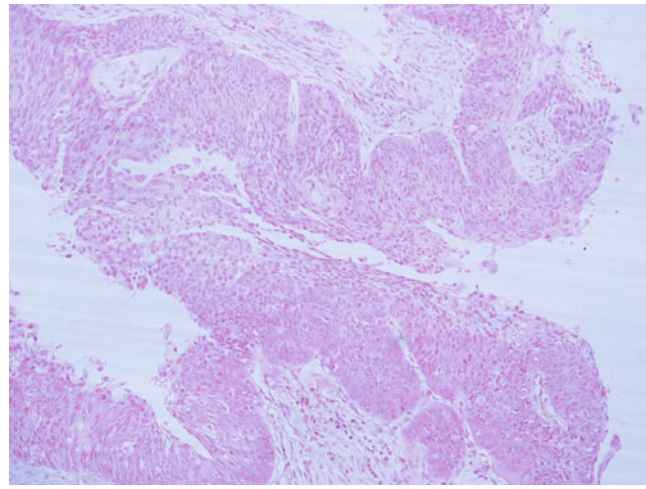

Fig. 5. A H&E section demonstrating over decalcification. In these sections there is loss of nuclear detail and in some cases it will not be possible to distinguish between vital and nonvital bone.

Supersensitive kits have allowed us to off set the cost of antibodies by titrating out to high dilutions, for example our laboratory uses Kappa at 1:50,000. As an addition to this we are able to stain our tissues with a minimum amount of antibody solution as the tissue sections are ringed using a hydrophobic "PAP" pen which holds the antibody within these confines and prevents the solution running off or drying out. An alternative to this are charged barrier slides which are produced with Teflon squares on the surface which act in the same way when the tissue is picked up in the correct area.

References

1. Bussolati G, Leonardo E (2008) Technical pitfalls potentially affecting diagnoses in immunohistochemistry. J Clin Pathol 61:1184–1192
2. Crespi R (1992) A method for histological examination of undecalcified teeth. Biotech Histochem 67(4):202–206
3. Donath K (1981) A method for the study of undecalcified bones and teeth with attached soft tissues. The Sage-Schiff (sawing and grinding) technique. J Oral Pathol 11(4):318–326
4. Frost HM (1958) Preparation of thin undecalcified bone sections by rapid manual method. Biotech Histochem 33(6):273–277
5. Woodruff LA, Norris WP (1955) Sectioning of undecalcified bone with special reference to radioautographic applications. Stain Technol 30:174
6. Callis GM, Sterchi DL (1998) Decalcification of bone: literature review and practical study of various decalcifying agents, methods and their effects on bone histology. J Histotechnol 21(1):49–58
7. Orchard GE, Torres J, Sounthararajah R (2008) Use of softening agents to improve the production of formalin fixed paraffin–embedded sections of nail tissue, an assessment. Br J Biomed Sci 65(2):68–70
8. Norton AJ, Jordan S, Yeomans P (1994) Brief high temperature heat denaturation (pressure cooking): a simple and effective method of antigen retrieval for routinely processed tissues. J Pathol 173:371–379
9. Bancroft JD, Gamble M (2007) Theory and practice of histological techniques, 6th edn. New York, Churchill Livingstone

Chapter 4

Bone Pathology

Kim Piper and Gail Valentine

Abstract

This chapter is an approach to bone pathology for a scientist rather than a histopathologist. It deals with the approach to cutting the bone biopsy, the relative merits of one method over another. The chapter also discusses the importance of correlation with both known clinical information, radiological appearances, and the final histology in reaching a diagnosis. A discussion of selected more common pathologies is covered, this is however not an exhaustive chapter on all bone pathologies.

Key words: Bone histopathology, Bone biopsy, Radiological skeletal interpretation

1. Introduction

This chapter deals with the histopathology of the bony skeleton and specifically excludes soft tissue pathology. It is not an exhaustive description of all bone pathology but serves to act as a sieve for reaching a reasonable list of differential diagnosis. The key to bone histopathology is good clinical correlation with both the radiological appearances and the clinical characteristics of the patient if known. Where possible the advice of a pathologist and radiologist is always valuable. It is worth noting at the outset that the bone pathologies that occur in the axial skeleton often present in different ages in the skull and facial bones. The examples provided are illustrative of the disease process itself rather than any postmortem agencies, which can complicate, but not exclude histopathological analysis.

Of course there are many differences between examining a bone for the purposes of reaching a diagnosis to treat a patient and that in the context of a forensic or archaeological examination. Nevertheless the same principle process of reaching a differential diagnosis remains the same. In the modern clinical setting the histopathology is often easier as the soft tissue element of the disease

Lynne S. Bell (ed.), *Forensic Microscopy for Skeletal Tissues: Methods and Protocols*, Methods in Molecular Biology, vol. 915,
DOI 10.1007/978-1-61779-977-8_4,

Table 1
A Surgical Sieve

Congenital/developmental Odontogenic cysts Cheurbism	*Traumatic* Fractures Anuerysmal bone cysts Solitary bone cysts
Degenerative Osteoarthritis	*Infective* Syphilis Tuberculosis Chronic and acute osteomyelitis
Idiopathic Fibro-osseous and cemento-osseous lesions Giant cell lesions	*Metabolic* Hyperparathyroidism Osteomalacia/Rickets Osteoporosis Scurvy
Neoplastic Primary bone and cartilage tumors Secondary metastasis	

process will be retained whereas in the forensic or archaeological setting this may be lost. The examination of bone pathology is normally conducted at the level of the light microscope using a routine hematoxylin and eosin stain. Whilst other stains may be used in the modern clinical setting, their use in skeletal remains will be limited.

When examining the skeleton which is thought to contain a disease process, it is worth noting that diseases are normally classified using a standard surgical sieve they are either developmental (congenital) or acquired. The acquired group is further subdivided into traumatic, degenerative, infective, idiopathic, metabolic, and neoplastic. Bone pathology is normally subdivided into radiolucent lesions, radiopaque lesions, or mixed lesions. Many pathologies are often initially radiolucent but mature to become radiopaque, e.g., fibrous dysplasia such that the appearances on a radiograph are only a snapshot in time. Brief examples of some of the common diseases in relation to the surgical sieve are given in Table 1 and some of these will be illustrated later in the chapter.

The principle of cutting up the bone specimen such that it can be processed by routine histopathological methods discussed in Chapter 3 is covered and an approach to the diagnosis explored.

The purpose of taking and processing a bone biopsy is to try to reach a firm histological diagnosis. In general a broad list of potential

diagnosis is made on the clinical appearance. This is further refined on the radiological appearances and where necessary a bone biopsy is taken. This is then processed and a firm diagnosis is reached.

2. Materials

The materials needed to reach a definitive histopathological diagnosis on a bone specimen are largely related to those that deal with processing the bone. These are covered within the earlier Chapter 3. Large bone specimens need to be cut into smaller pieces that will fit into a standard histopathological processing cassette such that they are no bigger than 25 mm by 12 mm by 5 mm in size. This can be achieved in one of four ways which will be covered in Subheading 3.

3. Methods

Once the appropriate clinical information has been gathered and radiology carried out using plain radiographs or MRI scans it may not be possible to reach a definitive diagnosis on these parameters alone. In these instances a bone biopsy may need to be obtained for histopathological examination. The bone biopsy can be obtained in one of four methods. Each method has its limitations and advantages and choice of method depends on the size and location of the lesion. Lesions that occur in the axial skeleton are sometimes easier to biopsy than those in the facial skeleton where the bones are often more complexly arranged precluding some of the biopsy techniques. The advantages and limitations of each biopsy method will be covered in Subheading 4 of the chapter.

3.1. Bone Biopsy Methods

1. Bone Saw
   This is the most low tech option. The bone is held by hand or in a normal woodworking vice and sawed with a junior hacksaw blade to produce a thin 5–10 mm bone biopsy. This is the easiest method to obtain a bone biopsy in a long bone in a large pathological lesion but is relatively destructive of the specimen itself (see Subheading 4).
2. Drill
   A diamond tipped fast drill similar to that in a dental surgery can produce a small biopsy sample. The bone can be held by hand or clamped in a wood working vice. This method has the advantage of being able to sample a relatively small area on most bones of the skeleton.

3. Diamond Saw
   These produce accurate and thin sections with little surrounding damage as they are water cooled. They are capable of cutting through teeth and producing fine saw cuts in otherwise difficult bones of the facial skeleton. Most large pathology departments will have access to one.
4. Decalcification
   This is covered in the previous section and will be needed on all the bone biopsies generated by the other methods prior to histological processing. In addition it can be used to decalcify whole bones which can then be cut with a normal scalpel blade. The disadvantage is that it may take weeks to decalcify large sections of bone, and the longer a bone is within the decalcification solution the more histological decalcification artifacts are generated. Once a bone biopsy of a suitable size has been obtained it is histologically processed as discussed in Chapter 3.

   Once you have the sample the process for all skeletal pathology should be

   Review the clinical appearances.

   Review the radiological appearances.

   Review the histological appearances.

   Make the final diagnosis.

As a principle for trying to reach a short list of potential differential diagnosis the principle is:

1. Examine the bone and determine the location of the lesion.
2. Radiograph the bone and determine the location of the lesion, whether the lesion is radiolucent, radiopaque, or mixed.
3. Determine whether the lesion is radiologically corticated or not and its effect on surrounding structures.
4. Determine the age of the patient if possible.
5. Produce a short list of possible pathologies.

Once you have this short list it is possible to decide whether a biopsy sample is needed or otherwise.

The following examples present some of the pathologies indicated in Table 1. The lesions described will include a brief description of the common clinical, radiographic, and histological appearances. This is not meant to be an exhaustive trawl through all bone pathologies but provides some of the more common pathologies or ones that might reasonably be expected to be seen in skeletal remains. It is possible to obtain a shortlist of the potential diagnosis by matching the clinical and radiological information with that provided below.

Fig. 1. Radiograph of the mandible demonstrating fusiform swelling of fibrous dysplasia and the so-called orange peel radiolucency which merges with the surrounding bone.

3.1.1. Fibrous Dysplasia

Clinical features: Depends on the bone involved and whether the condition is monostotic (1 bone) or polystotic (more than 1 bone) (1). Within the long bones the lesions are often incidental. In the facial skeleton they form swellings and facial asymmetry. The condition can be associated with syndromes often present in first 2 decades of life.

Typical location: Within the long bones the femoral neck is the commonest site and the facial skeleton, skull, and ribs in descending order.

Radiological features: Initially presents as an ill-defined radiolucency maturing to become a ill-defined radiopacity with a ground glass appearance (Fig. 1).

Histopathology: Hypocellular stroma with bony spicules in the so-called Chinese character formation. Osteoblastic rimming should be minimal (Figs. 2 and 3).

3.1.2. Simple Cyst

Clinical features: Typically first 2 decades of life and are often incidental findings (2).

Typical location: In children proximal humerus and proximal femur. In adults calcaneus and ilium. In the jaws presents as a well-corticated radiolucency that scallops between the tooth roots in the body of the mandible.

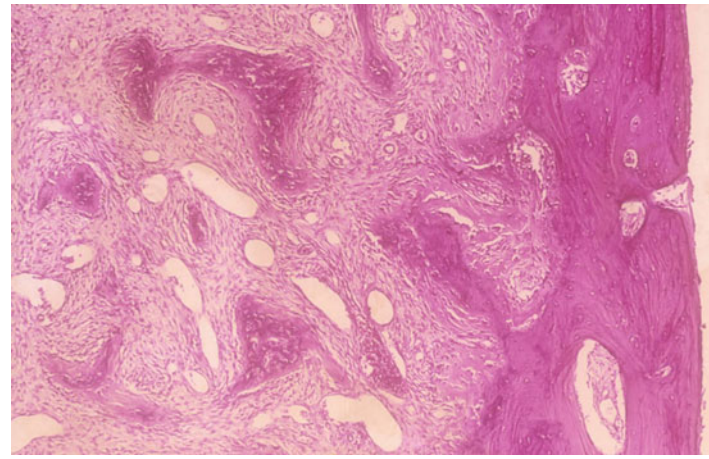

Fig. 2. Classical appearance demonstrating merging of the lesion with overlying normal bone.

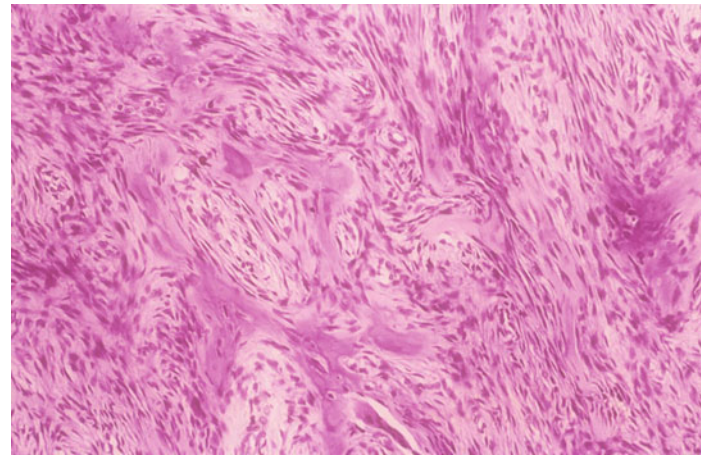

Fig. 3. Cellular fibrous tissue containing bony trabeculae without apparent osteoblastic rimming.

Radiological features: Unilocular well-corticated radiolucency centered in the medullary cavity (Fig. 4).

Histopathology: Scanty lining of fibrous tissue and occasional giant cells (Fig. 5).

3.1.3. Aneurysmal Bone Cyst

Clinical features: Non-neoplastic primary condition of bone which can grow at alarming rate. Most common in second decade of life often presenting with pain and swelling.

Typical location: Distal femur and proximal tibia are the most common sites, followed by the spine. More common in the mandible than the maxilla.

Fig. 4. Radiograph of the mandible showing a simple cyst within the body of the mandible. The lesion is well corticated and show scalloping between the tooth roots.

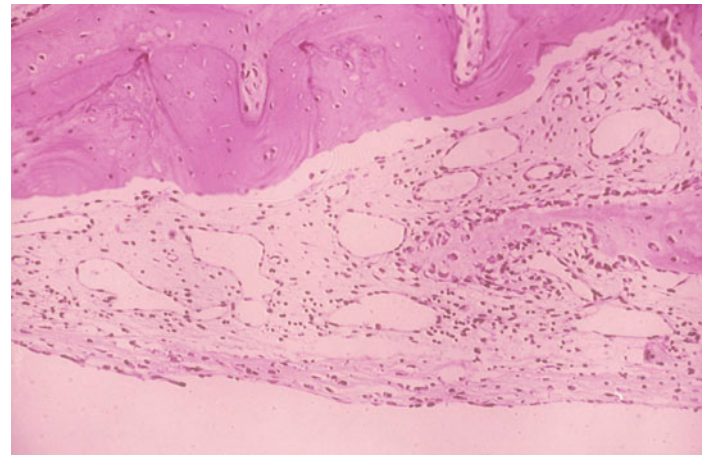

Fig. 5. Classical appearance of a simple cyst with only a scanty fibrous lining.

Radiological features: Radiolucency which is within the medullary cavity in the metaphysis of a long bone which can be well or poorly corticated (Fig. 6).

Histopathology: Solid and cystic areas. The cystic areas contain blood and are surrounded by a fibroblastic stroma containing giant cells and reactive bone formation (Fig. 7).

3.1.4. Bizarre Parosteal Osteochondromatous Proliferation

Clinical features: Normally young adults who present with rapid growth.

Typical location: Typically occur from the surfaces of the small bones of the hands (3).

Fig. 6. Aneurysmal bone cyst within the ramus and condylar head of the mandible. Note degree of cortication is less marked than the simple cyst.

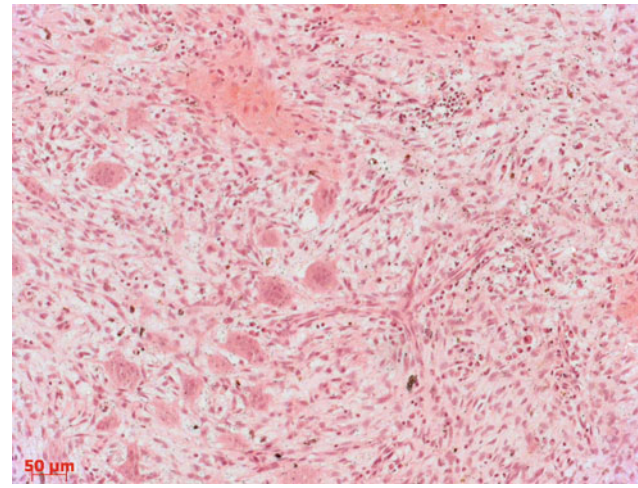

Fig. 7. A varied histological picture for aneurysmal bone cysts composed of a loose cellular fibrous stroma containing areas of hemorrhage and giant cells.

Radiological features: Densely mineralized mass that is attached to the surface but is not continuous with the cortex and medullary cavity unlike osteochondroma (Figs. 8 and 9).

Histopathology: Similar to a osteochondroma (Figs. 10 and 11).

3.1.5. Pagets

Clinical features: Older adults with a male dominance, presents with pain and progressive deformity. Rare in Africa and Asia (4).

Typical location: Innominate (hip) bone followed by sacrum and lumbar spine skull femur and tibia.

Radiological features: Sharply demarcated radiolucency with a thickened cortex and medullary bone. In the jaws often see hypercementosis of the teeth (Figs. 12 and 13).

Fig. 8. Radiograph of the left forefoot showing a bony lesion arising from the medial aspect of the big toe distal phalanx, consistent with a BPOP (*arrow*).

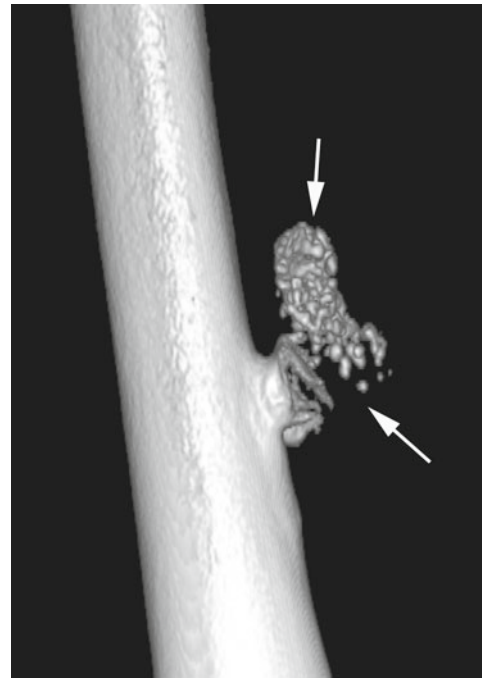

Fig. 9. 3D CT reconstruction of the right femoral diaphysis showing a mineralized lesion (*arrows*) in the medial soft tissues arising from the medial femoral cortex. Other imaging studies showed no continuity between the lesion and the femoral medulla, excluding the diagnosis of osteochondroma.

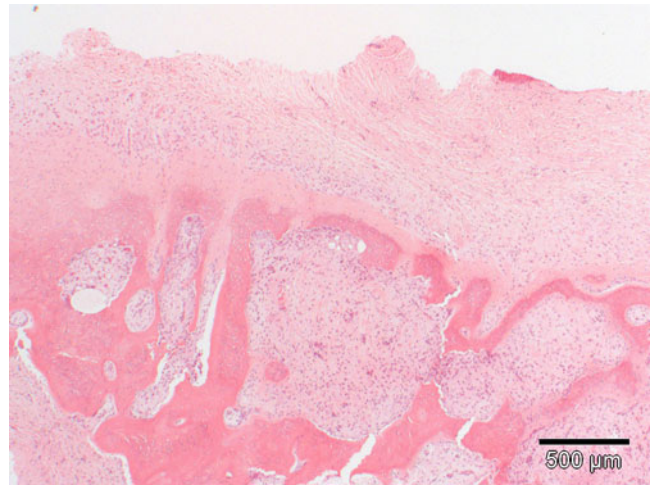

Fig. 10. A resected soft tissue lesion of the finger demonstrates fibromyxoid and chondroid tissue merging with woven and lamellar trabecular bone.

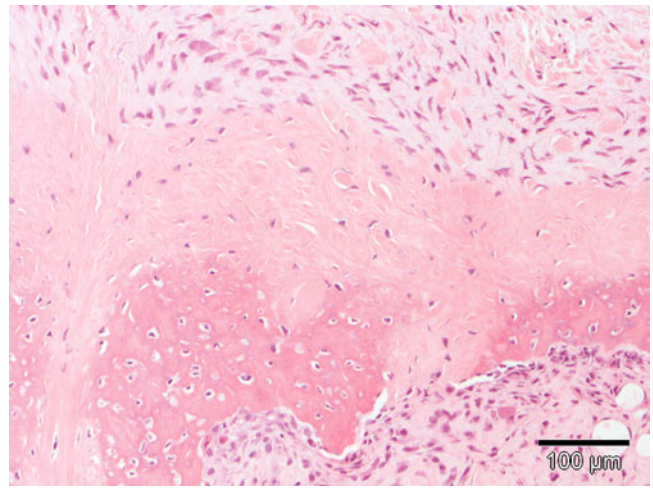

Fig. 11. The cartilaginous component of the lesion demonstrates the cellularity of the fibrocartilage.

Histopathology: Sclerotic bone which is thick and irregular with numerous resting and reversal lines (Fig. 14).

3.1.6. Giant Cell Tumor

Clinical features: Patients tend to be in the third or fourth decade of life with a slight female dominance. Recurrence is the main problem in these patients but metastasis is not a frequent phenomenon (5).

Typical location: Occur at ends (epiphyses) of long bones. Distal femur followed by the proximal femur is the most common site. These are followed by the distal end of the radius and the sacrum. These tumors tend not to be multicentric.

Fig. 12. Pagets patient showing osteoporosis circumscripta a clear line of radiolucency which gradually moves posterior in the skull vault.

Fig. 13. Pagets patient showing late stage so-called cotton wool radiopacity of the skull vault.

Radiological features: These present as eccentrically placed radiolucent lesions which although well corticated are rarely surrounded by a zone of sclerosis. If the tumor breaches the cortex then an eggshell of new bone is often produced (Figs. 15 and 16).

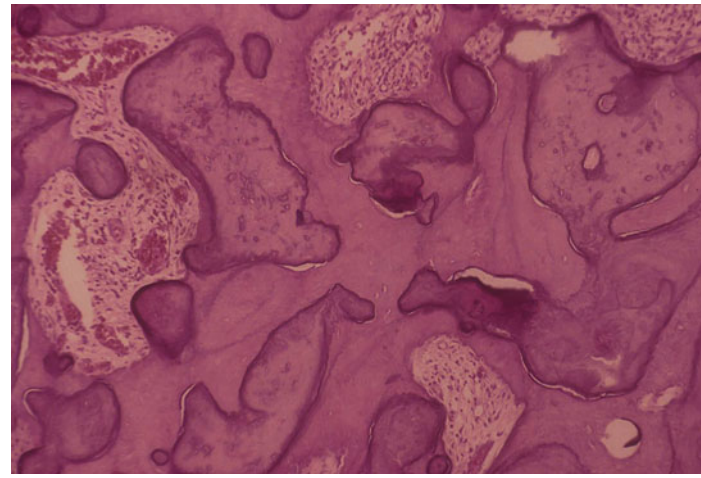

Fig. 14. Classical pagets histology showing dense basophilic bone containing numerous resting and reversal lines.

Fig. 15. Giant cell tumor AP radiograph of the left knee showing a poorly defined, subarticular lytic lesion of the lateral femoral condyle consistent with a GCT. Pathological fracture into the knee joint is noted (*arrow*).

Histopathology: Mononuclear rich stroma containing numerous giant cells. Mitotic activity is frequent but not atypical within the mononuclear population (Figs. 17, 18, 19, and 20).

3.1.7. Giant Cell Reparative Granuloma

Clinical features: Present in adolescents and young adults with a greater female preponderance (6).

Fig. 16. GCT axial T1W SE MRI showing the intermediate signal intensity lesion in the lateral femoral condyle (*arrows*) with associated joint effusion.

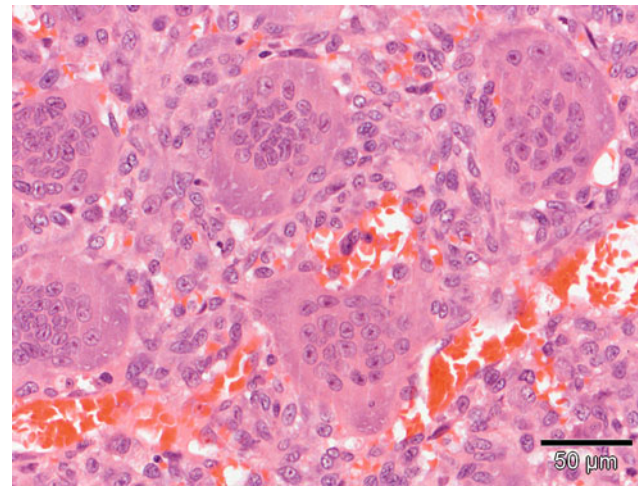

Fig. 17. GCT. Classical appearance of a giant cell tumor of bone showing an osteoclast-rich lesion composed of ovoid neoplastic mononuclear cells and conspicuous large osteoclast-like giant cells.

Typical location: Tooth bearing areas anterior to the first permanent molars more common in the mandible.

Radiological features: Well-defined multilocular radiolucency can present late with tooth exfoliation and bony expansion (Fig. 21).

Histopathology: Virtually identical to the giant cell tumor of the long bones (Fig. 22).

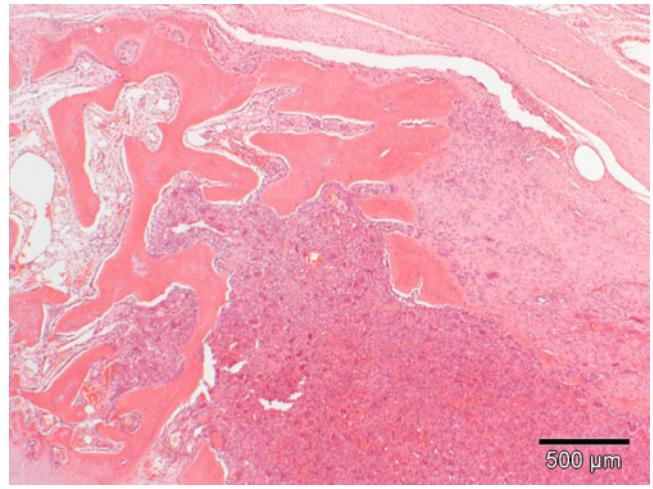

Fig. 18. GCT. A shell of peripherally sited reactive new bone formation is characteristic of this tumor.

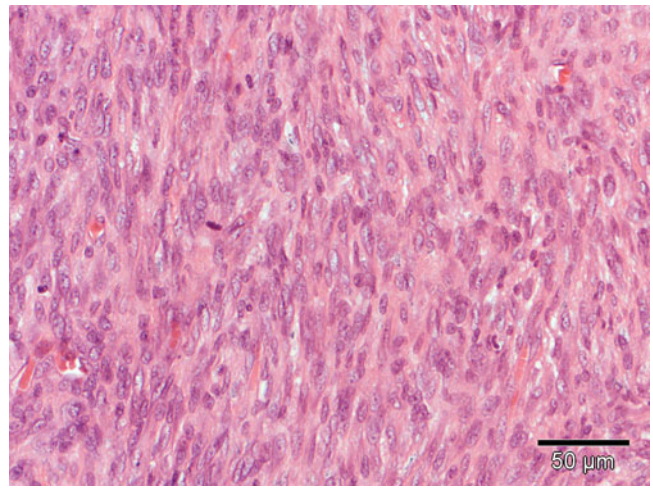

Fig. 19. GCT. A mononuclear fibroblastic overgrowth with mitotic figures is a feature not seen uncommonly.

3.1.8. Adamantinoma

Clinical features: Typically young adults and adolescents (7). Often long duration and may present with swelling or pain. Prognostically the path is normally indolent although late metastatic spread is reported.

Typical location: Tibia almost exclusively.

Radiological features: Multiple well-corticated radiolucencies within the mid cortex of the tibia. The radiolucent lesions are often of different size and surrounded by a zone of sclerosis (Figs. 23 and 24).

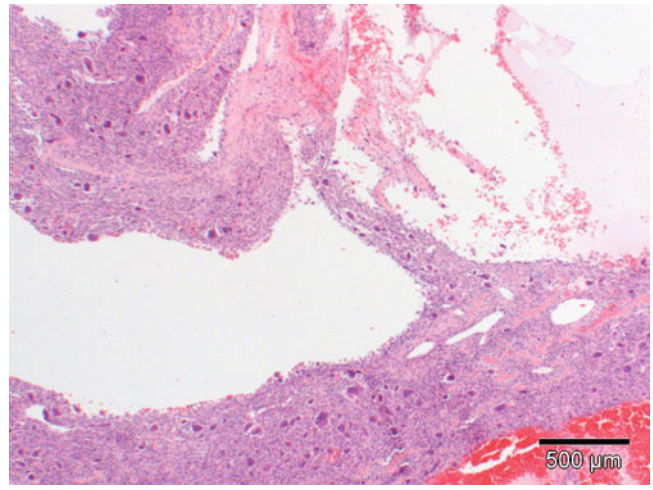

Fig. 20. GCT. Aneurysmal bone cyst-like change can also be seen and should not be mistaken for a telangiectatic osteosarcoma.

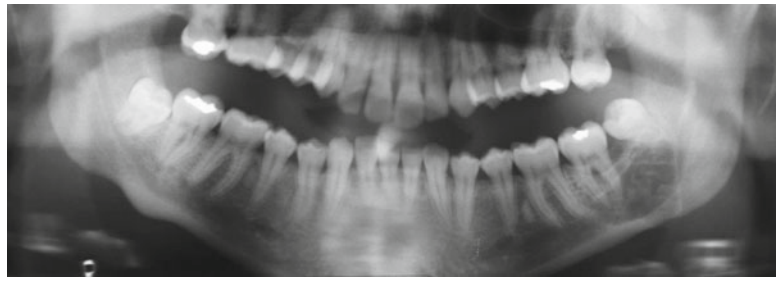

Fig. 21. Giant cell granuloma radiograph of the mandible showing a poorly defined lytic lesion in the left body and ramus of the mandible.

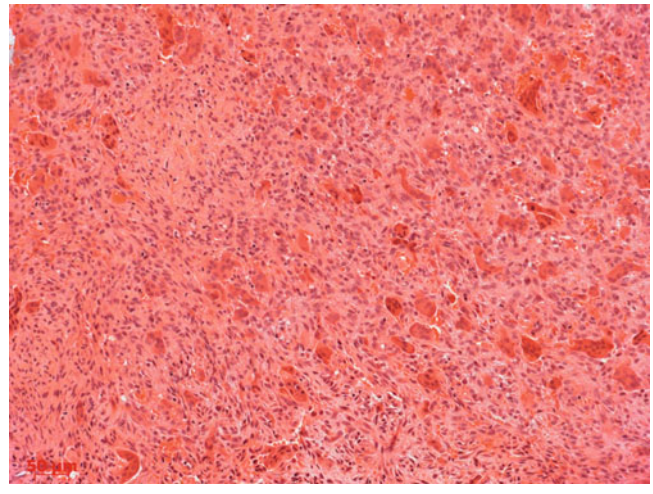

Fig. 22. Classical appearance showing bland mononuclear cells and clusters of osteoclast-like giant cells and areas of hemorrhage.

Fig. 23. Adamantinoma lateral radiograph of the lower limb showing a lobular, lytic lesion (*arrows*) within the anterior tibial diaphyseal cortex with extension into the medullary cavity. Note also further lesions in the distal fibula (*arrowhead*).

Fig. 24. Adamantinoma. AP radiograph of the right tibia showing a poorly defined lytic lesion (*arrows*) in the anterolateral aspect of the tibial diaphysis.

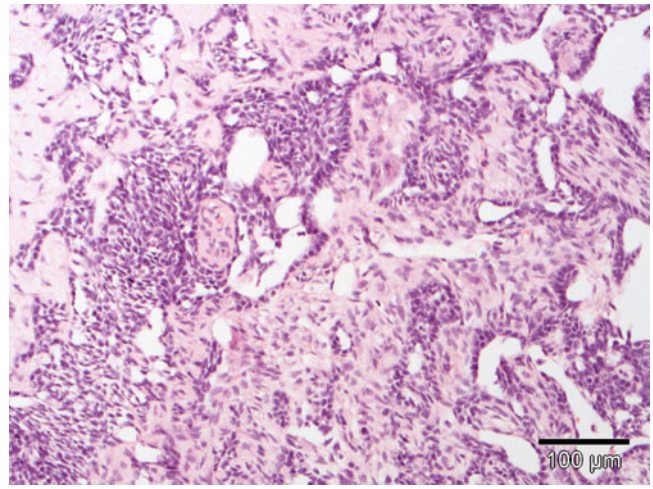

Fig. 25. Adamantinoma basaloid pattern showing easily distinguishable epithelial areas with intervening spindle cell.

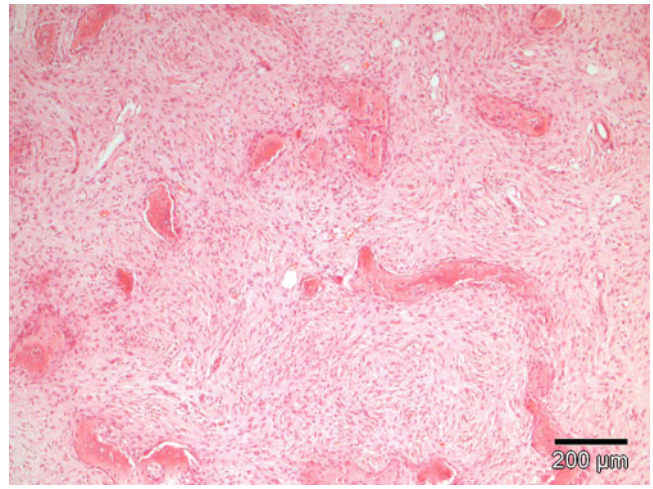

Fig. 26. Adamantinoma areas within the same tumor show an osteofibrous dysplasia (OFD) component comprising bland spindle cells in which there are irregular trabeculae of woven bone.

Histopathology: A range of patterns have been described (8) but all comprises a variably fibrotic background containing islands of epithelium. The epithelium often resembles that seen in an ameloblastoma but does not show any atypia (Figs. 25, 26, 27, and 28).

3.1.9. Osteochondroma

Clinical features: Often asymptomatic most patients present in the first 2 decades of life (9).

Typical location: Distal femur, proximal humerus, and proximal tibia.

Radiological features: Pedunculated or sessile projection arising from the cortex of the bone which merges with the lesional tissue.

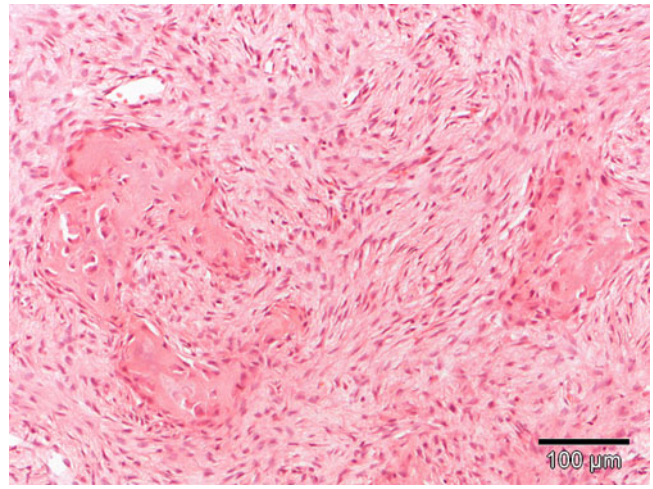

Fig. 27. Adamantinoma. The prominent osteoblast lining is a helpful feature in distinguishing OFD from fibrous dysplasia. Furthermore, a GNAS1 mutation, diagnostic of fibrous dysplasia, would not be detected in OFD.

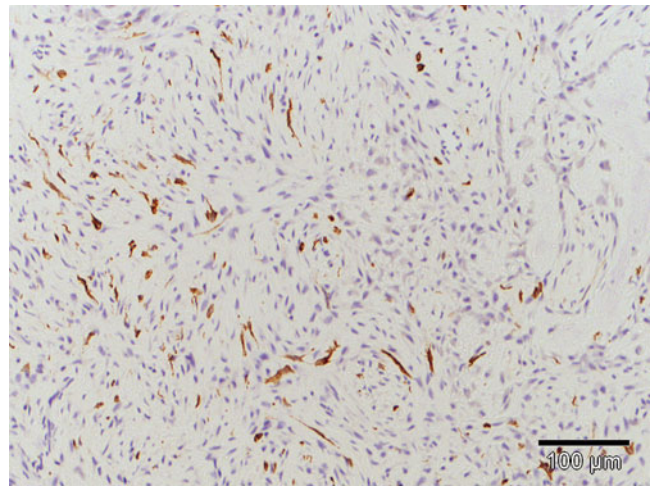

Fig. 28. Adamantinoma. Scattered epithelial cells highlighted by pankeratin (MNF-116) in the OFD areas would otherwise be missed.

The outer most part of the lesion expands to form a mushroom-shaped cap (Fig. 29).

Histopathology: The cap is composed of cartilage. Superficially the chondrocytes are arranged in clusters with the deep aspect arranged in columns. Bony trabeculae arise from the cartilage plate (Figs. 30 and 31).

3.1.10. Chondroma

Clinical features: Can be found at all ages although commonest in the second, third, and fourth decade. Typically present with pain and fractures of the small bones but asymptomatic in the long bones (10).

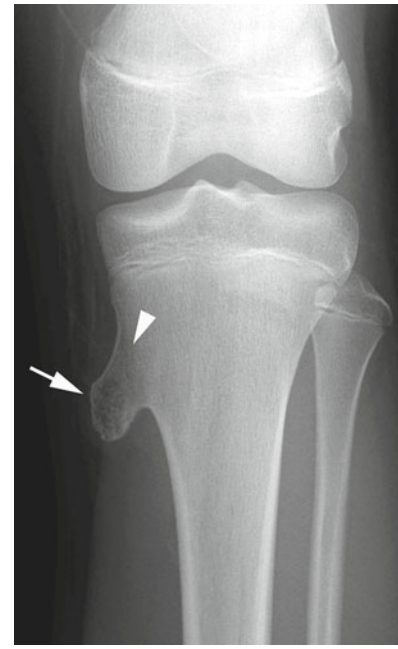

Fig. 29. Osteochondroma. AP radiograph of the right knee showing typical features of a small osteochondroma (*arrow*) arising from the medial proximal tibial metaphysis. Note the continuity between the lesion and the underlying tibial medullary cavity (*arrowhead*).

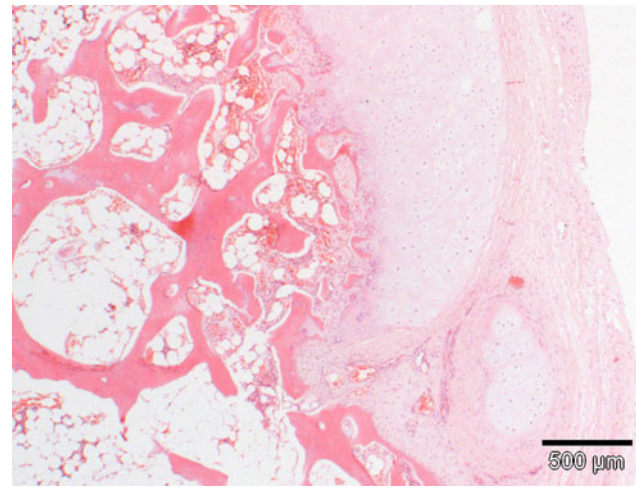

Fig. 30. Osteochondroma. A surface cartilaginous neoplasm composed of the outer perichondrium, with underlying cartilage cap and a stalk which is in contact with the underlying bone marrow.

Typical location: Common in small bones of the hands and feet where they are often symptomatic. Also seen in the proximal humerus, distal femur, and distal tibia where they are normally asymptomatic (1).

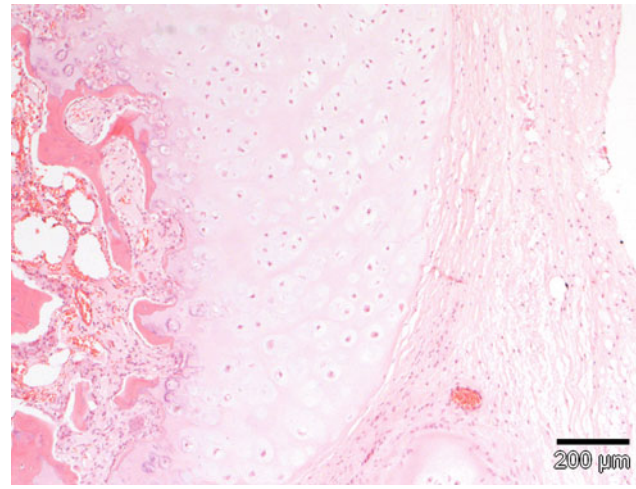

Fig. 31. Osteochondroma. A higher magnification highlighting the small nuclei of the chondrocytes, the maturing of cells with endochondral ossification.

Fig. 32. Enchondroma. AP radiograph of the index finger showing a lobular, lytic lesion (*arrows*) expanding the base of the middle phalanx.

Radiological features: Small bones—involve the entire bone and show thinning of the overlying cortex. In the long bones the tumor is normally in the metaphysic with slight to marked mineralization (Figs. 32 and 33).

Histopathology: Lobular growth pattern of hypocellular cartilage in the long bones with hypercellular cartilage in the small bones (Figs. 34 and 35).

Fig. 33. Enchondroma lateral radiograph of the index finger showing a lobular, lytic lesion (*arrow*) expanding the base of the middle phalanx.

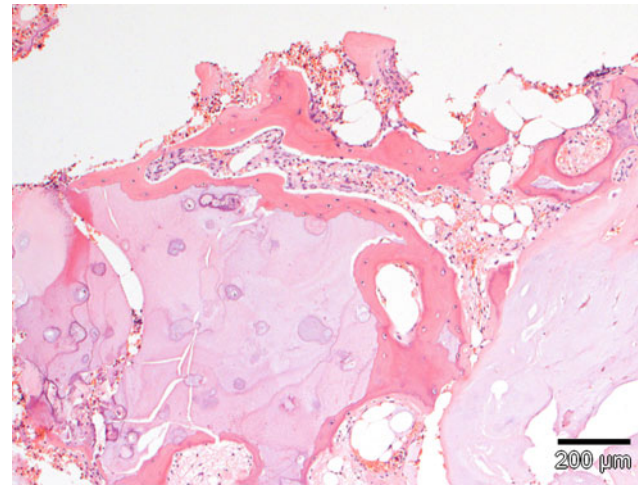

Fig. 34. Enchondroma. Multiple nodules of mature paucicellular hyaline cartilage encased by host lamellar bone.

3.1.11. Osteoma

Clinical features: Young adults and adolescents; 75% of patients are between 5 and 24. Normally less than 1 cm in size. Typically present with pain (1).

Typical location: Long bones particularly femur and tibia especially femoral neck.

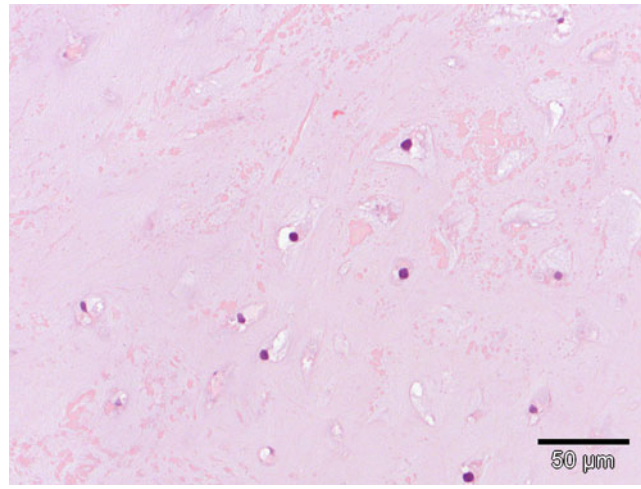

Fig. 35. Abundant hyaline cartilage matrix and uniform dispersed chondrocytes with small round hyperchromatic nuclei, situated within lacunar spaces in an Enchondroma.

Fig. 36. Radiograph showing a well-demarcated right frontal sinus osteoma.

Radiological features: Depends often on the site classically described as a radiolucent nidus surrounded by an area of sclerosis which can be 3–4 cm thick (Figs. 36 and 37).

Histopathology: The nidus comprises interlacing trabeculae showing variable mineralization and is demarcated from the surrounding sclerotic bone (Fig. 38).

Fig. 37. Part of a rotational tomogram showing a well-demarcated left mandibular osteoma.

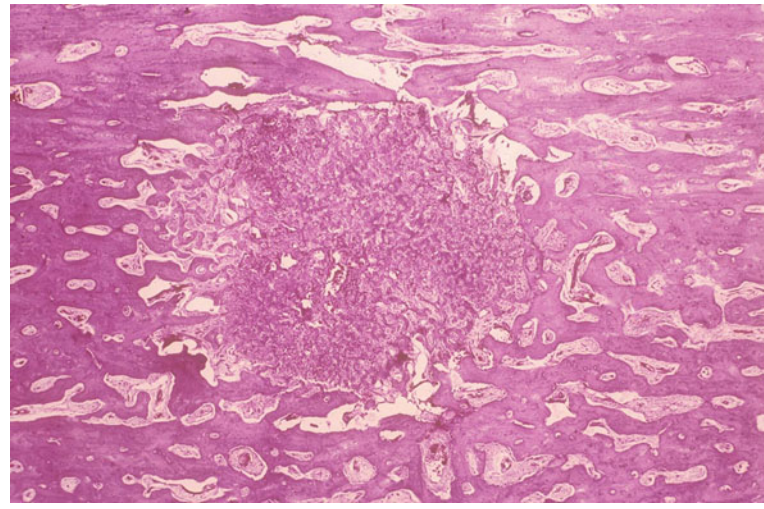

Fig. 38. Classical histology of an osteoma showing a central nidus which then matures to surrounding bone.

3.1.12. Osteosarcoma

Clinical features: Most common primary malignant tumor of bone occurs broadly as those that occur in the medullary cavity and those on the surface of the bone. The peak incidence for the long bones is the second decade of life apart from those patients with Pagets or prior irradiation (11). The tumor presents later in the jaws with most patients being older than 30.

Typical location: Long bones metaphyseal region especially the distal femoral metaphysis.

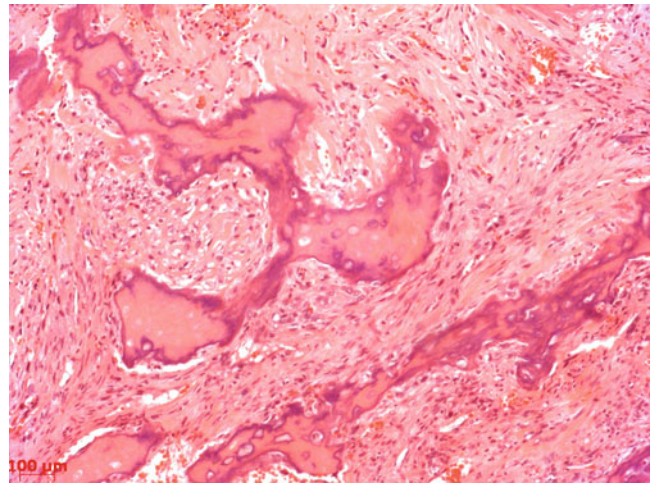

Fig. 39. Osteosarcoma histology showing poorly formed neoplastic bone in a variably pleomorphic and cellular stroma.

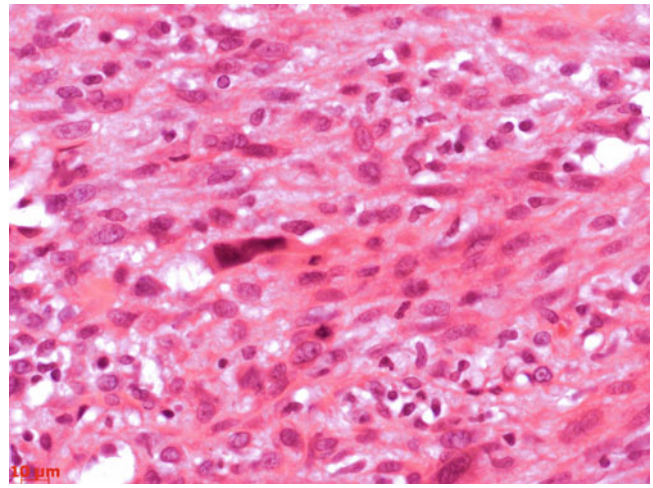

Fig. 40. Osteosarcoma histology showing the pleomorphic nature of the tumor cells.

Radiological features: Zone of destruction at metaphysic with little cortication often with periosteal new bone formation. In the jaws presents with tooth root resorption.

Histopathology: Poorly formed tumor bone is formed by malignant and pleomorphic osteoblasts (Figs. 39 and 40).

3.1.13. Myeloma

Clinical features: This is a disease of older adults, most common in the sixth and seventh decade, much more common in males representing 69% of the group. The prognosis is bleak with less than 10% of patients surviving 10 years whereas the solitary form has a much better prognosis with 68% surviving 10 years.

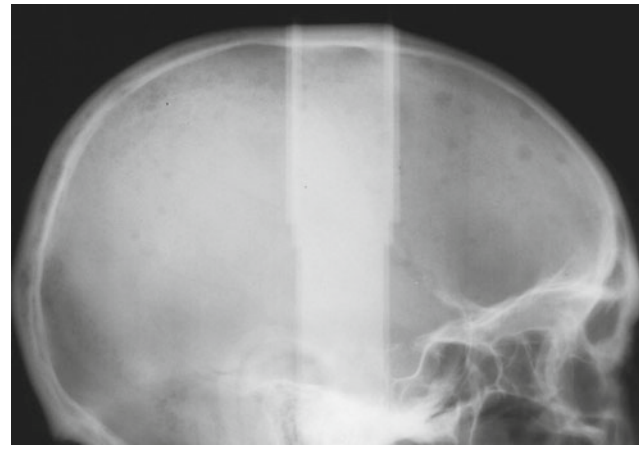

Fig. 41. Myeloma radiograph showing classical punched out radiolucencies in the skull vault.

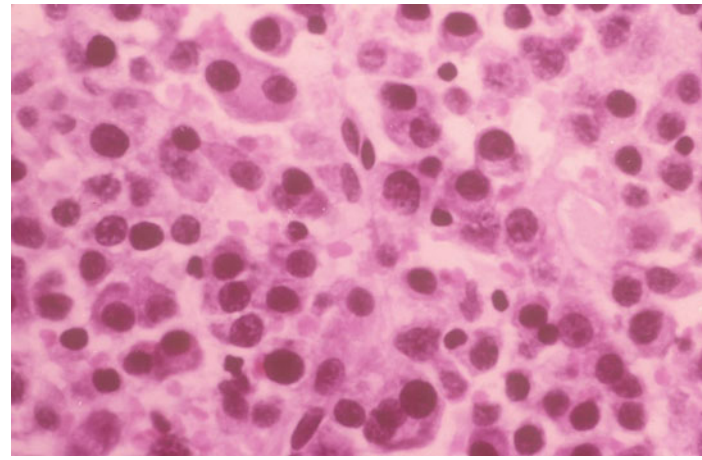

Fig. 42. Myeloma histology. Classical atypical pleomorphic plasma cells.

Typical location: Multiple myeloma presents typically in thoracic cage, skull, pelvis, and proximal femur and humerus. Solitary myeloma (plasmacytoma) tends to affect the spine, pelvic girdle, or ribs.

Radiological features: Punched out radiolucencies without surrounding sclerosis (Fig. 41).

Histopathology: Sheets of malignant plasma cells frequent binucleate forms (Fig. 42).

3.1.14. Dental Radiolucencies and Radiopacities

There are many radiolucencies that can be associated with teeth. These are often described as abscess cavities in the archaeological literature (12). Four of the most common lesions will be discussed here. The epithelial lining of the different cysts is diagnostic but only if sampled in noninflamed areas.

Fig. 43. Radicular cyst radiograph showing a well-circumscribed radiolucency at the apex of a molar tooth root. Note the tooth has been heavily restored.

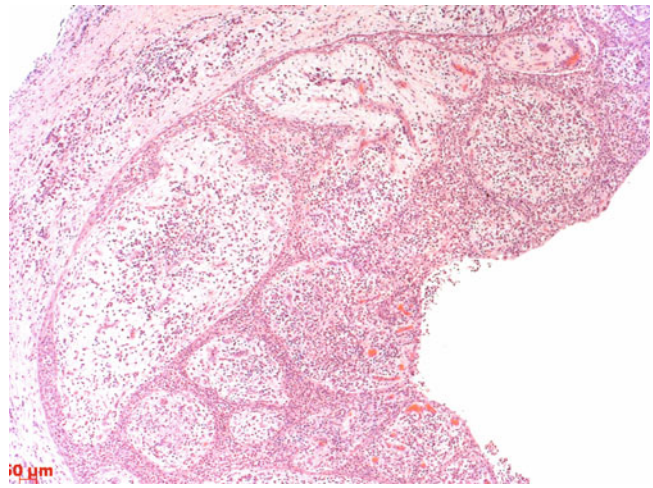

Fig. 44. Radicular cyst histology showing a fibrous cyst wall lined by arcading non-keratinized stratified squamous epithelium.

3.1.15. Radicular Cyst

Clinical features: The most common cyst forming 65% of all the dental cysts associated with nonvital teeth at the apex (13).

Typical location: The upper incisors peak incidence in the fourth to fifth decade.

Radiographic features: Well-corticated unilocular radiolucency associated with the apex of a tooth (Fig. 43).

Histopathology: Lined by arcading non-keratinized stratified squamous epithelium (Fig. 44).

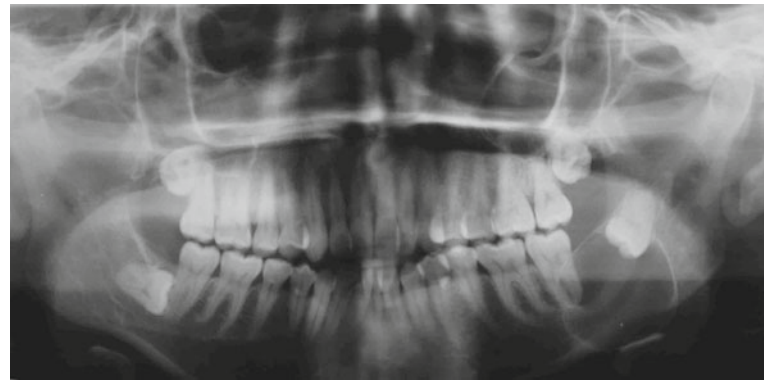

Fig. 45. Rotational tomogram showing a well-circumscribed radiolucency associated with an unerupted last molar tooth.

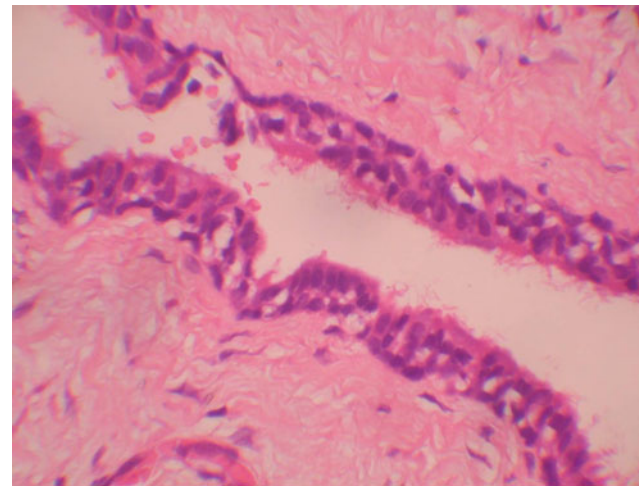

Fig. 46. Histology of a Dentigerous cyst showing a non-keratinized epithelial lining 2–5 cells thick showing area with cilia.

3.1.16. Dentigerous Cyst

Clinical features: Forms 20% of dental cysts associated with unerupted impacted teeth (13).

Typical location: Unerupted lower third molars and canines with a peak incidence in the third and fourth decades.

Radiographic features: Unilocular well-corticated radiolucency associated with an unerupted tooth (Fig. 45).

Histopathology: Lined by non-keratinized stratified squamous epithelium on a flat basement membrane (Fig. 46).

3.1.17. Odontogenic Keratocyst

Clinical features: These cysts often present late as they grow through the medullary bone with late buccal expansion, they form 5% of all cysts. They are associated with Gorlin Goltz or Basal cell nevus syndrome (14). This syndrome presents with bifid ribs, calcified falx cerbi, and multiple odontogenic keratocysts as well as numerous skin basal cell carcinomas.

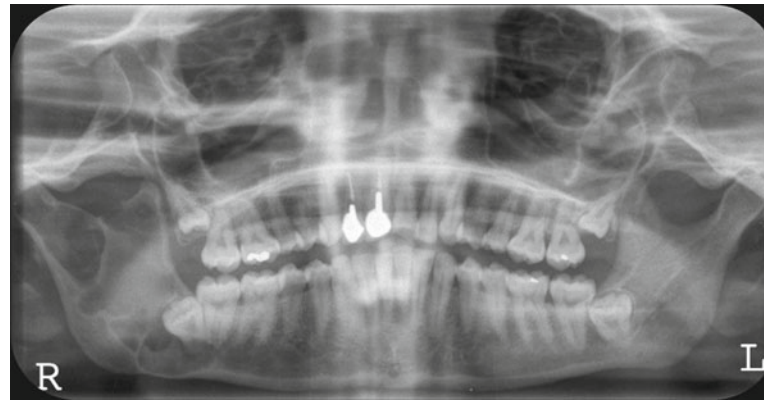

Fig. 47. Rotational tomogram showing a multilocular radiolucency in the right ramus and angle of the mandible known to be a keratocyst.

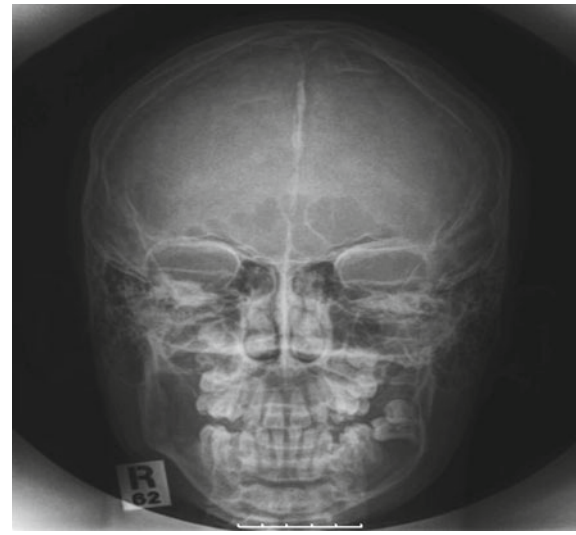

Fig. 48. AP Shull radiograph showing a calcified falx cerebri in a patient with Gorlin Goltz syndrome.

Typical location: Angle of the mandible and the ramus of the mandible with a peak incidence in the second and third decade.

Radiographic features: Multilocular radiolucency associated with tooth root resorption (Figs. 47 and 48).

Histopathology: The lining is thin and the epithelium is parakeratinized (Fig. 49).

3.1.18. Nasopalatine Cyst

Clinical features: Associated with vital maxillary incisors and forming 5% of cysts. Often asymptomatic.

Typical location: Maxillary incisors peak incidence in the fifth and sixth decade.

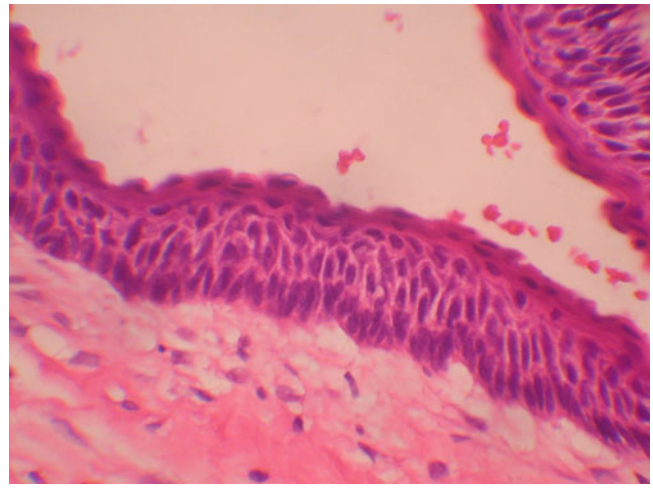

Fig. 49. Keratocyst histology showing a thin epithelial lining of parakeratinized stratified squamous epithelium. The basal cells are hyperchromatic and show reversal of nuclear polarity.

Fig. 50. Anterior occlusal radiograph showing a large midline palatal radiolucency from a nasopalatine cyst.

Radiographic features: Well-corticated radiolucency (Fig. 50).

Histopathology: Epithelial lining is non-keratinized stratified squamous or respiratory epithelium with neurovascular bundles in the wall (Fig. 51).

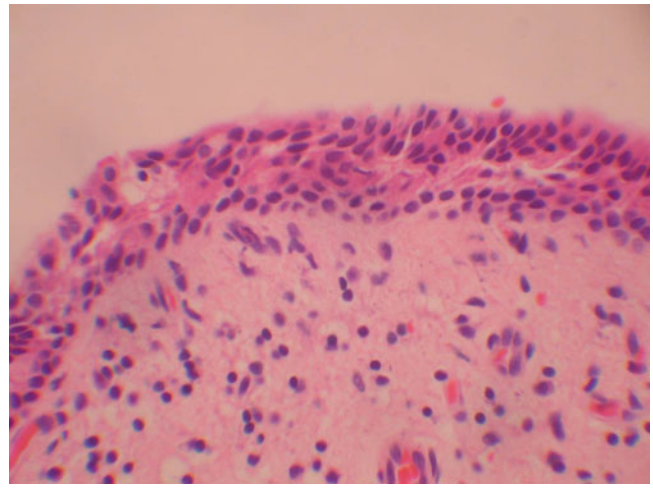

Fig. 51. Nasopalatine cyst histology showing the cyst lined by respiratory type epithelium with minimal inflammation. Neurovascular bundles should be seen in the cyst wall.

Radiopacities are also relatively common in the facial skeleton often being asymptomatic and discovered on routine dental radiographs. These largely fall into the group of the fibro- and cemento-osseous lesions that comprise both true neoplasms and dysplasia. Many of the odontogenic tumors may also present as mixed radiolucencies and radiopacities. These tumors are rare and only one which represents a hematoma the odontome will be discussed.

3.1.19. Cementoblastoma

Clinical features: Associated with tooth roots often present with pain and local enlargement a true benign neoplasm (15).

Typical location: More common in the mandible attached to the roots of premolar or molar teeth. 50% of people under 20.

Radiographic features: Radiopaque mass attached to the tooth root (Fig. 52).

Histopathology: Cemental mass with numerous resting and reversal lines attached to the tooth root (Fig. 53).

3.1.20. Ossifying/ Cementifying Fibroma

Clinical features: A benign lesion which is encapsulated unlike fibrous dysplasia.

Typical location: Jaw bones usually affecting adults.

Radiographic features: Presents as a mixed radiolucency–radiopacity with a clear demarcation from normal bone (Fig. 54).

Histopathology: Cellular fibrous tissue containing varying amounts of metaplastic bone and cemental-like tissue (Figs. 55, 56 and 57).

3.1.21. Periapical Cemental Dysplasia

Clinical features: Often symptomless affecting one or more vital teeth.

Typical location: Incisor region mandible more common in females and greater than 50 years of age (16).

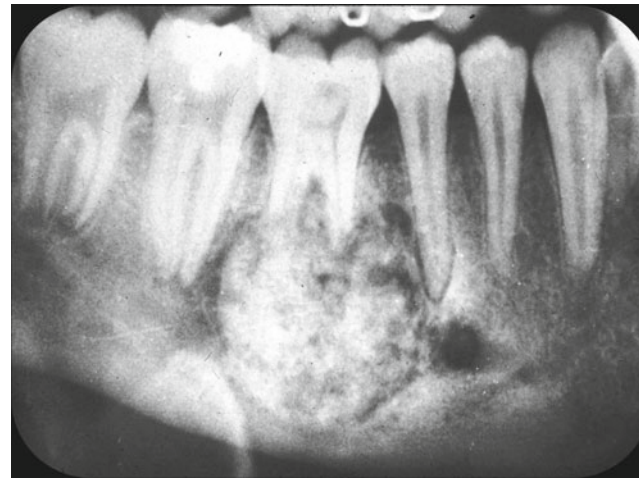

Fig. 52. Part of a rotational tomogram showing a dense radiopacity attached to the roots of the first molar tooth. Note the partial radiolucency surrounding the mass. The appearances are classical for a cementoblastoma.

Fig. 53. Whole mount of a decalcified tooth with an attached dense mass of cementum attached to the tooth root classical for a cementoblastoma.

Radiographic features: Radiolucent in early stages of maturing to become radiopaque (Fig. 58).

Histopathology: Fibrous tissue containing cellular fibrous tissue with progressive deposition of basophilic cemental tissue (Fig. 59).

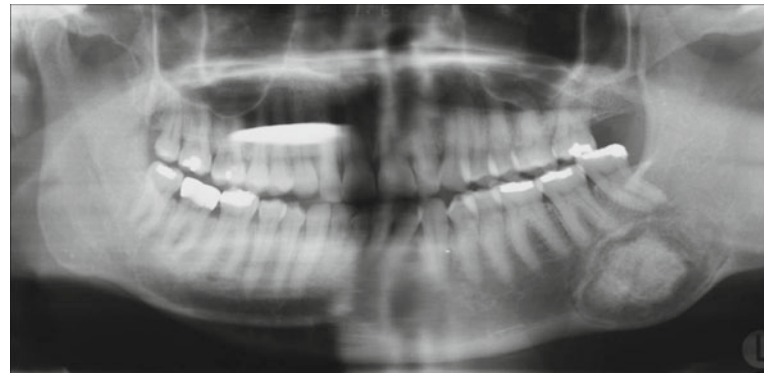

Fig. 54. Rotational tomogram demonstrating an Ossifying–cementifying fibroma showing a mixed radiolucent and radiopaque mass which is well corticated.

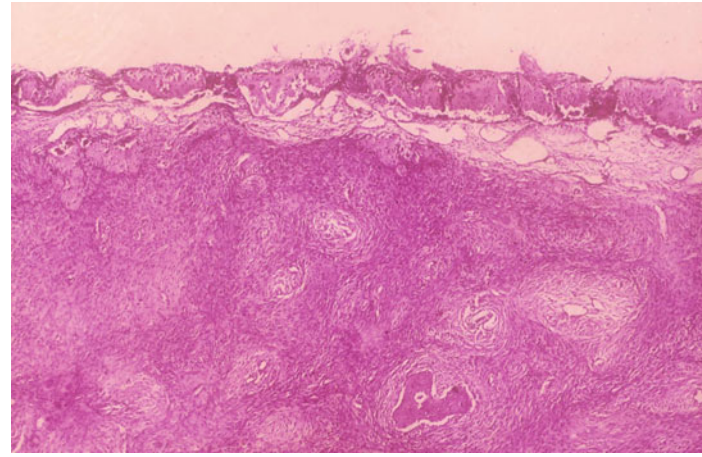

Fig. 55. Low power view of an Ossifying–cementifying fibroma demonstrating the distinct fibrous capsule from the overlying normal bone.

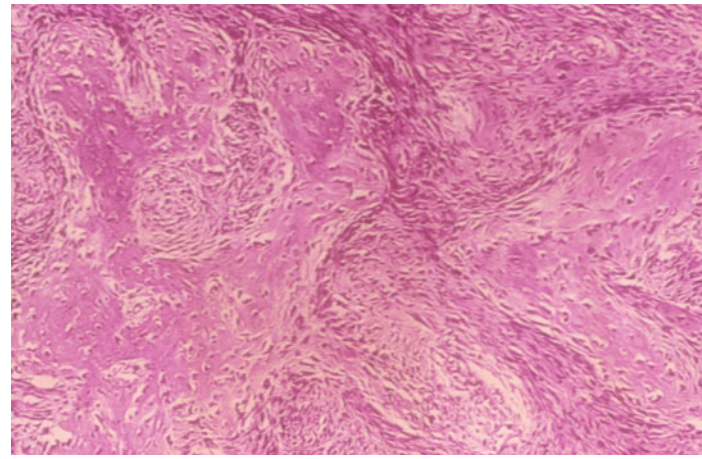

Fig. 56. Higher power view showing bone formation within a fibroblastic stroma.

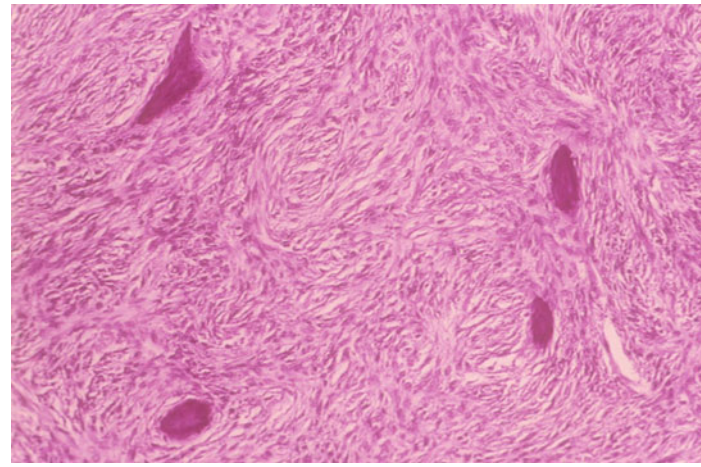

Fig. 57. Higher power view showing distinct cementum formation.

Fig. 58. Anterior occlusal radiograph of a case of periapical cemental dysplasia. Note late stage loss of lamina dura and radiopacity associated with the tooth roots.

3.1.22. Florid Cemento-Osseous Dysplasia

Clinical features: Often asymptomatic but may present as painless swellings.

Typical location: Occurs in the molar region of the jaws and typically affects more than one quadrant. More common in females over 50 especially of black ancestry.

Radiographic features: Poorly demarcated dense radiopacities (Fig. 60).

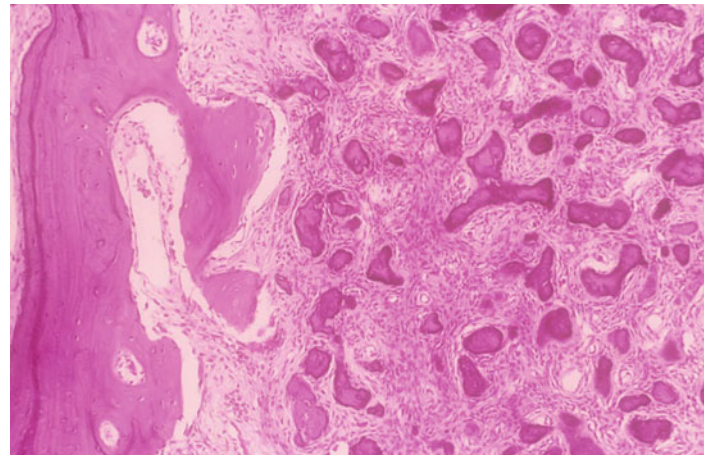

Fig. 59. Periapical cemental histology showing basophilic cemental masses embedded in a bland fibroblastic stroma.

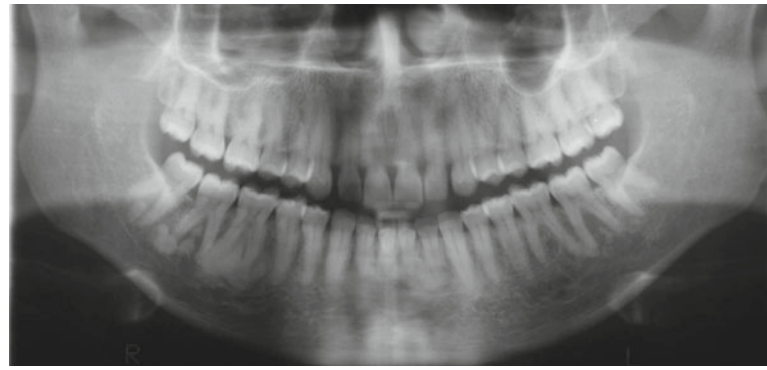

Fig. 60. Rotational tomogram of florid cemento-osseous dysplasia showing middle to late stage radiopacity associated with several molar teeth in the right mandible and early radiolucency associated with molar teeth in the left mandible.

Histopathology: Initially fibrous tissue but replaced by sheets of basophilic cemental tissues (Fig. 61).

3.1.23. Odontome

Clinical features: These are odontogenic hamartomas; they are the most common odontogenic tumor (15).

Typical location: Maxilla in the under 20s is often asymptomatic but may present with delayed eruption of the permanent dentition.

Radiographic features: Depends on the developmental stage present initially as a mixed lesion becoming more radiopaque with the development of the dental hard tissues (Fig. 62).

Histopathology: Complex odontomes have a haphazard arrangement of the dental tissues whereas compound odontomes are composed of denticles looking like little teeth (Figs. 63 and 64).

The pathologies described are not an exhaustive list of everything that might be encountered in the skeleton but serve to act as

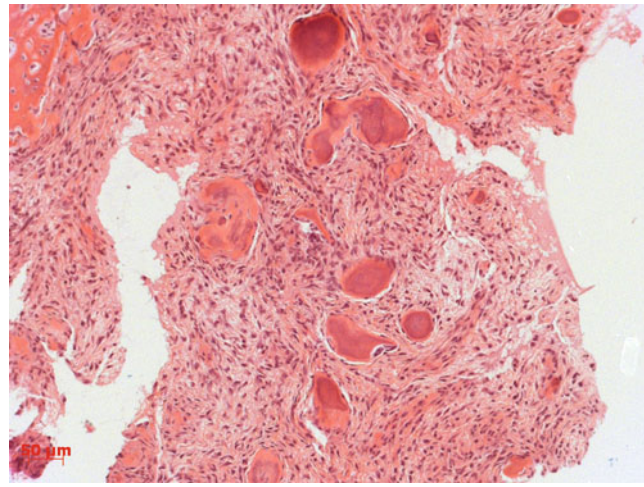

Fig. 61. Florid cemento-osseous dysplasia histology showing relatively early stage disease in which bone formation and rounded cemental masses are seen in a fibroblastic stroma.

Fig. 62. Rotational tomogram showing a displaced upper molar tooth and a dense calcified mass of a complex odontome.

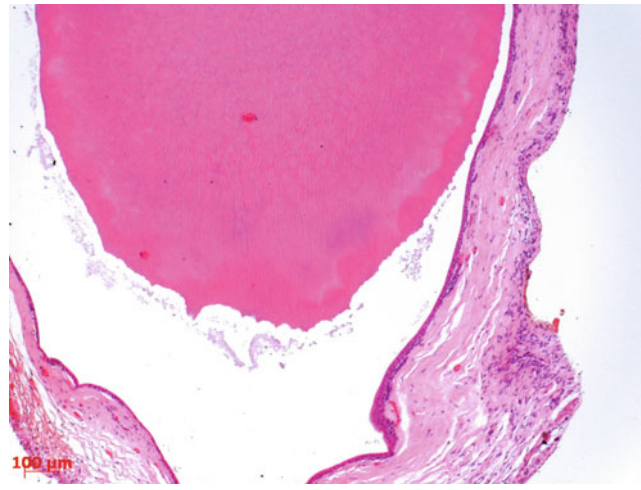

Fig. 63. Histology of a complex odontome showing disordered production of dental calcified material with no tooth like structures.

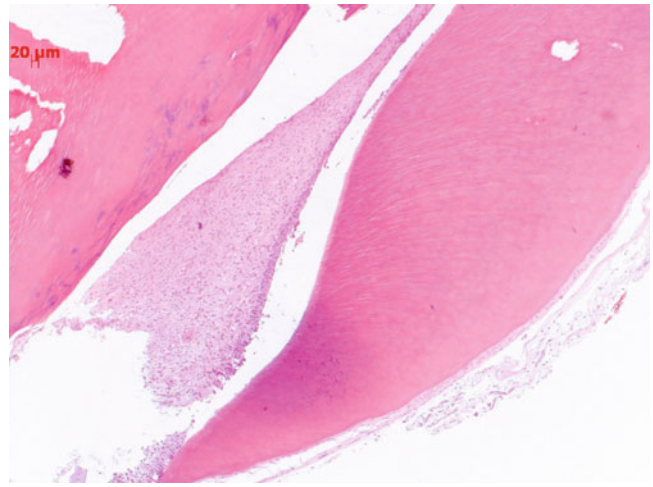

Fig. 64. Histology of a compound odontome where the hard tissues are arranged in small tooth-like structures.

an introduction to bone pathology. The diagnosis of any bone pathology relies on the triad of clinical, radiological, and histological presentation in order for an accurate diagnosis to be made. It is always worth seeking the advice of the local bone radiologist and histopathologist.

4. Notes

Where can it all go wrong? The most common mistakes in pathology come from overlooking the obvious and leaping to a meaningless conclusion. Great efforts in obtaining the most clinical information possible: age, location of the lesion, any other relevant factors such as a history of trauma is advised. Some lesions are very site specific and others occur rarely out of their age range so including these in a list of potential diagnosis is unlikely. Secondly use imaging as much as possible; this will demonstrate whether a lesion is corticated or not fused with the overlying bone or encapsulated and help to refine the list of potential diagnosis. Is the lesion radiolucent or radiopaque?

Secondly mistakes can occur when sampling the bone for histological processing. The bone saw technique is straightforward for the long bones of the axial skeleton as they are easily held by hand or gripped in a wood working vice. It is much harder to saw the ribs or any of the bones of the skull or facial skeleton and experience has shown that this is best avoided. It is very difficult to prevent the maxilla fragmenting in undesirable fashion or obtaining an accurate cut between the teeth. In my experience if preservation is key and only a small access cavity needed then the least

destructive is a fast dental handpiece. This is able to cut a small piece of bone that can be easily decalcified. If a larger biopsy is needed or a complete through and through section wanted then use of the diamond bone saw is advised. This is able to provide fine cuts through dense bone and teeth such that a thin slice of 5 mm is easily obtained. Complex specimens like the maxilla can be guided through by hand; it is a watercooled process and produces little artifact.

Decalcification

This is covered extensively in the Chapter 10. From the point of histopathology over decalcification is best avoided as this makes the diagnostic process extremely difficult. Once a specimen has been decalcified there is no rescue package available. With a precious specimen it is worth running a test piece of bone in the decalcification solution and checking the timings first. Once the sample is in the decalcification solution it should be checked daily to see if it is ready . However if the specimen is small 5 mm it is worth checking the decalcification more frequently to prevent over decalcification

Histopathological interpretation

H&E is the most useful stain in bone pathology, many of the special stains produce a great deal of artifact on decalcified material. The biopsy should be viewed at low power to obtain an overview of the key features, soft tissue element, bone or mineralized element, and how they interrelate to each other. Higher power views are rarely helpful. Once the key histological features have been obtained correlation with the radiological and clinical features is essential for reaching a firm diagnosis. Matching the pathology to a book or the descriptions provided above is fraught with misdiagnosis. Bone pathology relies heavily on interpretation from the clinical, radiological, and histological fronts to form the correct diagnosis.

The best advice is to seek help early to gain the maximum clinical and radiological interpretation before deciding whether you need an open biopsy to reach a conclusive diagnosis. If you do select the most appropriate method of gaining the sample and then watch it like a hawk in the decalcification solution. A test piece of bone of similar size to gauge timings is always wise.

References

1. Unni KK, Inwards CY, Bridge JA, Kindblom L, Wold LE (2005) Tumours of the bone and joints atlas of tumor pathology 4th Series Fasicle 2. Armed Forces Institute of Pathology, Washington DC, pp 46–59
2. Chigira M, Maehara S, Arita S, Udagawa E (1983) The aetiology and treatment of simple bone cysts. J Bone Joint Surg Br 65:633–637
3. Nora FE, Dahlin DC, Beabout JW (1983) Bizarre parosteal osteochondromatous proliferation of the hands and feet. Am J Surg Pathol 7:245–250
4. Cooper C, Dennison E, Schafheutie K, Kellingray S, Guyer P, Barker D (1999) Epidemiology of Paget's disease of bone. Bone 24(5 Suppl):3S–5S

5. Dahlin DC (1985) Caldwell lecture. Giant cell tumour of bone: highlights of 407 cases. AJR Am J Roentgenol 144:955–960
6. Whitaker SB, Waldron CA (1993) Central giant cell lesions of the jaws. A clinical, radiologic, and histopathological study. Oral Surg Oral Med Oral Pathol 75:199–208
7. Moon NF, Mori H (1986) Adamantinoma of the appendicular skeleton. Clin Orthop 204: 215–237
8. Weiss SW, Dorfman HD (1977) Adamantinoma of long bone. An analysis of nine new cases with emphasis on metastasing lesions and fibrous dysplasia like changes. Hum Pathol 8:141–153
9. Fechner RE, Mills SE (1993) Tumours of the bones and joints Atlas of tumour Pathology, 3rd Series Fasicle 8. Armed Forces Institute of Pathology, Washington DC, pp 79–83
10. Shimizu K, Kotoura Y, Nishijima N, Nakamura T (1997) Enchondroma of the distal phalanx of the hand. J Bone Joint Surg Am 79:898–900
11. Goorin AM, Abelson HT, Frei E 3rd (1985) Osteosarcoma: fifteen years later. N Engl J Med 313:1637–1643
12. Higham N (1987) Briganatia revisted. Northern Hist 23:1–1
13. Daley TD, Wysocki GP, Pringle GA (1994) Relative incidence of odontogenic tumours and oral and jaw cysts in a Canadian population. Oral Surg Oral Med Oral Pathol 77:276–280
14. Gorlin RJ, Goltz RW (1962) Multiple nevoid basal-cell epithelioma, jaw cysts and bifid rib: a syndrome. N Engl J Med 262:908–912
15. Sciubba JJ, Fantaisa JE, Hakn LB (2001) Tumours and cyst of the jaws third series atlas of tumor pathology 4th Series Fasicle 29. Armed Forces Institute of Pathology, Washington, DC
16. Neville BW, Albenesius RJ (1986) The prevalence of benign fibro–osseous lesions of the periodontal ligament origin in black women: a radiographic survey. Oral Surg Oral Med Oral Pathol 62:340–344

Chapter 5

A Histological Method That Can Be Used to Estimate the Time Taken to Form the Crown of a Permanent Tooth

M. Christopher Dean

Abstract

Teeth contain an incremental record of their growth in the form of periodic growth markings that are literally embodied within the structure of enamel. These can be revealed when ground sections of teeth are prepared for transmitted light microscopy. This chapter sets out one method for estimating the time taken to form the crowns of permanent teeth. First, the daily rates of enamel formation are estimated at three positions within the crown close to the enamel dentine junction (EDJ). Then a 200 μm length along an enamel prism that take ~80 days to form is followed out from the EDJ at the dentine horn. From this point a line is then tracked back along the direction of the oblique striae of Retzius that are contained within enamel to a lower position further along the EDJ. This procedure is repeated until the cervix of the tooth is reached. The total time for enamel formation is estimated by summing the number of 80 day segments traced out.

Key words: Enamel, Cross striations, Striae of Retzius, Crown formation time

1. Introduction

The crowns of teeth begin to form at different chronological ages. Deciduous tooth crowns all start to form before birth and the first permanent molar crowns at about the time of birth while other permanent tooth crowns (permanent incisors and canines) initiate within a few months of birth. The last teeth to form, the third permanent molars or wisdom teeth, initiate at around 9 years of age (1). If one knows, or can estimate, the age at crown initiation of a tooth type and if the remains of an individual who died has a tooth crown that is just completed, then it is possible to estimate the age at death by calculating the crown formation time from a longitudinal histological section of a tooth. This crown formation time is simply then added to the initiation time to give an estimate of age at death. A major problem with this is knowing the time of tooth

Lynne S. Bell (ed.), *Forensic Microscopy for Skeletal Tissues: Methods and Protocols*, Methods in Molecular Biology, vol. 915, DOI 10.1007/978-1-61779-977-8_5,

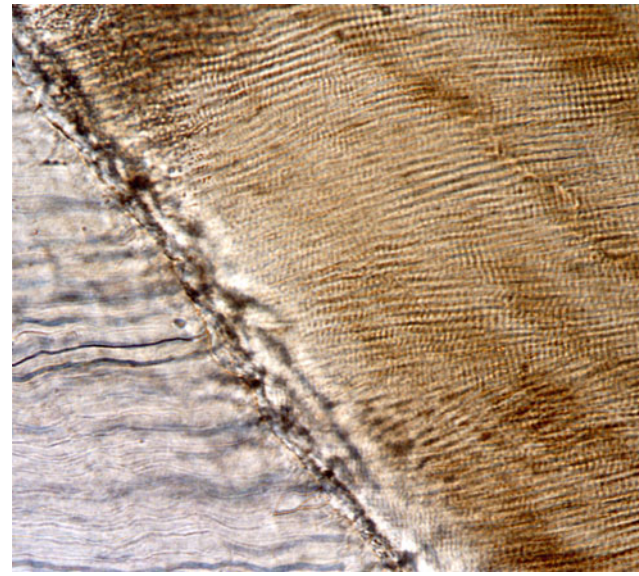

Fig. 1. The junction between dentine on the left and enamel on the right runs obliquely across this image. Thin brown enamel prisms (approximately 5 μm in diameter) pass from the EDJ towards the enamel surface and along their lengths small daily cross striations that seem to divide the prisms into alternating varicosities and constrictions are easily visible in this image. Rarely in practice are they as good as this. Adjacent cross striations are approximately 2.3 μm apart right up against the EDJ in this image but closer to 2.7 μm apart further away from the EDJ.

initiation but teeth that initiate closest to birth show the least variation in their initiation times. This is why in practice, permanent teeth that begin to form closest to birth are the most often used. Permanent canine crowns are usually completed by 5 or 6 years of age and since the permanent canine is usually forming by 6 months of age, this tooth is a good candidate to use to estimate the age at death of a young individual. Using tooth histology to estimate age at death beyond 5 or 6 years of age becomes fraught with problems because it is particularly difficult to transfer data collected from one earlier forming tooth to a later forming tooth and then accurately sum the time record contained within them. However, good new data for modern human tooth formation times determined from radiographs of children of known age are given in Liversidge (1), and these data can be used alongside the histological methods described here to estimate the chronological age of human remains.

The basic structural unit of enamel is the prism (sometimes also called an enamel rod). Enamel prisms are packed tightly together to make up a hard translucent tissue. Prisms radiate out from the enamel dentine junction (EDJ) towards the enamel surface (Fig. 1). Each prism is about 5 or 6 μm (μm) in diameter and is packed in a regular pattern with the prisms that surround it as, e.g., a bundle of pencils would be. Prisms never travel in straight lines but some run a straighter path than others towards the enamel

Fig. 2. Figure 2a is a low power image of a whole ground section of a lower lateral incisor taken with polarizing filters half- (or less) crossed. Figure 2b is of another tooth from the same individual and only shows the cuspal and mid-crown region of the enamel. Here the polarizing filters are fully crossed. A zig-zag of lines passing 200 μm out from the EDJ and then back along the direction of the long-period striae of Retzius to the EDJ again is shown and numbered 0–4 at the EDJ.

surface. Many prisms leave the EDJ roughly orthogonal to this tissue boundary but in the cuspal region of teeth prisms tend to incline more towards the cusp than they do in the mid-crown or cervical region of teeth.

The cells that form enamel (ameloblasts) secrete their matrix in a rhythmic manner (2–4). This creates a daily incremental marking (Fig. 1) along the lengths of enamel prisms usually described as daily enamel cross striations (5–9). Thin sections of teeth prepared for histological analysis can be used to reveal these markings in enamel (7, 10, 11). Counts of daily cross striations in the teeth of individuals with known dates of birth and death match very closely the number of days of life (12). Another, but longer period rhythm, that also slows dental hard tissue formation in a regular way is superimposed upon this daily rhythm (Fig. 2). In modern humans these coarser more prominent markings (sometimes called striae of Retzius (13) when they are very regularly spaced) usually occur every 7, 8, 9, or 10 days with a modal value of 8 days (4). The slope of these coarser oblique incremental markings make to the EDJ, together with counts of daily enamel cross striations, provides a way of estimating past rates and times of tooth formation

(8, 14–17). Long-period striae of Retzius in enamel also create a furrow or trough on the external surface of permanent tooth enamel. These so-called perikymata (waves around the tooth) are well preserved on many teeth that were not badly worn during life and they can be counted with scanning electron microscopy or even in oblique reflected light. Since counts of perikymata are equivalent to counts of long-period striae of Retzius within the tooth, they can be used to estimate enamel formation times when teeth cannot be sectioned histologically. However, the exact number of days between long-period striae of Retzius cannot be known unless the internal structure of the enamel can be visualized. It follows that estimates of crown formation times made in this way are less accurate than those made from sectioned teeth.

The method outlined in this chapter describes how to use a roughly 100 μm thick longitudinal ground section of a tooth to estimate crown formation time. It is essentially a method derived from the original approach used by Boyde (14) and Risnes (17) for estimating crown formation times. It assumes that something of the incremental structure of the enamel can be visualized with transmitted light microscopy (using crossed polarizing filters if need be) and that the available microscope has at least two objectives of approximately ×6 and ×25 magnification each. The method described here assumes the tooth, and therefore tooth section, is near perfectly preserved and sets out an ideal method of calculating crown formation time with the least error for workers who may not be experienced working with tooth histology. While many other methods and variations on the method set out here are possible, this first approach is recommended. It avoids needing to judge the number of days between long period lines and it can also be used on teeth where the cuspal or incisal enamel in teeth is worn to within 200 μm of the dentine horn. At some stage of the process it may not be possible to see or do exactly what is set out here. In this case, the method described here allows that a reference to modern human standards, with known confidence intervals, can be substituted for deficiencies in the data gathering process.

In short, the tooth section should first be scanned at low power under the microscope to identify the EDJ. Usually, the buccal EDJ and buccal enamel are chosen for further scrutiny. Some kind of incremental pattern is then usually visible with long oblique, sometimes even accentuated, striae running from the EDJ to the surface enamel (Fig. 2a, b). If no incremental pattern at all is visible under polarized transmitted light (and this can often be the case in some deciduous tooth sections), then the tooth section is unsuitable for further analysis of this kind. Once a coarse incremental structure is confirmed where the direction of enough striae can be followed from the cusp to the cervix of the tooth at low power, the tooth section should then be examined at higher power. At higher power well-preserved daily increments close to the EDJ in the

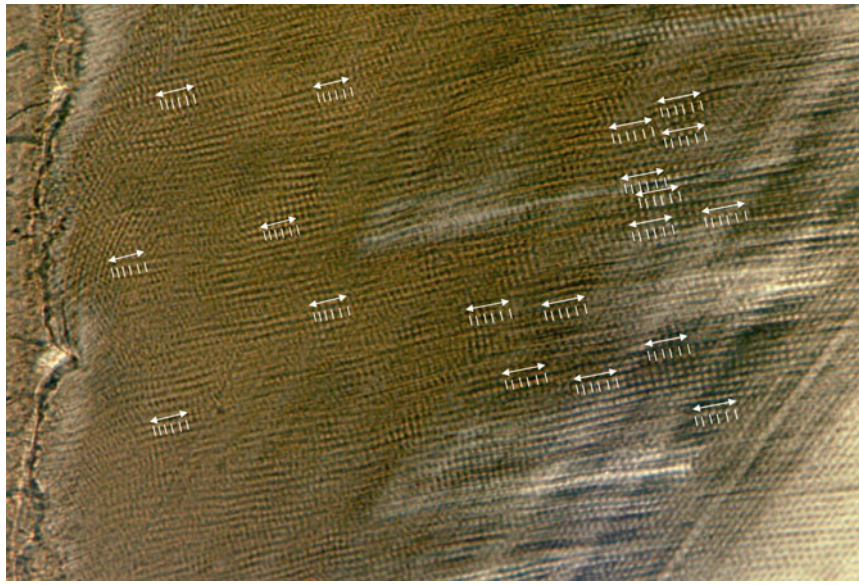

Fig. 3. High power image showing daily cross striations in enamel close to the EDJ. The EDJ is scalloped and hard up against the left hand margin of the image. *White lines* have been drawn over cross striations in groups of 6 (indicating 5 daily increments of enamel growth). The double *white arrows* show the measurements taken across each group. Each one is an average of 5 days growth and the grand average of all of them is a good basis for calculating the inner rates of enamel formation in each zone close to the EDJ. Six groups of prisms are shown in the inner zone and 13 in the outer zone of a 200 μm thickness of enamel but a third middle zone should also be represented (as indicated in Subheading 3). This ensures a good reliable average across what is usually a gradient of increasing enamel secretion rates. To indicate scale in this image, the inner cross striations are ~2.3 μm apart and those further out closer to 3 μm apart.

cusp, mid-crown, and cervix can be visualized (Figs. 1 and 3). Even if none at all can be seen it is still nonetheless possible to use data available for modern human samples to proceed with this technique.

Some kind of image must be recorded repeatedly at various stages of this procedure. This can be a simple photographic image made with a camera back fitted to the microscope and loaded with, i.e., 35 mm color film. This is a cheap and easy option since color film can be processed and printed to any size almost anywhere. Alternatively, many microscopes are fitted with digital cameras and a series of digital images can be used equally well with any computer software that can construct montages of several digital images (i.e., *Photoshop*) and the same or other software capable of making measurements or drawing straight lines onto the digital image (i.e., *Image-J* available online from NIH). Some thought should be given to how the data collected will be archived especially if many teeth are to be analyzed in this way.

The method described here begins with recording three high power images of daily increments within 200 μm of the EDJ in the cuspal, mid-crown, and cervical enamel. Average daily rates within this 200 μm zone are then calculated (Fig. 3). The method then proceeds with the construction of a long digital or photomontage of the whole length of the buccal EDJ at low power (Fig. 2b).

The procedure continues in the cusp at the dentine horn. A 200 μm line is first traced from the EDJ along the direction of enamel prisms just to one side of the complicated, twisted region of central cuspal enamel known as gnarled enamel that is best avoided. Then a line is tracked back from this point along the direction of the long-period striae of Retzius that run obliquely all the way back to the EDJ again. From this new position further along the EDJ the whole procedure is then repeated until a consecutive zig-zag of lines has been traced out from and back to the EDJ all the way from the dentine horn in the cusp to the enamel cervix (Fig. 2b). At this point the total crown formation time (or enamel formation time) can be calculated.

2. Materials

A longitudinal ground section of a tooth roughly 100 μm thick mounted on a glass slide with a clear mounting medium such as styrene-based *DPX*.

A light microscope equipped for polarizing transmitted light microscopy and fitted with a camera (either for digital images or film for photographic micrographs) and at least two objective lenses, one lower power and close to ×6 and one higher power and close to ×25.

3. Methods

3.1. Calculating Average Daily Rates at the EDJ

1. View the ground section using a ×6 or similar objective lens and locate the buccal aspect of the tooth under low power. This is easier to find than at high power.
2. Focus on the dentine horn and then switch to a ×25 or similar power objective lens.
3. Using the X and Y microscope stage controls, move along the length of the EDJ and look for and note three positions, one in the cuspal third, one in the mid-crown third, and one in the cervical third of the tooth where good easily visible daily cross striations can be seen close to the EDJ and for at least 200 μm into the enamel. Ideally they should look like those in Figs. 1 and 3.
4. Make a sketch of what you see and any landmark features like cracks or prominent contours that will make it easy for you to return to these positions later and indicate the three near-equally spaced regions (if possible) containing good daily cross striations that you plan to return to.

5. Remove the tooth section and place a graticule or micrometer slide under the microscope and record an image of this using the ×25 objective.
6. Replace the tooth section and return to the first cuspal region with good daily cross striations visible with the ×25 objective and record an image of this.
7. Record an image of the other regions you identified in the mid-crown and the cervical third.
8. Work with the images (either photomicrographs or digital images on screen) and identify 6 dark cross striations or 6 bright increments between them (Fig. 3) (see Note 1).
9. Place a marker (a spot or line) on each and measure the distance between first and sixth. Realize that there are 5 daily increments bounded by six lines or dots. The double white arrows in Fig. 3 extend across 5 days of increments and represent the length to be measured.
10. Use the image of the graticule or micrometer slide to calculate the magnification of the image you are working with and then divide the measurement corrected to micrometers (μm) you have taken by 5. This is the average length of a prism formed in a 24 h period which is the same as the linear daily rate of enamel formation in this position along a prism.
11. Repeat a series of measurements across 6 increments as many times as possible aiming for 10 averages close to the EDJ, 10 averages about 100 μm beyond the EDJ, and 10 averages approximately 200 μm from the EDJ. Six are identified close to the EDJ in Fig. 3 and 13 deeper into enamel (but none in the middle zone) just for illustrative purposes.
12. Now calculate an average within each of these three zones and take an overall grand average of the three.
13. This grand average (i.e., 2.5 μm) for the whole 200 μm thickness of enamel close to the EDJ must then be divided into 200 to give the average number of days taken to form this thickness of enamel (i.e., 200/2.5 = 80 days).
14. Now repeat this procedure on the mid-crown and cervical high power images of daily cross striations (see Note 2).

3.2. Calculating the Total Crown Formation Time

1. Replace the graticule or micrometer slide under the microscope and record an image of the scale using the lower power ×6 objective lens or similar.
2. Return to the longitudinal section of the tooth and use the X and Y microscope stage controls to position the dentine horn and enamel in this region within the field of view.
3. Position the dentine horn to one side of the field of view and the EDJ below it close to the bottom of the field of view but

still with some dentine beneath the EDJ visible as in Fig. 2b. Note however that only the cuspal third of the total tooth height is shown in this figure.

4. Record this image and move the section using the X and Y stage controls so that the new image that comes into view has moved cervically but still contains an overlapping portion of the old image (see Note 3).
5. Repeat this procedure along the whole length of the EDJ until the cervix is reached. This may take between 5 and 10 images depending on how long the tooth crown is.
6. Join each of the images together either as a single digital image or as a long photomontage and calculate the magnification factor using the image taken at stage 1 above and write this on the montage (e.g., 1 mm = 7.68 μm).
7. Start at the dentine horn (Fig. 2b) and draw a line out along a prism path for 200 μm (see Note 4).
8. Mark the position you start at the EDJ and label it zero. Also mark the point reached 200 μm out clearly.
9. Now from the second point track back to the EDJ along the direction of an oblique long-period stria of Retzius or accentuated line running parallel to these (see Note 5). Mark this new point on the EDJ that is always further away from the dentine horn number 1 as in Fig. 2b.
10. From here on, repeat the procedure of drawing a line out along a prism path for 200 μm and tracking it back to the EDJ along (or in parallel with) an oblique long-period stria of Retzius back to the EDJ. An example of what this looks like in the mid-crown is shown at high power in Fig. 4. It may take 10 or 15 repeats of this to reach the cervix of the tooth. The increments of length along the EDJ get smaller as you approach the cervix each time you do this but the last one or two may actually get larger as the rate of crown formation begins to speed up here just prior to the start of root formation. The end result is a zig-zag pattern of lines between the dentine horn and the cervix of the tooth.
11. At the last increment it may be necessary to use a shorter length along a prism path to be able to track back exactly to the cervix. In this case the number of days to form this thickness of enamel must be calculated separately than the other increments.
12. If the average number of days calculated to form each 200 μm thickness of enamel formed from the EDJ is the same in the cuspal, mid-crown, and cervical regions (say 80 days), then the total crown formation time is equal to the number of 200 μm long lines (minus the first one labeled zero) drawn on the montage multiplied by, e.g., 80 days.
13. If the number of days to form 200 μm of enamel thickness in the mid-crown calculated above is more than in the cuspal

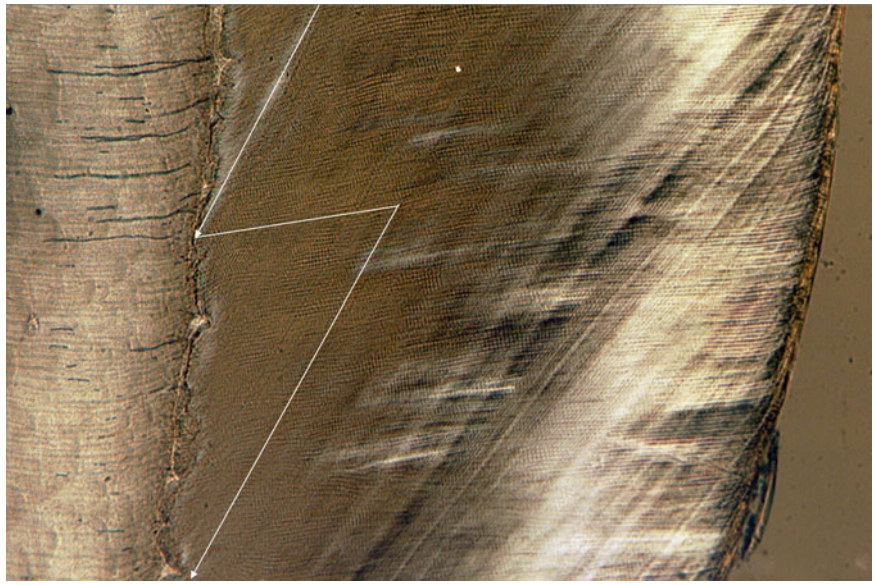

Fig. 4. The same region of mid-crown enamel as shown in Fig. 3 is show here at lower power to illustrate in greater detail how a line 200 μm is drawn out along enamel prisms and then back again to the EDJ parallel with the direction of the oblique slope of the long-period striae of Retzius. Striae can also be seen coming to the surface of the enamel as perikymata, but this is an example where it is too difficult to count the number of days between adjacent striae and perikymata. The method described in this paper avoids this problem altogether.

region, then the middle third of these increments needs to be adjusted accordingly and more days added.

14. Likewise, if the cervical increments take longer to form than those higher in the cuspal or mid-crown regions, the appropriate number of extra days needs to be added to these last few increments that formed more slowly (see Note 6).
15. It is always a good thing to check results against data for larger samples of modern human teeth. Reid and Dean (18) and Mahoney (19) have published data for permanent crown formation times that are useful in this respect.

4. Notes

1. Usually it is necessary to use polarized light to get really good images of daily cross striations but not always. For whatever reason, archaeological material is often better than modern material for seeing good daily increments—perhaps because enamel may be partially demineralized which accentuates incremental markings of all kinds. Sometimes it is impossible to see daily cross striations in sections of teeth. If this is the case, an average value can be used that has been derived from 20 modern

human permanent teeth (20). The formula for this is derived from a polynomial curve fitted to 20 modern human cuspal enamel trajectories and gives 80 days as the average time taken to form 200 μm of enamel from the EDJ. The formula is

$$8.699 + 0.367 \times \mathrm{ET}\mu\mathrm{m} - 0.00005216 \times \mathrm{ET}|$$

where ET μm = enamel thickness from the EDJ measured in micrometers (μm). This formula can be entered into a spreadsheet and any formation time in days estimated for any thickness of enamel up to ~1,500 μm from the cuspal EDJ. The upper and lower 95 and 5% confidence limits for the time taken to form 200 μm of enamel from the EDJ are ~70 and ~90 days respectively. In this way you can judge the fastest and slowest rates expected in a sample of modern human teeth and any departures from this range can be born in mind when looking back for sources of potential error.

2. Usually, the average values for each region of a crown are very similar but the reason for doing this in the cuspal, mid-crown, and cervical regions is to identify any slower rates, particularly in the cervical third of the tooth. This information will be used later to refine the final estimate crown formation time.
3. When preparing images to use in a montage of many images joined together it is important to leave some overlap between each image. This must be sufficient in printed photographs to be able to stick one photograph down on to the other in the correct position. With digital images less overlap is required but there must still be some. If in doubt it is better to end up with more overlap than is needed than none. Also bear in mind that many photographic processes that use automated printing systems actually produce photographs that are cropped (i.e., they end up not in proportion to the 35 mm film used with the edges cropped off) and which may, therefore, eliminate the overlap between sequential images.
4. If you draw an imaginary line directly vertical from the dentine horn, it is best to use this and choose prisms to follow that make an angle of 30–40° to the buccal of this as in Fig. 2. By avoiding the complex twisting prisms in the cusp of the tooth the estimate of 80 days to form enamel 200 μm thick here is then least error prone. The reason for choosing 200 μm as a consistent measure each time is to reduce the number of individual calculations for the time taken to form increments of enamel thickness beyond the EDJ. In practice any length can be used but estimates of the time taken become more error prone as the thickness increases. So 200 μm is a compromise that seems to work best and is easiest to do repeatedly. Also, a larger number of smaller lengths along the EDJ can be given an individual formation time of their own and the data collected are then maximized. These cumulative lengths can then

be plotted to produce a smoother curve of growth in tooth height along the EDJ against cumulative crown formation time than if they are irregular and very variable increments of length and time (see ref. (11) for examples of this). Reference (11) also describes how to continue into the root and calculate the formation time of any root formed beyond the enamel cervix.

5. Before beginning to take images along the EDJ, it is good to adjust the lighting and analyzer (the polarizing filter that you can rotate on the microscope) so that the direction of any long-period striae of Retzius and or accentuated markings running in the same direction as these are most easily visible. This should be checked at the cusp and at the cervix at the start, as changing things once you get going makes it very difficult to construct montages because features tend to change beyond all recognition when the polarizing filters are rotated even a little. Half-crossed polarizing filters often work quite well. Figure 2a, b shows examples of images with half-crossed polarizing filters and more fully crossed polarizing filters—the background is totally black when the polarizing filters are completely crossed. There is, however, no need to have them totally crossed to visualize clear incremental markings of any kind. It sometimes helps to draw dotted lines along easily visible long-period or accentuated increments in the same region of a tooth section. Then even if no actual line exists in the exact place required, it is much easier to place a line parallel with those dotted in either side of it.
6. Inner enamel is usually fairly constant in its formation rate within an individual and usually there is not much difference in the time taken to form 200 μm of enamel thickness in the cervix than in the cusp. Where there is a difference, it is usually in the last 3 or 4 cervical-most increments where each 200 μm thickness of enamel might take up to 5 or 10 days longer to form than in the cusp or mid-crown. Some sections of teeth are so good that it is actually possible to count the number of daily increments along each 200 μm prism length. When this is possible, it is clearly a good way of checking the previous calculations made at high power of how many days formation exist within the increment used.

Acknowledgements

I am grateful to Lynne Bell for inviting me to contribute to this volume. The method described here is a variation on that originally described by Boyde (10, 14), Risnes (17), and Antoine (12) in previous studies that made estimates of enamel formation times in modern human permanent teeth.

References

1. Liversidge HM (2009) Permanent tooth formation as a method of estimating age. In: Koppe T, Meyer G, Alt KW (eds) *Frontiers of Oral Biology; Interdisciplinary Dental Morphology*. Karger, Basel
2. Bromage TG (1991) Enamel incremental periodicity in the pig-tailed macaque; a polychrome fluorescent labelling study of dental hard tissues. Am J Phys Anthropol 86:205–214
3. Bromage TG, Lacruz RS, Hogg R, Goldman HM, McFarlin SC, Warshaw J, Dirks W, Perez-Ochon A, Smolyar I, Enlow D, Boyde A (2009) Lamellar Bone is an incremental tissue reconciling enamel rhythms, body size and organismal life history. Calcif Tissue Int 84(5): 388–404
4. Smith TM (2006) Experimental determination of the periodicity of incremental features in enamel. J Anat 208:99–113
5. Boyde A (1976) Amelogenesis and the strucvture of enamel. In: Kramer IRH, Cohen B (eds) Scientific Foundations of Dentistry. W. Heinemann Medical Books Ltd., London
6. Boyde A (1979) Carbonate concentration, crystal centres, core dissolution, caries, cross striation, circadian rhythms and compositional contrast in the SEM. J Dent Res 58: 981–983
7. Boyde A (1989) Enamel. In: Oksche A, Vollrath L (eds) Handbook of microscopic anatomy, vol 2, Teeth, Springer, Berlin
8. Boyde A (1990a) Developmental interpretations of dental microstructure. In: De Rousseau, Jean C (eds) Primate life history and evolution: monographs in primatology, vol 14. Wiley-Liss Inc, New York
9. Shinoda H (1984) Faithful records of biological rhythms in dental hard tissues. Chem Today 162:34–40 (In Japanese)
10. Boyde A (1990) Confocal optical microscopy. In: Duke PJ, Michette AG (eds) Modern microscopies: techniques and applications. Plenum Press, New York
11. Dean MC (2009) Growth in tooth height and extension rates in modern human and fossil hominin canines and molars. In: Koppe T, Meyer G, Alt KW (eds) Frontiers of Oral Biology; Interdisciplinary Dental Morphology. Karger, Basel
12. Antoine D, Hillson S, Dean MC (2009) The developmental clock of dental enamel: A test for the periodicity of prism cross-striations and an evaluation of the likely sources of error in histological studies of this kind. J Anat 214:45–55
13. Retzius A (1837) Bemerkungen über den inneren Bau der Zähne, mit besonderer Rücksicht auf dem in Zahnknochen vorkommenden Röhrenbau. (Müllers) Arch Anat Physiol 1837:486–566
14. Boyde A (1963) Estimation of age at death of young human skeletal remain from incremental lines in dental enamel. Third International Meeting in Forensic Immunology, Medicine, Pathology and Toxicology, pp 36–46
15. Boyde A (1964) The structure and development of mammalian enamel. PhD Thesis, University of London
16. Shellis RP (1984) Variations in growth of the enamel crown in human teeth and a possible relationship between growth and enamel structure. Arch Oral Biol 29:697–705
17. Risnes S (1986) Enamel apposition rate and the prism periodicity in human teeth. Scand J Dent Res 94:394–404
18. Reid DJ, Dean MC (2005) Variation in modern human enamel formation times. J Hum Evol 50:329–346
19. Mahoney P (2008) Intraspecific variation in M1 enamel development in modern humans: Implications for human evolution. J Hum Evol 55:130–146
20. Dean C, Leakey MG, Reid D, Schrenk F, Schwartz GT, Stringer C, Walker A (2001) Growth processes in teeth distinguish modern humans from *Homo erectus* and earlier hominins. Nature 414:628–631

Chapter 6

The Determination of Age in Subadult from the Rib Cortical Microstructure

Margaret Streeter

Abstract

Studies on adult bones have demonstrated the age-associated accumulation of histomorphological characteristics that have been used to develop age at death estimation methods. These methods are unsuitable for use with subadult bones because the rapid and extensive turnover and replacement of cortical bone that occurs with growth and development removes any age-associated variables such as osteon numbers. The qualitative analysis of 72 rib samples from individuals of known age has identified a sequence of developmental stages in the growing rib. Recognition of the systematic pattern of changes in the subadult rib has resulted in the development of a four phase qualitative method of age estimation applicable to the subadult rib cortex.

Key words: Bone histology, Subadult rib cortex, Qualitative age estimation

1. Introduction

Histological estimation of age at death has gained increasing use by forensic anthropologist. Complimenting methods based on gross morphology, histological aging also provides alternatives in cases of fragmentary or degraded bone. Until recently, however, histological aging methods were limited to the adult skeleton. Although remodeling begins in early prenatal life (1, 2) the rapid growth and modeling drift that occurs in subadult bones results in a poor correlation between age and any quantifiable histomorphological structures that could be used to determine age. The qualitative analysis of a sample of ($N = 72$) subadult fifth, sixth, or seventh ribs (45 males and 27 females) taken at autopsy from individuals of known age (2–21 years, mean 14.1 ± 5.2 years) has identified a sequence of developmental stages in the growing rib. These clearly defined and easily recognizable patterns were used to develop a rapid and easy four-phase method of age assessment that is applicable to the subadult rib cortex (Fig. 1).

Lynne S. Bell (ed.), *Forensic Microscopy for Skeletal Tissues: Methods and Protocols*, Methods in Molecular Biology, vol. 915,
DOI 10.1007/978-1-61779-977-8_6,

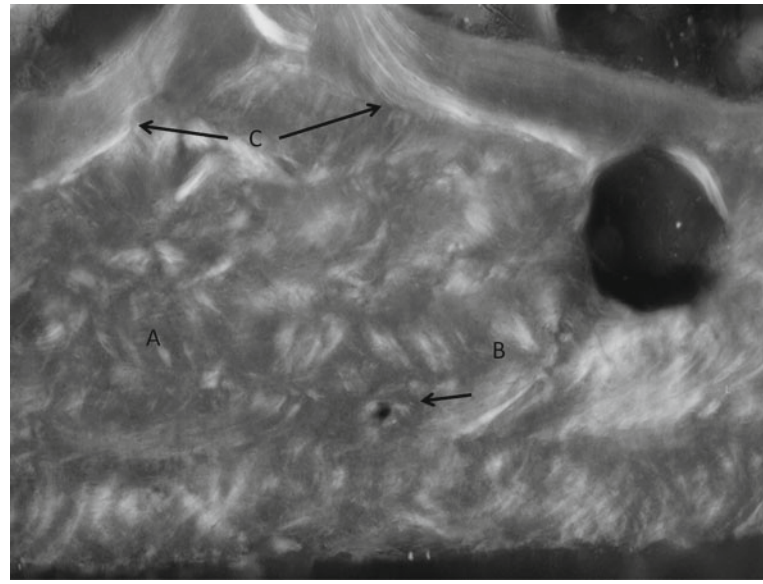

Fig. 1. Pleural cortex of woven bone (**a**) containing primary vascular canals (**b**) and primary lamellar bone (**c**) deposited on endosteum (×100 polarized).

2. Materials

1. Cross section of a subadult rib ±100 μm thick mounted on a standard glass microscope slide and cover slipped.
2. A standard light microscope fitted with low power and high power (×40, ×100, and ×200) magnification and a light polarizer.

3. Methods

The bone microstructure of the subadult rib undergoes a predictable series of developmental stages that correlate with specific age ranges. An understanding of histological terms and the underlying bone biology is necessary to correctly interpret the bone histomorphology. Therefore, the following terms and definitions are used to describe the morphology employed in this subadult aging method.

Woven bone—quickly formed, highly mineralized, but less well organized than lamellar bone. Characterized by the appearance of a tweed or woven pattern, this type of bone is only discernable with the aid of polarized light (Fig. 1a).

Primary lamellar bone—unremodeled lamellar bone formed during modeling on periosteal or endosteal surfaces and deposited in parallel layers (Fig. 1c).

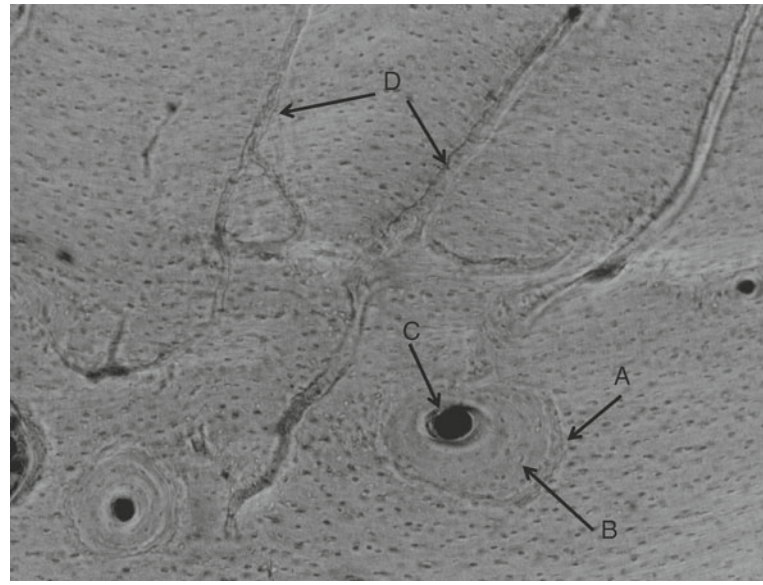

Fig. 2. Primary lamellar bone containing a Type I drifting osteon (**a**) formed from concentric lamellae (**b**) with an eccentric Haversian canal (**c**). Note numerous Volkmann's canals (**d**) (100×).

Primary vascular canals—blood vessels that were originally located on the periosteal or endosteal surfaces of bone but subsequently have been incorporated into the cortex as layers of lamellar bone were deposited over them during modeling (Fig. 1b).

Concentric lamellar bone—lamellar bone formed secondarily during remodeling characterizing Haversian systems (secondary osteons) (Fig. 2b).

Haversian canals—central canal located in secondary osteons that contain blood vessels, lymphatic tissue, and nerves (Fig. 2c).

Volkmann's canals—transverse non-Haversian canals that connect to Haversian and Primary vascular canals (Fig. 2d).

Type I osteons—secondarily formed Haversian systems resulting from the tethered resorption and then deposition of discrete packets of bone. Concentric lamellae that are circumscribed by a reversal line and contain a central Haversian canal (Fig. 2a).

Drifting osteons—osteons formed by the same resorption followed by deposition of lamellar bone that creates the common Type I osteons but they are elongated in cross section (at least twice as long as they are wide) and characterized by eccentric Haversian canals (Fig. 2a).

Matching the micromorphological characteristics of a given rib cross section with the description of one of the four age phases (Table. 1) provides a phase and the associated age range (see Notes 1, 2, and 3).

Table 1
Summary of rib phases

Phase	Primary lamellar bone	Remodeling	Woven bone	Cutaneous cortex	Pleural cortex
Phase I—less than 5 years	Rare, small areas on pleural-endosteal and cutaneous-periosteal surfaces initially	Rare	Most of both cortices	Thinner, mostly woven bone, many primary vascular canals	Thicker, some woven bone, primary lamellae form initially endosteally
Phase II—5–9 years	New primary lamellar bone on pleural cortex	Large drifting osteons on pleural cortex originating at periosteum	Some areas on cutaneous cortex, rare woven bone on pleural cortex	Thinner, mostly intracortical woven bone, many primary vascular canals	Thicker, largely primary lamellar bone, few drifting osteons many Volkmann's canals
Phase III—10–17 years	Both cortices intracortically	Drifting osteons on both cortices	Thin rind on cutaneous-periosteal surface	Thinner, mostly lamellar bone with some remodeling, periosteal woven bone, large resorptive bays (drifting osteons)	Thicker, denser remodeling still some areas of primary lamellar bone
Phase IV—18–21 years	Both cortices	Both cortices, fewer drifting osteons more Type I osteons	None or rare	Thinner, dense remodeling, osteons 3–4 rows deep, primary lamellar bone periosteally	Thicker, dense remodeling, osteons 3–5 rows deep, occasional areas of primary lamellar bone

Phase I: (less than 5 years of age). The developing rib cortex is initially composed of woven bone. The margins of the marrow cavity are indistinguishable at first but the medullary space becomes more clearly defined and the trabeculae of the marrow cavity become distinct from the cortex in the later years of this first phase. Modeling drift is discernible as the deposition of circumferential lamellar bone gradually replaces the natal woven bone. This transition occurs first on the pleural cortex. The newly deposited primary lamellar bone accumulates first on the pleural-endosteal and later on the cutaneous-periosteal cortices through drift. Osteoclastic resorption, on the other hand, is evident as the scalloped surfaces (Howship's lacunae) along the pleural-periosteal and the cutaneous-endosteal margins. Intracortical remodeling in the form of drifting osteons begins late in this phase. The cutaneous cortex is chiefly comprised of woven bone while the pleural cortex is distinguished by the appearance of primary lamellar bone that contains many Volkmann's canals.

1. Scan the entire rib cross section at low magnification (×40) to identify the pleural and cutaneous cortices (see Note 4). The pleural cortex is consistently wider than the cutaneous and the costal grove is located on the inferior surface of the pleural cortex (3). Note the presence or absence of the marrow cavity.
2. At a higher magnification (×100 or ×200 as necessary to identify histological structures) scan the pleural cortex and note:
   (a) Presence or absence and location of woven bone (see Note 5).
   (b) Presence or absence of primary lamellar bone.
   (c) Presence or absence of primary vascular canals.
   (d) Presence or absence of osteons.
      - Location.
      - Orientation relative to the periosteum and endosteum.
      - Density (number of rows deep) from periosteum to endosteum.
   (e) Type of osteon morphology (drifting, or Type 1).
   (f) Presence of Volkmann's canals.
3. Scan the cutaneous cortex also at a higher magnification (×100 or ×200 as necessary to identify histological structures) and note:
   (a) Presence or absence and location of woven bone.
   (b) Presence or absence of primary lamellar bone.
   (c) Presence or absence of primary vascular canals.
   (d) Presence or absence of osteons.

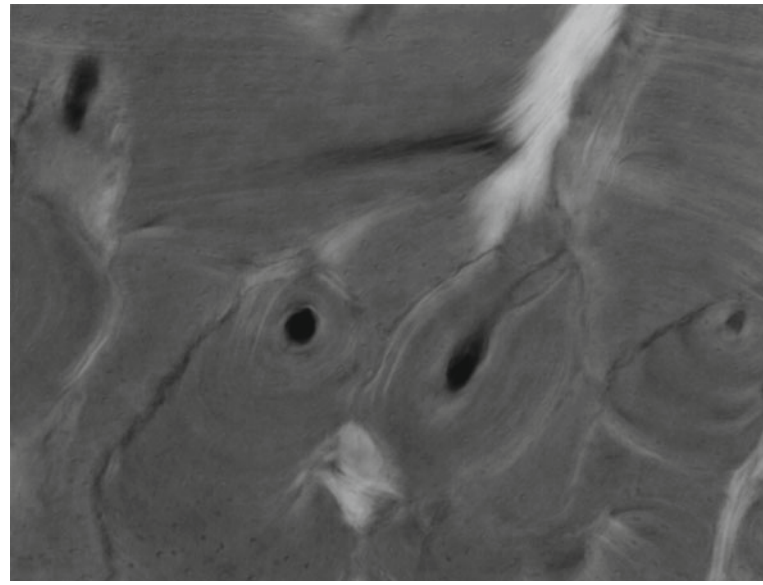

Fig. 3. Drifting osteons in a trajectory from periosteum to endosteum (100×).

- Location.
- Orientation relative to the periosteum and endosteum.
- Density (number of rows deep) from periosteum to endosteum.

(e) Type of osteon morphology (drifting, or Type 1).

(f) Presence of Volkmann's canals.

Phase II (5–9 years). The defining feature of this phase is the evidence of intracortical remodeling in the form of drifting osteons a unique characteristic of the subadult cortex (4). These drifting osteons form first in the primary lamellar bone near the periosteal surface of the pleural cortex. They are often aligned in parallel rows drifting on a trajectory from the periosteum toward the endosteum (Fig. 3). Many of these drifting osteons are incompletely formed with active bone deposition observable on one side ("the tail") of the wide, eccentrically oriented, vascular canal and resorption indicated by the presence of the scalloped Howship's lacunae on the opposite side of the canal perimeter (4). In phase II, differences in the thickness of the two cortices are frequently marked. The pleural cortex is often two to three times the width of the thinner cutaneous cortex. Another consistent feature of this phase is the large number of Volkmann's canals that are dispersed throughout the pleural cortex, many of them linking osteons and the periosteal and endosteal surfaces. In contrast, the cutaneous cortex is typified by a very porous appearance produced by the presence of large resorptive bays. Inspection at high magnification reveals the

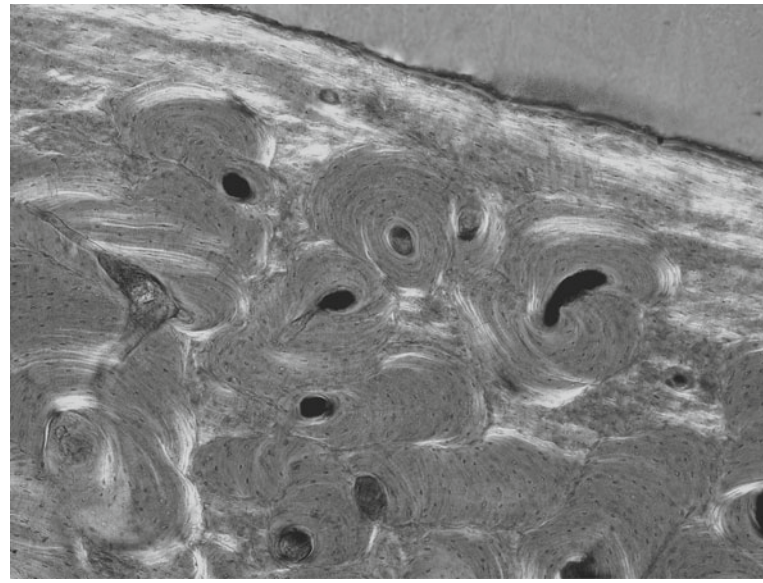

Fig. 4. Cutaneous cortex with drifting osteons 3–4 deep from periosteum to endosteum. Note the unremodeled primary lamellar bone at the periosteum (×100 polarized).

characteristic simultaneous resorption and formation fronts of very large drifting osteons (Fig. 3). Modeling (cortical) drift is evident in the resorption (scalloped surface) on the pleural-periosteal and cutaneous-endosteal surfaces while formation (smooth surface) occurs on the pleural-endosteal and cutaneous-periosteal surfaces. As a result of this drift, the trabeculae that were originally formed as part of the marrow cavity can often be seen incorporated into the pleural cortex. Scattered patches of woven bone may still be observed intracortically especially on the cutaneous cortex.

Phase III (10–17 years). On both cortices, the primary lamellar bone is increasingly remodeled with drifting osteons often two or more rows deep. A typical characteristic of this phase is the thin rind of primary lamellar or woven bone that can be seen along the cutaneous-periosteal surface (Fig. 4). This unremodeled bone is often interspersed with primary vascular canals, a reflection of the accelerated cortical modeling typical of the increase in the growth rate associated with this age range.

Phase IV (18–21 years). The two rib cortices have a more adult morphology with Type I osteons becoming more common and fewer drifting osteons. The accumulation of Haversian systems often reaches a density three or more rows thick resulting in the creation of osteon fragments. Volkmann's canals may still be seen on unremodeled areas of the pleural cortex but primary vascular canals are rare.

4. Notes

1. The phase descriptions are intended as a guide in the identification of age ranges. Therefore, the overall morphological trend as it relates to a given phase should be considered.
2. We have found that it is sometimes only possible to assign a rib to an early or late stage of a phase (e.g., late phase II or early phase III).
3. Micromorphology that deviates from the pattern described above for the four phases could be an indication of a disturbance in normal growth.
4. Continually adjusting the fine focus will facilitate the identification of the more indistinct structures such as Volkmann's and primary vascular canals.
5. The contrast-enhancing qualities of polarized light aid in the visualization of woven bone and improve the quality of the image. Viewing of archeological samples in particular is improved by the use of a polarizer.

References

1. Burton P, Nyssen-Behets C, Dhem A (1989) Haversian bone remodeling in human fetus. Acta Anat 135:171–175
2. Baltadjiev G (1999) Micromorphometric characteristics of osteons in compact bone of the growing tibia of human fetuses. Acta Anat 154:181–185
3. Landeros O, Frost HM (1966) Comparison of amounts of remodeling activity in opposite cortices of rib in children and adults. J Dent Res 45:152–158
4. Robling AG, Stout SD (1999) Morphology of the drifting osteon. Cells Tissues Organs 164:192–204

Chapter 7

Rib Histomorphometry for Adult Age Estimation

Christian Crowder, Jarred Heinrich, and Sam D. Stout

Abstract

Estimating the age at death in the adult skeleton is problematic owing to the biological variability in morphological age indicators and the differential response to environmental factors over an individual's life. It is becoming increasingly important for anthropologists to improve age estimates through the use of multiple age indicators and various modalities of assessment (e.g., macroscopic, microscopic, and radiological). Lack of instructional texts describing how to prepare histological samples and evaluate bone under the microscope has been a restricting factor in the widespread use of current histological methods within the field of forensic anthropology. The limited use of histological methods for age estimation often lies in the misunderstanding that the preparation and evaluation of cortical bone thin sections is a highly technical and an expensive endeavor. Like any method of age estimation, the researcher/practitioner must be guided through the analytical process to ensure reliable and repeatable results. This chapter provides a step-by-step instructional guide in the preparation and evaluation of histological samples removed from the sixth rib for histological age estimation.

Key words: Histomorphology, Histomorphometry, Microscopy, Age Estimation, Forensic Anthropology

1. Introduction

Histological and histodynamic parameters of age-related bone remodeling have been well documented in the anthropological literature for various skeletal elements (1–16). Although histological methods of age estimation were introduced nearly 5 decades ago, methods remain under-utilized by physical and forensic anthropologists compared to methods that employ more traditional gross skeletal age indicators (e.g., pubic symphysis, fourth rib, auricular surface). The premise of histological age estimation is based upon clinical and anthropological research demonstrating that the turnover of BSUs (bone structural units), known as secondary osteons, occurs in cortical bone at a predictable rate over an individual's lifetime. This relationship should be evident in nonpathological

Lynne S. Bell (ed.), *Forensic Microscopy for Skeletal Tissues: Methods and Protocols*, Methods in Molecular Biology, vol. 915,
DOI 10.1007/978-1-61779-977-8_7,

adult bone until remodeling rates begin to fluctuate after the 6 decade of life, as homeostasis is compromised by senility (17) and an asymptote for observable osteonal structures is reached. The asymptote occurs when the bone has become completely remodeled so that new osteon creations simply replace older ones and the proportion of the cortex that is remodeled does not increase (18, 19).

When considering the current histological methods available in the literature, the analysis of the sixth rib has undergone considerable improvements and method validation making them the most reliable methods available (2, 11, 20–22). However, validation studies suggest that inexperience in preparing and evaluating slides often results in erroneous analyses and interpretations, which may be one of the leading factors attributing to the infrequent application of histological methods within the field (20). Methods, as presented in journal articles, often do not provide adequate instruction for histological analysis owing to the limited space to discuss the nuances of sample preparation and bone histomorphology. There are publications available that specifically address hard tissue sample preparation and the authors urge the readers to explore this literature (for examples see (23–25)). While this chapter also provides an in-depth instructional guide to preparing undecalcified hard tissue samples, it is unique in that it presents step-by-step instructions for the histological analysis of cortical bone from the midshaft of the sixth rib using methods developed by Dr. Sam D. Stout and colleagues (2, 10, 11).

2. Materials

The following are examples of materials and equipment typically use to prepare undecalcified hard tissue sections for microscopic analysis.

2.1. Tissue Procurement

Autopsy saw.

Dremel Rotary Tool.

Dremel Reinforced Fiberglass Cutting Disc.

2.2. Tissue Preparation and Embedding

Degreasing chemicals: Acetone, Clear-Rite™ 3, Xylene.

Embedding molds (Peel-A-Way Embedding Molds) and Mold Release Agent.

(Buehler) Epothin Epoxy Resin (100 parts resin to 39 parts hardener).

(Buehler) Epothin Epoxy Hardener (39 parts hardener to 100 parts resin).

(Buelher) Ultramet 2005 Sonic Cleaner.

(Buelher) Ultramet 2 Sonic Cleaning Solution (1 part solution to 20 parts water).

Decompression chamber/vacuum.

Labels.

Indelible pen.

2.3. Thin Section Preparation

(Buelher) IsoMet 1000 Precision Saw.

(Buelher) Isocut Plus Cutting Fluid (1 part fluid to 20 parts water).

(Buelher) Ecomet 400 Variable Speed Grinder.

(Buelher) Carbimet Disc 320/P400 12″ (30.5 cm) Diam.

(Buelher) Ultraprep Diamond Mounted Disc.

(Buelher) Diamond Wafering Saw.

(Buelher) Microcut Discs 12″ Grit 800.

Micrometer.

2.4. Sample Mounting and Cover Slipping

Crystal bond.

Protocol Secure Mount Mounting Medium.

(Fisher) Premium Microscope Slides Plain—3″ × 1″ × 1 mm.

(Fisher) Microscope Cover Glass 12-543-01 22 mm × 44 mm -2.

Kimwipes.

(Fisher) Transfer Pipettes Disposable Polyethylene.

2.5. Microscope and Accessories

Compound Microscope with ×10 Ocular Lens, and ×10 and ×20 Objective Lenses.

Merz Counting Reticule.

Polarizing filter.

Microscope Digital Camera with Image Capturing Software.

3. Methods

There are several methods that may be used in the preparation of samples for histological analysis. The authors, in their laboratories, use the tissue preparation methods presented in this chapter and describe some of the variations in these methods. Ultimately one may utilize any method that produces histological thin sections for 2-D microscopic evaluation. Regardless of preparation method, there are a few requirements in order to obtain optimal and reliable results. Thin sections must be ground to a final thickness between 75 and 50 μm and slides should be cover slipped to optimize the optics for microstructure resolution.

In 1986, Dr. Sam D. Stout introduced the method for estimating age using the sixth rib in a case report published in the Journal of Forensic Sciences. The method was largely based on clinical research performed by Dr. Harold Frost and colleagues at the Henry Ford Hospital during the 1960s and 1970s. Since the introduction of Stout's method of age estimation using sixth rib histomorphometry, Stout and colleagues have continued to modify the method and increase the size of the reference population (2, 11). The most recent improvement by Cho et al. (2) provides for a more robust and versatile method and, therefore, the authors recommend it for use in the forensic setting. Forensic casework often involves disarticulated remains with commingled or fragmentary ribs, which may cause uncertainty in rib seriation resulting in the inability to positively identify the sixth rib. According to a pilot study by Crowder and Rosella (21), nonsixth ribs, namely 4 through 7, can provide similar osteon population density (OPD) values compared to those of the sixth ribs, which is the established standard rib for histological age estimation. Historically the sixth rib midshaft was evaluated in clinical studies during the 1950s and 1960s because it was the preferred location for bone biopsies in living subjects.

3.1. Sample Preparation

3.1.1. Procurement, Maceration, and Delipification

1. At autopsy, access to the left and right sixth ribs is possible when the chest plate is removed. A Stryker saw or loppers may be used to procure the samples from the chest plate. Once the ribs are removed, standard maceration procedures to remove soft tissue should be followed (26–28).
2. Once the soft tissue is removed, a Dremel (rotary) tool with reinforced cutting discs can be used to remove a 4 cm transverse section of bone from the middle third of the rib. The rib section should be large enough for multiple thin sections to be removed and small enough to fit into the embedding mold.
3. Remove debris from the surface of the sample or inclusions in the medullary cavity by placing the sample in an ultrasonic cleaner with 20 parts water to 1 part cleaning solution (e.g., Buehler Ultramet 2 Sonic Cleaning Solution) for 5–10 min.
4. Remove bone grease by placing the sample in a Clear-Rite™ 3 bath (or other degreaser) for 24–72 h. Clear-Rite™ 3 will remove lipids, which cause diminished slide quality, without causing the sample to become brittle. Xylene or acetone may also be used to remove lipids; however, extended soaking in these chemicals will make the bone brittle or chalky.

3.1.2. Embedding

1. Prior to embedding a tissue sample it is important to prepare the molds. Pour a thin layer of the embedding medium (mixture described below) into the empty molds and allow it to set for 1 day. This step is performed before the tissue is ready for

Fig. 1. Rib midshaft section embedded in resin mold.

embedding and will provide a platform for the sample to ensure that the base of the sample is not exposed.

2. When the sample is ready to embed, mix epoxy resin and hardener (100:39 ratio by weight for Buehler Epothin Epoxy solutions). Stir the solution for 2 min. Avoid aggressively stirring to reduce the air bubbles introduced to the solution.
3. Label each specimen using a pencil or indelible pen and record the case number, rib number, and side on the label.
4. Place the rib sample and label into the prepared mold. Peel-A-Way® Embedding Molds have a slot designed to hold the label. Mix the desired amount of the epoxy solution in the manner described in Step 2. Pour the mixed solution into the molds containing sample and label and completely cover the sample (It should be noted that some molds may require the use of a release agent so the mixture does not adhere to the sides) (Fig. 1). Place the molds into a vacuum chamber and depressurize samples until the epoxy solution has infiltrated the cancellous bone and the air bubbles are removed (see Notes 1 and 2). While keeping the sample submerged, use tweezers or a probe to align the sample so that it is parallel with the long side of the mold. Ensure the label is properly secured and visible. Allow the sample to cure for 1 day.

3.1.3. Sectioning, Grinding, and Polishing

1. To cut thick sections, a precision sectioning saw is recommended but not required. While a Buehler IsoMet saw is utilized in this protocol, other precision sectioning saws are available with similar cutting mechanics (for example: Leco, Smartcut, CT3, Petrothin).
2. Add cutting fluid (20 parts water and 1 part Buehler Isocut Plus Cutting Fluid) to the fluid reservoir of the IsoMet. Tightly

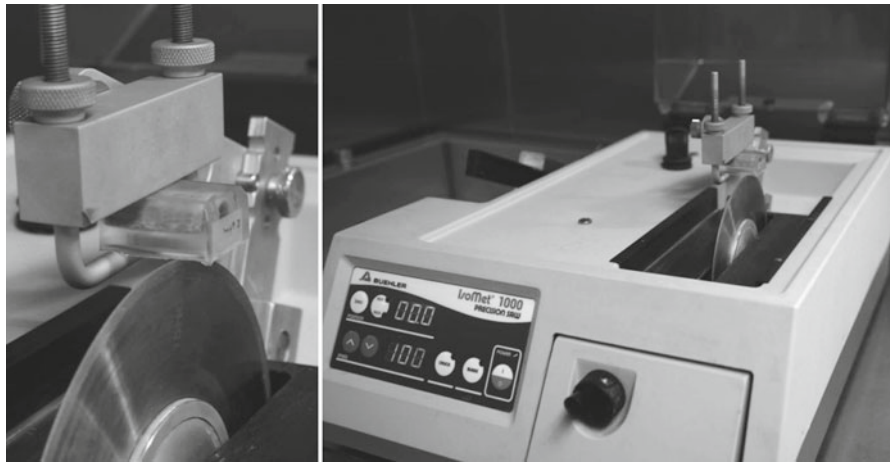

Fig. 2. Positioning of the embedded sample for removing a cross section using an Isomet saw.

secure the diamond wafer blade and check to make sure the fluid level is high enough to submerge the cutting portion of the blade. Secure the embedded sample in the chuck and position it so that a cross section of the bone will be cut perpendicular to its length. Fasten the chuck to the cutting arm of the IsoMet saw and move the arm using the dial so that the blade will transect the rib (Fig. 2). Zero out the dial for the position of the cutting arm prior to sectioning the bone.

3. Add weights to the far side of the arm to counter the weight of the cutting arm. Adjust the amount of counterweight necessary to counter balance the weight of the arm, chuck, and the sample. If insufficient counterweight is used, the sample may bear down on the blade and cause it to fracture.
4. Set the saw speed to 100 rpm and slowly lower the sample on to the blade. During the initial sectioning, monitor the blade and chuck for movement such as wobbling or bouncing. If the chuck is wobbling, immediately stop the blade and tighten the blade and/or chuck-arm assembly before you resume cutting. Add additional counterweights if the chuck is aggressively moving up and down. Aggressive side-to-side movement will cause the blade to fracture.
5. After the initial waste cut (a section removed to provide a well-defined surface for the first usable thick section), raise the chuck arm and, using the dial, move chuck over (towards the blade) 1 mm to produce a 1 mm thick section from the second cut. Using the same counterweight and speed settings, start the blade and slowly lower the sample onto the blade. After a thick section is cut, place the section between two slides and clamp the sample with small binder clips to keep section flat, preventing warping. Make additional 1 mm thick sections until

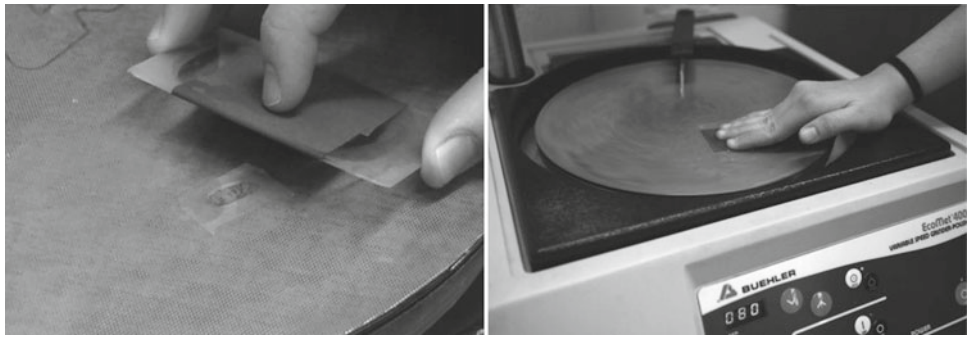

Fig. 3. Technique using a glass slide and a piece of sand paper as gripping device to facilitate the grinding/polishing of the rib thick section on a grinding wheel.

the desired number of sections has been removed from the sample block (see Note 3).

6. Prepare a specimen gripping device and the grinder-polisher for grinding the thick section. A Buehler Ecomet Variable Speed Grinder is used in this example, but other specimen grinder-polishers are available (for example: Leco, Struers, Sinowan, Smartcut). Cut a piece of adhesive coarse fine sandpaper and adhere it to a slide to create gripping device. If preferred, manufactured handheld gripping devices are available for this process. Place a diamond mounted disc or sand paper on the grinder, turn on the water, and start the wheel at 80 rpm until the grinding disc is completely covered in water. Remove the thick section from between slides held with binder clips, moisten it with water, and place on wheel. Place the coarse gripping device on top of sample and start wheel at 80 rpm with the water on (Fig. 3). Apply even pressure with fingers. Stop the wheel and evaluate the sample periodically to ensure even progress and sample thickness. As the sample becomes transparent, check the sample for debris (often found in the medullary cavity). If there is debris, place sample in the sonicator for 1–5 min. If the sample is very thin and/or delicate this procedure can damage the sample so it should be done before the sample becomes too thin.
7. Once sample becomes translucent against the gripping devices surface, place it in between two slides and the check the clarity under the microscope. Continue grinding as needed. If necessary, use a digital micrometer to measure the thickness of the thin section. The final thickness of the thin section should measure between 75 and 50 μm. (see Notes 4 and 5).
8. Once the thin section is between 75 and 50 μm, inspect it for striations produced from the sandpaper grit. If striations are present, polish the thin section with a polishing disc and diamond suspension fluid using the same protocol mentioned

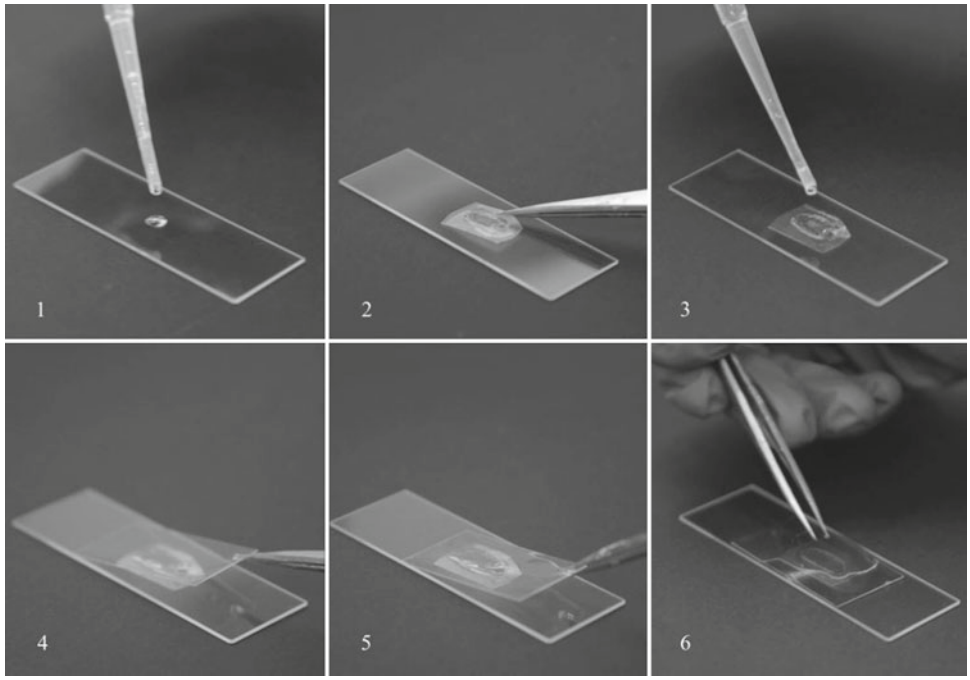

Fig. 4. Steps in mounting a rib thin section to a slide.

above. When the striations have been removed, gently wash the section in a water bath to remove the polishing fluid. The section can be dried by placing it in a Kimwipe between two slides to keep it flat or by dipping the thin section in an alcohol bath and blotting of the excess.

3.1.4. Mounting and Cover Slipping Thin Sections

1. Take a new 3″×1″×1 mm slide and using a pipette, place three drops of mounting medium on to center of slide (Fig. 4 step 1). Tilt the slide in a circular fashion to evenly spread the secure mount to roughly cover the same surface area as your prepared thin section. Remove the thin section from between the two slides using fine tweezers and carefully place the sample on the mounting medium, using the tweezers to flatten the sample against slide (Fig. 4 step 2, see Note 6). Push out any air bubbles that may be trapped under thin section. Place three to four drops of mount medium on top of the thin section (Fig. 4 step 3c).
2. Using tweezers, dip a 22 mm×44 mm cover slip in Clear-Rite™ or xylene and draw off any excess with a paper towel. Carefully place the edge of the cover slip down at the boundary of the mounting medium (Fig. 4 step 4). Slowly lower the cover slip onto the slide (Fig. 4 step 5). It should be noted that the use of xylene may result in air bubbles appearing under the cover slip over time as the medium dries. Thus, the use of xylene may not facilitate long-term use of prepared slides.

3. Once the mounting medium starts adhering to the cover slip, release the cover slip. Using tweezers, very gently press down at the center of the cover slip to facilitate the mounting medium spreading and equalizing under the cover slip (Fig. 4 step 6). Observe the profile of the slide. If it is not level or the mounting medium does not cover the complete slide, air pockets will form under the cover slip and compromise the optics of the slide. If necessary, apply additional pressure with the tweezers to even out the cover slip. If there does not appear to be enough mounting medium, apply single drops with the pipette to the junction between the cover slip and the slide at the portion with insufficient mounting medium. Capillary action will disperse the mounting medium under the cover slip. (see Notes 7 and 8).

3.1.5. Drying and Storing

Allow the slide to dry flat for at least 1 day before reading. Keep the slide flat for 2–4 weeks (or until fully dried) before storing it in a microscope slide box. If excess mounting medium dries on the top of the cover slip and obscures the thin section, wait until the slide is fully dried (2 weeks) before removing the excess. Once the slide is dry, gently wipe xylene on the surface of the cover slip to dissolve the excess mounting medium that is obscuring the view of the sample (see Note 9).

3.2. Histological Analysis

Histological analysis for the sixth rib method requires the use of 10×, 16×, or 20× objectives coupled with a 10× eyepiece (ocular) producing an overall magnification of ×100, ×160, and ×200, respectively. For the most accurate results a 20× objective should be utilized, although the aforementioned lower objects may be used. One should never perform this method using an objective lower than 10×, owing to the difficulty in locating and differentiating osteonal structures. To record certain histological variables through the microscope, an eyepiece reticule is required. A 100 square gridded reticule is often used for histomorphometric measurements; however, others may be suggested by various histological methods. The sixth rib methods were developed using a Merz counting reticule described in detail below. Prior to the evaluation of slides one must calibrate the microscope and calculate the reticule area. While microscope calibration and evaluation may be performed using image capturing systems and computer software, these viewing formats should not take the place of direct microscope observation. Instead they augment microscopic analysis or may be used for other measurements, such as cortical area and osteon area. This will be covered in Subheading 3.2.2.

3.2.1. Calibration for Manual Measurement

In preparation for histological analysis the microscope should be calibrated to ensure accuracy in the collection of histomorphometric variables. Analysts should be familiar with calculating the following: total magnification, field size, and counting reticule area.

Table 1
Viewfield diameters (FN 22, 10× eyepiece)

Objective magnification	Diameter (mm)	Field area (mm^2)
4×	5.5	23.76
10×	2.2	3.80
20×	1.1	0.95
40×	0.55	0.86

Compound light microscopes contain two lens systems, an ocular and an objective. The total magnification is calculated by multiplying the magnification of the ocular by the magnification of the objective. A 10× ocular with a 20× objective selected produces a total magnification of 200×. The field number (FN) is referred to as the diaphragm size of eyepiece in mm units, which defines the image area. This number is typically written on the ocular casing. The diaphragm diameter actually seen through eyepiece is known as the practical field of view diameter or viewfield diameter, which is determined in the following formula:

$$D = \frac{\text{Eyepiece FN}}{M_{\text{ob}}} \text{(mm)}$$

The objective magnification (M_{ob}) is the magnification of the objective currently in use (e.g., ×10, ×20). Table 1 lists the viewfield diameters for common objectives using ×10 oculars. The field area can then be calculated once the diameter is calculated. To check the viewfield diameter calculation use a stage micrometer and count how many divisions of the ruler fit across the diameter of the field of view. If the two methods do not produce the same result, then the microscope may have a tube lens magnification factor greater than 1×. If this is the case, then the objective magnification should be multiplied by the tube magnification in the above formula.

Similar steps are used to calculate the reticule area. The best way to calibrate a reticule is to use a stage micrometer. Usually a reticule is placed in the right ocular since, in most heads, the right ocular does not have a focusing ring. If you look through the microscope with a reticule in the eyepiece you can see the image through the reticule. The Merz reticule creates a region of interest (ROI), which is delineated by a square with six parallel wavy lines containing tick marks at regular intervals. The tick marks within the ROI allow for the counting or measuring of structures. It is within the ROI in which histological variables will be collected. Measure the length of the ROI and then the height of the ROI by

Table 2
Merz counting reticule areas by objective[a]

Eye piece magnification	Objective magnification	Hit distance (mm)	Hit area (mm^2)	Grid area (mm^2)
10×	4×	0.41	0.1681	6.052
10×	10×	0.16	0.0256	0.922
10×	20×	0.08	0.0064	0.230

[a]Measurements may vary according to reticule and microscope

turning the ocular so the reticule rotates. Once the total area is calculated by multiplying the two ROI measurements, divide it by the number of tick marks or "hits" on the reticule. To directly calculate the area of each "hit" on the reticule you can measure the distance between "hits" and calculate the area for an individual tick mark. For example, at 200× the distance between "hits" is 0.08 mm. Therefore the area for one "hit" is 0.0064 mm^2. These values may change slightly between microscopes and gridded reticules, so one should always calibrate first when using different equipment. Furthermore, this calculation must be performed for every objective that will be used for the analysis. Table 2 lists the Merz reticule areas for standard objectives to demonstrate the area changes as magnification is increased or decreased.

Calibration for digital analysis should be performed using techniques specific to the software being utilized. Typically an image of the stage micrometer is captured through the microscope's digital camera and uploaded by the image capture software. The user then selects the calibration function and sets the calibration standards for the software.

3.2.2. Collecting Histological Data

The sixth rib method is most accurate when 100% of the thin section is evaluated; however, the methods does allow for only 50% of the bone section to be evaluated in a checker board pattern. This technique is useful when the sample is cracked or contains areas of diagenesis, which precludes a reliable evaluation of such areas. Diagenesis refers to the chemical, physical, and biological changes that skeletal remains undergo after initial deposition (29). Such is often the case with archaeologically derived samples. It has also been suggested that multiple thin sections from the same rib should be evaluated to limit error caused by spatial variation of histological structures between serial sections of bone (known as incoherence). The number of additional sections is dependent upon the amount of cortical bone present within the rib thin sections. Frost (30) recommends that 50 mm^2 of bone be evaluated, which may require 2–5 serial sections. In our experience, evaluating two thin

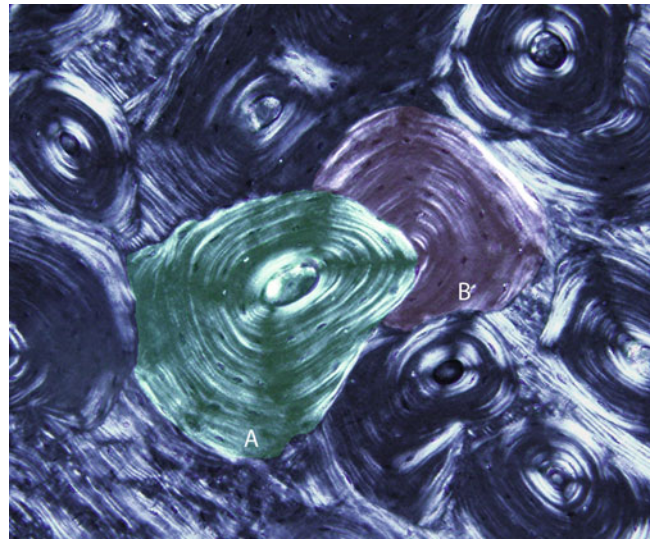

Fig. 5. Example of an intact (**a**) and fragmentary (**b**) secondary osteon in a histological thin section from a rib.

sections is adequate to account for the variations in microstructures between sections.

The following variables are collected for the analysis of the cortical bone using the Cho et al. (2) method:

1. *Total area of bone sampled* (*Sa.Ar.*): Amount of cortical bone evaluated calculated by the number of reticule "hits" overlaying the cortex for each microscopic field. The sum of the "hits" is multiplied by the area represented by one hit on the reticule, yielding a total area of cortical bone evaluated in a rib thin section. Sa.Ar. is expressed in mm^2.
2. *Number of Intact Osteons* (*N.On.*): secondary osteons with at least 90% of their Haversian canal perimeters intact or unremodeled (Fig. 5). Half or more of an osteon's area needs to fall within the counting reticule to be counted. Refer to Robling and Stout (31) for an in-depth description of intact secondary osteons
3. *Number of Fragmentary Osteons* (*N.On.Fg.*): secondary osteons in which 10% or more of the perimeters of their Haversian canals, if present, have been remodeled by subsequent generations of osteons (Fig. 5). This variable also includes remnants of preexisting secondary osteons that no longer contain a Haversian canal. Fragmentary osteons for which half or more of their area fall within the counting field are counted. Refer to Robling and Stout (31) for a more in-depth description of intact secondary osteons.

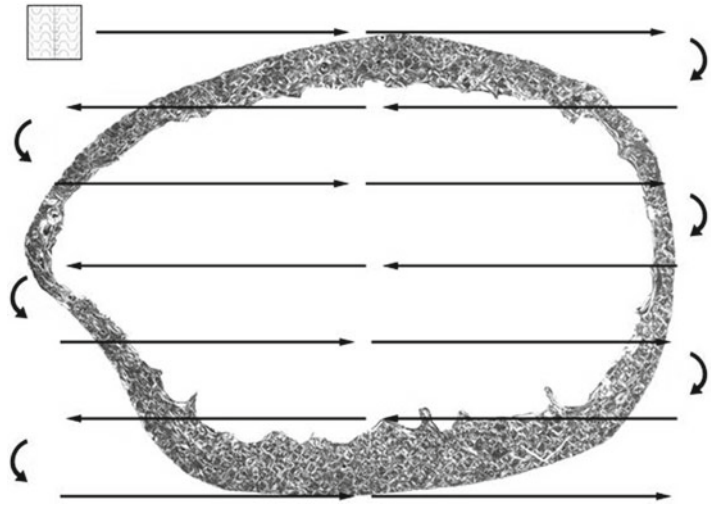

Fig. 6. An example grid path for microscopy data collection of a rib cross section. Another technique is to follow the cortex around the rib cortical area.

4. *OPD* (#/mm^2): This variable is the sum of N.On. and N.On. Fg. divided by Sa.Ar.
5. *Relative Cortical Area* (*Ct.Ar./Tt.Ar.*): the relative amount of cortical bone in cross-sectional area of bone, or the ratio of cortical bone area (Ct.Ar.) to total area (Tt.Ar.) of a rib cross section.
6. *Mean Osteonal Cross-Sectional Area in mm2* (*On.Ar.*): the average area of bone contained within the cement lines of structurally complete osteons for each rib specimen. Osteons were considered structurally complete if their reversal lines were intact. Complete osteons with Haversian canals that deviated significantly from circular should be excluded (see Note 10). Mean area is calculated as the average cross-sectional area of a minimum of 25 complete osteons per cross-section.

Evaluating these structures is a slow process and requires constant manipulation of the microscope's fine focus and light. Both polarized and nonpolarized light should be used to provide full resolution of structures during assessment. Positioning of the reticule and the path of data collection should be planned before analysis begins. Typically one should start in one location and evaluate the bone in rows or columns until all of the bone section has been evaluated (Fig. 6 as an example). Be careful not to overlap the area evaluated or you will be evaluating a portion of the area twice, which will alter the overall histological structure counts. Once the path of data collection is determined, data collection can begin (see Note 11).

With the reticule superimposed over the bone thin section, the first step in data collection is to record the number of "hits"

within the ROI over the rib cortex, excluding the cancellous bone. This is called the point count technique. Once the point, or "hit," count is completed, tally the number of intact and fragmentary secondary osteons within the ROI. Repeat the procedure until the entire cross section is evaluated. In the event the analyst encounters a field that is fragmented or difficult to read owing to diagenetic changes, skip the field and continue. If more than 50% of the bone is affected or one side of the rib is not readable, another rib thin section should be prepared several millimeters away from the location of the first thin section. Figure 7 provides an example for recording data using the Merz reticule and the format of the data sheet. It is important to practice reading several fields to become comfortable with the data collection technique.

Once the entire cross section is evaluated or "read," cortical area and osteon area measurements should be performed. There are two methods used to collect this data: direct measurement using the Merz reticule or indirect measurement using digital images and computer software. Both methods require the total area of the rib cross section, including the medullary cavity, to be measured. If using the Merz reticule, the point count technique described previously is employed over the entire cross section where area is captured by recording reticule "hits." Typically this should be performed at a lower magnification (i.e., 100×). To calculate the relative cortical area, divide the cortical area by total rib area. Similar techniques are used to calculate the average osteon area; however, the magnification should be between 200× and 400× to increase accuracy when using the reticule. An easier and more accurate technique to record area measurements is to capture digital images and create a photomerge of the entire cross section.

If a digital microscope camera is available, capture images of the entire cortex using the 10× objective lens. It is necessary to include a scale in one of the images for calibration in certain systems. If the image capturing software being used does not include a scale function, take a picture of a stage micrometer using the same objective lens, as long as the dimensions of images are not modified, this picture can be used to calibrate the image analyzing software. Once digital images of the entire cortex have been captured, image editing software, such as Photoshop, can be used to merge the images into a single picture of the cross section. Image analyzing software, such as Image J, can be then calibrated to the cross section image if a scale is incorporated. Using an area outline tool, the total rib area and medullary area can be measured. These measurements allow for the calculation of cortical area and relative cortical area. Medullary area is determined by observing the transition from cortical bone to cancellous bone (see Note 12). A similar

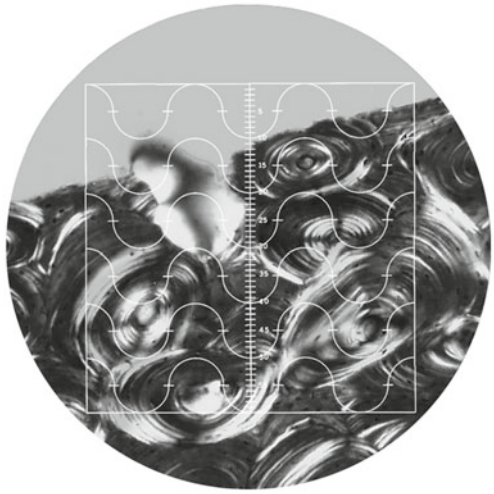

Date: _____ Analyst: _____
Slide ID: _____ Magnification: _____

# Fields	# Hits	# Intact	# Fragment
1	24	2	2
2	13	3	1
3	36	8	5
4	**26**	**4**	**2**
5	9	2	1
6	34	7	3
7	23	5	1
Sum	165	31	15

Fig. 7. An example of data recording using Merz reticule. The *highlighted cells* on the table correspond to the microscopic image on the *left.*

technique can be used to measure average osteon area by outlining the reversal lines of intact osteons.

3.2.3. The Age Estimate

Once the histological variables are collected they are inserted into the appropriate regression equation. Cho et al. (2) developed regression equations from a reference sample of 103 African-Americans and 51 European-Americans (36 from the Stout and Paine (11) study). Sixty-nine individuals from the African-American sample and 34 individuals from the European-American sample were used as a developmental set, leaving 34 African-Americans and 17 European-Americans to form the validation sample. Results indicated that age changes in histological structures are different between the two ancestral groups, namely osteon area and relative cortical area, while sex differences within the groups are negligible. Ancestry-specific equations were developed, as well as general equations that can be used if ancestry is unknown or intermediate. The parameters for the equations can be adjusted if the proportions of African- and European-Americans from the region of origin are known (see Note 13). A regression equation for fragmentary rib cross sections was also constructed. The regression equations are presented in Table 3. The output for the equations will provide a point age estimate. The standard error of the regressions should then be used to calculate the confidence interval. The procedure to calculate confidence intervals can be found in publications such as Giles and Klepinger (32) and Sokal and Rohlf (33).

3.3. Conclusion

Bone is in a constant state of turnover from birth until death. This provides a temporal record of remodeling events, which forms the basis for quantitative histological methods of age estimation.

Table 3
Regression equations from the Cho et al. (2) method

African-American	Age = 38.029 + 1.603(OPD)—51.228(Ct.Ar/Tt.Ar.)
European-American	Age = 38.029 + 1.603(OPD)—88.210 (On.Ar)—51.228(Ct.Ar/Tt. Ar.) + 57.441(Ct.Ar/Tt.Ar.)
Unknown ancestry[a]	Age = 29.524 + 1.560(OPD) + 4.786(Ct.Ar/Tt.Ar)—592.899(On.Ar)
Unknown ancestry and Incomplete cross section[a]	Age = 37.982 + 1.375(OPD)—699.581(On.Ar)

[a]This equation is adjusted depending on target population demographics

Despite the general consensus that age-related changes are reflected, to some degree, in the microstructure of bone, the numerous difficulties in reproducing and evaluating results from previous histological studies have been a deterrent in their use as a conventional method for the estimation of adult age at death. The goal of this chapter is to mitigate this deterrent through the detailed description of sample preparation and evaluation using one method for histological age estimation. Because histological methods require some level of experience, anthropologists must be familiar with the literature and calibrate their technique through the assessment of intra-observer error prior to applying histological methods to research or forensic casework.

4. Notes

1. Placing the sample in a vacuum ensures that the embedding solution is sufficiently pulled into the medullary cavity. Vacuums may contain heating elements which should not be used with certain embedding resins. Consult the Material Safety Data Sheet (MSDS) for the embedding material.
2. Depending on the sample and mold, the embedding solution may bubble over during the decompression process. It is recommended to place the cassette on a disposable tray to facilitate easy clean up of the decompression chamber.
3. If the remaining portion of the embedded sample is too small to fit in a chuck, the sample can be mounted directly to a slide for sectioning. Crystalbond™ and Wafer-Mount™ washaway adhesives are ideal materials for temporarily mounting objects that require sectioning, polishing, and other machining processes. These adhesives exhibit high bond strength and adhere quickly. They are removed by reheating and cleaning with a wide range of different solvents. Use a hot plate or slide warmer to warm

the slide. Once the slide is warm, place the adhesive on the slide until there is enough of the medium to cover the base of the sample. Quickly remove slide from hot plate using tweezers and press the sectioned and polished side of the embedded sample firmly and evenly to the adhesive. Hold until the adhesive hardens. Ensure the embedded sample is evenly mounted on the slide. If not, use heat to loosen the adhesive and reset. Using the slide-holding chuck, mount the slide and move dial until the slide and chuck are flush with wafering blade. Set dial to zero and move the chuck 1.2 mm to the left side (away from the blade) and begin cutting. Once cut, the thick section can be removed from the slide by placing it on the hot plate again (over heating the slide will compromise the sample's integrity).

4. It is crucial to be vigilant in monitoring the grinding process as the sample starts to become translucent. Failing to do so can result in destroying the thin section.
5. If the embedding material starts to warp, it can peel away from the sample. While this may not affect any following steps, it is important to be careful not to destroy the periosteal surface of the bone. Subsequent grinding after removing this other layer of embedding material can result in minor destruction of the periosteal surface of the rib.
6. Some specimens may exhibit a cloudy appearance caused by diagenetic agents that will impede histological analysis. Dipping the thin section in Clear-Rite™ 3 or xylene prior to placing it on the slide often removes much of the obscuring "cloudiness."
7. Improper mounting will result in air bubbles forming under the coverslip and failure of the slide. In the event of the formation of significant air bubbles, place the slide in a xylene bath for 6–24 h or until the coverslip becomes loose. Leaving the thin section for extended periods of time will destroy the thin section as xylene will dissolve the embedding material and make the bone sample brittle. Remove the thin section and place between two clean slides if the sample is warped.
8. Using the minimal amount of protocol possible and inspecting the coverslip placement for parallel orientation and close proximity to the slide will minimize the likelihood of slide failure. In some cases, the thin section can become extremely warped and prove problematic to mount. In these cases, prolonged placement between two slides secured with binder clips prior to mounting is recommended. Often cutting away excess embedding material will reduce thin section warping.
9. When removing excess mounting medium, it is important that the xylene does not dissolve the seal connecting the cover slip and the slide. If this occurs, you can fill the defect with additional mounting medium using a pipette.

10. The authors suggest using this criterion—Intact osteons with a Haversian canal that have a maximum diameter more than twice its minimum diameter are excluded from area measurements.
11. Prior to collecting histological data, the analyst should adjust the ocular focal lens to the specifics of their vision. Closing their left eye and looking through the right ocular, the analyst should focus the specimen. Once in focus, the analyst should close their right eye and look through the left ocular. If the specimen is out of focus, use the focus ring on the left ocular to focus the specimen. Looking through both oculars, the specimen should be in sharp focus. Failure to perform this step may result in eye strain and headaches.
12. Determining the boundary of endosteal cortical bone, where it transitions to cancelous bone, is subject to observer interpretation. When tracing the medullary area, the analyst should identify the point where intracortical remodeling ends and the trabeculae begins. In a sense, the analyst "clips" away the trabeculae from the border of the endosteum.
13. Developing custom equations: It should be noted that population census data may not correlate to forensic populations at autopsy. Thus, less accuracy is expected with these modifications to the equations.

References

1. Ahlqvist J, Damsten O (1969) A modification of Kerley's method for microscopic determination of age in human bone. J Forensic Sci 14:205–212
2. Cho H, Stout SD, Madsen RW, Streeter MA (2002) Population-specific histological age-estimating method: a model for known African-American and European-American skeletal remains. J Forensic Sci 47(1):12–18
3. Clarke DF (1987) Histological and radiographic variation in the parietal bone in a cadaveric population. Thesis, Anatomy Department, The University of Queensland
4. Cool SM, Hendrikz JK, Wood WB (1995) Microscopic age changes in the human occipital bone. J Forensic Sci 40(5):789–796
5. Curtis J (2004) Estimation of age at death from the microscopic appearance of the frontal bone. Masters Thesis, University of Indianapolis, Indiana
6. Ericksen MF (1991) Histological estimation of age at death using the anterior cortex of the femur. Am J Phys Anthropol 84:171–179
7. Kerley ER (1965) The microscopic determination of age in human bone. Am J Phys Anthropol 23:149–164
8. Kim Y, Kim D, Park D, Lee J, Chung N, Lee W, Han S (2007) Assessment of histomorphological features of the sternal end of the fourth rib for age estimation in Koreans. J Forensic Sci 52(6):1237–1241
9. Singh IJ, Gunberg DL (1970) Estimation of age at death in human males from quantitative histology of bone fragments. Am J Phys Anthropol 33:373–382
10. Stout SD (1986) The use of bone histomorphometry in skeletal identification: the case of Francisco Pizarro. J Forensic Sci 31(1): 296–300
11. Stout SD, Paine RR (1992) Brief communication: histological age estimation using rib and clavicle. Am J Phys Anthropol 87:111–115
12. Stout SD, Dietz WH, Işcan MY, Loth SR (1994) Estimation of age at death using cortical histomorphometry of the sternal end of the fourth rib. J Forensic Sci 39(3): 778–784
13. Stout SD, Marchello AP, Perotti B (1996) Brief communication: a test and correction of the clavicle method of Stout and Paine for histological age estimation of skeletal remains. Am J Phys Anthropol 100:139–142

14. Thompson DD (1979) The core technique in the determination of age at death in skeletons. J Forensic Sci 24(4):902–915
15. Thompson DD, Galvin CA (1983) Estimation of age at death by tibial osteon remodeling in an autopsy series. Forensic Sci Int 22: 203–211
16. Yoshino M, Imaizumi K, Miyasaka S, Sueshige S (1994) Histological estimation of age at death using microradiographs of humeral compact bone. Forensic Sci Int 64:191–198
17. Wu K, Schubeck H, Frost M, Villanueva A (1970) Haversian bone formation rates determined by a new method in a mastodon, and in human diabetes mellitus and osteoporosis. Calc Tissue Res 6:204–219
18. Frost HM (1987) Secondary osteon populations: an algorithm for determining mean bone tissue age. Yrbk Phys Anthropol 30:221–238
19. Frost HM (1987) Secondary osteon population densities: an algorithm for estimating missing osteons. Yrbk Phys Anthropol 30:239–254
20. Dudar JC, Pfeiffer S, Saunders SR (1993) Evaluation of morphological and histological adult skeletal age-at-death estimation techniques using ribs. J Forensic Sci 38(3):677–685
21. Crowder C (2005) Evaluating the use of quantitative bone histology to estimate adult age at death. Ph.D. dissertation, University of Toronto, Department of Anthropology
22. Crowder C, Rosella L (2006) Assessment of intra- and intercostal variation in rib histomorphometry: its impact on evidentiary examination. J Forensic Sci 52(2):271–276
23. Frost HM (1958) Preparation of thin undecalcified bone sections by rapid manual method. Biotech Histochem 33(6):273–277
24. Maat G, Van Den Bos R, Aarents M (2001) Manual preparation of ground sections for the microscopy of natural bone tissue: update and modification of Frost's 'rapid manual method'. Int J Osteoarchaeol 11(5):366–374
25. Anderson C (1982) Manual for the examination of bone. CRC Press, Boca Raton
26. Steadman D, DiAntonio L, Wilson J, Sheridan K, Tammariello S (2006) The effects of chemical and heat and maceration on the recovery of nuclear and mitochondrial DNA from bone. J Forensic Sci 51(1):11–17
27. Fenton TW, Birkby WH, Cornelison JC (2003) A fast and safe nonbleaching method for forensic skeletal preparation. J Forensic Sci 48(2):274–276
28. Rennick SL, Fenton TW, Foran DR (2005) The effects of skeletal preparation techniques on DNA from human and nonhuman bone. J Forensic Sci 50(5):1016–1019
29. Pfeiffer S (2000) Palaeohistory: health and disease. In: Katzenberg MA, Saunders SR (eds) Biological anthropology of the human skeleton. Wiley-Liss Inc., New York
30. Frost HM (1969) Tetracycline based histological analysis of bone remodeling. Calcif Tissue Res 3:211–237
31. Robling AG, Stout SD (2000) Histomorphometry of human cortical bone: applications to age estimation. In: Katzenburg MA, Saunders SR (eds) Biological anthropology of the human skeleton. Wiley-Liss Inc., New York
32. Giles E, Klepinger LL (1988) Confidence intervals for estimates based on linear regression in forensic anthropology. J Forensic Sci 33(5):1218–1222
33. Sokal RR, Rohlf FJ (1995) Biometry: the principles and practice of statistics in biological research, 3rd edn. W. H. Freeman and Co., New York

Chapter 8

Age Estimation Using Tooth Cementum Annulation

Ursula Wittwer-Backofen

Abstract

In Forensic Anthropology age diagnosis of unidentified bodies significantly helps in the identification process. Among the set of established aging methods in anthropology tooth cementum annulation (TCA) is increasingly used due to its narrow error range which can reach 5 years of age in adult individuals at best. The rhythm of cementum appositions of seasonally different density provides a principal mechanism on which TCA is based. Using histological preparation techniques for hard tissues, transversal tooth root sections are produced which can be analyzed in transmitted light microscopy. Even though no standard TCA preparation protocol exists, several methodological validation studies recommend specific treatments depending on individual conditions of the teeth. Individual age is estimated by adding mean tooth eruption age to the number of microscopically detected dark layers which are separated by bright layers and stand for 1 year of age each. To assure a high reliability of the method, TCA age diagnosis has to be based on several teeth of one individual if possible and needs to be supported by different techniques in forensic cases.

Key words: Age diagnosis, Tooth cementum annulation TCA, Tooth histology

1. Introduction

Age diagnosis based on annual periodicity of tooth cementum formation is increasingly used in anthropology and gains particular importance in forensics as it is helpful in the identification process of unknown bodies (1, 2). Known as tooth cementum annulation (TCA) the method has been developed since the 1980s (3, 4) and is the actual method of choice for proving a precise age at death assessment (5, 6). However, it still suffers from the fact that the physiological and structural biological background of the respective cementum, that surrounds the tooth root dentine as a thin

Lynne S. Bell (ed.), *Forensic Microscopy for Skeletal Tissues: Methods and Protocols*, Methods in Molecular Biology, vol. 915,
DOI 10.1007/978-1-61779-977-8_8,

layer, is not well elucidated. Tooth cementum is formed by mineralization during the growth of the desmodontal fibroblasts during lifetime. This formation takes place in a periodical rhythm leading to alterations in mineral crystal orientation which can be seen as alternating dark and bright cementum layers in microscopic images of the respective acellular extrinsic fiber cementum. The regularity of the periodicity as a circannual rhythm is well documented (7–9). It is of great advantage that once formed, the tooth cementum as a hard tissue in the body does not undergo alterations during lifetime and is relatively stable even over long postmortem intervals.

TCA analysis can be performed by cutting thin ground sections of the middle third area of the tooth root. Usually root cross sections are used which is described here, but occasionally longitudinal sections are prepared (10). As the TCA age diagnosis requires invasive techniques a set of methods for information storage by documentation is described including the production of tooth replica. After cleaning and mounting of the unstained and undecalcified sections the microscopic identification of highest quality cementum areas is a crucial step during the process (11). The selection of adequate magnification, light source, focus and aperture settings significantly contribute to precision of age diagnosis. The number of annual incremental lines is evaluated by manual counting directly under the transmitted light microscope or using imaging software after microscopic image acquisition. In this step observer training as well as the number of evaluable sections and images and their quality prove as major quality attributes. First attempts towards automatic counting by application of image analysis algorithms have been made (12, 13) but are still in the phase of methodological development. So far, no general applicable solution is available and it shows that semi-automatic procedures might be most helpful in supporting manual counting.

A final age diagnosis is performed by adding the root formation age to the mean number of counted cementum layers as cementum formation starts after the termination of the relevant tooth root development. The error range of individual age diagnosis can reach 0.8 years at best for young adults (14) or 2–3 years for the whole age range (2, 15).

There is still controversial discussion on the general applicability (16–18), as well as on the precision of age diagnosis, or on reproducibility of the age assessment by the TCA method which will be addressed in the methods section.

2. Materials

2.1. Isolation of Teeth from the Jaws

Dental extraction gripper, (self-made cushioned out of foam plastic)

2.2. Preparation of Teeth

1. Digital camera with macro equipment.
2. Microcaliper with needle cuspids (0.05 mm precision), light box (any customary X-ray observer or self-made light box, see Note 1).
3. *Form production*: Silicon rubber, highly tear-resistant, color: white with 2–4% silicon hardener (Glorex, CH), plastic form (height 1.5–2 cm, diameter or side length 3 cm), *Replica production*: Stewalin mold compound (Glorex, CH) or any compound with the properties of excellent casting precision: Fast even hardening, extremely hard, nonchalky surface, brilliant white shade, *Finish*: acrylic colors, transparent varnish (nail hardener).
4. Microtool rotary saw with diamond-coated thin cutting wheel (Dremel 4000, Bosch Leinfelden, GER).
5. Vacuum thermo cabinet (Heraeus Vacutherm VT6025 or Binder VD23-115) alternatively Exsiccator with rotary vane pump, Manometer, 1 mL DNA tubes (PCR tubes) with rack, *embedding medium*: Epoxy resin Biodur E12 mixed with 28% of hardener Biodur E1 (Biodur Products, Heidelberg, GER).

2.3. Separation of Tooth Roots

Micro-tool rotary saw with diamond-coated thin cutting wheel (Dremel 4000, Bosch Leinfelden, GER)

2.4. Specimen Preparation

Form for specimen holder sockets (maximum diameter 30 mm) for Leica SP1600, epoxy resin with hardener (K-Mount powder, K-mount solution, Medim MDS, Giessen, GER)

2.5. Sawing of Sections

Leica SP1600 (Leica Biosystems Nußloch, GER), forceps, perforated cages for histology with cap

2.6. Preparation of Microscopic Slides

Polishing (if necessary): Logitech Compact 50 Thin Section Polishing System (Logitech, Glasgow, UK), *Cleaning*: alcohol (70%, 96%, abs.), Xylene, four glass container (100 mL) with cover, forceps, highly absorbent paper tissues, *Mounting*: microscopic slides with labeling section, coverslips, mounting medium (Roti-Histokitt, Carl Roth Karlsruhe, GER)

2.7. Microscopy

Transmitting light microscope (Leica DMRXA) with lenses ×10, ×20, ×40, camera adapter, digital camera (Leica DC250), Multilevel image database and image processing software (Leica IM1000, all Leica Microsystems, Wetzlar, GER)

3. Methods

3.1. Selection of Suitable Teeth for TCA Preparation

Generally, all teeth are suitable for TCA analysis as cementum layers are generally formed in the jaws. The use of third molars should be avoided as their formation age varies considerably with age and thus leads to broader age ranges. Another reason to avoid the use of third molars is their highly variable form which might lead to disturbances of the annual cementum apposition. Similar problems can occur with all other multirooted teeth at the region of root bifurcations. Thus, most validation studies are focused on single-rooted teeth namely incisors, canines or premolars. These tooth types fulfill in most cases the precondition of a single-rooted tooth and therefore should be used. It is recommended to select teeth which are still located in the alveolar bone at the beginning of the procedure. Here, teeth are best protected against soil diagenesis influences such as mechanical abrasion, chemical destruction or infiltration by microorganisms. As well, the selected teeth should not be damaged. The influence of dental caries, dental attrition, or gingival regression on the TCA method is not fully identified yet and has been discussed in the literature controversially (2, 4, 15, 19, 20). Therefore healthy teeth are to be preferred if available.
In forensic cases at least two teeth should be selected to validate results.

3.2. Handling of Teeth Prior to Invasive TCA Processes

As TCA analysis represents an invasive method which delivers results by the destruction of tooth roots it has to be kept in mind that the original tooth is not available for further analysis. Information of the original tooth form can be stored by photographic documentation, tooth measurements, and casts prior to any invasive process.

1. Photographic documentation should include occlusal, buccal, lingual, mesial, and distal surfaces accompanied by a scale in the object plane. The graphic resolution should allow the recognition of surface details. This may help in the search of causal effects in the case of abnormal microscopic structures or results.
2. In order to provide support for later TCA age estimation tooth root length and translucency should be measured. This allows the application of the age estimation technique based on tooth root transparency (21, 22). The resulting error range is wider compared to TCA results but allows to control for disturbing effects in TCA analysis when TCA results fit into the broader age band delivered by root transparency (see Note 1).
3. Maximum total tooth length as direct distance from the highest crown cusp to the tip of the root is measured with a high precision caliper. This helps later on to fuse the original crown with the cast and allows to control for the root area during the cutting process.

4. The production of tooth replica allows for later reconstruction of the original dental situation and soft tissue facial reconstructions. In a first step the form is produced. Prepare a rectangular or round form with a diameter of app. 3 cm and a height of 2 cm. Any plastic box of that size can be used. Mix silicon rubber with 2–4% silicon hardener and fill the form. Knock the form cautiously on the table for about 15 min until no more air bubbles are visible on top of the silicon rubber. Rub the tooth slightly with petroleum jelly for easy removal. Place the tooth carefully on top of the mass and wait until the tooth subsides totally in the mass. Mark the area where the tip of the root is placed. After approximately 3 h the mass is hardened. Cut the silicon form with a scalpel by removing small slices from the form at the side of the tip of the root until you reach the tip. Be careful to prevent the destruction of the embedded tooth. As soon as the tip of the root is exposed, cut cautiously along the surface of the tooth (just one linear cut). Subsequently, bend the form and remove the tooth. Don`t break the form while bending. For the replica production mix one part of water with four parts of Stewalin. Fix the form on the side where the cut for tooth extraction was made to avoid bridging while pouring the compound. Fill the compound with a plastic pipette into the hole of the form produced by cutting to the root tip. If the hole is too small, carefully enlarge. Knock the form gently on the table without spilling the compound mass. Make sure all air is removed from the form. After 30 min hardening the tooth can be removed from the form. If insertion of the tooth replica into the alveolar bone is intended, coloring of the tooth replica with acrylic colors according to the appearance of the original tooth can be performed. Finally, seal the tooth crown with transparent nail hardener to imitate the shiny enamel tooth structure.
5. If it is necessary to follow the exact placement of the cementum image on the root surface area for image comparison between different sections, it is helpful to set a marker on the root surface which easily can be recognized during microscopic work (see Note 2).
6. Embedding of fragile teeth: If the tooth shows fractures, splits due to diagenesis processes or was exposed to high temperatures or water it needs to be embedded, otherwise it will break during the section cutting process. As dentine and enamel represent dense tissues compared to bone it is crucial to assure for complete penetration of the selected hardener. Due to viscosity of hardener this is achieved by vacuum infiltration solely. Otherwise the hardener delivers just a hard collar around the root but does not fix the dentine and cementum tissue of the tooth root. Prepare tubes as small as possible to include the whole tooth. In most cases 1 mL DNA tubes are sufficient.

Try to insert the tooth with the crown up when still dry. Stick tubes into the rack and prepare the hardener by mixing 10 g of the epoxy resin Biodur E12 with 2.8 g of the hardener E1. This amount should be sufficient for 2–4 tubes. Do not prepare smaller amounts unless you can assure for the exact weight proportion of resin and hardener. Fill a small amount of the compound into the tube and insert the tooth with the crown up. Subsequently, fill up the tube so that there is at least 3 mm material above the highest point of the crown. Leave the tubes open and put the rack with the tubes into the vacuum thermo cabinet. Increase vacuum at room temperature slowly until air bubbles slowly raise. Do not apply too high vacuum to let the hardener compound simmer. Apply vacuum for 12 h, then regulate back to room pressure and raise the temperature to 35 °C without moving the tube rack. Leave for 48 h and cool down. Before removing the embedded teeth from the tube, test for full hardening of the embedding material. It is recommended to carry a few tubes with just embedding material through the process for such tests.

3.3. Separation of Tooth Roots

In forensic cases the original tooth crown should be removed from the root for further steps in the identification process. Cut off the root at the enamel-dentine junction with a high speed rotary saw tool using a diamond-coated thin cutting wheel (see Note 3).

3.4. Preparation of Cutting

Although the decalcification of the teeth is described by several authors (3, 10) good results were achieved using undecalcified teeth (2, 11, 15). Currently, the use of undecalcified teeth is predominant and is recommended as most validation studies are based on this procedure.

The tooth has to be well fixed in a specimen clamping device to guarantee that any movement of the tooth during the sawing procedure can be excluded. If the Leica saw microtome SP1600 is used, employ the plastic form the company provides to cast sockets that hold the specimen (see Note 4). You can use any fast hardening epoxy resin (Biodur E12 is much too slow) which takes no more than 10 min to harden depending on the percentage of hardener. Make tests before you apply to teeth. Mix the compound to a honey-like consistency and fill the form almost completely. Immediately insert the tooth crown or, if you have removed the crown, the cutting area into the compound and hold the root tip vertically until the compound hardens. The curing process takes about 1 h (Fig. 1).

3.5. Sawing of Histological Sections

If a saw microtome with an internal rotating diamond-coated saw blade like the water-cooled Leica SP 1600 is used, later time-consuming polishing of the sections can be avoided. Insert the socket into the arm of the saw in such a position that the blade starts sawing from the smaller buccal or lingual root surface. This gives additional

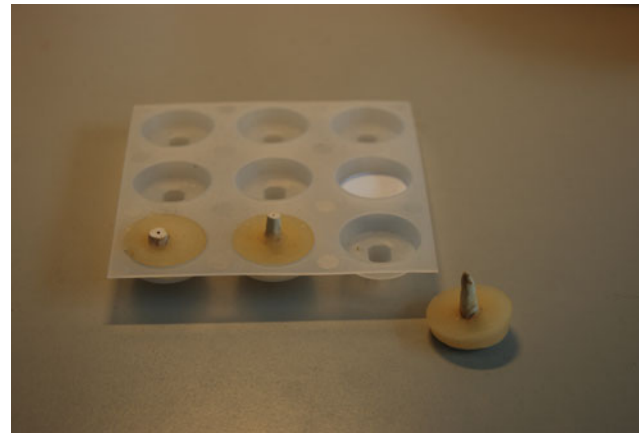

Fig. 1. Teeth with embedded crown as fixation for the specimen holder in the sawing arm.

stabilization during the sawing procedure and has the advantage that smaller cutting marks do not run parallel to the cementum lines over a broader area of the root surface (see Subheading 3.9). Take care that the socket is well fixed. It is necessary to cut the specimen advance with low speed to avoid heavy cutting marks. Depending on the root diameter a section takes approximately 7–10 min. Remove the root tip at the level of one-third of the whole root length and retain it (see Note 5). Then start sawing the sections with a thickness of 60–80 µm by adding the material loss due to the sawing blade which depends on its rate of wear. Therefore the sawing arm has to be lifted between 350 and 380 µm (see Note 6) for each new cut. Thickness of sections vary considerably from below 10 µm up to 500 µm in the different studies, but sections of 70–100 µm are predominantly used (2, 11, 15) (Fig. 2).

The progression of the sections should be noted by treating each section individually with section numbers. This can be performed best by storing each section in a small plastic mesh histocontainer. Usually 10–12 sections can be made until the socket is reached. The section area should cover in any case the middle third of the root.

3.6. Preparation of Microscopic Slides

Polishing of the sections sometimes is necessary when using different saws with outside cutting wheels. It can be performed under control of the section thickness and has the advantage that no tooth areas have to be excluded due to small cutting marks which may mimic or cover cementum layers. On the other hand, practical experience has shown that smaller cutting marks oblique to the cementum band help in the manual counting process. Blinded tests have shown that polishing and standardized section thickness does not improve counting results. Therefore the author recommends not to polish the sections.

Unstained sections deliver good contrast between hyper- and hypomineralized cementum layers. Occasionally stained sections

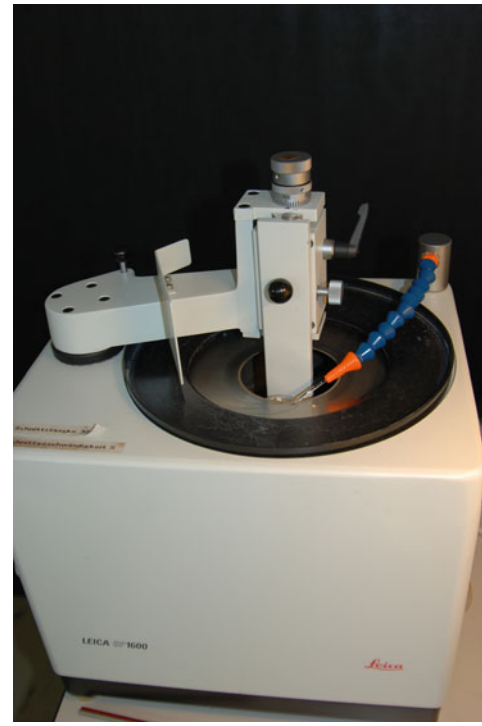

Fig. 2. The water-cooled Leica 1600 microtome with diamond-coated blade during the tooth root sectioning.

are used (3, 10) which do not deliver better results in thicker sections but are necessary when very thin sections do not deliver sufficient contrast in the microscopic transmitting light. Most studies use unstained sections, which is recommended here as well.

Prior to mounting the sections have to be cleaned from sawing dust and have to be dehydrated. Use the histocages in which the sections were placed after sawing and immerge the sections successively in containers with 70% alcohol (2 min.), 96% alcohol (30 s.), and abs. alcohol (30 s.) subsequently. Dry the histocages with tissues after each treatment to avoid a contamination of the different concentrations. Finally immediately before mounting dip the histocages for 30 s. into Xylene. Work with Xylene has to be performed under a fume hood. Remove the section from the histocage using forceps and drain surplus Xylene onto a paper tissue. Transfer the section on a labeled microscopic slide and cover it with three drops of a Xylene-based mounting media. For unpracticed persons it is advantageous to use rather more mounting medium to avoid contracting of the medium to the root surface while drying. Cover the section carefully with a cover slip and eventually remove existing air bubbles by carefully tapping the surface of the cover slip. Let the mounting medium dry for at least 3 days until it has reached its final degree of hardness and refraction index.

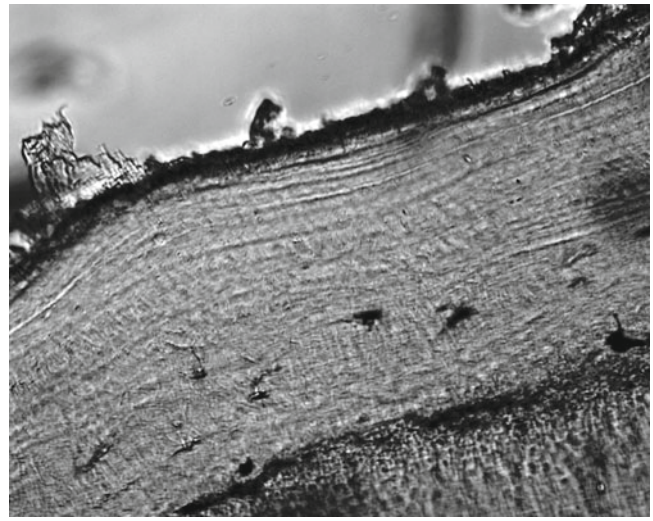

Fig. 3. Typical wave-like cementum layer which does not show the tooth cementum annulation (TCA) relevant acellular extrinsic fiber cementum. The section is assumed to be too close to the root tip and has to be eliminated for further TCA analysis.

3.7. Microscopy

The tooth cementum band is visualized by transmitting light microscopy and can be seen in magnifications from ×100 to ×400.

A major requirement in forensic cases is to guarantee the reproducibility of cementum counting. This can be achieved easily by taking digital images directly from the microscope in defined tooth root areas. Most comfortable microscopic systems allow the storage of images in individually defined (besides others provided by Leica, Zeiss, Olympus) image databases together with information about the microscopic settings such as magnification, light source, focus, or position of the microscopic stage that can easily be reproduced.

The search for best counting areas should be made systematically by following the outer border of the root section completely until surrounded. A track ball control of the microscopic stage is very helpful here. Not every section is suitable for TCA counting. Sections with wave-like pattern of cementum layers with diverging or bunching layers not parallel to the dentine margin or with a considerable amount of cell inclusions have to be omitted. In such cases a section closer to the root tip which consists of a different acellular cementum tissue was cut (Fig. 3).

Likewise not every part of the cementum band within a section is suitable for counting. Especially low image contrast, inclusion of artifacts, root fractures, or narrowing in root bifurcation in the cementum band may occur. Such areas should be excluded from further analysis as well as areas showing cutting marks parallel to the cementum band. This could lead to counting mistakes as is shown in poorly preserved skeletal materials (23). Images should be taken from areas of best quality of each of the suitable sections.

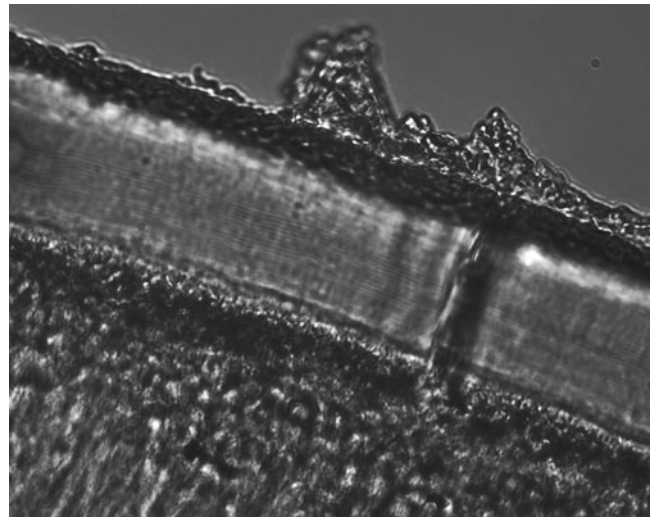

Fig. 4. Good quality cementum band showing the acellular extrinsic fiber cementum in ×200 magnification. Unstained and undecalcified section, contrast enhanced image suitable for the TCA counting procedure.

It is recommended to store a ×10 image overview over the whole section together with the detailed higher magnification images in order to be able to control the quality and size of the section at any time. For later counting images should be acquired with magnifications of ×200 and ×400 (2, 11) (Fig. 4) although good results were achieved with low magnifications of ×20–×40 (24).

Although the number of images or counts proposed by different labs varies considerably, the number of images should be as high as possible in forensic cases.

An area can appear different under the microscope when changing the focus layer. This may occur due to the fact that the root surfaces converge towards the tip and thus cementum layers are not cut completely horizontally to their longitudinal axis. This "moving line effect" depends on the thickness of the section and can be demonstrated when focusing through the section. Generally the acquisition of images should be made in order to find a maximum number of cementum layers.

The cementum layers are seen best under the microscope with a certain degree of aperture closure. It should be avoided to completely close the aperture as this may result in uncontrolled light dispersion effects especially at the outer margin of the section.

For subsequent counting procedures it is advantageous to locate the cementum layer horizontally (see Note 7).

3.8. Image Enhancement

Images stored in a database can moderately be treated with graphical image enhancement tools such as contrast and brightness improvements to optimize the countability of the cementum layers. This may help to accent pale layers but on the other hand bears

the risk that irradiations cover other layers. Therefore image enhancement should be done carefully under control of the original image which should never be overwritten and always be kept as reference.

3.9. Image Analysis: Cementum Layer Counting

Although studies presented first automatic counting procedures (12, 13) by developing specific algorithms (see Note 8), this way of image analysis with the exception of methodological studies is not accepted yet. The major reasons are first that automatic counting did not lead to constantly stable results compared to manual counts, second that no user-friendly software tools exist, third that software counting procedures are time consuming and fourth that they still need user-interactions defining starting and stop lines or the area of interest.

Automatic counting software aimed to overcome the problems connected with manual counting such as high inter-observer variability, limited reproducibility, high cementum quality variability, and great time effort. Therefore manual counting procedures are still predominantly applied.

The initially developed direct counting at the microscope ocular is still used (11) and bears advantages such as the possibility to modify the focus to make all layers visible, the control of cutting marks and the control of position at the root surface area all the time. As disadvantageous proved the facts that first reproducibility is not given, second that areas in the ocular window outside of the root usually are very bright when light intensity is high to count cementum layers and third that counting errors may occur when no image markers can be set on each of the counted layers.

Thus, a major number of specialists apply image analysis systems which besides image enhancement provide tools for marking each cementum line, for turning images, for zooming details, or for carrying out measurements.

In a first step the cementum start line as border line to the root dentine has to be located. Usually a broader bright band indicates the starting area where the innermost regular dark line has to be addressed as first cementum layer. The counting of the dark lines towards the outer margin of the tooth root following the formation sequence has proved as best practice. To avoid counting errors and to reproduce the results it is recommended to mark each counted line as image overlay (see Note 9) (Fig. 5). Important features are the detection of an intact outer margin, a decision about sufficient line contrast for counting and the parallel course of the cementum layers. It is recommended to exclude images, sections, or even whole teeth from counting if these requirements are not fulfilled.

The focus effect (see Subheading 3.7) of “moving lines” may serve as methodological explanation for the occasionally observed line doubling, counting each line twice on its section surface and again in a certain deeper layer of the section.

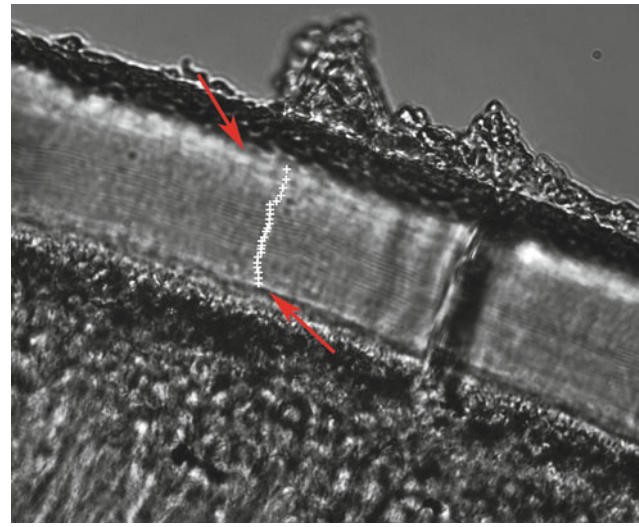

Fig. 5. TCA image with counting overlay marking each cementum layer, the eruption layer as borderline between dentine and cementum, and the outer root surface layers. Lower central incisor of a 27-year-old male person, counting 20 cementum layers (added by 6.6 years as mean eruption age and resulting to an age estimation of 26.6 years).

It is recommended for forensic cases to count as many images and sections as possible. Best evaluations can be achieved by blinded reproduced counts, implementation of several observers as well as a good observer training which helps to develop good experience to reach stable and observer-consistent counting results (6). Even the consideration of the different tooth surface quadrants may influence the counting result (5, 18).

3.10. Age Estimation

A final age diagnosis requires the identification of the highest probability of numbers of cementum layers. If enough counts exist the highest density of the counting distributions should correspond to the mean number of lines. Thus, occasionally occurring outlier counts can be detected and eliminated. If highest probabilities extend over a range of line numbers it is appropriate to give a range of probable counts. This/these cementum annulation counts have to be added to the tooth root formation age which corresponds to the eruption age validated by large sample sizes and provided worldwide variability given as tooth type specific and sex-specific age (25). A validation study with fresh modern teeth samples delivered 2 s confidence intervals of 2.5 years (2) respectively 2–33 years (18) but can exceed these error ranges if postmortally effected teeth were involved.

3.11. Validation of Results

After age diagnosis has been achieved the results should be compared to age estimates based on diverse methods (see Subheading 3.2) respectively skeletal traits (26, 27). If overlapping results tend to a central age diagnosis for the TCA analysis in two

different teeth and other dental and skeletal aging traits there is good support for the age at death or age at tooth loss. If diverge age estimates occur it has to be controlled whether TCA results may be incorrect or whether the aging process of skeletal traits differs from the chronological age diagnosis by TCA analysis.

4. Notes

1. Tooth root length and root translucency according to the Lamendin method modified by Prince and Koenigsberg can easily be measured using a cost-effective self-made light box by placing a 100 W light bulb into a small nontransparent plastic box. Take care that the bulb does not touch the walls and cover it with a plate of frosted glass.
2. A practical way of marking the root area which can be detected during microscopic work is to saw a superficial notch longitudinally all along the tooth root in a specific area of the tooth root, for example, the buccodistal quadrant. The same small diamond-bladed wheel tool which is described for cutting off the tooth crown can be used here. The marker is seen on the surface of the sections after sawing. If it is always placed in the same direction during mounting (for example, marker top right towards the label section of the microscopic slide) all sections are adjusted to the same direction and section areas can better be compared.
3. To avoid breaking of the crown, use an elastic pad and a cushioned gripper to place and hold the tooth and cut smaller incisions from different sides.
4. If the SP1600 plastic form is used, which is equipped with a cavity for the sample specimen to be covered with the embedding material, you have to improvise, as tooth roots are longer than the cavity. Use the form inversely with the tip of the root at the top by covering the cavity completely with a paper sheet of exactly the diameter of the holder. Write the specimen number with a pencil on the bottom side before. That helps in tracking the correct specimen number through the procedure.
5. To avoid losing your sections by means of the water jet (and that happens occasionally) cover the end of the waste water tube with gauze and flood the water container. You will find your root tip or section sticking at the gauze.
6. The thickness can be tested on the first sections. If separated dark and light cementum bands can be recognized when tentatively putting the dry sections on an object slide and examining in a ×200 microscopic magnification the height adjustment

seems to be adequate. It is completely transparent when the section is too thin and completely opaque when too thick. Take care that the adjusting screw to lift the sawing arm is in a low position that enough lifting is possible to saw all sections of the root.

7. As not all areas of interest are located horizontally to the camera on the object stage in most equipment the camera adapter can be untightened and the camera can be turned until the cementum area is horizontal. Image acquisition in this position helps to avoid information loss connected with the later turning of the images for counting.
8. Klauenberg uses a Hidden Markov random field in defining the mean width of cementum layers defined on images by gray scale detection followed by dividing the width of the cementum band area by this value. Czermak et al. use software that scans incremental lines "line-by-line" and counts the identified gray scale peaks in a beforehand manually selected region-of-interest (ROI). Each ROI is counted automatically up to 400 times by the program and is afterwards statistically evaluated.
9. It is not helpful to count the lines along a line perpendicular to the cementum layers as the image quality differs considerably across the cementum band within small areas. Additionally, line interruptions and line bifurcations may lead to counting errors. First attempts towards automatic counts by grey scale detections along an axis through the cementum band therefore did not prove to be practicable. It is rather helpful to follow each line from one side to the other and to decide for counting based on its stability over a broader range of the respective image window.

Acknowledgments

The author would like to thank M.A. Melanie Künzie for her help in the manuscript work and for technical assistance. A major part of the work has been supported by the Max Planck Society.

References

1. Stott GG, Sis RF, Levy BM (1982) Cemental annulation as an age criterion in forensic dentistry. J Dent Res 61:814–817
2. Wittwer-Backofen U, Gampe J, Vaupel JW (2004) Tooth cementum annulation for age estimation: Results from a large known-age validation study. Am J Phys Anthropol 123: 119–129
3. Charles KD, Condon K, Cheverud JM, Buikstra JE (1986) Cementum annulation and age determination in Homo sapiens. I. Tooth variability and observer error. Am J Phys Anthropol 71:311–320
4. Condon K, Charles KD, Cheverud JM, Buikstra JE (1986) Cementum annulation and age determination in Homo sapiens. II.

Estimates and accuracy. Am J Phys Anthropol 71:321–330

5. Lippitsch A, Grupe G (2007) Variability of the apposition of the acellular, extrinsic fibre cementum and its influence on the tooth cementum annulation technique in humans: The influence of physical demands and functional morphology. Doc Archaeobiolo 5:87–112
6. Wittwer-Backofen U, Buckberry J, Czarnetzki A, Doppler S, Grupe G, Hotz G, Kemkes A, Larsen CS, Prince D, Wahl J, Fabig A, Weise S (2008) Basics in paleodemography: a comparison of age indicators applied to the early medieval skeletal sample of Lauchheim. Am J Phys Anthropol 137:384–396
7. Lieberman DE (1994) The biological basis for seasonal increments in dental cementum and their application to archaeological research. J Archaeol Sci 21:525–539
8. Schroeder HE (2000) Orale Strukturbildung: Entwicklungsgeschichte. Struktur und Funktion normaler Hartgewebe und Weichgewebe der Mundhöhle und des Kiefergelenkes, Thieme-Verlag
9. Cool SM, Forwood MR, Campbell P, Bennett MB (2002) Comparisons between bone and cementum compositions and the possible basis for their layered appearances. Bone 30: 386–392
10. Kvaal SI, Solheim T (1995) Incremental lines in human dental cementum in relation to age. Eur J Oral Sci 103:225–230
11. Grosskopf B (1989) Incremental lines in prehistoric cremated teeth. A technical note. Z Morphol Anthropol 77:309–311
12. Czermak A, Czermak A, Ernst H, Grupe G (2006) A new method for the automated age-at-death evaluation by tooth-cementum annulation (TCA). Anthropol Anz 64:25–40
13. Klauenberg K, Lagona F (2007) Hidden Markov random field models for TCA image analysis. Comput Stat Data An 52:855–868
14. Meinl A, Huber CD, Tangl S, Gruber GM, Teschler-Nicola M, Watzek G (2008) Comparison of the validity of three dental methods for the estimation of age at death. Forensic Sci Int 178:96–105
15. Kagerer P, Grupe G (2001) On the validity of individual age-at-death diagnosis by incremental line counts in human dental cementum. Technical considerations. Anthropol Anz 59: 331–342
16. Lipsinic FE, Paunovich E, Houston DG, Robison SF (1986) Correlation of age and incremental lines in the cementum of human teeth. J Forensic Sci 31(3):982–989
17. Renz H, Radlanski RJ (2006) Incremental lines in root cementum of human teeth—a reliable age marker? HOMO 57:29–50
18. Klevezal GA, Kirillova IV, Shishlina NI, Sokolov AA, Trunova (Selkova) Yu E (2006) Growth layers in tooth dentin and cementum: problems and perspectives of their use in the study of fossil and subfossil mammal remains including humans. In: Grupe G, Peters J (eds) Microscopic examinations of bioarchaeological remains. Verlag Marie Leidorf, Rahden/Westf
19. Kargerer P, Grupe G (2001) Age-at-death diagnosis and determination of life-history parameters by incremental lines in human dental cementum as an identification aid. Forensic Sci Int 118:75–82
20. Grosskopf B, Denden JM, Krüger W (1996) Untersuchung zur Zementapposition bei Parodontitis marginalis profunda. Dtsch Zahnärztl Z 51:295–297
21. Lamendin H, Baccino E, Humbert JF, Tavernier JC, Nossintchouk RM, Zerilli A (1992) A simple technique for age estimation in adult corpses: the two criteria dental method. J Forensic Sci 37(5):1373–1379
22. Prince DA, Ubelaker DH (2002) Application of Lamendin's adult dental aging technique to a diverse skeletal sample. J Forensic Sci 47(1): 107–116
23. Roksandic M, Vlak D, Scjillaci MA, Voicu D (2009) Technical note: applicability of tooth cementum annulation to an archaeological population. Am J Phys Anthropol 140:583–588
24. Bojarun R, Jankauskas R, Garmus A (2004) Altersbestimmung mithilfe von Wachstumslinien des Zahnzements. Rechtsmedizin 14:405–408
25. Adler P (1967) Die Chronologie der Gebissentwicklung. In: Harndt E, Weyers H (eds) Zahn-, Mund- und Kieferheilkunde im Kindesalter. Die Quintessent, Berlin
26. Jackes M (2000) Building the Bases for Paleodemographic Analysis: Adult Age Determination. In: Katzenberg MA, Saunders SR (eds) Biological Anthropology of the Human Skeleton. Wiley-Liss, New York
27. Kemkes-Grottenthaler A (2002) Aging through the ages: historical perspectives on age indicator methods. In: Hoppa RD, Vaupel JW (eds) Paleodemography. Age distributions from skeletal samples. Cambridge Studies in Biological and Evolutionary Anthropology 31. Cambridge University Press, Cambridge

Chapter 9

Dental Topographic Analysis of the Molar Teeth of Primates

Zachary S. Klukkert, John C. Dennis, Francis M'Kirera, and Peter S. Ungar*

Abstract

The study of tooth form is informative about the relationship between teeth and the material properties of foods consumed. Studies of dental functional morphology depend on precise characterization of relevant aspects of crown form; the occlusal surfaces of primate molar teeth are studied in 3-dimensional space more and more commonly today. Dental topographic analysis is becoming an increasingly popular method for studying tooth form, given its ability to characterize functionally relevant aspects of tooth form from an entire occlusal surface. This landmark-free approach has been especially valuable in studies of the effects of tooth wear on shape. Mean slope and relief, for example, have been found to be informative about the function of molar teeth in both living and extinct primates. Instructions for the use of this approach are provided here.

Key words: Tooth shape, Tooth function, GIS, 3D morphology

1. Introduction

The quantitative characterization of functionally relevant aspects of tooth shape can provide insights into the dietary adaptations of an animal. Such characterizations have been difficult to make, and data have been difficult to compare between specimens, because shape changes with wear. Because tooth crowns wear with use, and landmarks used in common measurements are quickly obliterated, it is difficult to compare individuals. This is problematic because there are very few unworn specimens available, especially in the paleontological and archeological records, available for study (1).

Dental topographic analysis permits the measurement and comparison of occlusal tooth surface features without the use of landmarks. Three dimensional point cloud data are collected from

*To whom correspondence should be addressed.

Lynne S. Bell (ed.), *Forensic Microscopy for Skeletal Tissues: Methods and Protocols*, Methods in Molecular Biology, vol. 915, DOI 10.1007/978-1-61779-977-8_9, © Springer Science+Business Media, LLC 2012

an occlusal surface, and then used to interpolate a virtual surface for analysis. The tools used to collect the initial point clouds depend on the resolution required for the particular sample and research question. Tools used to date vary from electromagnetic digitizer (2) to touch probe scanner (3, 4), laser scanner (1, 5), and confocal microscope (6). Following the collection of point cloud data, a surface is modeled and analyzed using Geographic Information Systems (GIS) Software.

GIS software is used first to interpolate a tooth's surface from point clouds, then to measure features on that surface in the same way that it is more typically used to study geographic surfaces across space (1, 3, 7–9). Because dental topographic analysis allows characterization of a surface without the use of landmarks, it permits analysis and comparison of variably worn teeth. The inclusion of worn specimens in analyses results in a dramatic increase in sample size, particularly for species that wear their teeth quickly.

Changes in a tooth's shape with wear likely affect its functional efficiency for breaking down food (10–12). This notion should be considered in light of an expectation that selection should favor mechanisms that maintain or improve function with normal use (8, 9, 13–19).

While dental topographic analysis is a relatively new approach, researchers have already examined several functionally relevant aspects of tooth form using GIS protocols on scanned point clouds representing tooth surfaces (e.g. (1–3, 6–9, 19)). Slope and relief of molar occlusal surfaces, for example, have been shown to correlate well with broad diet category (1, 8). The slope variable reflects mean slope, or change in elevation, across an occlusal surface, and relief is calculated as the ratio of 3D surface area of the occlusal table to its corresponding planimetric area (1, 8). Both slope and relief have been demonstrated to be higher in folivores, which regularly consume tough, fibrous foods (e.g. *Gorilla gorilla gorilla*), and to be lower in soft-fruit specialists (e.g. *Pan troglodytes troglodytes*) (1, 8). These values correspond with sharp molar crests for shearing and slicing in gorillas and lower, rounder cusps for crushing and grinding in chimpanzees.

As molar teeth wear down, slope and relief values tend to decrease (1, 8, 17, 20). In other words, teeth get flatter as they wear. Still, differences in slope and relief between species tend to be consistent at given stages of wear. This suggests that comparisons between species are possible, but require some control over the degree of gross wear (1, 8, 20).

The instructions presented here provide the steps used for extracting mean slope and relief values from digital elevation models (DEMs) generated from 3D point clouds that were collected from molar tooth surfaces (Fig. 1). ArcGIS 9.2 (ESRI Inc., Redlands CA) is used here as a model software to demonstrate the generation and analysis of a DEM. A very basic familiarity with

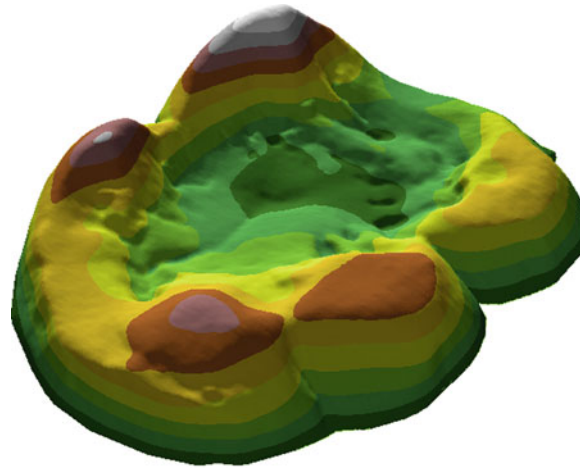

Fig. 1. Dental topography uses geographic information systems to analyze the occlusal surface of a tooth like a landscape. The digital elevation model seen here is a chimpanzee molar tooth, with bands depicting changes in crown height, or elevation.

ArcGIS 9.2 is assumed for these instructions. The details of the procedure can be modified to achieve the same results using a number of popular GIS programs.

Before analysis begins, it is important to define the surface of interest for comparability among specimens. The orientation of the original surface is important in this context, because surfaces are scanned and analyzed in 2.5D (one *z*-value for a given *x*, *y* pair) for this procedure. First, the original specimen is oriented so as to maximize mesiodistal and buccolingual dimensions of the crown (this approximates the plane of the occlusal row). The area of interest, defined as the occlusal table, is the proportion of the scan confined in horizontal space by the sides of the tooth crown and vertically by the surface from the highest point on the surface to the lowest point in the occlusal basin. Surface characterization involves three basic steps.

1. Import of point cloud data collected from the tooth surface.
2. Generation of a virtual model of the tooth, and cropping of the surface to be analyzed.
3. Surface analyses.

2. Data Format

Various instruments are used to collect 3D point cloud data from tooth surfaces for virtual surface analysis and the default format for data exported varies. These instructions describe the import of files in the American Standard Code for Information Interchange

(ASCII) format. ASCII is widely used, and many software packages have the option of converting point cloud files to this format. The files should include data points collected in the form of *x*, *y*, and *z* coordinates representing each surface at a fixed spacing along the axes. The point spacing and vertical resolution used for this model is 25 μm, but this can vary depending on the question of interest and the equipment used (see above).

3. Methods

3.1. Preparation

Before data acquisition, it is helpful to develop a directory structure so that each specimen gets its own directory (many files will be generated in the course of data acquisition and analysis). Further, ASCII files should be inspected in a text editor to make sure there is no header or other metadata before the *x*,*y*,*z* coordinates are listed. Finally, in the text file, *create* a header by typing in "x,y,z" in front of the first coordinate and hit enter. Save the modified file and proceed to import.

3.2. Importing Tooth Scan Data

1. Open ArcMap, make sure that "Spatial Analyst," "3D Analyst," and "Editor" extensions are all turned on and their respective toolbars visible.
2. Under the Tools menu, select "Add xy data," select your ASCII text file with *x*,*y*,*z* coordinates, accept that you will not be able to select features.
3. Right-click on the "txt" layer and select DATA, EXPORT, accept default name and select OK to add export_output as layer.
4. In the Spatial Analyst toolbar, select INTERPOLATE TO RASTER, IDW, set *z* field to "z," set output cell size to "0.025" (or the appropriate cell size if different), and name output raster as "dem_idw."

3.3. Finding the Lowpoint

1. Open ArcCatalog, add two new shapefiles, both polygons. Call one "lowpoint" and the other one "crop" (see Note 1).
2. Switch back to ArcMap. Using the "Add Data" button, add the "lowpoint" file and choose OK that it cannot be projected.
3. In Spatial Analyst, select SURFACE ANALYSIS; CONTOUR. For input, select the "dem_idw" file. Accept the default settings and save the layer as "cont_dem."
4. In the Editor toolbar, select START EDITING. If the dialog opens, check to make sure that the proper working folder is selected, the "lowpoint" file will be listed. In the Editor tool

bar (see Note 2), find TASK, select "Create New Feature" and for TARGET select the "lowpoint" file.

5. Draw a polygon using the sketch tool, drawing around the lowest contour in the center of the basin (see Note 3).
6. In Editor, select SAVE EDITS, then select STOP EDITING.
7. Right-click on the "lowpoint" raster layer, open JOINS AND RELATES and select JOIN. Then choose to select points by location. Then select the "export_output" layer. Check "Minimum" and accept the default name "join_lowpoint."
8. Right-click on the new "join_lowpoint" layer, open the attribute table and record "Minimum z" (see Note 4).
9. At this point the following layers and files are no longer needed and may be deleted to maintain a clutter-free workspace: "txt" layer, "export_output," "lowpoint," "join_lowpoint."

3.4. Cropping

1. Click the Add Data button, and select the "crop.shp" file.
2. In the Editor toolbar, select START EDITING. For TASK select "Create New Feature" and for TARGET select the "crop" shape file.
3. Using the sketch tool, draw a *liberal* polygon around the tooth where there is no contact with any adjoining teeth (see Note 5).
4. In the Editor toolbar, select SAVE EDITS, and STOP EDITING.
5. In the Spatial Analyst toolbar, select CONVERT, and FEATURES TO RASTER. Input the appropriate cell size, in this model 0.025, for the output cell size. Save the new raster as "crop."
6. Select the new "crop" raster file, then in the Spatial Analyst toolbar select RECLASSIFY. Where it calls for the raster file to be reclassified, ensure the new "crop" file is selected. The value "1" should be in the first "New value" cell and "NoData" in the cell below that (this is the default reclassification). Save the file as "crop_rc."
7. In Spatial Analyst, select the RASTER CALCULATOR. Enter the following formula: (crop_rc)*(dem_idw). Click on EVALUATE. The resulting surface will be saved temporarily as "Calculation."
8. In the Spatial Analyst toolbar, select RASTER CALCULATOR. Enter the formula (Calculation)>=(x.xx), where "x.xx" is the lowpoint that you recorded earlier. Click on EVALUATE. This will be saved temporarily as "Calculation2."
9. In the Spatial Analyst toolbar, select RECLASSIFY. Ensure the new "Calculation2" file is selected. For the "New value" cells,

change the defaults to "NoData," "1" and "NoData" so that the raster only contains data for the area output by the raster calculator above the lowpoint. Save this raster as "crop_2."

10. In Spatial Analyst, select RASTER CALCULATOR and input the following formula: (crop_2)*(dem_idw). Click EVALUATE. The resulting surface will be saved temporarily as "Calculation3."
11. Right-click "Calculation3," select DATA and then select MAKE PERMANENT. Save the layer as "dem_cropped" (see Note 6).
12. At this point all of the layers and files except "dem_cropped" may be removed to maintain a clutter-free workspace.

3.5. Data Collection

1. Slope: The slope statistic is the mean slope of the entire occlusal surface. To calculate this value, select Spatial Analysis, choose SURFACE ANALYSIS and then select SLOPE. Input the cropped DEM ("dem_cropped") and accept the defaults. Next, double click the new slope layer and select the source tab. Scroll down to the "Statistics" section and record mean and standard deviation scores.
2. Relief: "Relief" is calculated as the ratio of the surface area to the planimetric area. To find these values, select the "dem_cropped" layer and open the 3D Analyst menu, select SURFACE ANALYSIS and choose AREA/VOLUME. Select the cropped DEM and click the "Calculate Statistics" button. Record the planar "2D" and "Surface" (3D) areas.

4. Notes

1. Make sure that you create these files in the working folder where the coordinate data file is saved.
2. The Editor toolbar has two parts that are important to these instructions. The first is the drop down menu that can be accessed by clicking the mouse on the Editor icon. The second is the TASK and TARGET boxes where the user specifies what is to be done to which layer. These boxes will be found to the side of the Editor icon by default.
3. It is prudent to use the magnifying tool to zoom in so as to ensure correct placement. If there are two or more disparate zones that are equally low, then make your polygon larger to include both. This polygon need not be extremely precise so long as the point with the lowest elevation (z-value) is in the target area. One issue that may come up in extremely worn teeth is when the lowest area of the occlusal surface is at or

below the dentine enamel junction (DEJ). In this case a decision must be made about whether to (1) exclude the tooth from analysis, (2) define the lowest point as concurrent with the DEJ, or (3) include the tooth and use the described method but ensure that there is a wear category built into the final analysis that includes specimens with such an extreme condition.

4. This is the "lowpoint" value, write it down as it will be used for the cropping step. Rounding the exact value to the lower (representing a lower *z*-value) third decimal place is recommended if the exact value is not used.
5. Where there is a bridge between teeth, or nearby objects in the scan, zoom in and carefully draw a line between the teeth, using the contour lines as a guide.
6. It is helpful to also double click "Calculation3" in the contents window, go to GENERAL tab and change the name to "dem_cropped." This changes the name of the layer in the working area.

Acknowledgements

First we thank Lynne Bell for the invitation to contribute to this volume. We would also like to extend our thanks to Lucy Zucotti, Malcolm Williamson, and John Wilson for their assistance with development of the protocols that served as the foundation for this work. Finally, we are grateful to Tuna Kalayci and Katie Simon for comments and discussion that contributed to developing the updated procedures.

References

1. Ungar PS, M'Kirera F (2003) A solution to the worn tooth conundrum in primate functional anatomy. Proc Natl Acad Sci 100(7): 3874–3877
2. Zuccotti LF, Williamson MD, Limp WF, Ungar PS (1998) Technical note: modeling primate occlusal topography using geographic information systems technology. Am J Phys Anthropol 107:137–142
3. King SJ, Arrigo-Nelson SJ, Pochron ST, Semprebon GM, Godfrey LR, Wright PC, Jernvall J (2005) Dental senescence in a long–lived primate links infant survival to rainfall. Proc Natl Acad Sci 102(46):16579–16583
4. Ungar PS (2007) Dental functional morphology: the known, the unknown, and the unknowable. In: Ungar PS (ed) Evolution of the human diet. Oxford University Press, New York
5. Bunn JM, Ungar PS (2009) Dental topography and diets of four old world monkey species. Am J Primatol 71(6):466–477
6. Jernvall J, Selanne L (1999) Laser confocal microscopy and geographic information systems in the study of dental morphology. Palaeontol Electron 2(1):1–18
7. Ungar PS, Williamson M (2000) Exploring the effects of tooth wear on functional morphology: a preliminary study using dental topographic analysis. Palaeontol Electron 3(1):1–18
8. M'Kirera F, Ungar PS (2003) Occlusal relief changes with molar wear in *Pan troglodytes*

troglodytes and *Gorilla gorilla gorilla*. Am J Primatol 60:31–42

9. Evans AR (2005) Connecting morphology, function and tooth wear in microchiropterans. Biol J Linn Soc 85:81–96
10. Teaford MF (1983) The morphology and wear of the lingual notch in macaques and langurs. Am J Phys Anthropol 60:7–14
11. Maier W (1984) Tooth morphology and dietary specialization. In: Chivers DJ, Wood BA, Bilsborough A (eds) Food acquisition and processing in primates. Plenum Press, New York
12. Crompton AW, Wood CB, Stern DN (1994) Differential wear of enamel: a mechanism for maintaining sharp cutting edges. In: Bels VL, Chardon M, Vandewalle P (eds) Biomechanics of feeding in vertebrates: advances in comparative and environmental physiology. Springer, Berlin
13. Rensberger JM (1973) An occlusion model for mastication and dental wear in herbivorous mammals. J Paleont 47(3):515–528
14. Kay RF (1975) The functional adaptations of primate molar teeth. Am J Phys Anthropol 43:195–216
15. Rosenberger AL, Kinzey WG (1976) Functional patterns of molar occlusion in platyrrhine primates. Am J Phys Anthropol 45:281–298
16. Lanyon JM, Sanson GD (1986) Koala (*Phascolarctos cinereus*) dentition and nutrition. II. Implications of tooth wear in nutrition. J Zool 209:169–181
17. Dennis JC, Ungar PS, Teaford MF, Glander KE (2004) Dental topography and molar wear in *Alouatta palliata* from Costa Rica. Am J Phys Anthropol 125:152–161
18. Lucas PW (2004) Dental functional morphology; how teeth work. Cambridge University Press, New York
19. Evans AR, Wilson GP, Fortelius M, Jernvall J (2007) High-level similarity of dentitions in carnivorans and rodents. Nature 445:78–81
20. Ungar PS (2004) Dental topography and diets of *Astralopithecus afarensis* and early. Homo J Hum Evol 46:605–622

Chapter 10

Chemical Analyses of Fossil Bone

Wenxia Zheng and Mary Higby Schweitzer

Abstract

The preservation of microstructures consistent with soft tissues, cells, and other biological components in demineralized fragments of dinosaur bone tens of millions of years old was unexpected, and counter to current hypotheses of tissue, cellular, and molecular degradation. Although the morphological similarity of these tissues to extant counterparts was unmistakable, after at least 80 million years exposed to geochemical influences, morphological similarity is insufficient to support an endogenous source. To test this hypothesis, and to characterize these materials at a molecular level, we applied multiple independent chemical, molecular, and microscopic analyses to identify the presence of original components produced by the extinct organisms. Microscopic techniques included field emission scanning electron microscopy, analytical transmission electron microscopy, transmitted light microscopy (LM), and fluorescence microscopy (FM). The chemical and molecular techniques include enzyme-linked immunosorbant assay, sodium dodecyl sulfate polyacrylamide gel electrophoresis, western blot (immunoblot), and attenuated total reflectance infrared spectroscopy. In situ analyses performed directly on tissues included immunohistochemistry and time-of-flight secondary ion mass spectrometry. The details of sample preparation and methodology are described in detail herein.

Key words: Dinosaur soft tissues, Fossil, Ancient proteins, Molecular paleontology, Analytical paleontology, Paleoimmunology

1. Introduction

If ancient biomaterials recovered from biomineralized fossil tissues can be shown to be endogenous to the extinct organisms from which they are recovered, they will provide novel opportunities to study molecular evolution. Recovery of ancient biomaterials, including fibrous bone matrix, blood vessels, and apparent osteocytes, from exceptionally preserved fossils (e.g., Fig. 1) had been demonstrated morphologically (1, 2), but morphological similarity is insufficient to address the source of these components after millions of years of interactions with surrounding geochemical influences. Therefore, we conducted chemical and molecular analyses to identify

Lynne S. Bell (ed.), *Forensic Microscopy for Skeletal Tissues: Methods and Protocols*, Methods in Molecular Biology, vol. 915,
DOI 10.1007/978-1-61779-977-8_10,

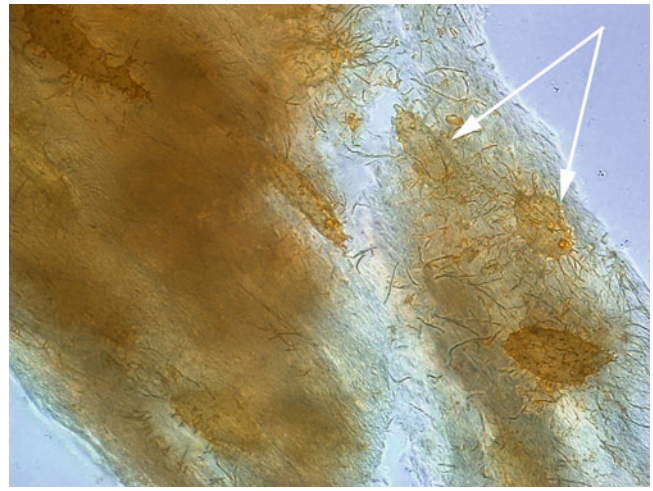

Fig. 1. Material remaining after demineralization of dinosaur bone. Extensive filipodia arising from elongate microstructures consistent with vertebrate osteocytes (*arrows*) are surrounded by *white* fibrous matrix. Color differences between the microstructures and matrix indicate different chemical microenvironments during diagenesis.

the chemical composition, and hence the source of these materials. While demonstration of endogeneity ultimately rests on sequence data, the methods and details of those techniques are beyond the scope of this paper (3). Here, we discuss some of the methods we applied to fossil bone and the resulting soft tissues housed therein, and the procedures used to support claims of endogeneity beyond sequence data. Characterization of these materials may ultimately transform the study of evolution, increase understanding of environmental and chemical stability of organic compounds over time, and contribute direct evidence of organismal responses to global climate change, all of which require the critical perspective of deep time. Because the potential information to be gained by the study of original organic components in fossil tissues is great, then, optimizing methods of analyses is critical to future studies.

Chemical models based on extrapolation from harsh benchtop experiments or kinetics predict that all informative organic remains will degrade past recognition after ~100,000 years (usually much less) (4–11), thus the endogeneity and characterization of the materials we recovered from multiple samples of dinosaur bone were contested. The controls used in our molecular and chemical analyses of fossil bone were as critical as specific methods employed for demonstrating endogeneity and lack of exogenous contamination, and we discuss these here as well. Finally, because fossil material is usually valuable and certainly a "nonrenewable" resource, and because our methods are destructive, we discuss the rationale behind the methods we chose. These were designed to progress from microscopic observation to chemical analyses, and focus on gaining the most information from the least amount of sample destruction.

2. Materials

2.1. Demineralization

1. Six-well Costat® cell culture plates from Corning Inc., individually sterilized.
2. E-pure water with a resistivity of 18.2 mega-ohms (MΩ/cm). E-pure water and all solutions are filter-sterilized using 0.22 µm polyethersulfone (PES) bottle top filters for each experiment (see Note 1).
3. 0.5 M EDTA pH 8.0 demineralization buffer, prepared with ethylenediamine tetraacetic acid disodium salt dehydrate (EDTA), molecular biology grade, ≥99% from Sigma, stored at room temperature (RT) (see Note 2).

2.2. Whole-Bone Chemical Extraction for ELISA and Western Blot

1. 0.5 M EDTA pH 8.0 demineralization buffer, stored at RT (see Note 2).
2. Extraction buffer: 6 M guanidine hydrochloride (GuHCl), 0.1 M Tris pH 7.4 stored at RT (see Note 3).
3. Sterile mortar and pestle.
4. Dialysis: Pierce Slide-A-Lyzer* Dialysis Cassettes 12–30 mL 3,500 MWCO, or Pierce SnakeSkin tubing, 3,500 MWCO; 10 and 5 mL syringes from BD Biosciences and needles used for dialysis cassettes.
5. Sterile 50 mL centrifuge tubes.
6. Sterile 120 mL glass bottles.

2.3. Vessel Extraction Buffer

1. Proteinase inhibitor buffer PBSi: 1 protease inhibitor tablet from Roche in 50 mL phosphate-buffered saline (PBS).
2. DNAse I buffer: 200 U DNAse I (Sigma) in 50 mL 1 M NaCl.
3. Deoxycholate buffer: 1:1 mixture of homogenization buffer PBSi and 4% deoxycholate buffer.
4. Digestion buffer: 1 ku/1 mL collagenase (CLSPA, Worthington) in Proteinase inhibitor buffer PBSi.
5. Cold 95% ethanol.
6. 2 mL micro centrifuge tubes.

2.4. Electrophoretic Separation by SDS-PAGE

1. Resuspension buffer: 20 mM Potassium dihydrogen phosphate ($KH_2PO_{4)}$ in 5% (v/v) acetonitrile (ACN), adjust pH to 7.0 with 2 M HCl.
2. Cell lysis buffer: 50 mM Tris, pH 7.5, 0.15 M NaCl, 0.1% SDS, 1% Triton X-100, 1% Deoxycholate, and protease mix (Roche, 1 tablet for 50 mL buffer). Stored at 4 °C.
3. 4× Laemmli buffer: 2.4 mL 1 M Tris pH 6.8, 0.8 g SDS stock, 4 mL 100% glycerol, 0.01% bromophenol blue in 2.8 mL water

(Store aliquots at –20 °C, and add 100 µL beta-mercaptoethanol (BME) to 1 mL aliquot just before use).

4. 2× sodium dodecyl sulfate polyacrylamide gel electrophoresis (SDS-PAGE) sample buffer: 7 mL 0.5 M Tris–HCl pH 6.8, 7 mL 10% (w/v) SDS, 7 mL glycerol, enough bromophenol blue to darken, stored as 1-mL aliquots at –20 °C. Add BME to 3.6% (e.g., 36 µL BME to 1 mL 2× sample buffer) before using under the hood.
5. Running buffer: BupHTM Tris-HEPES-SDS Running Buffer (Pierce).
6. 4–20% precast gradient gel (Pierce #25204) with a gel size of 8 cm × 5.8 cm × 1 mm, a well volume of 50 µL used according to manufacturer's specifications.
7. Molecular weight markers (Pierce, #26691).

2.5. Silver Staining

1. Fixer: 50% (v/v) methanol, 12% (v/v) acetic acid aqueous solution.
2. Washing solution: 50% ethanol.
3. Sensitizing solution: 0.2 g/L sodium thiosulfate.
4. Silver nitrate solution: 2 g/L silver nitrate, 1 mL/L formaldehyde.
5. Developing solution: 60 g/L sodium carbonate, 1 mL/L formaldehyde, 30 mL sodium thiosulfate (0.2 g/L).
6. Stop solution: Coomassie destain solution (10% ethanol, 5% (v/v) acetic acid aqueous solution).

2.6. Western Blot

1. Cell lysis buffer: 50 mM Tris, pH 7.5, 0.15 M NaCl, 0.1% SDS, 1% Triton X-100, 1% Deoxycholate, and protease mix (Roche, 1 tablet for 50 mL buffer). Stored at 4 °C.
2. 4× Laemmli buffer: 2.4 mL 1 M Tris pH 6.8, 0.8 g SDS stock, 4 mL 100% glycerol, 0.01% bromophenol blue in 2.8 mL water, (Aliquots stored at –20 °C, add 100 µL BME to 1 mL aliquot just before use).
3. 2× SDS-PAGE sample buffer: 7 mL 0.5 M Tris–HCl pH 6.8, 7 mL 10% (w/v) SDS, 7 mL glycerol, enough bromphenol blue to darken, stored as 1-mL aliquots at –20 °C. Add BME to 3.6% (e.g., 36 µL BME to 1 mL 2× sample buffer) before using under the hood.
4. Millipore "Immobilon" polyvinylidene fluoride (PVDF) Transfer Membranes PVH00010.
5. Semi-dry transfer buffer: Prepare 10× anode I stock with 30 mM Tris (MW121.4), 10× anode II with 300 mM Tris and 10× Cathode stock with 25 mM Tris, 40 mM 6-aminocaproic acid. Dilute 10× stocks to 1× transfer buffer with water and add methanol to a final concentration of 20% (v/v).

6. BioRad extra thick blot paper.
7. Tris-buffered saline with Tween (TBS-T): Prepare 10× TBS stock with 1.37 M NaCl, 27 mM KCl, 250 mM Tris–HCl, adjust pH to 7.4 by 6 M HCl. Dilute 100 mL with 900 mL water and add 1 mL Tween20 to make TBS-T for use.
8. Blocking buffer: 5% nonfat milk in TBS-T prepared fresh immediately before use.
9. Chemiluminescent visualization (for detection of HRP): Pierce SuperSignal Weat Pico Chemiluminescent substrate, used as directed.
10. X-ray film (Kodak BioMax light film, Sigma).
11. Kodak GBX developer.
12. Kodak GBX fixer.
13. Secondary antibody: Goat Anti-Rabbit IgG (whole molecule)–Peroxidase (Sigma) (1:5,000).

2.7. ELISA

1. ELISA plates: Immulon 2HB Ubottom (Thermo Scientific).
2. Phosphate-buffered saline (PBS) pH 6.86–6.88: Prepare a 10× PBS pH 6.86 stock solution with 0.1 M Na_2HPO_4, 0.1 M NaH_2PO_4,1.3 M NaCl, adjust pH to 6.86–6.88 by adding NaOH pellets (2.5 g/1 L) to approach proper pH, then adding 5 M NaOH solution drop by drop (see Note 4) until desired pH is reached. For working buffer, dilute stock 1:10 with distilled water, readjusting pH if necessary.
3. Wash buffer PBS-T: PBS w/0.1% (v/v) Tween 20.
4. Blocking buffer: 5% (w/v) Bovine serum albumin (BSA) in PBS with 0.005% (v/v) Tween20 and 0.05% (w/v) Thimersol (see Note 5).
5. Enzyme detection buffer: Add 1 *p*-Nitrophenyl phosphate tablet (Sigma) to 10 mL 1 M diethanolamine buffer, pH 9.8, 0.5 mM $MgCl_2$ (see Note 6).
6. 12-channel Pipettor.
7. 1 mL Adjustable Pipettor.
8. Titer-top (EMS).
9. Secondary antibody: Goat Anti-Rabbit l g (H + L) alkaline phosphatase conjugate (Invitrogen) (1:2,000).

2.8. Embedding and IHC

1. Demineralization buffer: 5%(w/v) Trichloroacetic acid (TCA) aqueous solution for bone matrix collection, 0.5 M EDTA pH 8.0 demineralization buffer (see Note 2) used for vessels collection.
2. Fixation buffer: 4% formaldehyde solution made from paraformaldehyde in 0.2 M Cacodylate buffer pH 7.4 (see Note 7).

3. Cold cacodylate buffer: 0.2 M sodium cacodylate, adjust pH to 7.4 with 0.2 M HCl.
4. Dehydration solution: 70% ethanol.
5. Infiltration solution: LR White embedding medium (EMS, hard grade): 70% ethanol, 2:1 ratio (see Note 8).
6. LR White resin: hard grade from EMS, stored in the dark at 4 °C. Use under ventilation in hood. (see Note 9).
7. Gelatin capsules (EMS).
8. Teflon-printed slide: 6-well, 8 mm well diameter from EMS.
9. 10× PBS pH 7.4: add 0.1 M NaH_2PO_4 (8.28 g NaH_2PO_4, FW 119.9 in 600 mL water) to 0.1 M Na_2HPO_4 (28.4 g Na_2HPO_4, FW 141.96 in 2 L water) until pH 7.4 is reached, stored refrigerated at 4 °C.
10. PBS buffer pH 7.4: Add 100 mL 10× PBS pH 7.4 to 900 mL water, add 8.5 g NaCl.
11. PBS w/0.5%Tween 20(PBS-T): Add 100 mL 10× PBS to 900 mL water, add 8.5 g NaCl and 5 mL Tween 20.
12. Digestion buffers:
    (a) Collagen digestion buffer: 1 mg/mL collagenase A (Roche) in Dulbecco's phosphate-buffered saline (D-PBS) pH 7.2 (see Note 10).
    (b) Elastin digestion buffer: Elastase (MP Biomedicals) 0.2 mg/mL in 0.2 M Tris/HCl, pH 8.8.
13. Antigen retrieval: proteinase K (PCR Grade, Roche) 25 μg/mL in PBS.
14. Primary antibody dilution buffer: add 2 g BSA, 0.2 g gold fish skin gelatin, and 0.1 g sodium azide to 200 mL 0.01 M pH 7.2 PBS.
15. Staining dishes with covers (Fisher) for ten slides.
16. Blocking buffer: 4% normal goat serum (NGS) in PBS.
17. Fluorescent label: Avidin/FITC (Vector A-2001), dilute 1:1,000 in PBS.
18. Mounting medium: Vectashield H-1000 (Vector).
19. Secondary antibodies:

Vector Biotinylated Goat Anti-Rabbit l g (H + L) BA-1000 diluted 1:500 in blocking buffer (4% NGS in PBS).

Vector Biotinylated Goat Anti-Mouse l g (H + L) BA-9200 diluted 1:500 in blocking buffer (4% NGS in PBS).

2.9. Primary Antibodies Used in IHC, ELISA, and Western Blot

1. Mouse monoclonal [OCG4] to Osteocalcin; Abcam (ab13421). Immunogen: full length bovine protein. (Diluted 10 μg/mL in primary antibody dilution buffer for immunohistochemistry [IHC]).

2. Rabbit polyclonal to Elastin from Abcam (ab21610). Immunogen: Elastins pooled from pig, human, dog chicken, rat, and cow (diluted 1:75 in primary antibody dilution buffer for IHC, diluted 1:300 in 5% (w/v) nonfat milk in TBS-T for western blot).
3. Rabbit polyclonal to Osteocalcin from Abcam (ab35078). Immunogen:syntheticpeptide:H2N-GFQEAYRRFYGPV-OH conjugated to keyhole limpet hemocyanin (KLH), corresponding to C terminal amino acids 37–49 of Human Osteocalcin. (diluted 1:40 in primary antibody dilution buffer for IHC, diluted 1:50 in 5% BSA blocking buffer for ELISA, diluted 1:400 in 5% nonfat milk in TBS-T for western blot).
4. Rabbit polyclonal to Chicken collagen I from USBiological (C7510-13B) Immunogen: Chicken Collagen Type I extracted and purified from chicken skin. (Diluted 1:40 in primary antibody dilution buffer for IHC, diluted 1:400 in 5% BSA blocking buffer for ELISA, diluted 1:400 in 5% nonfat milk in TBS-T for western blot).
5. Rabbit polyclonal to ostrich hemoglobin, BRF 1923, NCSU (produced in-house, diluted 1:75 in primary antibody dilution buffer for IHC, diluted 1:200 in 5% nonfat milk in TBS-T for western blot).
6. Rabbit polyclonal to ostrich whole bone extracts, BRF 51621-B, NCSU (produced in-house, 1:75 in primary antibody dilution buffer for IHC, diluted 1:400 in 5% BSA blocking buffer for ELISA).
7. Rabbit anti-laminin affinity isolated antigen specific antibody (Sigma), diluted 1:75 in primary antibody dilution buffer for IHC, diluted 1:200 in 5% nonfat milk in TBS-T for western blot.

2.10. Equipment

1. Zeiss dissecting microscope.
2. Zeiss Axioskop 2 plus, Zeiss Stemi 2000-C or an Olympus BX61.
3. Sterile, dedicated forceps.
4. Glass microscope slides and cover slips.
5. Zeiss professional imaging for microscopy software.
6. Thermo Electron FTIR with Nexus 470 bench and an ATR OMNI Sampler with Ge crystal. Spectra are obtained at a resolution of 4 cm^{-1} and a scan number of 64.
7. LABCONCO Freezone 18 freeze dryer.
8. Mini-Protean Tetra Cell (BioRad).
9. PowerPac HC Power Supply (BioRad).
10. Trans-Blot SD Semi-Dry Electrophoretic Transfer Cell (BioRad).
11. Leica EM UC6 *Ultra*-microtome.

12. SPECTRA max PLUS plate reader (Molecular Devices Corporation).
13. Analytical Balance 0.0001 g resolution.
14. pH meter.
15. Micro centrifuge.
16. Incubator shaker.

3. Methods

We employed multiple independent methods to characterize the soft tissues recovered from fossil bone. Some, including field emission scanning electron microscopy (FE-SEM), LM, and FM, required only demineralization of the bone fragments to reveal the vessels, cells, and matrix. For transmission electron microscopy (TEM) and IHC, these materials were further treated by infiltrating and embedding in a resin (e.g., LR White). Additional analyses, including Western blots and/or ELISA, required chemical extraction of either whole bone or vessels.

3.1. Demineralization and Collection of Cells, Tissues, for Microscopy and in situ IHC

Fragments of dinosaur bone or other fossil bone (for full list of fossils, see (2)) were demineralized to remove the mineral component of bone. This procedure is commonly used to study the ultrastructure of extant biomineralized material, including bone, and was required to identify and document the presence of soft tissues within the bony matrix of fossil bone.

1. Fragments of fossil bone were placed in 6-well plates, covered with 0.5 M EDTA (pH 8.0) demineralization buffer, then incubated for days to weeks at RT (Fig. 2) until no further changes in mineral state were observed.
2. The demineralization solution was exchanged daily or every other day and the process monitored by observation and photodocumented under low power (dissecting) microscopy until no minerals can be visually detected, and/or the remaining tissues are soft and pliable. Vessels and fibrous tissues were collected using sterile forceps, and removed to new 6-well plates, then rinsed multiple times in sterile distilled water (Fig. 2f).
3. For ATR-IR, the material was collected and lyophilized after thorough washing. Immediate analysis is optimal; however material can also be stored at −80 °C for future analyses. If the latter, bring to RT before opening the container to avoid water condensation. (see Note 11)
4. "Osteocytes" were too small to be seen with the dissecting microscope; and so were collected by running a sterile pipette across

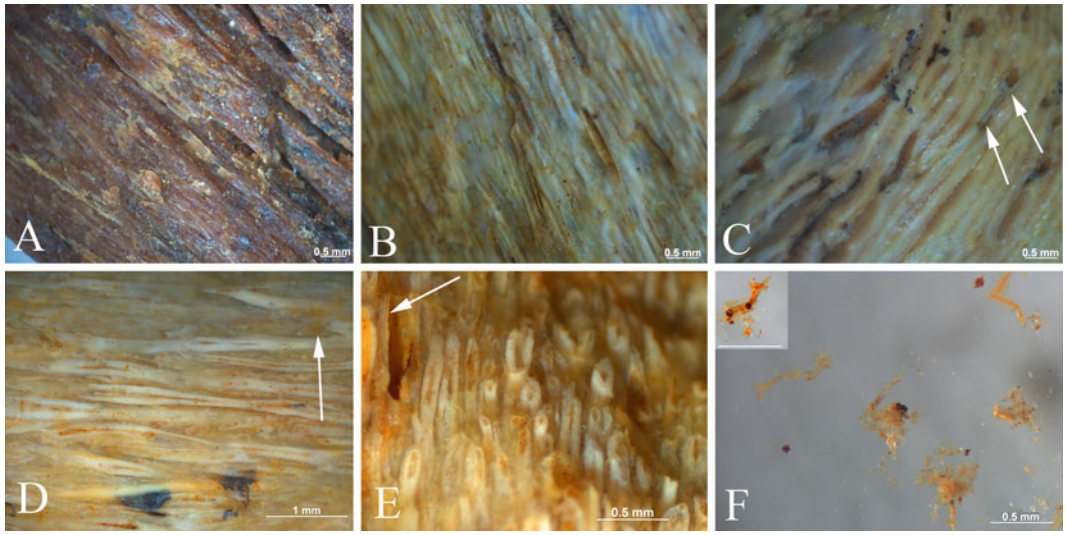

Fig. 2. Progressive demineralization of fossil bone. (**a**) Dinosaur bone before demineralization. (**b**) After 2 days in EDTA (described in text) definite color change is seen in overall bone, bone is less crystalline, and vessel channels become more distinct. (**c**) Higher magnification of bone in (**b**) shows emerging translucent "vessel" (*arrow*) within bony channel. (**d**) After 14 days, clumps of tissue representing emerging vessels and some matrix can be seen (*arrow*). (**e**) After 15 days, vessel channels emerge from bone matrix, and soft vessel lining can be seen along the wall of the bony tubes (*arrow*). (**f**) Isolated vessels removed from bone to separate wash wells as described. Transparent, pliable vessels occasionally contain round red microstructures (*inset*). Scale bars = 0.5 mm, except (**d**), where bar = 1 mm.

the bottom of the demineralization wells and pipetting into new wells filled with sterile water. Samples were allowed to settle, water was carefully removed and fresh water added multiple times until most of the EDTA was removed from the samples.

5. For light and SEM microscopy, demineralized vessels, cells and matrix were air dried on glass slides.
6. For IHC and TEM, materials were dehydrated in ethanol, infiltrated with embedding medium and allowed to polymerize (see Subheading 3.8).

3.2. Whole Bone Chemical Extraction for ELISA, Western Blot

1. Fossil bone fragments were ground to fine powder using sterilized mortar and pestle (baked at 520 °C overnight), and approximately 2.5 g bone powder was aliquoted to sterile 50 mL tubes. Negative controls consisted of comparable amounts of sediment treated in an identical manner to fossil bone, and an equal number of empty tubes (buffer blank). Demineralization buffer (10 mL) was added to sample and negative controls, and incubated overnight at RT with rocking. Tubes were centrifuged at 6,000 g for 15 min to pellet. All controls were exposed to each step of the extraction process in tandem with fossil bone to detect lab induced contaminants.
2. The supernatant resulting from each condition (sample, sediment, and blank) was collected and pooled. This is designated "EDTA fraction."

First Extraction

3. The pellet obtained from the above procedure (see Note 12) was resuspended in 5 mL demineralization buffer, and incubated for 3 days at RT with rocking. After centrifugation, the EDTA supernatant was collected, designated "EDTA super" and stored at 4° C. Extraction buffer (5 mL) was again added to the remaining pellet and incubated with samples/controls at 60 °C for 20 h with gentle agitation, then centrifuged at 6,000 × *g* for 15 min. The supernatant was combined with "EDTA super," and designated "first Extraction."
4. First extraction was injected into Pierce Slide-A-Lyzer® Dialysis Cassettes (12–30 mL 3,500 MWCO), or Pierce SnakeSkin tubing, 3,500 MWCO, and dialyzed against 4 L water at 4 °C with constant stirring. Water was changed twice daily for 4 days.
5. Dialysate was removed to preweighed, sterile glass bottles and shell frozen at –80 °C (see Note 13).
6. After lyophilization to completion, dialysate was weighed to calculate yield.

Second Extraction

7. Pellet remaining from first extraction was resuspended in 5 mL extraction buffer, incubated with gentle agitation for 48 h at 60 °C, centrifuged at 6,000 × *g* for 15 min, and supernatant collected and stored at 4 °C. This fraction is designated as "GuHCl super."
8. The pellet remaining after centrifugation above was resuspended in 5 mL of extraction buffer, incubated at 60 °C overnight with gentle agitation, and centrifuged as above. The supernatant was added to "GuHCl super" and together designated "second extraction."
9. The second extraction was dialyzed and lyophilized, and yield calculated as described above.

3.3. Chemical Extraction of Dinosaur Vessels (see Note 14)

1. Vessels were collected with sterile forceps as they emerged from demineralizing bone fragments, place in new wells and wash multiple times in sterile water (1).
2. Proteinase inhibitor buffer was added and vessels homogenized, then centrifuged at 15,700 g for 10 min at RT.
3. The resulting pellet was resuspended in 1 mL DNAse I buffer, incubated at 4 °C for 2 h with gentle agitation, centrifuged as described above, and supernatant retained.
4. The pellet was resuspended in 1 mL deoxycholate buffer, vortexed, and incubated for 4 h at RT with gentle agitation, then centrifuged as described. Supernatant was reserved for later analyses; resulting pellet was washed three times in sterile water, then incubated in 1 mL digestion buffer overnight at 37 °C.

5. After centrifugation, the supernatants were pooled and to each 200 µL of supernatant, 1 mL cold 95% ethanol was added to precipitate. The solution was mixed with vortexing and incubated for 1 h at 4 °C.
6. After precipitation, samples were centrifuged at 13,000 rpm for 10 min at RT, pellet resuspended in 2× SDS-PAGE sample buffer (see Subheading 3.4) and subjected to electrophoretic separation for silver staining or western blot

3.4. Electrophoretic Separation by SDS-PAGE

1. Samples prepared as described in Subheading 3.2 and/or Subheading 3.3 were subjected to electrophoretic separation by SDS-PAGE as follows (see Note 15)
   - To visualize organic material by silver staining gels: Approximately 1.5–2 mg of lyophilized extract of bone or sediment was solubilized in 20 µL resuspension buffer consisting of 20 mM KH_2PO_4 in 5% ACN, pH 7.0, then mixed with 20 µL 2× SDS-PAGE sample buffer .
   - Bone extracts were subjected to electrophoresis and Western Blot by resuspending 2 mg lyophilized bone extract in 30 µL cell lysis buffer, then mixed with 10 µL 4× Laemmli buffer.
   - Vessels recovered from fossil bone and prepared as above were resuspended directly in 2× SDS-PAGE sample buffer.
2. Samples were incubated with sample buffer for 5 min at 95 °C to denature.
3. All samples were vortexed until well mixed, centrifuged at 3,300×*g* for 6 min, and immediately store on ice until loaded onto precast gels.
4. BupHTM Tris-HEPES-SDS running buffer (prepared as directed) was added to both upper and lower chambers of the gel unit. 40 µL of sample or control (in buffer) or 1 µL molecular weight markers were loaded to designated wells. Electrophoresis was performed at a constant voltage of 120 V for approximately 1 h (Fig. 3a, b). (see Note 16)
5. After electrophoresis, the gels were either stained with silver nitrate for visualization (Fig. 3c) (Subheading 3.5) or semi-dry transferred to membrane for western blotting (Subheading 3.6)

3.5. Silver Staining Protocol

1. Gels resulting from electrophoresis (Subheading 3.4) were placed in fixative for at least 1 h (see Note 17), then washed three times for 20 min each in wash solution (50% ethanol).
2. Incubate gel for 1 min in 0.2 g/L sodium thiosulfate, then rinse three times for 30 s each in water.
3. Gel was soaked in chilled silver nitrate solution and incubated in the dark for 30 min at 4°C.

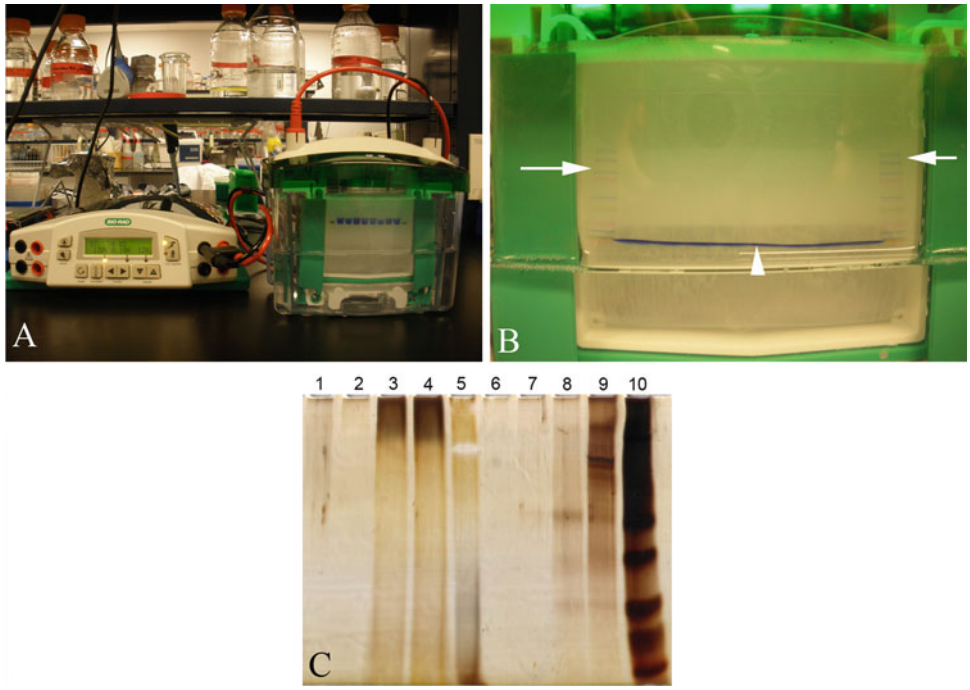

Fig. 3. Electrophoresis of chemical extracts of fossil bone. (**a**) BioRad gel rig, with power supply (*left*) and running gel (*right*). The *dark* line represents the dye front migrating with electric current. Compounds of very low molecular weight will run slightly ahead of this line, and can be lost if the dye is allowed to run off the gel. (**b**) Closer view of gel in buffer showing molecular weight markers (*right* and *left* sides, *arrows*) and *dark* dye front (*arrowhead*). (**c**) Extracts of dinosaur bone and controls, electrophoresed onto SDS-PAGE, then subjected to silver staining as described in text. (15) Lanes are as follows: (1) First extraction, control (buffer only); (2) sediment, First extract; (3, 4) dinosaur bone First extract; (5) dinosaur bone, TCA extraction protocol; (6, 7) sample buffer control; (8) extant avian bone, EDTA fraction; (9) extant avian bone, First extract; (10) molecular weight markers.

4. After incubation, silver nitrate solution was discarded, and gel rinsed twice for 20 s each with distilled water. (Critical: no longer than 1 min maximum each rinse).
5. Place the gel in developer until desired staining is attained then reaction is stopped by placing gel in Coomassie destaining solution. Developer may need to be exchanged more than once.

3.6. Western Blot (see Note 14)

1. After electrophoretic separation of bone or vessel extract using SDS-PAGE (see Subheading 3.4) proteins were transferred from the gel to PVDF membrane using a semi-dry transfer apparatus (Trans-blot, BioRad).
2. Gels were equilibrated in 1× cathode transfer buffer to remove electrophoresis buffer salts and detergents (12).
3. PVDF membranes were cut to dimensions of the gel, soaked in methanol for 15 s, rinsed with water for 5 min and equilibrated in 1× Anode I transfer buffer.

4. BioRad extra thick blot papers were cut to the dimension of the gel, and completely saturated by soaking in appropriate transfer buffer.
5. The transfer materials were assembled as follows: blot paper saturated in Anode II buffer was placed directly on the anode plate of the semi-dry transfer unit. Blot paper saturated with Anode I buffer was added, then membrane, gel and finally blot paper saturated with cathode buffer. A glass pipette or test tube was gently rolled across the surface to exclude all air bubbles each time a new layer is added. Transfer apparatus was closed tightly, and a current of 180 mA was applied for ~1 h to ensure complete transfer of protein to membrane.
6. After transfer, the membrane was incubated in blocking buffer for 30–60 min at RT to prevent spurious antibody binding.
7. Primary antibody (Subheading 2.9) was diluted to desired concentration in 5% nonfat milk in TBS-T blocking buffer, applied to membrane and incubated overnight at 4 °C with rocking.
8. Membrane was rinsed briefly in TBS-T buffer, then wash three times for 5 min each with TBS-T buffer on the shaker to remove unbound antibody.
9. Diluted secondary antibody (see Subheading 2.6) was incubated with membrane for 1–1.5 h at RT with agitation, then washed in TBS-T as described above.
10. Binding was detected using Pierce SuperSignal Weat Pico Chemiluminescent substrate as directed. Briefly, substrate solution is mixed 1:1 ratio, applied to membrane and incubated 1 min. Excess solution is removed by blotting, and membrane is exposed to Kodak BioMax light films (Sigma) in the dark (see Note 18)
11. Film was developed and fixed in Kodak GBX solutions as directed.

3.7. Enzyme-Linked ImmunoSorbent Assay

1. Lyophilized whole bone extract (Subheading 3.2) was suspended in PBS to a final concentration of ~20 mg/mL, and 100 µL was added to ELISA plate wells. One row of wells was reserved to serve as a reference, or "plate blank" by adding only PBS (Fig. 4a). Data from these wells were used to determine background, and subtracted from sample data. Plates were incubated 4 h at RT or overnight at 4 °C. Prior to each incubation, plates were covered with Titer-Top to prevent dehydration.
2. After incubation, sample was removed, and 200 µL 5% BSA blocking buffer was added to each well and incubated for 4 h at RT to reduce spurious or nonspecific binding. Buffer was removed by vigorously shaking the plate repeatedly upside down.

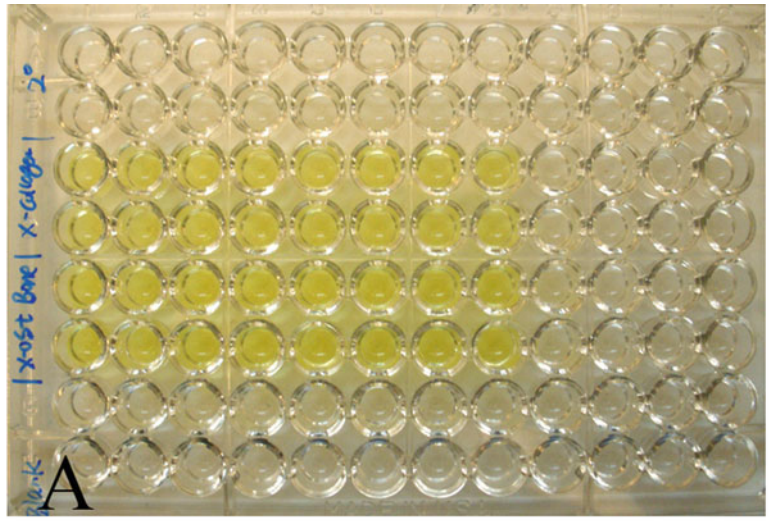

	1	2	3	4	5	6	7	8	9	10	11	12
A	H-1st	H-2nd	H-E...	S-1st	anti-collagen S-2nd	S-ED...	C-1st	C-2nd	C-E...	Ostrich	BL	Blank BL
B	H-1st	H-2nd	H-E...	S-1st	S-2nd	S-ED...	C-1st	C-2nd	C-E...	Ostrich	BL	BL
C	H-1st	H-2nd	H-E...	S-1st	anti-Ostrich S-2nd	S-ED...	C-1st	C-2nd	C-E...	Ostrich	BL	BL
D	H-1st	H-2nd	H-E...	S-1st	S-2nd	S-ED...	C-1st	C-2nd	C-E...	Ostrich	BL	BL
E	H-1st	H-2nd	H-E...	S-1st	anti-osteocalcin S-2nd	S-ED...	C-1st	C-2nd	C-E...	Ostrich	BL	BL
F	H-1st	H-2nd	H-E...	S-1st	S-2nd	S-ED...	C-1st	C-2nd	C-E...	Ostrich	BL	BL
G	H-1st	H-2nd	H-E...	S-1st	2 0 only S-2nd	S-ED...	C-1st	C-2nd	C-E...	Ostrich	BL	BL
H	H-1st	H-2nd	H-E...	S-1st	S-2nd	S-ED...	C-1st	C-2nd	C-E...	Ostrich	BL	BL

B

Fig. 4. Example of enzyme-linked immunosorbant assay (ELISA) conducted on bone extracts. (**a**) Fully developed assay after all incubations shown in 96-well ELISA plate with enzyme detection buffer added. *Yellow* color indicates positive antibody reactivity. (**b**) Absorbance data quantified and displayed with SPECTRA max PLUS plate reader software softMax pro. Labeled boxes correspond to distribution of bone samples in (**b**). The *colored boxes* show numerical quantification of absorbance data. *Higher numbers* correspond to positive antibody binding. The *nonshaded areas* correspond to the "plate blank," and contained no antigen.

3. Primary antibodies were diluted as described in 5% BSA blocking buffer (see Subheading 2.9) and 100 µL were aliquoted to wells, and incubated with antigen overnight at 4 °C.
4. Antibodies were removed as described in (#2), plate vigorously washed 6–10 times in wash buffer (PBS-T), and remaining solution wicked away by turning the plate upside down on paper towels.
5. AP-conjugated secondary antibody (see Subheading 2.7) was diluted 1:2,000 in blocking buffer, and100 µL was incubated with each sample in wells for 4 h at RT.

6. Plates were washed ten times as described above to remove unbound antibody.
7. Antibody binding was detected using enzyme detection buffer, then quantified at 405 nm using a SPECTRA max PLUS plate reader to measure absorbance at 10 min intervals in the first hour then 30 min intervals until completely developed (Fig. 4b).

3.8. IHC of Bone and Vessel Recovered from Fossil Samples

1. Bone matrix from 5% TCA demineralization, or vessels from EDTA demineralized fossil bone fragments (1, 2, 13) were collected, rinsed multiple times in water to remove buffer, then cut into small pieces.
2. Tissues were fixed in fixation buffer for 2 h at RT, (see Note 7), then rinsed two times for 5 min in cold cacodylate buffer.
3. Samples were dehydrated with two changes of 70% ethanol for 30 min each, then equilibrated with a 2:1 mixture of LR White and 70% ethanol infiltration solution for 1 h. After equilibration, samples were infiltrated with three changes of undiluted LR White for 1 h each time.
4. Infiltrated samples were placed in gelatin capsules, capsules filled completely with undiluted L.R. White and tightly capped to exclude air. Samples were allowed to polymerize for 24–48 h at 60 °C. (see Note 19)
5. After polymerization, capsules were removed. Polymerized blocks were trimmed, mounted to Leica EM UC6 *Ultra*-microtome (Fig. 5a–c) and 200 nm sections were taken with a glass or diamond knife (Fig. 5d) and collected on knife boats (Fig. 5e) (14). Wrinkled sections trap antibodies and may lead to false positives. If wrinkling is a persistent problem, wave a wooden applicator saturated with phenol or xylene over the floating section on knife boat. Do not touch the section with the phenol or xylene, or the polymer will melt. Teflon-printed slides were filled with sterile water droplets, and sections collected from boats using a section retrieval loop (14), were floated on water droplets (Fig. 5f). Slides were dried by placing on a hot plate at 50 °C to flatten sections and evaporate water, then oven dried at 45 °C overnight to completion.
6. Prior to exposure to antibody, negative controls were prepared as follows: (1) Secondary antibody only (sections were incubated with blocking buffer instead of primary antibody; all other steps were identical to test samples); (2) selected sections were exposed to digestion by enzymes specific to target antigen (below).
    - Collagen digestion: Sections of demineralized bone were incubated with 1 mg/mL collagenase A (Roche) in D-PBS for 1 h at 37 °C with one change of enzyme to demonstrate antibody specificity.

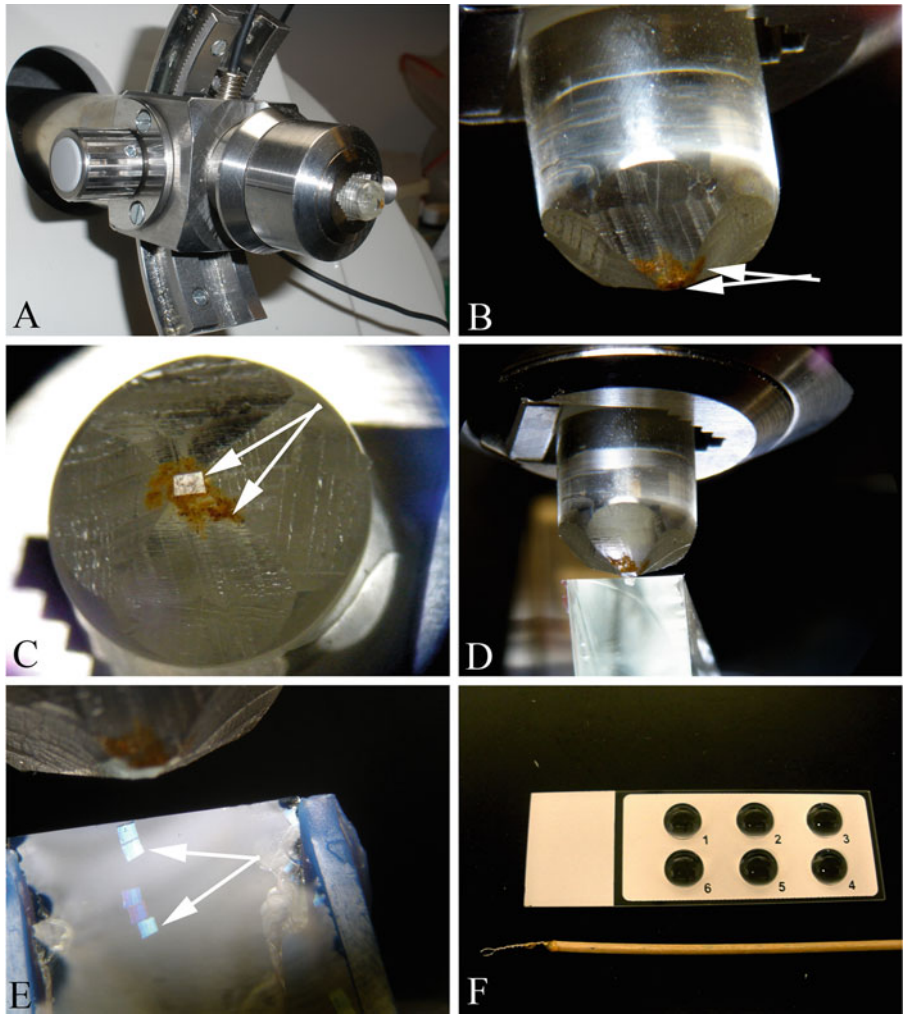

Fig. 5. Procedure for sectioning demineralized fossil samples. (**a**) Polymerized block mounted to the segment arc and inserted into the specimen arm of ultra-microtome. (**b**) Higher magnification of tissues in block; *arrows* show shadow of embedded material. (**c**) Trimmed block, showing tissue on face and deep to cutting surface (*arrows*). (**d**) Block face moving across the cutting surface of glass knife. (**e**) 200 nm sections floating on sterile water in knife boat. (**f**) Teflon-coated 6-well slide with water droplets on which sections are floated, then dried for immunohistochemistry. A specimen loop, used to collect sections from knife boat and apply to water droplets is shown at the *bottom.*

- Elastin digestion: Vessel sections were incubated with elastase (MP Biomedicals, 0.2 mg/mL) in 0.2 M Tris/HCL pH 8.8 for 1 h with one change to remove elastin epitopes without affecting other proteins. Diminished binding demonstrates antibody specificity.

7. All sections (samples and negative controls) were then incubated with proteinase K (25 µg/mL in 1× PBS) antigen retrieval buffer at 37 °C for 15 min to expose antigen.
8. Slides were washed with PBS (pH 7.4) two times for 5 min each in a staining dish.

9. After washing, sections were incubated with 0.5 M EDTA pH 8.0 three times for 10 min each to etch any mineral that might remain adherent to fossil tissues, then washed with PBS-T three times for 5 min each, followed by two 5 min PBS washes.
10. Nonspecific binding of antibodies was prevented by adding 100 μL blocking buffer (4% NGS in PBS) to each well and incubating for 2 h or longer at RT.
11. Excess blocking buffer was removed and 100 μL primary antibody (or antibody dilution buffer for negative controls) at described dilutions (see Subheading 2.9) was incubated with sections overnight at 4 °C.
12. After incubation, sections were washed in PBS-T three times for 5 min each, then PBS two times for 5 min each to remove unbound antibody.
13. Sections were incubated at least 2 h at RT with biotinylated secondary antibody diluted in 4% NGS in PBS (see Subheading 2.8, item 19).
14. Wash sections with PBS-T and PBS as described above (item 12).
15. Fluorescent label (Avidin/FITC) diluted to appropriate concentration, was applied to sections to cover, and incubated with sections for 1 h at RT in the dark, then washed as above in complete darkness (see Note 20)
16. Vectashield H-1000 mounting medium was applied to all sections, and cover slips were added by lowering onto liquid at an angle to reduce air bubbles. Data were integrated and recorded using an Epifluorescence Microscopy (Zeiss Axioskop 2 plus) with professional imaging software from Zeiss.

4. Notes

1. "Water" in this chapter refers to E-pure water with a resistivity of 18.2 MΩ-cm, filter-sterilized using 0.22 μm PES bottle top filter. Unless stated otherwise, all solutions should be prepared in this grade of water. All solutions except HCl and NaOH are filter-sterilized using 0.22 μm PES bottle top filters for each experiment. All pipette tips, micro centrifuge tubes, centrifuge tubes, pipettes, cleaned glassware, containers, graduated cylinder, and dedicated forceps, used in each experiment are either presterilized or autoclaved 30 min at 120 °C in the lab.
2. To make 0.5 M EDTA pH 8.0, add 186.1 g Ethylenediamine tetraacetic acid disodium salt dehydrate (EDTA) (molecular biology, ≥99% Sigma, FW 372.24) to 800 mL water, the disodium salt of EDTA will not go into solution until the pH of the solution approaches 8.0, while stirring, gradually add

20.0 g NaOH, adjust with water to volume 950 mL, continually adjust pH to 8.0 with 6 M NaOH, add water up to 1 L.

3. To make 6 M GuHCl, 0.1 M Tris pH 7.4 extraction buffer, first prepare 0.1 M Tris buffer pH 7.4 buffer by dissolving 12.1 g Trizma base (Sigma, FW 121.14) in 800 mL H_2O, adjust pH to 7.4 with 6.0 M HCl, adjust final volume to 1 L with water. Then dissolve 286.59 g GuHCl (FW 95.53) in 0.1 M Tris buffer pH 7.4 to a final volume of 500 mL.
4. To prepare 1 L 10× PBS pH 6.86 stock solution, dissolve 14.2 g Na_2HPO_4 (F.W. 141.96), 13.8 g NaH_2PO_4 (F.W. 137.99), 75.9 g NaCl and 2.5 g NaOH pellets to 900 mL water, then add 5 M NaOH solution drop by drop to pH 6.86–6.88, adjust to a final volume of 1 L with water.
5. *Thimersol is toxic*. To prepare 5% (w/v) BSA in PBS with 0.005% (v/v) Tween20 and 0.05% (w/v) Thimersol, weight 12.5 g BSA to 200 mL PBS, add 6.25 mL 2% Thimersol and 12.5 μL Tween 20, heat the solution slightly on a stirring hot plate to get the BSA to dissolve. Bring it to a final volume of 250 mL with PBS, filter-sterilize after cooling with a 0.22 μm PES filter, store at 4 °C.
6. 1 M diethanolamine buffer, pH 9.8, 0.5 mM $MgCl_2$: Add 97 mL of diethanolamine (Sigma D8885) and 100 mg magnesium chloride hexahydrate ($MgCl_2 \cdot 6H_2O$ MW203.31) to 800 mL of water, adjust pH to 9.8 with 10 M HCl and bring the volume to 1 L with water.
7. A 4% formaldehyde fixation buffer made from paraformaldehyde in 0.2 M Cacodylate buffer pH 7.4 should be prepared under a fume hood because of the toxicity of the formaldehyde fumes. To prepare 8% formaldehyde solution, dissolve 4 g of paraformaldehyde in 50 mL water heated to 60–70 °C (steaming) with stirring, add drops of 1 M NaOH and stir until clear, cover, and cool to RT (14). To make 4% formaldehyde fixation buffer, mix 8% formaldehyde solution and 0.4 M cacodylate buffer (pH 7.4) in 1:1 ratio and adjust pH to 7.4 with 0.4 M HCl.
8. LR White embedding medium may become milky with the addition of 70% ethanol. To avoid this, slowly add one part of 70% ethanol drop by drop to two parts of L.R. White, and shake gently.
9. This resin is the resin of choice for immunocytochemical procedures because it is an acrylic resin and thus is somewhat water miscible. it is easier to probe LR White-embedded tissues with immunolabels than those embedded in epoxide resin (14).
10. To make D-PBS: Mix 0.2 g of KCl, 0.2 g of KH_2PO_4, 8 g of NaCl, 1.15 g of Na_2HPO_4, 0.1g $CaCl_2$ and 0.1g $MgCl_2.6H_2O$ in water, bring the final volume to 1 L, and adjust the pH to 7.2–7.4 (14).

11. The IR absorption bands of EDTA overlap those of the peptide backbone, therefore it is critical to remove all EDTA remaining associated with sample by multiple washings.
12. The pellet is resuspended either with vigorous vortexing or pipetting up and down to break up the pellet.
13. All samples must be shell frozen to expedite the lyophililzation process. to accomplish this, add desired amount of extract to a sterile glass bottle, place at a slant in a –80 °C freezer to maximize surface area of fluid, and turn the bottle once every 15 min, adjust time depending on the amount of sample, until a water ice shell forms along the sides of the bottle. A thinner layer of frozen materials around the inside of the container improves the efficiency and overall speed of the freeze drying process, prevents breakage of the container, and minimizes molecular damage through rapid freezing.
14. This protocol is provided by Dr. Raghu Kalluri (Harvard University).
15. We tested and compared several buffers; the multiple resuspension buffers listed here were optimal for our samples.
16. Watch gel carefully as the end of the run approaches. If the blue dye front is allowed to run off the gel, smaller fragments of protein that run in advance of the front may be lost.
17. The gel can be kept in fixative for 24–48 h if necessary.
18. Exposure to film: Multiple exposures of 5 s to 1 min should be done to determine optimum exposure time; usually increase or decrease exposure time based on the signal observed in the initial 10 s exposure. Very weak signal requires more exposure time which may be accomplished by leaving the film exposed to the membrane in an x-ray cassette; alternatively, re-run gel with a higher concentration of sample.
19. Residual air will slow or cause incomplete polymerization, so remove as much as possible by filling bottom half of capsule completely and pressing down with top half to tightly seal.
20. Light leakage will photobleach the label, so be sure the incubation chamber is fully protected.

References

1. Schweitzer MH, Wittmeyer JL, Horner JR, Toporski JK (2005) Soft-tissue vessels and cellular preservation in Tyrannosaurus rex. Science 307:1952–1955
2. Schweitzer MH, Wittmeyer JL, Horner JR (2007) Soft tissue and cellular preservation in vertebrate skeletal elements from the Cretaceous to the present. Proc R Soc Lond Ser B Biol Sci 274:183–187
3. Asara JM, Garavelli JS, Slatter DA, Schweitzer MH, Freimark LM, Phillips M, Cantley LC (2007) Interpreting sequences from mastodon and *Tyrannosaurus rex*. Science 317:1324–1325
4. Vass AA, Barshick SA, Sega G, Caton J, Skeen JT, Love JC, Synstelien JA (2002) Decomposition chemistry of human remains: a new methodology for determining the postmortem interval. J Forensic Sci 47:542–553

5. Lindahl T (1993) Recovery of antediluvian DNA. Nature 365:700. doi:0.1038/365700a
6. Hoss M (2000) Neanderthal population genetics. Nature 404:453–454. doi:0.1038/35006551
7. Eglinton G, Logan GA (1991) Molecular preservation. Philos Trans R Soc Lond Ser B 333:315–328
8. Bada JL, Wang XYS, Hamilton H (1999) Preservation of key biomolecules in the fossil record: current knowledge and future challenges. Philos Trans R Soc Lond Ser B 354:77–86
9. Briggs DEG, Evershed RP, Lockheart MJ (2000) The biomolecular paleontology of continental fossils. Paleobiology 26:169–193
10. Briggs DEG (2003) The role of decay and mineralization in the preservation of soft-bodied fossils. Annu Rev Earth Planet Sci 31:275
11. Stankiewicz BA, Briggs DEG, Michels R, Collinson ME, Flannery MB, Evershed RP (2000) Alternative origin of aliphatic polymer in kerogen. Geology 28:559–562
12. BioRad Trans-Blot SD Semi-Dry Electrophorectic Cell Instruction Manual Catalog number 170-3940
13. Schweitzer MH, Suo Z, Avci R, Asara JM, Allen MA, Teran Arce F, Horner JR (2007) Analyses of soft tissue from Tyrannosaurus rex suggest the presence of protein. Science 316:277–280
14. Dykstra MJ, Reuss LE (2003) Biological electron microscopy theory, techniques and troubleshooting, 2nd edn. Kluwer Academic/Plenum Publishers, New York
15. Schweitzer MH, Zheng W, Organ CL, Avci R, Suo Z, Freimark LM, Lebleu VS, Duncan MB, Vander Heiden MG, Neveu JM, Lane WS, Cottrell JS, Horner JR, Cantley LC, Kalluri R, Asara JM (2009) Biomolecular characterization and protein sequences of the Campanian hadrosaur *B. canadensis*. Science 324:626–631

Chapter 11

Identifying Postmortem Microstructural Change to Skeletal and Dental Tissues using Backscattered Electron Imaging

Lynne S. Bell

Abstract

A number of papers have been published over a 100 year period describing postmortem microstructural change to bone and teeth in humans and other mammals. Much of the work is descriptive and has used a number of microscopic methods, which introduce changes during preparation, and are limited by the resolving power of that technique. Backscattered electron imaging in a scanning electron microscope (BSE/SEM) has been used successfully applied to on normal skeletal tissues and is an excellent method to document postmortem changes to bone and tooth microstructure. In forensic science, archaeology, and paleontology there is a collective interest in understanding early death history and subsequent treatment and deposition of the body. To this end the main microstructural changes are provided as a means of identification, and practical suggestions to circumvent misinterpretation due to artifacts created by employing the BSE imaging method.

Key words: Taphonomic, Forensic, Post Mortem, Diagenesis, Microstructure, Bone, Dentine, Enamel, Backscattered Electron Imaging

1. Introduction

Microstructural change to skeletal tissues has been documented in human and mammal skeletal tissues in forensic and archaeological contexts. These changes are observable at the micron scale and can be highly localized, or alternatively extensively distributed throughout the affected tissues. The causative agents that create such changes are not specifically known, but generally are ascribed to bacterial, fungal, and marine-based organisms. The observed types of change are specific and have been associated with terrestrial, marine, and lacustrine environments. The importance of identifying and documenting postmortem microstructural change to skeletal tissue is because it represents both a serious form of

Lynne S. Bell (ed.), *Forensic Microscopy for Skeletal Tissues: Methods and Protocols*, Methods in Molecular Biology, vol. 915,
DOI 10.1007/978-1-61779-977-8_11,

contamination for other analytic protocols, and it represents an important source of taphonomic information that can give insight into the perimortem and postmortem history of the body.

The changes themselves alter tissues by removing, adding, and/or reorganizing the affected tissues. The type of tissue: bone, dentine, cementum, and enamel have differing structural organizations and are differentially composed of mineral and organic. The organization and the composite nature of the tissue can affect the distribution of the invading postmortem change, and this adds to the complexity of identifying and understanding the driving mechanisms behind them. This complexity has been added to by the types of technology used to observe these changes at the microscopic level. The changes themselves were observed as early as 1864 (1) and many of the studies that followed, often curiosity-driven, utilized light microscopy. These may have been stained or unstained sections between 50 and 100 μm thickness, either decalcified and wax embedded or untreated. Depending on the method of preparation, the observed postmortem change to tissue appeared to be different partly as an outcome of the preparation itself, and because of the causal taphonomic agent. Another problem with light microscopy is the upper end of resolution being low and the compounded problem of light scattering throughout the section. Backscattered electron imaging in a scanning electron microscope (BSE/SEM) has proven to be an effective tool for documenting postmortem microstructural change (2, 3). It has increased resolution over ordinary light microscopy and avoids compressed information from light scattering and resultant blurring of features. The BSE/SEM block itself remains intact, with no chemical pretreatment of the sample prior to embedding, and the mineral and organic changes that occur as an outcome of diagenetic change may be viewed directly using this method. This form of imaging has performed well with the full range of normal skeletal tissues (4), and has been particularly useful to document postmortem alteration, otherwise known as diagenesis.

2. Morphological Method for Identification of Postmortem Microstructural Change to Bone, Enamel, and Dentine

2.1. Image Contrast

The principle behind BSE imaging and its application as an imaging tool in electron microscopy has been described in this volume by Jones. Its application to the skeletal tissues was first described by Jones and Boyde (4, 5), and its application was extended to detailing normal bone and tooth microstructure and bony pathological change (6, 7). Other than tooth enamel, which is almost entirely mineral, the other skeletal tissues are composite tissues, composed of both mineral (imperfect hydroxyapatite) and organic (mostly Type I collagen and smaller proteins). Whilst BSE imaging has

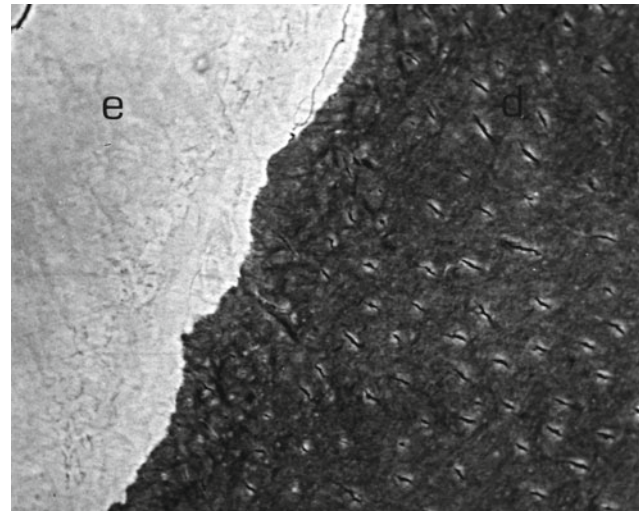

Fig. 1. Characteristic density image and morphology of enamel (e) seen as near white, and dentine, seen as less dense and so darker relative to enamel tissue. BSE/SEM image field width (FW) 180 μm.

been used as a means to demonstrate atomic number differences between say metallic materials, in the skeletal tissues, backscattering provides information on bulk density but the signal is also affected by the tissue arrangement. Hence tooth enamel, being almost entirely mineral with tight mineral packing returns a larger number of backscattered electrons and appears almost white (Fig. 1). Whilst bone and dentine have greater porosity with less mineral and more organic than enamel, they have reduced backscattering and the resultant image contrast is reduced and image appears grey (Figs. 1, 2, and 3). BSE/SEM imaging of skeletal tissues cannot be used to quantitate atomic number as it is applied to polished metals, but with biological tissue, here skeletal tissues, it provides a qualitative indication of bulk density composition.

Postmortem microstructural change or diagenetic change alters both the tissue arrangement and can either increase or decrease the local packing density of mineral. Other extraneous minerals may be added into the changed tissue milieu, which will alter both the bulk density localized to the focal area affected, as well as the number of backscattered electrons that exit the block face. This dual affect on fast electron scattering is the main reason why BSE/SEM imaging is more powerful as a method to detect postmortem microstructural change, than it is to ascribe atomic number compositional meaning to areas of changed contrast. Similarly if there is no tissue at all, a hole, then this will show as a black area, since no backscattering is occurring at that location. In bone and dentine there are natural holes where the cellular and vascular tissues were once situated antemortem, and are integral to identifying that tissue. However, postmortem alteration introduces

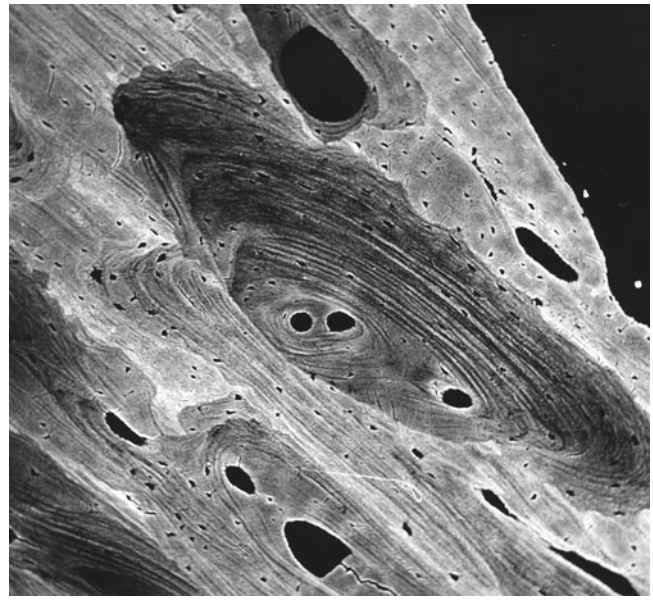

Fig. 2. Bone from cranial vault of 12-year-old girl. Relatively younger bone can be seen center field relative to older osteonal systems, and interstitial lamellae which appear relatively brighter. BSE/SEM image FW 855 μm.

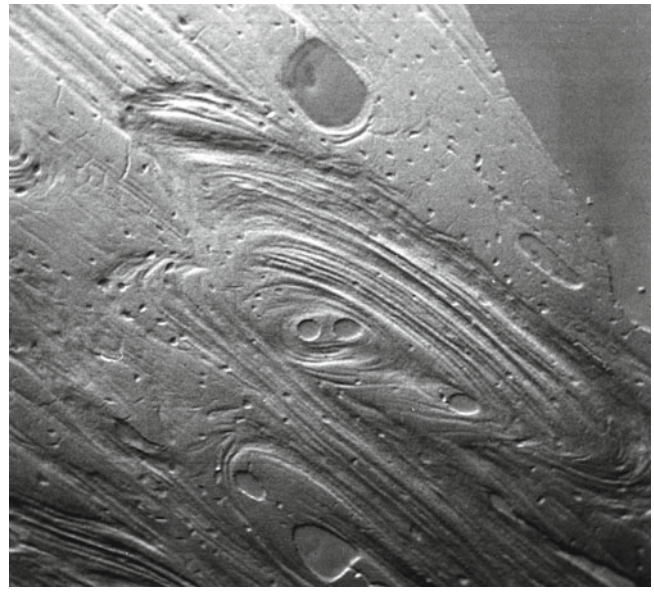

Fig. 3. Topographic image of same field as Fig. 11.1, with the east and west quadrants of detector subtracted. Polishing artifacts create edges (edge artifacts) caused by the differential hardness and orientation of collagen to the block face. BSE/SEM image FW 855 μm.

a number of other holes of varying dimensions, and these too help identify that postmortem alteration has occurred. The morphology of such changes helps to identify that particular type of postmortem alteration as it alters the morphology of that tissue, and also its full extent and distribution may be mapped within the sample using this imaging method.

2.2. Identifying Bacterial Change in Bone

Before beginning to identify postmortem change to skeletal tissues it is important that the normal appearance of the tissue is fully understood. In skeletal tissues we are dealing with bone, enamel, dentine, and cementum (see Note 1). Additionally, due to the developmental nature of these tissues, occasionally calcified cartilage (Fig. 4) or mineralized osteocytes (Fig. 5) may be included within normal tissue (see Note 2). Similarly, pathological change to bony development or normal bone turnover can dramatically alter the normal morphological and mineral density appearance of that tissue.

The normal appearance of bone depends on the orientation of the section. Usually sections are viewed in their transverse orientation. Human bone has a characteristic arrangement of cylindrical structures known as osteons. These osteons develop at different times and remain in the tissue until they are remodeled out. This can take a period of 15–18 years (8), and this means that many osteonal systems will exist side-by-side. Older osteonal systems will have more mineral per unit volume, and will appear more dense than systems which are relatively younger. The density range for human tissue is 1.6–2.4 g/cm^3 (8). Each osteonal system is created in layers known as lamellae and within each lamellae are osteocyte lacunae, themselves interconnected to a network of osteocyte

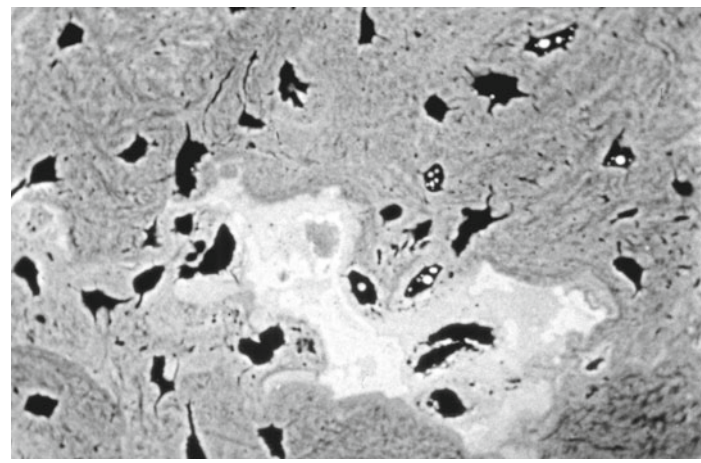

Fig. 4. Calcified cartilage is seen as a high density tissue within bone and is an outcome of normal bone development where cartilage is not remodeled out and replaced with bone. BSE/SEM image FW 180 μm.

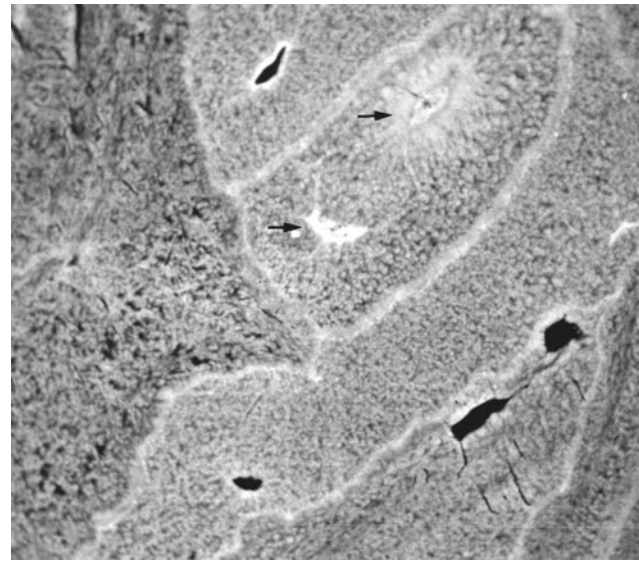

Fig. 5. Two mineralized osteocytes (see *arrows*) situated in a small interstitial bone packet from the fourth rib of a 91-year-old male. This is a typical location for mineralized osteocytes to occur in bone i.e., in groups and in older osteonal relic bone. BSE/SEM image FW 50 μm.

lacunae via osteocytic canaliculae (Fig. 2). As new systems are remodeled in to make new bone, older systems are partially removed. Hence, osteonal systems are often bisected sometimes multiple times by later forming systems.

When assessing density changes to the BSE signal from any BSE/SEM image it is important to inspect the topography of the surface of the block face at that field. This is done by turning two quadrants in the BSE detector off to create a pseudo topographic image (Fig. 3) (see Note 3). Given that bone has a mixture of densities due to its normal maturation, and that the orientation of collagen fibrils changes direction within individual osteonal systems, then some topography is inevitable. However, too much topography will create "edge artifacts" which cause more electrons to escape at that edge creating the erroneous appearance of increased density.

Bacterial change to bone creates a general disruption to bony microstructure and alters mineral density in both directions. BSE/SEM is well suited to detecting this type of change (see Note 4), and can resolve image quality to below 1 μm. Bacterial change is affected by the orientation of the bony tissue itself, but this can be hard to see when large amounts of bone are affected (Fig. 6). Because this type of change alters the net density of affected tissue locally, it is important to check for topography on the block face as detailed before. The edges of bacterially changed foci can cause an edge artifact as a result of polishing, causing the rim to become brighter (Fig. 7). The foci is providing a clear boundary, and hence

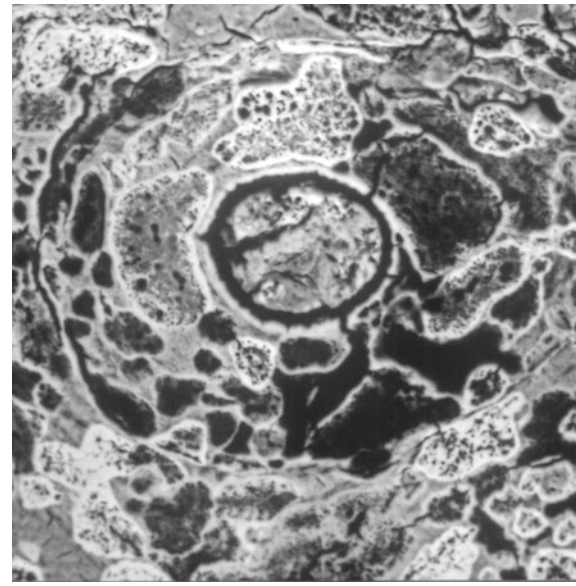

Fig. 6. Transverse section (TS) of midshaft archaeological tibia. A single osteon is enclosed and surrounded by bacterial diagenetic alteration. The diagenetic foci are seen as high and low density focal areas that track gross collagen direction. Individual osteocyte lacunae can also be seen within these diagenetic foci. Small areas of recognizable bone are seen as light grey within a largely changed area of bone. BSE/SEM image FW 185 μm.

Fig. 7. Topographic image of Fig. 6. Polishing artifacts have caused surface relief and can be seen to cause edge artifacts. Edge artifacts cause a net increase in BSEs leaving block face at those areas which cause a brightness. However, diagenetic foci have altered densities both above and below normal bone density and this too contributes to differential polishing. BSE/BSE image FW 185 μm.

the edge, but there an increase in density. However, local increases in density are a feature of this type of change and many foci of varying sizes will be evident within individual osteonal systems and will exhibit real high density increase, usually at the boundaries of individual foci (Figs. 6 and 8). There are also areas that return no signal and appear black, and are essentially holes within the bone created by the bacterial ingress (Fig. 8). Another feature is the cement line on the most external aspect of an osteon appears to limit some of the bacterial foci (Fig. 9), but this is not always the

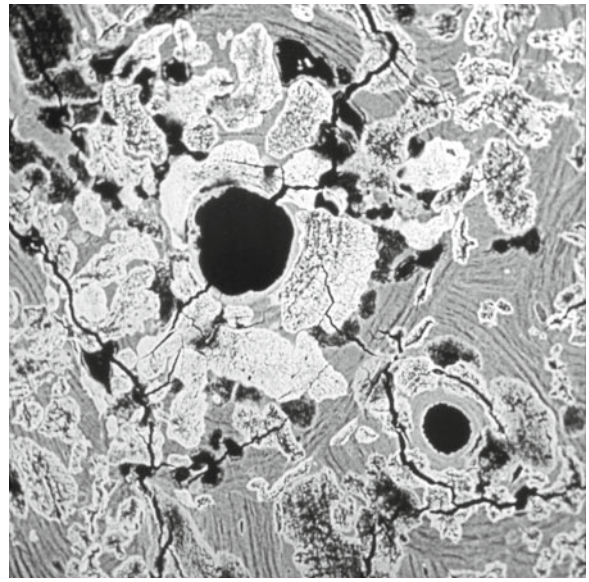

Fig. 8. TS anterior midshaft archaeological tibia. A number of high density foci are seen within this single secondary osteonal system. Internal to these high density foci are small 1 μm diametered holes. BSE/SEM image FW 300 μm.

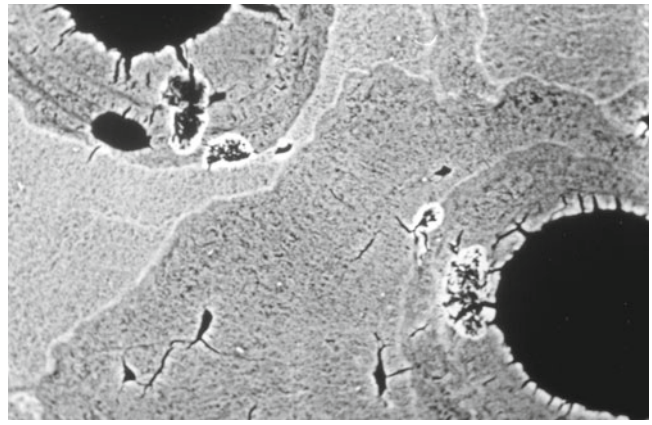

Fig. 9. Bacterial-type foci seen spreading from Haversian canal to associated osteocyte lacuna. Other foci extend to the cement line boundary and are seen either as high density foci or as areas of black indicating virtually an empty space where bone has been removed. BSE/SEM image FW 270 μm.

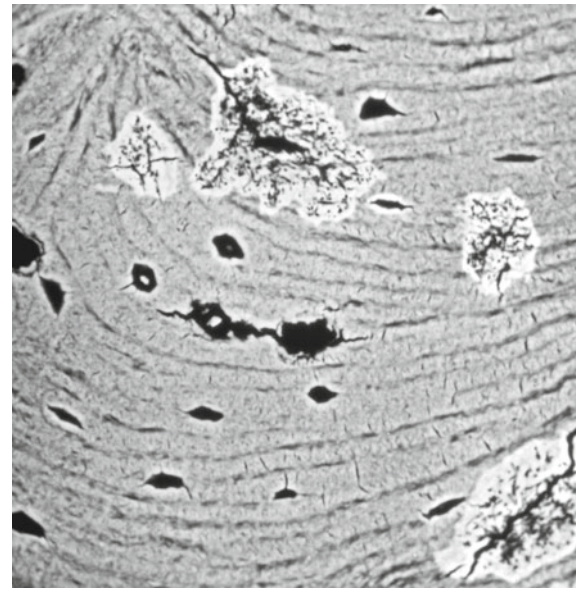

Fig. 10. Bacterial ingress seen extending from a single osteocyte lacuna. Other osteocytes exhibit demineralization boundaries or enlargement. This is typical of early stage spread of this common bacterial change to bone. BSE/SEM image FW 120 μm.

case, particularly when bacterial ingress is widespread. Looking for early changes helps to understand the driving distribution of this change and why it is connected to the postmortem vasculature and osteocytic cell spaces of bone. Initial foci are often seen on single osteocyte lacunae either connecting across from the Haversian canal, or focused on individual osteocyte lacunae, with corresponding increase in density associated with small 1 μm-sized pores at the center of these foci (Fig. 10). These higher density foci may coalesce to form a larger block of affected tissue, infact, bony tissue is largely replaced, but even in these areas, intact bone is often detectable interstitially between bacterial foci (Fig. 11) (see Note 5).

Most publications will report transverse sectional information on bony change. However, a longitudinal section of bacterial change reveals more information on the nature of this type of postmortem change (Fig. 12). Bacterial foci in longitudinal section show how the foci stream with the cylindrical arrangement of the osteons, revealing that individual foci can have considerable depth or by extension volume. Another feature that is common with this type of postmortem change is that the external circumferential lamellae are often intact and unaffected (Fig. 12). Bacterial change may be easily identified in longitudinal section.

2.3. Identifying Bacterial Change in Dental Tissues

Enamel is not affected by postmortem bacterial alteration in the same way as bone and dentine. Enamel is almost entirely mineral and unlike bone and dentine, has no vascular supply. Once erupted into the living mouth it is effectively a dead tissue. However, it can

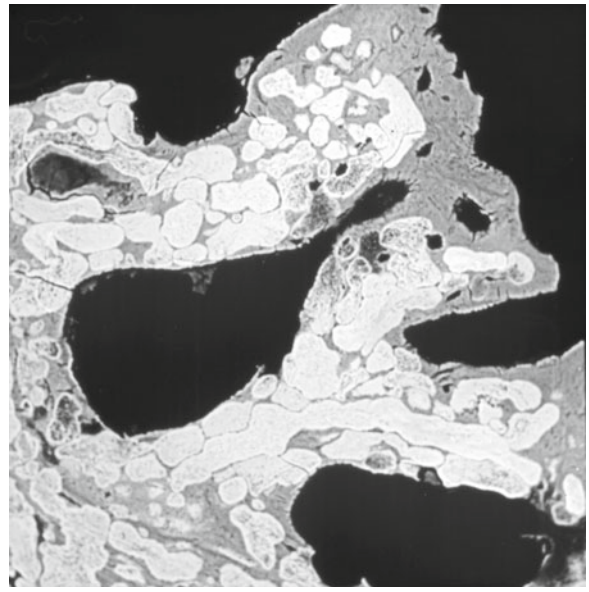

Fig. 11. TS anterior midshaft femur archaeological bone. Primary osteonal bone forming in adult bone, seen as periostitis macroscopically. Many high density bacterial foci are seen streaming through this new bone. SEM/BSE image FW 300 μm.

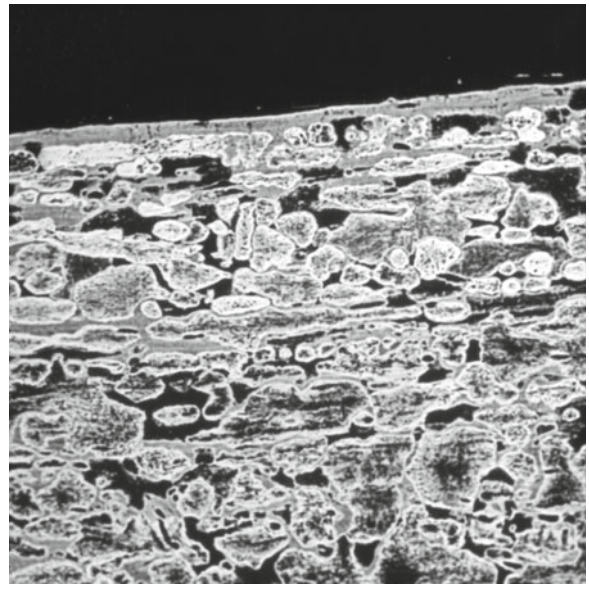

Fig. 12. Longitudinal section (LS) of anterior midshaft archaeological femur. Extensive bacterial diagenetic change which stream with the long axis of osteonal systems. Foci are seen to elongate in this axis creating larger areas of changed bone volumetrically. Information on diagenetic foci may be extended viewing the LS. BSE/SEM image FW 325 μm.

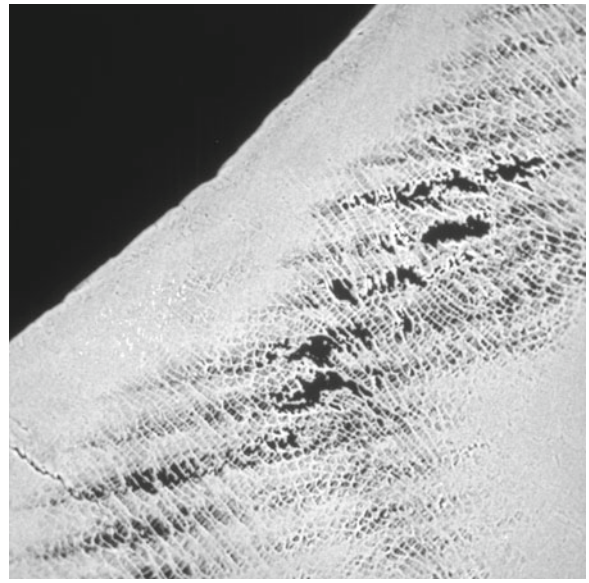

Fig. 13. White spot lesion to enamel in a maxillary canine. Funneling demineralization evident and etching-up of the enamel prisms (or rods). Micro-cavitation evident, but typical of this type of lesion is the remineralized outer surface of enamel. This type of caries is a antemortem event. BSE/SEM image FW 430 μm.

be affected by bacterially driven caries, and this may be seen as cavities, fissure caries, or white spot lesions macroscopically. The main way to determine if the change observed is microscopically caused by an in vivo caries, is to look at the distribution of the lesion (see Note 6). A carious focal lesion is the classic in vivo microscopic morphology, where a demineralization and remineralization can be seen together, usually with micro-cavitation (Fig. 13). One feature that is common in white spot caries is that the outer boundary of the lesion, which connects directly to the mouth, remineralizes, and although the enamel has changed, it provides a functional barrier. However, the micro-cavitation beneath represents an obvious subsurface weakness (Fig. 13). As a recap, to distinguish antemortem bacterially driven change from postmortem change, the external distribution of the destructive foci is the key.

Dentine is compositionally almost identical to bone, but has a very different tissue organization. The BSE/SEM density grey level for dentine is therefore almost the same as bone (Fig. 14). The tissue is permeated by a porous structure called dentine tubules, and surrounding those tubules is an area of mineral which increases density and so BSE contrast at the tubule boundaries, and this is known as peritubular dentine (see Note 7). In the area of coronal dentine larger cavities known as interglobular dentine, may be seen usually in groups and are normal areas of once unmineralized dentine, and in skeletonized remains these are seen as empty cavities, seen as black in BSE imaging, in skeletonized tissue (Fig. 14) (see Note 8).

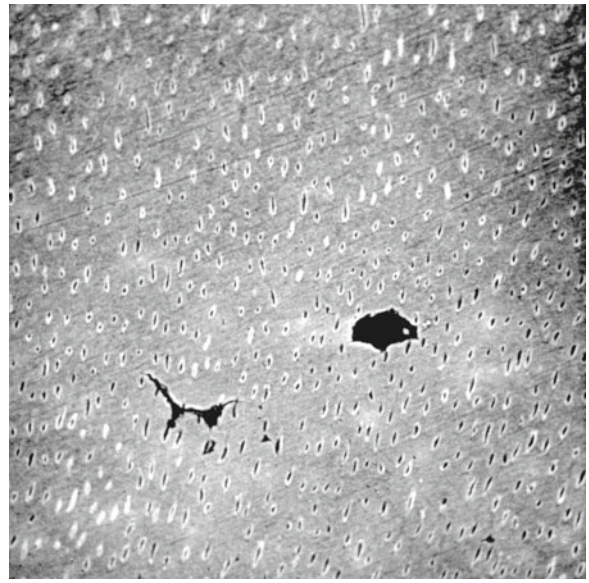

Fig. 14. Area of interglobular dentine in the coronal area of dentine in a maxillary canine. This is a normal and often common microstructural feature of dentine and forensically will present as an empty space as seen here. However, it represents an area of unmineralized dentine, which, during decomposition disappears to render a void. This has a very characteristic appearance and should not be confused with diagenetic alteration. BSE/SEM image FW 170 μm.

Dentine may also be affected by antemortem caries and this can be seen in relation to a leaky filling, more commonly at the neck of the tooth, or lower, as gingival recession increases. As with enamel, noting the location of the bacterial alteration will inform on whether a lesion was created antemortem or postmortem.

Postmortem bacterial ingress is distinct in its distribution from the antemortem described above. It is seen extending from the root apex and outwards from the entire pulpal aspect. Initial foci will track at right angles to the peritubular dentine direction following the intertubular branching network, and producing large streaming holes (Fig. 15). This behavior is identical to the early bacterial diagenetic distribution in bone, where the osteocytic network is utilized to spread throughout the bone tissue. Similar enlarged bacterial foci can also be seen affecting dentine which look very similar to those seen in bone (Fig. 16). As with bone the remineralized foci are permeated by small 1 μm diameter sized holes. Again, this is associated with postmortem bacterial-type ingress.

2.4. Marine and Lacustrine Exposure

This type of change is highly distinctive and can be easily identified using BSE/SEM imaging. The change is characterized by tunnels and originates on the external aspect of the affected tissue, and is unaffected by the tissue organization. The tunnels may have diameters of 5–7 μm (Fig. 17), and importantly have a clean free-edge with

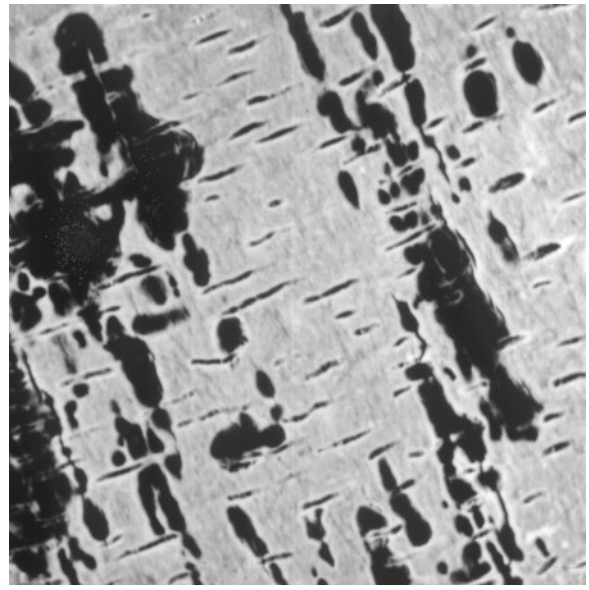

Fig. 15. Diagenetic bacterial ingress is seen streaming through apical dentine at right angles to dentine tubular direction, causing a demineralization and removal of the mineral/organic fraction of dentine. The orientation of ingress tracks the intertubular dentinal branching network. This is identical behavior to that seen in bone, where the osteocytic network is similarly utilized. BSE/SEM image FW 430 μm.

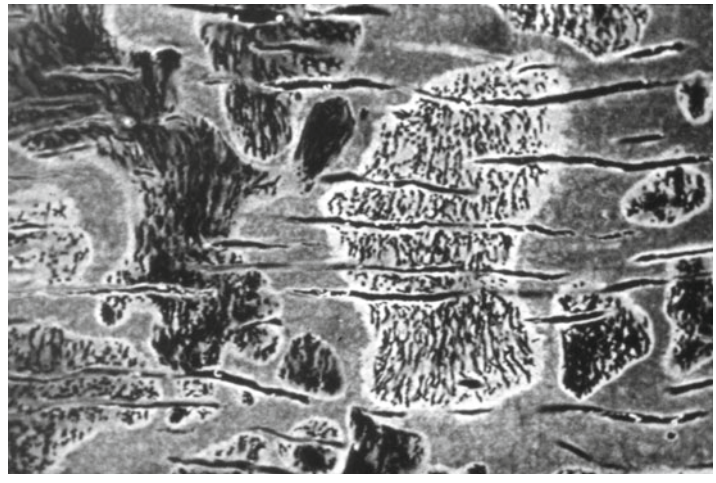

Fig. 16. The remineralized and increased density bacterial foci may also be seen in dentine. Similar bacterial foci with increased density, permeated with small 1 μm-sized holes. Other diagenetic foci have similar morphology, but have attained a lower density. These foci track the intertubular dentinal branching network. The peritubular dentine is largely preserved. BSE/SEM image FW 170 μm.

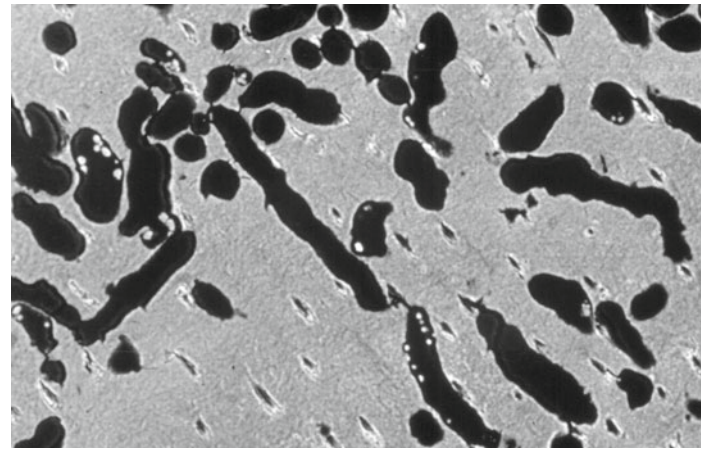

Fig. 17. Marine type change sea in shallow and intertidal contexts. Invading tubules seen here in dentine, although all tissues excepting enamel may be affected, extend from the external aspect of the tooth inwards. Tubule diameter may vary, here 5–7 μm, depending on the invading organism. What is characteristic of this type of postmortem change is there is no demineralization or remineralization boundary present at the tubule boundaries. BSE/SEM image FW 200 μm.

no evidence of demineralization or remineralization (see Note 9). However, it is possible to have a number of larger tubules, than the one described here and is dependent on the microorganism responsible. What is common however, is the distribution is always initially external and peripheral, tunneling to varying depths within the affected tissue. This distribution has been seen in relation to marine exposure (9) and more recently in a single lacustrine context (10). In bone this distribution is clearly demarcated (Fig. 18). Similarly in dentine the exposed surface of the dentine will be tunneled and this can extend under the enamel from the neck, tracking against but not into the enamel dentine junction (Fig. 19). Some use is made of the peritubular network, but the distribution seems to be otherwise little affected by the invader. What is important to note with this type of change, is that the enamel is never affected. Or rather, has not to date, been documented as affected. Whilst this is not understood, it reflects on the nature of the tunnel formation, the mechanism of which remains unknown, since no low pH tissue remineralization has been detected.

2.5. Terrestrial Exposure

This change can only be detected using microscopy. It is a post skeletonization event and is the result of terrestrial surface exposure. It has a peripheral distribution and extends approximately 50–100 μm into bone (Figs. 20 and 21). It is seen as a dark band in bone, which indicates a diffuse loss of density, but the composition of the affected tissue is unknown. Morphologically it is a distinct change, which can lead to partial delamination and micro-cracking of bone (see Note 10).

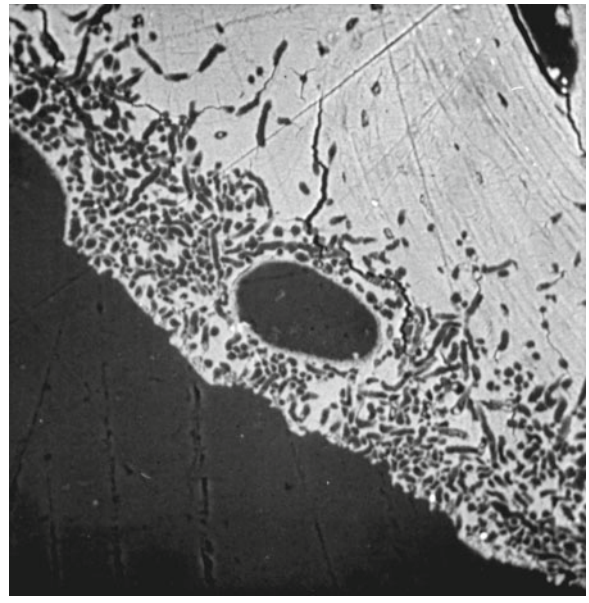

Fig. 18. Identical postmortem ingress of marine microorganism with identical tubule diameter and peripheral distribution. Confocal image FW 500 μm.

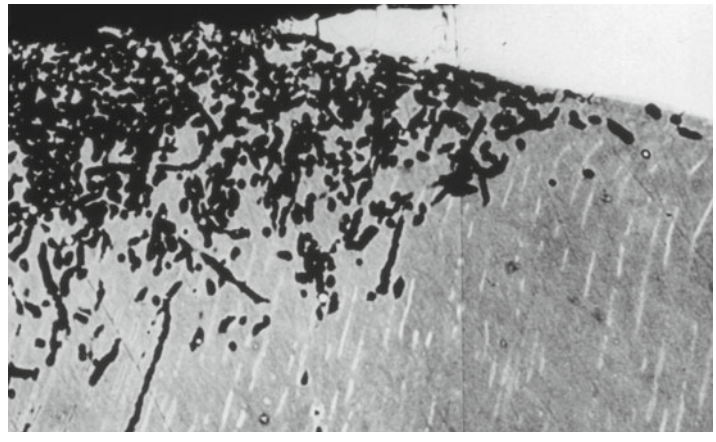

Fig. 19. Marine microorganism invasion of dentine which has undermined enamel for a short distance. To date, enamel has not been observed affected by this type of postmortem change. Tunnels do not appear to have a clear orientation as seen with bacterial-type change. The most characteristic morphology is the distribution extending from the external aspect inwards. Tunnel diameters are highly constrained. BSE/SEM image FW 430 μm.

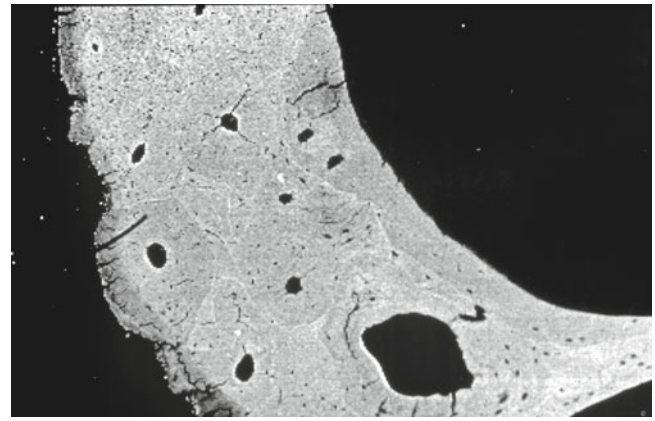

Fig. 20. Terrestrial exposural change seen as a slight band of demineralization to the external aspect of bone. The demineralized band is consistent in depth and cannot be seen with ordinary light microscopy. BSE/SEM image FW 2,000 μm.

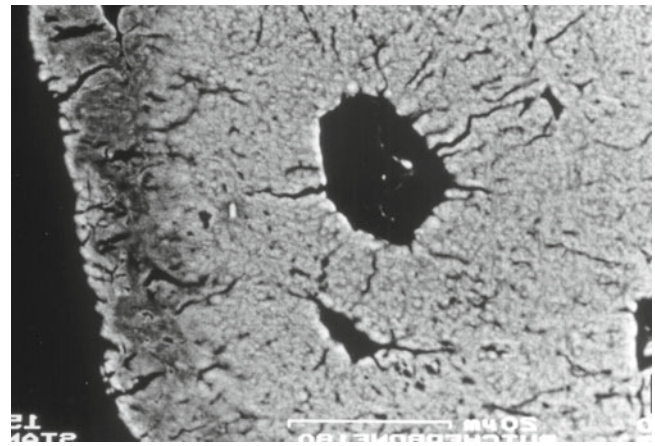

Fig. 21. Higher power image of Fig. 20 showing intact bone beneath this band of demineralization. BSE/SEM image FW 425 μm.

3. Final Remarks

From a forensic and taphonomic standpoint postmortem microstructural change to the skeletal and dental tissues provides important information regarding decomposition history and body deposition. One of the difficulties in making a clear assessment and classifying this type of alteration is the type of microscopy used and the preparation method itself. The utility of BSE/SEM imaging provides a method whereby tissue may be embedded with little or no pretreatment, it has excellent resolving power, and provides information on micromorphological change and associated density for the skeletal and dental tissues.

4. Notes

1. Dental calculus is technically an invasive composite accretion of mostly mineralized bacteria found on teeth within the living mouth. In this regard it is different to postmortem, or bacterially derived caries, whilst sharing near identical behavior to postmortem invasion of teeth, has a specific distribution which is distinct to postmortem invasion. This is a real complexity, but easily differentiated by discerning the distribution of these antemortem carious lesions to the distribution of postmortem change. Basically the antemortem distribution of caries is different to postmortem. Antemortem caries is focal, whilst postmortem caries-like lesions are more diffuse and spread across a larger part of enamel surface of the tooth.
2. Calcified cartilage may be identified as being included within normal bone. It has a characteristic high density appearance and its edges are usually characterized by osteoclastic resorption lacunae formed by cartilage being remodeled out during normal bone turnover. Calcified cartilage may be seen at any location in the skeleton (Fig. 4). Mineralized osteocytes are associated with normal bone turnover also, but seen usually in mature adult bone in the interstitial lamellae, representing the oldest bone packets. These mineralized osteocytes have a characteristic appearance and may be identified using BSE/SEM imaging and they are often seen in groups (11) (Fig. 5).
3. There are other ways to create a surface image in an SEM and this might involve mixing the signal from the secondary electron (SE) detector with the BSE detector signal.
4. Light microscopy, unless it is confocal, provides a poor image of bacterially derived postmortem alteration. This is caused by light scattering and internal reflection causes a general blurring of structures. This can be overcome to some degree by using directional light, circularly polarized light is a better choice, but there is still a problem with internal reflection and the resultant degrading of the image.
5. It is important to check large areas of increased density for topography to rule out possible edge artifact.
6. Postmortem change to enamel will be seen as looking similar to in vivo caries, but its distribution is different. Poole and Tratman (12) reported demineralization to human enamel tissue which extended over the entire surface. This type of distribution is not seen in the living mouth. The microbial agent for this remains unknown, but for mineral to be affected local pH must fall below pH 4 for demineralization to begin.

7. Over polishing can cause an edge artifact and this will mimic peritubular mineral. This can be determined by checking the surface topography of the block face as previously described.
8. Certain pathological conditions such as childhood Rickets, cause faulty mineralization of the dentine and results in large amounts of coronal inter-globular dentine. When large amounts are detected a pathological cause should be considered.
9. Confocal microscopy has demonstrated that these tunnels bifurcate. It is recommended that inspection of an uncoated block be made prior to BSE/SEM imaging, when dealing with this type of change. A recent study by Wissak (13), demonstrated that many different diameters of tunnels may be created by differing marine microorganism, and bifurcation, along with tubule diameter is an important classifier.
10. This type of change is hard to detect using normal transmission light microscopy.

References

1. Wedl C (1864) Uber einen im Zahnbein und Knochen keimenden Pilz. Akademie der Wissenschaften in Wien. Sitzungsberichte Naturwissenschaftliche Klasse ABI. Mineralogie, Biologi Erdkunde 50:171–193
2. Bell LS, Skinner MF, Jones SJ (1996) The speed of post mortem change to the human skeleton and its taphonomic significance. Foren Sci Int 82(129):140
3. Bell LS, Boyde A, Jones SJ (1991) Diagenetic alteration to teeth in situ illustrated by backscattered electron imaging. Scanning 13:173–183
4. Boyde A, Jones SJ (1983) Backscattered electron imaging of skeletal tissues. Metab Bone Dis Relat 5:145–150
5. Boyde A, Jones SJ (1983) Backscattered electron imaging of dental tissues. Anat Embryol 168:211–226
6. Jones SJ, Boyde A (1987) Scanning microscopic observations on dental caries. Scanning Microscopy 1:1991–2002
7. Bell LS, Jones SJ (1991) Macroscopic and microscopic evaluation of archaeological bone: backscattered electron imaging of putative pagetic bone. Int J Osteoarchaeol 1:179–184
8. Bell LS, Cox G, Sealy JC (2001) Determining life history trajectories using bone density fractionation and stable light isotope analysis: a new approach. Am J Phys Anthropol 116:66–79
9. Bell LS, Elkerton A (2008) Human remains recovered from a sixteenth century mass fatality: unique marine taphonomy in human skeletal material from the medieval warship the Mary Rose. Int J Osteoarchaeol 18:523–535
10. Pesquero MD, Ascaso C, Alcala L, Fernandez-Jalvo Y (2010) A new taphonomic bioerosion in a Miocene lakeshore environment. Palaeogeogr Palaeocl 295:192–198
11. Bell LS, Kayser M, Jones C (2008) The mineralized osteocyte: a living fossil. Am J Phys Anthropol 137:449–456
12. Poole DFG, Tratman EK (1978) Post mortem changes on human teeth from late upper palaeolithic/mesolithic occupants of an English limestone cave. Arch Oral Biol 23:1115–1120
13. Wisshak M, Gettidis M, Freiwald A, Lundalv T (2005) Bioerosion along a bathymetric gradient in a cold-water temperate setting (Kosterfjord, SW Sweden): an experimental study. Facies 51:93–117

Chapter 12

How to Approach Perimortem Injury and Other Modifications

Peter Andrews and Yolanda Fernández-Jalvo

Abstract

Perimortem damage recorded on bone indicates the immediate processes affecting animals or humans at or near the time of death. In many cases the agents producing the modifications may be identified based on modern comparative studies. Perimortem alterations or injuries may occur as a result of human action, the subject of forensic studies, and it is clearly important to distinguish these from other taphonomic processes and agents. We describe those modifications occurring at the time of death, including linear marks, pits and perforations, rounding of ends of bones, cracking of bone tissues, digestion, discoloration and staining, breakage and fragmentation, and disarticulation, with added notes about later occurring modifications that mimic the perimortem modifications.

Key words: Taphonomic process, Taphonomic agent, Perimortem, Mammals, Humans, Vertebrates

1. Introduction

There are many potential causes for the presence of vertebrates, including humans, at a fossil site. The study of the bone surface modifications lets us know why and how these individuals died and why they were accumulated in that site. This has many aspects, from processes affecting individual organisms to those affecting whole communities, but here we will be considering only the perimortem effects, meaning those occurring at or near the time of death, and the agents that produce them. Process is defined as the action of a taphonomic agent (1), the agent being the immediate cause of modifications. The evidence by which process is identified is the effect it has, the biological, chemical, and physical modifications on fossil bones, but these modifications can better be identified and interpreted by comparisons with observed processes produced by known agents acting on previously unmodified bones at the present time.

Lynne S. Bell (ed.), *Forensic Microscopy for Skeletal Tissues: Methods and Protocols*, Methods in Molecular Biology, vol. 915,
DOI 10.1007/978-1-61779-977-8_12,

There is a large literature on vertebrate taphonomy, well described and summarized by Lyman (1) and see references therein; Shipman (2), Brain (3), and Binford (4). An important link between forensic studies and taphonomy has been established through the edition of two books by Haglund and Sorg (5, 6). This is an interesting connection as taphonomy, like forensic studies, investigates evidence of both biotic and abiotic causes of death. This includes site formation, what Haglund and Sorg (5) refer to in forensic literature as the scene reconstruction. Taphonomy extends research to investigate environmental factors during the history of the past that gave rise to fossils as well as trace fossils which are signs of activity of past organisms such as footprints and coprolites. Such information is the basis of taphonomic research (see Note 1).

2. Methods for Identifying Perimortem Modifications on Bone

Perimortem processes are those acting at or near the time of death. These processes act both before and after skeletonisation, such as butchering or predation before and diagenetic changes to skeletal remains soon after death. Perimortem processes may be inorganic, resulting from sediment movement or rock falls, or organic, resulting from animal action (including humans), and both the context and the bone surface modifications provide the evidence by which these processes may be distinguished. Modifications produced by these processes include linear marks, pits and perforations, rounding of ends of bones, cracking of bone tissues, digestion, discoloration and staining, breakage and fragmentation, and disarticulation. Each of these will be briefly described and examples from scanning electron microscopy (SEM) analysis illustrated to show the nature of the modifications.

2.1. Linear Marks

Linear marks are defined as marks with lengths more than four times their breadths. They are grooves penetrating the surface of the bone either by incision, where the bone tissue is cut into, or by chemical solution, where the bone tissue has been penetrated by chemical action. Inorganic perimortem marks are seen as linear striations made by human tool use, and organic marks as gouges by animal tooth, claw or beak against bone. There are ten characteristics distinguishing the linear marks as follows: cross sectional widths, whether multiple or single, presence/absence of internal micro-linear marks, linear length, depth, location, direction, frequency, branching of linear marks, and whether straight or curved. Some of these may be confused with marks made some time after death by trampling (see Note 2).

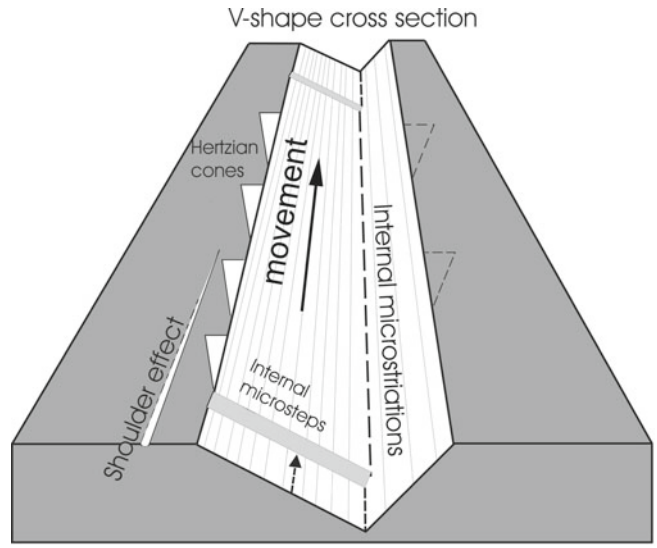

Fig. 1. Cut-mark scheme (*broken arrow*: direction). V-shape cross section. Lateral Hertzian cones (criteria of directionality, and sometimes handedness). Internal micro-steps (criteria of directionality). Multiple and fine internal micro-striations. Shoulder effect (parallel to cut-mark, made by irregularities of the edge of the stone tool).

Linear marks with V shaped cross section on bone are produced by stone objects which are harder than bone, and the agent can be either human action with a tool at or soon after death (Fig. 1), or postmortem movement of the bone against a hard object, for instance during trampling or transport. These marks penetrate the outer surfaces of bones or teeth by physical action, and in the process they remove some tissue and displace other tissue. Stress patterns set up during the incision accumulate tissue in front of the cutting edge, and this tissue is periodically displaced to form Hertzian cones along both sides of the striation (7). They are normally only evident along one side of the cut (8). Directionality of the cut may be indicated by the Hertzian cones (Fig. 1) and internal micro-steps at the interior of the cut (7). Supination at the end of the linear mark, whereby the striation curves to one side as contact with the bone by the object making the mark ceases, may also indicate directionality (9). Linear marks with U-shaped cross section are produced by animal action and are generally broader than cut marks.

The size of V shaped linear marks varies depending on the size and shape of the producing agent, being narrow with a sharp blade such as an obsidian flake, and broader with a core stone tool such as a hand axe or a retouched stone blade. Depth and breadth of linear marks are related, with deeper cuts also being generally broader.

Linear marks may be simple or compound, grouped or independent, and they sometimes appear similar to decorative marks.

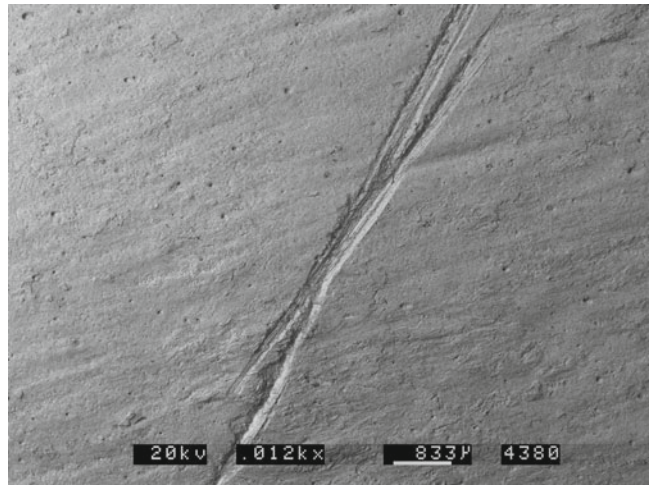

Fig. 2. Scanning electron microscopy (SEM) microphotograph showing the typical X shape when cutting is produced by a stone tool edge retouched on both sides (see (50)). It is produced by a single movement as the angle of the tool changes during the cutting motion. Gorham's cave.

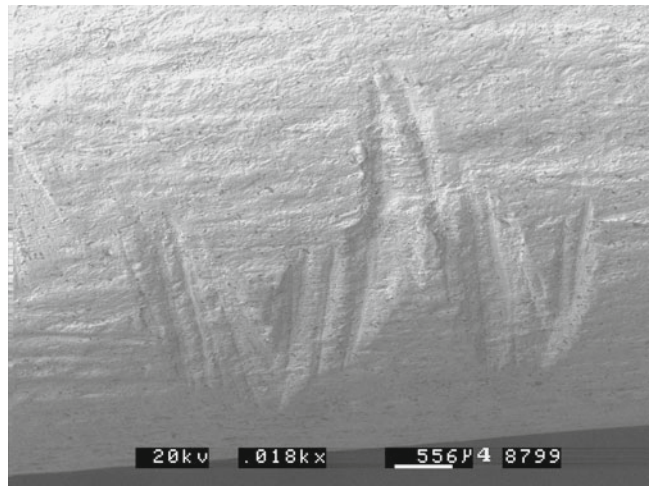

Fig. 3. SEM microphotograph of sawing cuts. These marks have been interpreted as engraving, but each of the "groups" of incisions is actually compound marks made by single strokes, with consistent directionality towards the superior aspect of the shaft. This is taphonomically interpreted as filleting of the arm muscles progressively along the shaft, not a decoration (51).

Multiple marks may also be made by sawing action, where a bone is contacted several times in succession when tough tendons or muscle are being detached from the bone (Figs. 2 and 3).

Sharp single edges such as flakes or metal tools produce single striations without any additional marks outside the main striation, but in general micro-striations are present within the main linear

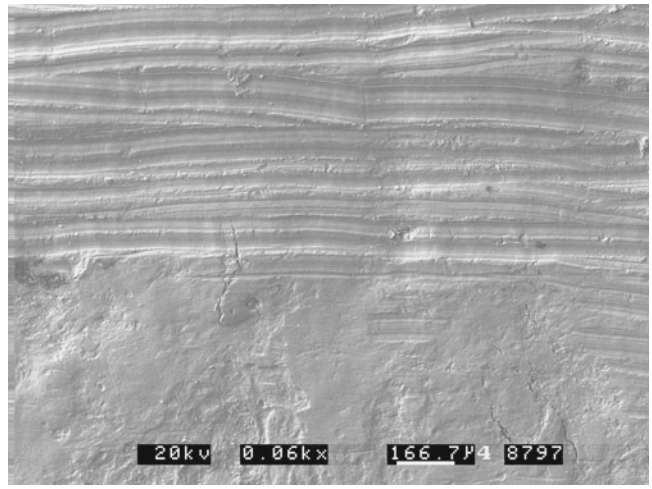

Fig. 4. SEM microphotograph of scraping marks. These marks are characterized by holding the stone tool edge transversally to the direction of motion. The aim can be cleaning the edge when cutting or cleaning the bone from fat before breaking it to extract the marrow. From Gough's Cave (51).

mark when marks are made by stone (Fig. 2). Modern marks made on fossil bones, for example during preparation of the fossil, are distinguished by a different set of striations (see Note 3). Stone edges with uneven surfaces or retouched edges produce multiple striations both within a single major cut, because several parts of the edge may contact the bone surface simultaneously, and outside the main cut, where protuberances from the stone edge come in contact with the bone. The former may cut deeply into the bone, but the latter produce shallow striations alongside the main linear mark. The widths of marks made by stone depend on the characteristics of the stone edge, the depth to which the linear mark penetrates and the raw material used (10, 11). Broader areas of linear marks are generally referred to as scrapes, and they can be caused by transverse movement of stone across a bone surface, scraping bone surfaces to clean the bone or the stone edge (Fig. 4).

The location of linear marks made by human action can usually be related to parts of bones where muscle or tendon insertions are present, for example when they detach muscle, tendon or skin from the bone during butchery or defleshing. Human teeth may also leave linear marks on the bone surfaces of animal bones during chewing. Human tooth marks are microscopic, shallow and short, more similar to rodent gnawing than to carnivore chewing. This is basically because humans gnaw the bone surface superficially. Marks made by animal action may occur on limb bone shafts but they are often concentrated at the articular ends of bones.

The size of marks made by animal action is extremely variable. Measured dimensions of scores are the minimum diameter of the

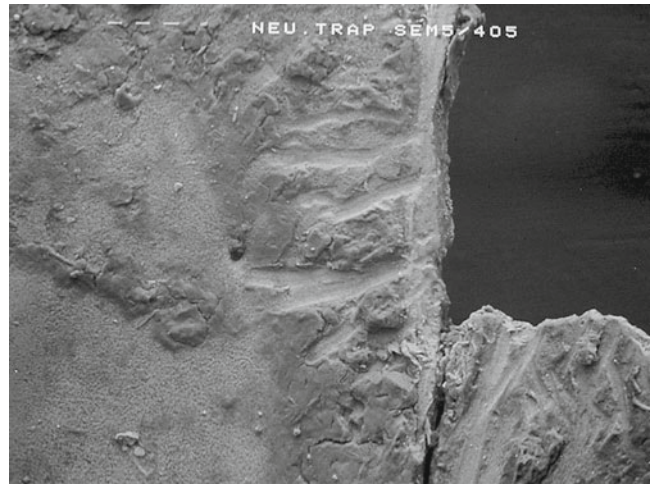

Fig. 5. SEM microphotograph. Smooth U-shaped linear marks made by shrews (*Sorex araneus*) on the internal surface of the tibia of a rodent trapped and killed and mostly consumed by the shrew.

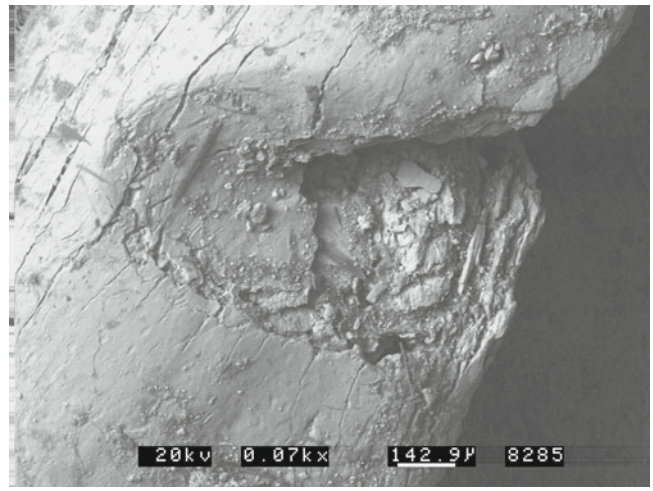

Fig. 6. Linear chewing mark from mongoose showing bone gouged out and dragged along the direction of the bite.

feature (12). Large animals produce both large and small linear marks during chewing while small animals make only small marks (Fig. 5). Rather than using the average size of marks, it is better to use the maximum size, for example the average of the five largest marks on a bone or assemblage (this issue will be discussed in greater detail in the next section). Carnivore tooth marks may be confused with marks made later by herbivore chewing (see Note 4) (Fig. 6).

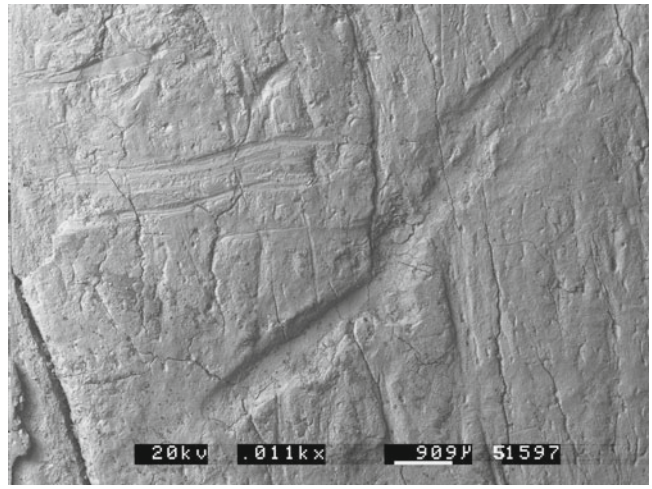

Fig. 7. SEM microphotograph of a linear mark made by vulture beak. Olkarien Gorge, Tanzania.

Many carnivore linear marks have smooth contours, but frequently they have uneven surfaces where fragments of bone have been stripped away by the pressure of the teeth (Fig. 6). Linear tooth marks are single and unbranched, and they vary greatly in length. Their direction is partly determined by the shape of the bone, so that marks on mid-shafts of long bones tend to be transverse to the long axis of the bone, while marks on the ends of bones may be both transverse and parallel to the long axis, with all angles in between.

Linear marks made by birds are usually very superficial as their beaks are not powerful enough to penetrate any but the thinnest bone. The marks are broad and flat bottomed, may be long, and are either straight or curved (Fig. 7).

2.2. Pits and Perforations

Pits and perforations are defined as superficial marks on the surfaces of bones, and perforations as marks that penetrate into the underlying tissue of the bones. Both have lengths less than four times their breadth to distinguish them from linear marks. They vary greatly in size and depth of penetration depending on the agent that produces them, but they also vary with location on bones, whether diaphysis or epiphysis, for example, or young or old individuals, or mammal or lower vertebrate.

Perimortem pits and perforations can again be distinguished between inorganic marks such as percussion marks made by human tools or organic marks made by animal teeth. Many of the organic processes produce distinctive cone-shaped perforations that are broad on the surface and narrow interiorly, with surface bone depressed into the pit (Figs. 8 and 9). Inorganic processes generally produce broad-based perforations with irregular edges

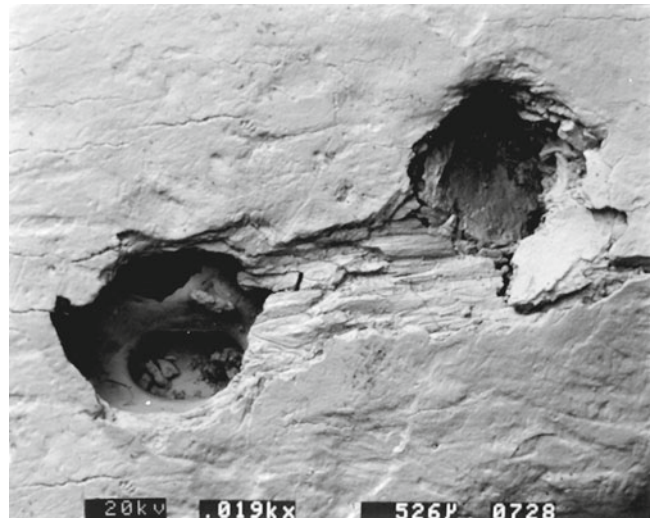

Fig. 8. SEM microphotograph of tooth print of a carnivore premolar of the size of a fox on a small sized mammal.

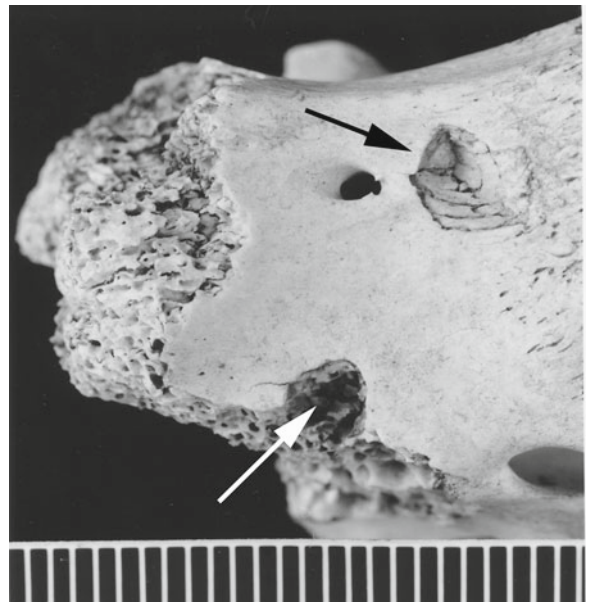

Fig. 9. Puncture marks are characterized by inverted cone shape, with depressed cortical bone covering the bottom and walls of the puncture. Two examples show inverted cone impressions (*above*) and arcuate shape of the rim at the broken edges (*below*). Both are produced by vertical compression.

(Fig. 10), although some agents such as sharply pointed rocks can also produce cone-shaped perforations. Location and depth of pits and perforations follows the classification first proposed by Andrews and Fernández-Jalvo (12).

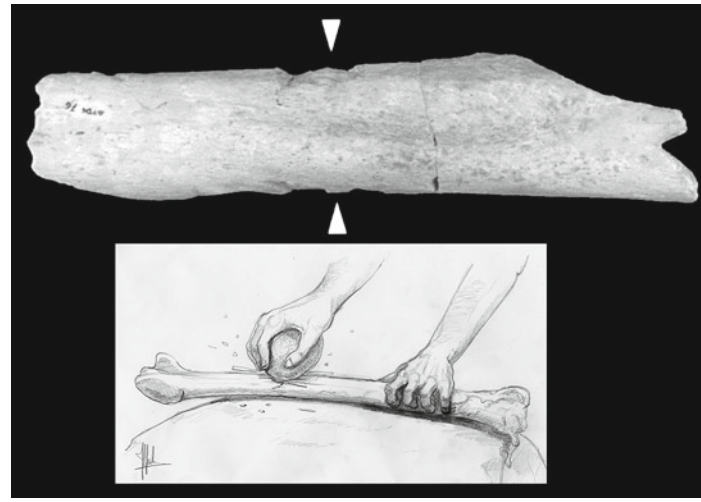

Fig. 10. Impact notches or percussion marks consist of pits of variable sizes and depths. These are produced when the bone is held on a hard solid surface and smashed with a stone as shown in the drawing. (52).

Fig. 11. Pits and perforations from hyaena chewing: bone flakes chewed by spotted hyaena *Crocuta crocuta*. Sutcliffe collection.

By far the most common source of pits and perforations in bone is chewing or gripping by carnivores, and this typically produces conical or inverted cone-shaped perforations into or through the surfaces of bones (Fig. 9). Tooth marks are frequently associated with bone breakage, in which case tooth mark profiles may be present along the broken edges (Fig. 11). Multi-cusped teeth make marks distinct from single cusped teeth (Fig. 8). Location of the marks is also important, for marks made on the diaphysis of bones

are generally shallower than marks made on the softer epiphyseal bone, where tooth perforations may penetrate deeply below the surface.

Another factor to take into account is the potential size relationship between predator and prey. Small tooth marks on large mammal bone may be produced both by large predators, for example if the marks are on the diaphysis of the bone or are made by the predator's incisors, or they may be produced by the smaller teeth of small predators. In contrast, large tooth marks on large mammal bone can only be made by large predators (again taking into account the location of the marks). Therefore, the actual size range, and in particular the upper end of that range, provides the data that are most useful for identifying size or type of predator. Similarly, tooth mark sizes on small mammal bone are of greater value when the full range is provided, rather than mean values, and it is the largest marks that provide an indication of the type of predator. As in the case for linear marks, the average of the five largest pits and perforations is more diagnostic of predator size than the average of all marks.

Carnivore perforations may displace surface bone down into the interior of the bone, although the fragments of bone may be lost during the long process of preservation and fossilization (Fig. 8). Humans may also produce punctures or pits, but these mainly occur at the broken edges of thin bones (ribs, metapodials or phalanges of small sized animals). In such cases, traits are undistinguishable from small mammalian carnivores except for the specific location of human's chewing.

Percussion notches differ from carnivore marks in being broader and shallower (13, 14) and less variable in size. Notches produced by carnivore teeth tend to be narrower and more semicircular (15). Broad-based perforations made by human butchery or dismemberment of carcasses are the result of impacts or percussion marks on the surfaces of bones, and they may be superficial or penetrate deeply into the underlying tissues, depending in part on their location. On the diaphyses they are shallow, equivalent to categories "a" or "b" respectively in our tooth mark classification (12), and they are generally shallower than marks on articular ends (category "c"). Percussion notches also occur on bones broken to gain access to bone marrow, but in this case only part of the impact remains on the broken edges of the bone. These are equivalent to category "d" and "e" on our tooth mark classification scheme (see Note 5). Impact marks may be associated with spiral breaks since the bone has to be fresh to retain marrow (15). It should be noted that percussion producing irregular but broad-based perforations in the surfaces of bones may be produced by trampling, simulating the effects of percussion during butchery (see Note 6).

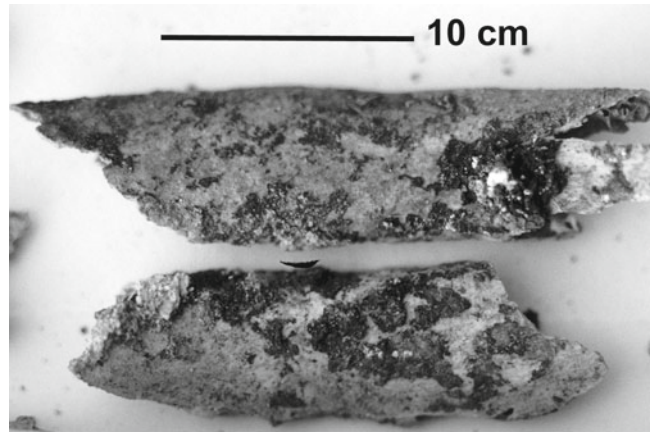

Fig. 12. Carbon staining on the ribs of a very old human individual from Çatalhöyük. The ribs had not been burnt, but the staining is the result of carbon residues due to inhalation of smoke, and it is only seen on very old individuals. (16).

2.3. Discoloration

Discoloration of bone is not generally a perimortem modification, but some differences may be seen in small mammals. For example, some avian predators prey on earthworms, and since earthworms ingest soil while feeding, the mineral or organic elements in the soil may stain the vertebrate bones. Digested bones otherwise tend to be clean and light in color.

Black staining on human bones may occur in exceptional circumstances. The skeletons of old individuals from Çatalhöyük, Turkey had carbon accretions deposited on the inner surfaces of their ribs due to smoke inhalation during life (Fig. 12) (16). The houses at Çatalhöyük had no ventilation, so when heating or cooking took place inside the house, the single room dwelling would have filled with smoke. Constantly breathing this smoke over many years accumulated inert carbon residues in the lungs of the inhabitants, so that in old age the lungs would have had heavy carbon residues. On death, and after the lungs decayed, the inert carbon remained and accumulated on the inner surfaces of the ribs on the lower side of the body. This feature was observed on 7 out of 10 old individuals in the 1995–1999 excavations at Çatalhöyük, but it was absent from all young/middle-aged adults and juveniles (16).

2.4. Rounding

Rounding of bones as a perimortem effect is seen only as a result of digestion. Small mammal bones may have broken ends or protuberances of intact bone rounded (Fig. 13), and this has been observed most frequently on bones recovered from carnivore scats (17). Fragmented large mammal bone may similarly have ends of broken bones rounded when ingested by large predators such as hyaenas. Many postdepositional processes also produce rounding of bones, such as transport, wind action, or sediment movement (see Note 7).

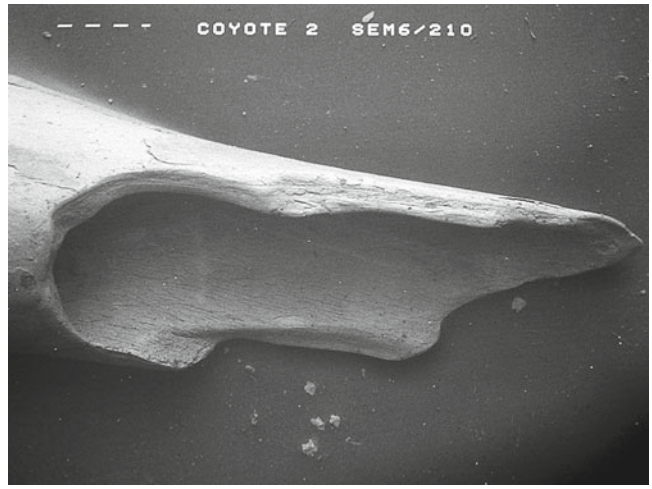

Fig. 13. Rounded end of bone ingested by coyote (*Canis latrans*). The bone was broken during ingestion by the coyote, and the rounding of the broken end occurred during digestion.

Localized distribution of rounding on bones may also be a result of human use of the bones (1, 18), and this has a superficial similarity to the abrasion produced by carnivore digestion. A series of bone points from Mumbwa cave include one undoubted bone tool (19) that shows a clear pattern of scratches parallel to the long axis of the bone fragment, but it also includes a number of rounded bone points which bear no indication of human manufacture. Backwell and d'Errico (20) also described manufactured bones by early hominins from Swartkrans (South Africa).

2.5. Cracking

Cracking of the surfaces of bones and teeth is defined as the opening up of splits and cracks penetrating beneath the surface of the bone but without any obvious loss of surface tissue. It is caused by shrinkage of bone which could be due to loss of water and/or organic matter from the bone as a result of digestion. The surface of a digested bone at a SEM-microscopic level (1,000–3,000×) has the appearance of being torn apart, with longitudinal as well as lateral displacement of surface tissue. Extensive cracking develops with time, temperature, or concentration of enzymes. Similarities between digestion and enzymatic activity have been shown by Denys et al. (21) and Fernandez-Jalvo & Marin Monfort (22). The digested bone may be both rounded and cracked, and this characteristic microscopic "torn" cracked surface establishes the distinction from abrasion (Figs. 14 and 15). Similar cracking is formed during postdepositional weathering of bones.

On teeth, shrinkage affects dentine initially, but as the dentine shrinks from loss of collagen it may be followed by splitting

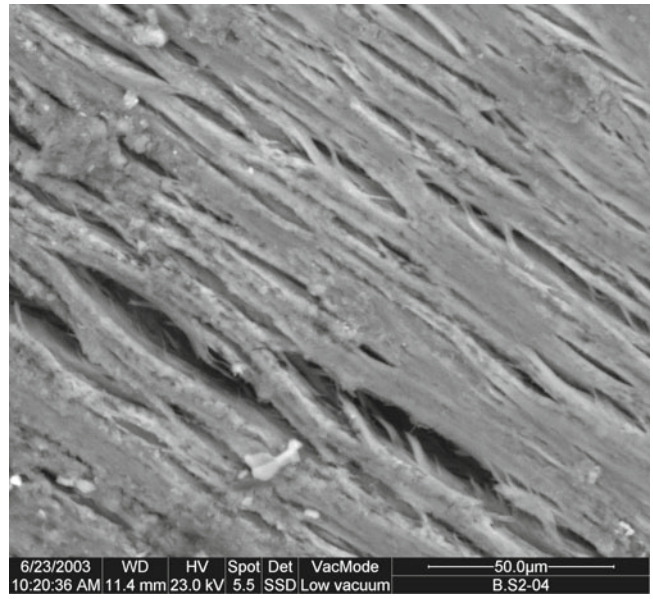

Fig. 14. Modern amphibian bone digested by fox: detail of cortical bone tissue acquiring a torn appearance after digestion.

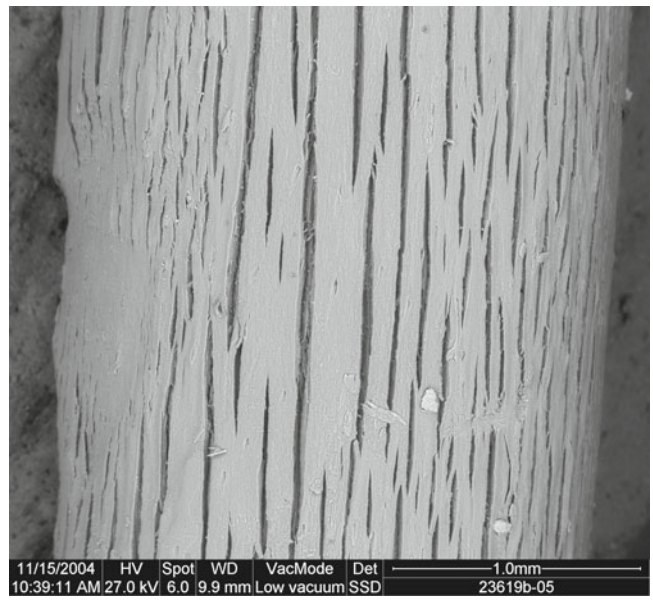

Fig. 15. Cracking of bone treated with enzymes. SEM microphotograph of avian bone (*Anas crecca*) from taxidermic collection. Extensive cracking develops with time, temperature, or concentration of enzymes. Similarities between digestion and enzymatic activity has been shown by Denys et al. (21) and Fernandez-Jalvo & Marin Monfort (22).

of the enamel. Flaking of the surfaces of bones is defined as loss of surface tissue, exposing underlying bone to varying depths (exfoliation). Flaking is usually associated with cracks in the bone, but the effects of digestion are rarely so strong as to produce this effect. On the other hand, flaking is common during weathering, forming the next stage during progression of weathering.

2.6. Digestion

Digestion has two perimortem effects on bone: modifications to the surface of the bone and chemical alteration to the internal structure. They are both the product of high levels of acidity and digestive enzymes in the predators' digestive systems. The former produces acid etching of bone surfaces while digestive enzymes break down the organic constituents of bone and produce rounded edges. Degrees of digestion vary between predators, with some species having higher acidity levels in their digestive tracts than others (23). The degrees of digestion may depend on the state of hunger of the predator, such that a hungry predator may retain a meal in its stomach until everything is digested, and the predator's age, with juveniles typically producing higher levels of digestion than adults. This explains both the variation observed in degrees of modification and the fact that some micromammal individuals are completely digested and never recovered from the pellets or scats of the predator (24–27).

Digestion may be localized or may extend over the whole surface of bones. This distinction tends to be correlated with type of predator, with all over digestion occurring in large mammal predators such as hyaenas and large reptiles like crocodiles (28). In these, the bone is comminuted and the fragments rounded by digestion. In the case of teeth, digestion by crocodiles may completely remove the enamel. In contrast to this, avian predators that regurgitate the bones of their prey produce localized digestion, which is concentrated on epiphyses and articular surfaces but is most apparent on the teeth (Figs. 16 and 17). Destruction may be so great as to completely destroy the articular ends of bones or the tooth enamel (see Note 8), and this applies particularly to small mammals which can be ingested whole and all parts of the skeleton subjected to digestion. Birds and amphibians ingested whole by predators have similar tissue loss, particularly with penetration of the articular end.

On teeth, the effects of digestion are primarily loss of enamel, starting by thinning of enamel, which may expose the prism structure of the subsurface enamel. Six categories of digestion (see Note 9) can be recognized (17, 29), leading to loss of tissue at exposed places like the enamel-dentine junction, alveolar margin, or salient angles of teeth, and at its most extreme all enamel may be lost. This can happen with only minor modification of the dentine, which, because it is less heavily mineralized than enamel, is less affected by the acidity in the predators' stomachs. The digestion categories

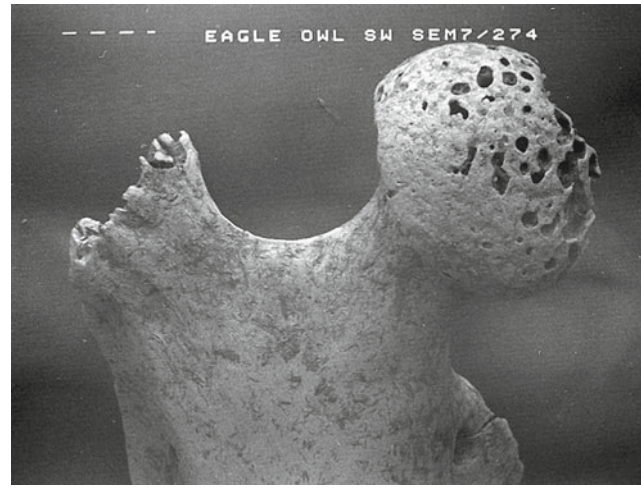

Fig. 16. Arvicolid femur with moderate digestion by eagle owl *Bubo bubo* showing cracking and splitting of the bone surface. (17).

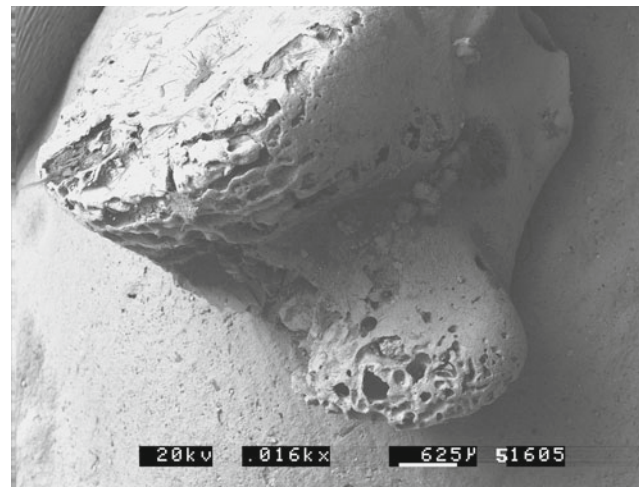

Fig. 17. Digested bird bone, distal end of a bird humerus digested by jackal showing the surface perforated by the action of the acid juices of the mammalian carnivore. (17).

differ between different types of mammal, so that arvicolid teeth are more strongly affected than insectivore teeth and murid teeth (see Note 10). Variations in digestion are shown in Figs. 18, 19, 20, 21 and 22.

Similar digestion categories have been set up for rodent incisors (17) with four categories involving loss of enamel (30). A fifth category is now also recognized (29) of extremely light digestion consisting of light pitting of the enamel surface, with no loss of enamel. Light digestion has loss of enamel at the tip of the incisor but no other modification other than the light pitting seen above.

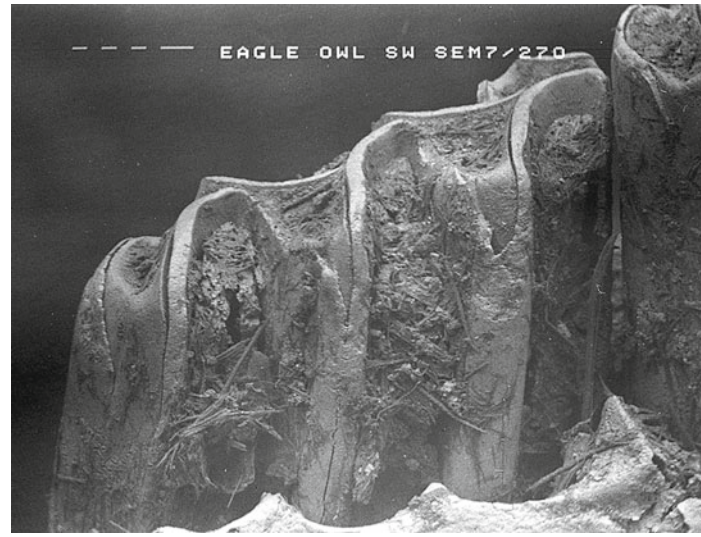

Fig. 18. Arvicolid molar with moderate digestion by eagle owl (*B. bubo*), showing removal of enamel along half the length of the salient angles from the occlusal surface. (17).

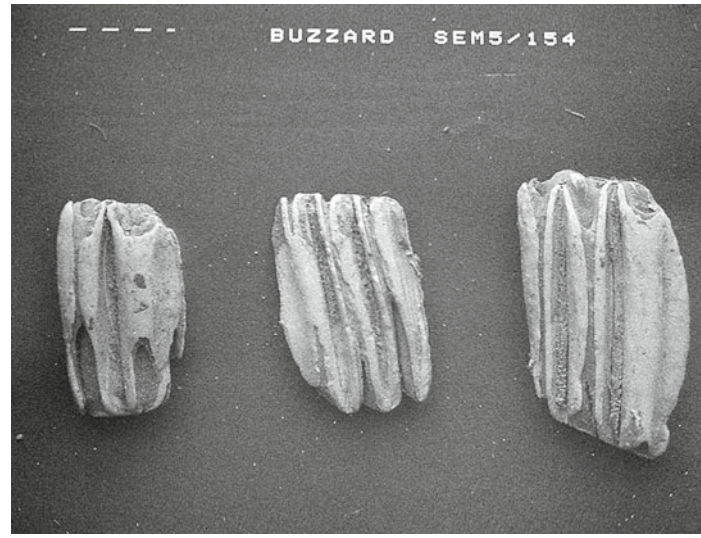

Fig. 19. Arvicolid molar with heavy digestion by buzzard (*Buteo buteo*) ranging from moderate digestion (*left*) to heavy digestion (*middle*) and extreme digestion (*right*) all digested by *Buteo buteo*. (17).

Moderate digestion also tends to have greatest modification at the tips of the incisor, but it also produces extensive damage along the rest of the crown, with limited areas of removal of the enamel. Heavy digestion has extensive enamel loss all along the crown but with islands of enamel remaining. Extreme digestion has removed all or most all of the enamel, with tiny islands of enamel only

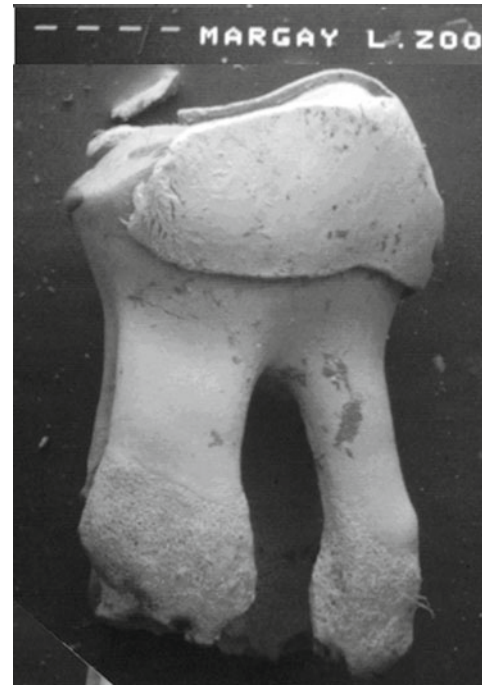

Fig. 20. Murid molar digested by margay (*Felis wiedii*) in London Zoo. Digestion is heavy and the penetration from the enamel-dentine junction is particularly evident. The roots and dentine of the occlusal surface are unaffected, but the enamel junction on the wear facets has also been affected.

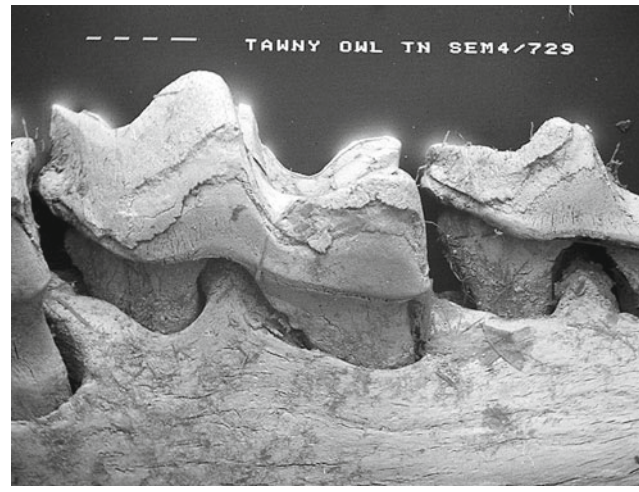

Fig. 21. Soricid molar digested by tawny owl (*Strix aluco*). This is heavy digestion, with the enamel completely removed from the surface of the dentine (17).

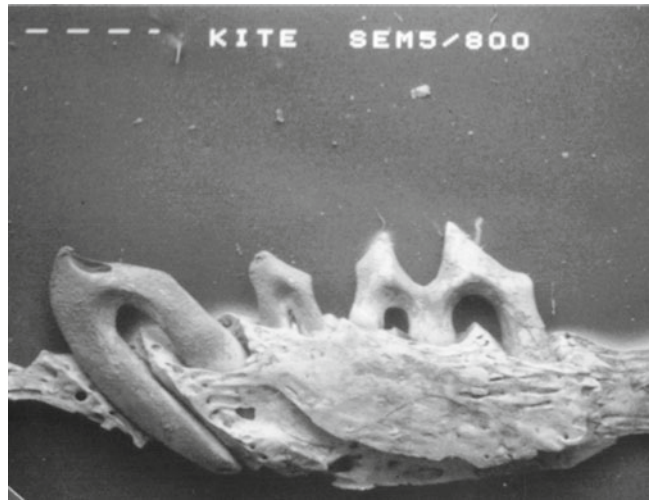

Fig. 22. Mole mandible digested by red kite (*Milvus milvus*). This is heavy digestion, with the enamel partially removed from the enamel-dentine junction. (17).

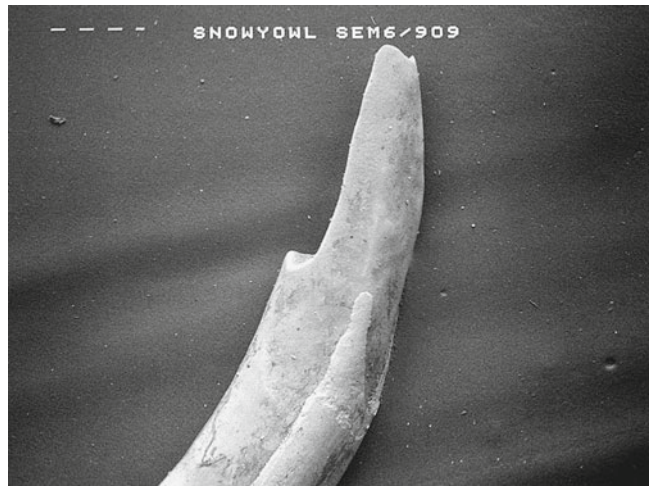

Fig. 23. Arvicolid incisor with light digestion by snowy owl (*Nyctea scandiaca*) concentrated on the tip of the incisor where the enamel is totally removed. The dentine may be slightly digested, producing a wavy outline. (17).

remaining, and at its most extreme the whole structure of the tooth collapses. These stages are shown in Figs. 23, 24, 25, and 26. Because of the overall similarity in different rodent groups, digestion of the incisor is the single most diagnostic element for small mammals.

The question whether the digestion of animal bones in the digestive system of predators is due to acidity or digestive enzymes is beyond the scope of this paper. There are large differences in the

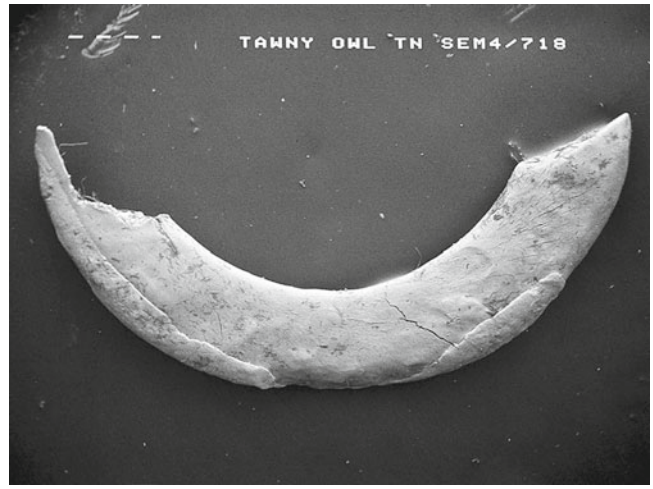

Fig. 24. Arvicolid incisor showing moderate to heavy digestion by tawny owl (*S. aluco*), which has removed much of the enamel, exposing the dentine along the length of the tooth except for islands of enamel not fully removed. (17).

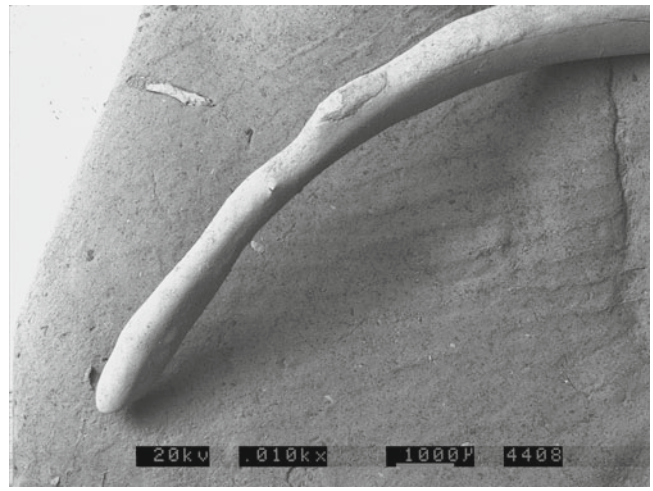

Fig. 25. Murid incisor with heavy digestion by polecat (*Mustela putorius*). Most of the enamel has been removed by digestion, and the dentine is rounded. (17).

degree of damage to ingested prey remains in different predator species, and it appears that there is an approximate relationship between the level of acidity in the predators' stomachs and the degree of damage, but this is clearly not the whole story, not least because the relationship between acidity level and degree of damage has not been adequately quantified as yet.

Experimental work separating the effects of acids (HCl) and enzymes (pronase) has allowed us to understand better the effects

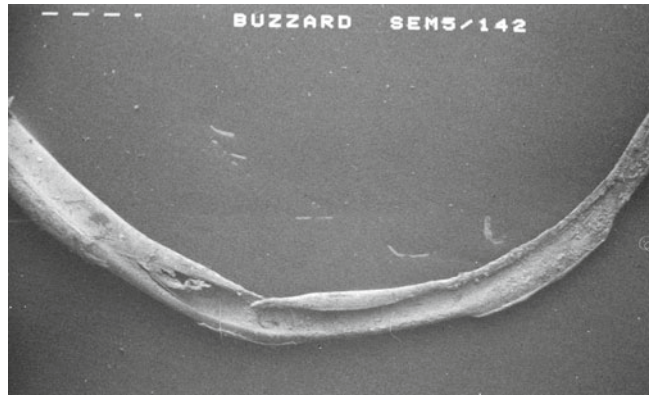

Fig. 26. Murid incisor with extreme digestion by buzzard (*B. buteo*). The main trait at this stage of digestion is the loss of the recognizable shape of the incisor, almost complete absence of enamel, and collapse of the structure in on itself. (17).

of digestion by predators (21). Acid by itself causes dissolution of the mineral constituents of bone, and teeth treated experimentally by HCl entirely remove the mineral component of the teeth, leaving a soft and malleable tooth. This condition is rarely seen in predator assemblages with the exception of those subject to crocodile digestion (crocodiles have almost no enzymes in their gastric juices). The effects of enzymes by themselves are closer to the condition in predator assemblages, with penetration of bone surfaces and removal of thin articular bone to expose cavities beneath.

Articular ends of limb bones may be modified in ways that could be mistaken for carnivore activity, either by digestion or by scooping out of the articular ends (4, 31–33). This modification mimics carnivore action, producing highly corroded surfaces of the bone (see Note 11).

2.7. Breakage

Breakage—perimortem breakage is caused by predation by carnivores and/or butchery by humans. The characteristics of broken bone depend very much on the type of bone and on the pressure imposed on it by the agent involved. The type of bone includes both the skeletal element involved, its developmental age (mature or immature), and the time since the death of the individual (Fig. 27). The condition of the bone, whether green or dry, results in different breakage patterns, but this is imperfectly correlated with bone age as much depends on the depositional microenvironment. Element shape is also important, and small compact bones such as carpals and tarsals, with few projecting processes, tend to be resistant to breakage (1). Patterns of breakage are often not diagnostic, and it is difficult to distinguish between many of the agents producing the breakage.

The classification of break morphology of vertebrate bone is based on Villa and Mahieu (34) and it is described in terms of fracture

Fig. 27. Remains from a lion kill showing breakage of juvenile wildebeest. The broken bones have spiral breaks with acute smooth edges and on the right some gnawed ends of bones. The shaft circumferences are mostly still intact. Lions are not adapted to break large or adult bones because their teeth are weaker than canids and hyaenids. However, lions can break bones of very young animals. Courtesy of Peter Jones.

outline, fracture angle, fracture edge, and the extent of survivorship of the shaft circumference of long bones (see Note 12).

Three other indicators of breakage are peeling, measurement of the shaft circumference of long bones, and deformation of ends. Peeling produces heavily jagged surfaces (35), leaving a roughened surface with parallel grooves or fibrous texture (Fig. 28). It is produced "when fresh bone is fractured and peeled apart similar to bending a small fresh twig from a tree branch between two hands" (35) (see Note 13). The extent to which the circumference of shafts of limb bones is intact is used to describe the completeness of limb bone shafts (Fig. 29) (see Note 14). Human chewing (as well as chimpanzees) may also produce breakage or deformation usually at the tip of thin bones as a result of bending bones by pushing up or down the bone using the hands and holding the ends between the upper and lower cheek teeth. This shape results from the difficulties that flat–cusped molar teeth have in crushing hard bone tissues to suck the marrow content (Fig. 30).

The morphology of breaks on small mammal bones is similar to that on large mammals (36). Spiral breaks are common, but the splitting of limb bones when it occurs renders most skeletal elements unidentifiable. Some predators of small mammals produce no breakage of the bones of their prey, for example owls typified by barn owls (17). There are some owls, however, that produce

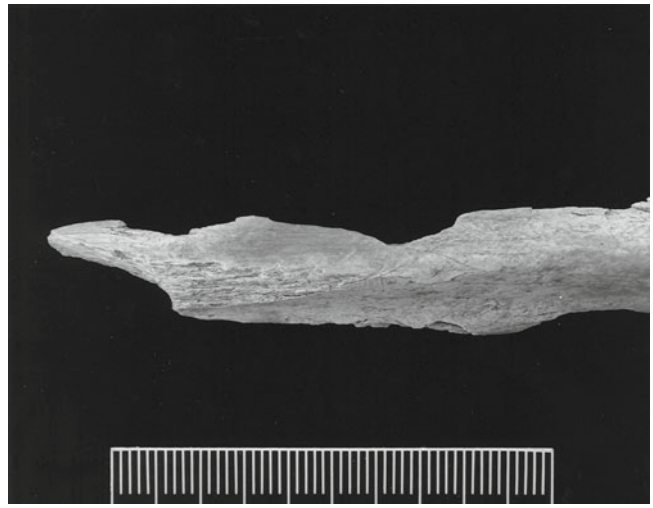

Fig. 28. Peeling of bone from Gough's Cave showing the characteristic pattern of roughened exfoliated surface produced when a fresh bone is snapped in two. This fossil was recovered from Gough's cave (UK) and is a left human ulna (GC87-209) with extensive peeling at the proximal end.

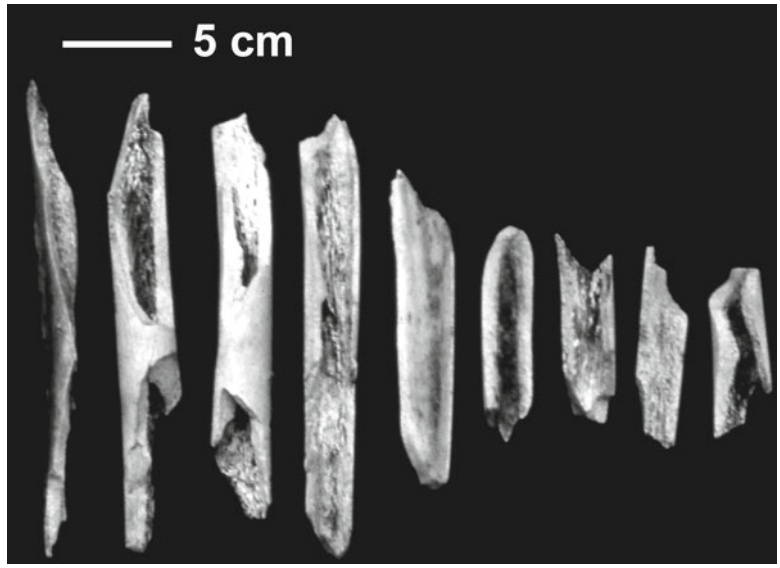

Fig. 29. Breakage of human femora by spotted hyaena, Kajiado collection (Tanzania). Femora fragments chewed and broken by spotted hyaenas, *C. crocuta*.

intermediate and variable breakage, and diurnal raptors and mammalian carnivores may produce up to 100 % breakage (see Note 15).

2.8. Disarticulation

Disarticulation is the separation and dispersal of skeletal elements from their anatomical position. The only perimortem effect is the disarticulation of animal carcasses by carnivore or human action,

Fig. 30. Deformation of bones chewed by humans, comparing a modern comparative sample with bone from Gough's Cave. The modern pig rib chewed by a woman is on the *left* and on the *right* is an human metatarsal, GC87-30 from Gough's Cave (UK). The extensive deformation of the proximal ends, with depressed flakes of bone and splaying of the ends, is similar on both bones, and may indicate human chewing on the metatarsal from Gough's Cave (51).

and there is a sequence of disarticulation of skeletons, similar in outline although differing in details, depending on the species, size of the animal, and environmental factors (37–39) (see Note 16).

The pattern of disarticulation may differ in some respects when it is the product of butchery. At the Garnsey bison kill site, disarticulation was extensive, although the bone assemblage had been subject to fluvial disturbance (40). The most commonly articulated elements were feet and lower portions of forelimbs (from the radius down), and this differs from carnivore-ravaged bone assemblages (40). It also differs from the mammoth butchery site at Colby (41), where the phalanges were subject to the greatest destruction. There were also occasional short portions of vertebral column at both the Garnsey and Colby sites, with portions of thoracics, lumbars, and cervicals being preserved, and this is consistent with naturally occurring disarticulation and also with human disturbance.

The lack of disarticulation may indicate an accidental death, human burial or, at least, lack of predator or scavenger access to the skeleton.

3. Final Remarks

Perimortem damage recorded on bone is the result of the immediate processes affecting animals or humans at or near the time of death. Forensic studies concentrate on this time interval, focusing on the cause of death and possible distinction of criminal vs. natural processes. However, a big difficulty is the identification of human intra-specific killing during prehistoric periods, because projectiles were absent or at least not powerful enough to damage the bone. In this respect, taphonomic studies investigating prehistoric cannibalistic practices are the closest aspect to forensic studies, but even in these cases, evidence of killing cannot be accurate or reliable. The distinction of humans feeding on other humans can be distinguished from funerary rituals if the discarded human remains are mixed with the bones of other animals and subjected to the same butchery techniques (see Note 17). In order to identify specific perimortem alterations or injuries arising from human action, other taphonomic processes and agents that are mimicking them have first to be discarded. Here we have tried to describe in detail those modifications occurring at time of death, with added notes about later occurring modifications that mimic the perimortem modifications.

4. Notes

1. Techniques of observation to identify bone modifications. The systematic analysis of the bone or fossil surface requires the use of microscopic techniques including light binocular microscopy and, sometimes, SEM. Detectors used on the SEM can be either secondary electrons (SE) to observe the topography, or backscattered electrons (BSE) to observe changes in the density slightly beneath the surface, or both of them combined. Low vacuum SEMs or environmental microscopes (ESEMs) are noninvasive techniques and bones and fossils may be directly introduced into the SEM chamber with no particular preparation technique (i.e., coating) to be directly analyzed at high magnification and high resolution. Conventional SEMs may also be used, but samples will need to be coated with carbon or gold to prevent anomalies (electronic charging) in the observations. This is important when making observations during experimental work when intermediate stages need to be observed. Experimental work and observations of modern bones help us to understand and interpret signs and modifications observed on fossils. Microscopic observations

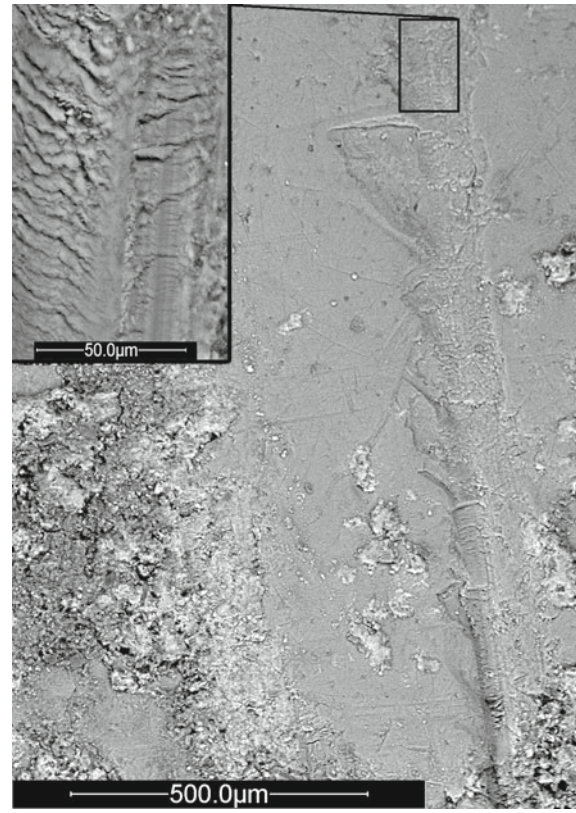

Fig. 31. Fossil cut today using a stone tool. The resulting cut appears more fragile with big hertzian cones on the *left* side indicating the cut motion was from *bottom* to *top*. On the *left* side, detail of the interior of the striation showing abundant microsteps that are characteristic of modern cuts on bone already fossilized.

allow us to characterize and distinguish marks to identify the etiology of these modifications (Fig. 31).

2. Mimicking linear stone tool cut marks: trampling marks. An aspect frequently treated in palaeoanthropology is the distinction between linear marks produced by stone tools and those produced by bone friction against a rocky subtract or coarse sediment (42, 43). This action is frequently due to trampling by large animals on bones whereby the bones are rubbed against surface stones, or are moved against subsurface stones or sediment when bones are buried to shallow depths (10). This action causes multiple scratch marks that may closely resemble cut marks in morphology, including features such as long linear striations, hertzian cones developed and internal striations within the main cut. They differ, however, in being generally less deep, very much more abundant, with little or no proximity to areas of tendon or muscle attachment, and transverse to long axes of long bones (Figs. 32 and 33).

Fig. 32. Linear cuts caused by trampling. Fossil from Miocene deposits at Concud. The marks are very long and thin and mimic cut marks induced by stone tools, but the absence of humans at this age (7.5 Ma) exclude the possibility of cut marks. Concud (Teruel, Spain) late Miocene of Spain.

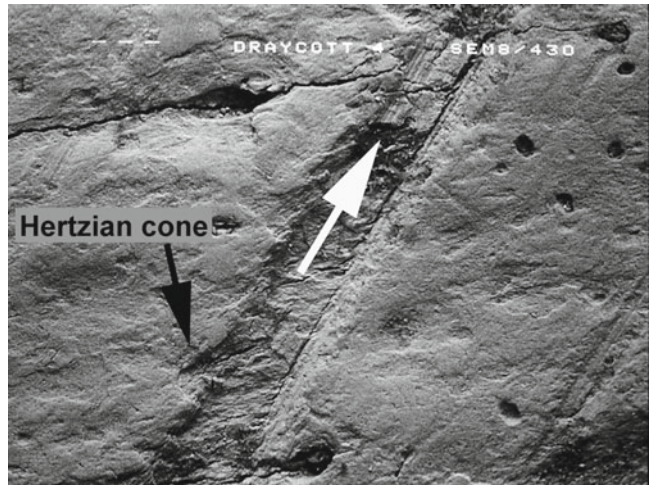

Fig. 33. SEM microphotograph of a modern bone from Draycott showing isolated scratches of trampling marks. These marks are distinctive from cut marks as the cross section is flat. However, other characteristic traits, such as internal microstriation and internal microsteps (*white arrow*) and lateral Hertzian cones (*black arrow*), can be formed by trampling.

3. Distinction between ancient and modern cut marks on fossil bones. When fossil bones are cut today using a stone tool, the interior of the cut appears more broken up and brittle than fresh cut marks (Fig. 31). Modern cut marks made on fossils also have fewer longitudinal internal micro-striations and a higher frequency of internal micro-steps that run transversally to the length of the striation (22).

4. Mimicking linear marks of carnivore chewing: herbivore chewing. Grooves similar to carnivore chewing marks may also be produced by herbivores. They chew bones (osteophagia) to obtain minerals that are deficient in their diet, such as phosphates (44, 45). At an early stage of chewing these grooves may be confused with carnivore chewing marks. A distinctive indication of bones chewed by herbivores is to find cracks on the bone surface with grooves superimposed, i.e., occurring later than the cracking. Cracks are formed when bones are exposed on the ground and become dry due to weather exposure. At later stages of herbivore chewing, bones acquire a characteristic forked shape (Fig. 34), and the presence of this type of shape reinforces the incidence of herbivore chewing.
5. Categories of pits and perforations: the letters following six of the seven categories below refer to the definitions in Andrews and Fernández-Jalvo (12). The seven categories are as follows:

   Shallow pits on diaphyses of limb bones (a).

   Deep perforations on shafts of limb bones (new).

   Deep perforations on articular ends of bones (c).

   Deep perforations on the edges of breaks (d, e).

   Deep perforations along edges of split bones (f).

   Multiple perforations on the bone surface made by multicusped teeth (g).

   Deep perforations on anatomical bone ends or edges (h).
6. Mimicking carnivore tooth marks: percussion marks. Impact notches or percussion marks consist of pits of variable sizes and depths. These are produced when the bone is held on a hard solid surface and smashed with a stone. These scratches suggest that the bone was already clean of meat and broken for marrow extraction, in contrast to chop marks to dismember a bone still covered by meat. Percussion marks may be similar to tooth marks when viewed with the naked eye. Microscopic examination shows that percussion pits are usually accompanied by abrasions and scratches caused by friction of the bone against the stone that hammered it, or the anvil surface where the bone was resting when it was struck (described by Turner (46) as hammerstone-anvil scratches).
7. Other sources of rounding may be distinguished by the greater extent of the rounding over all surfaces of the bone, for example during transport (47, 48), or polishing by wind action. Microscopic scratches or microscopic pitting on the rounded surface may be observed at SEM high magnification. Polished ends of bones may be the result of trampling, for example when a bone is fixed in position in the soil and the end is exposed to

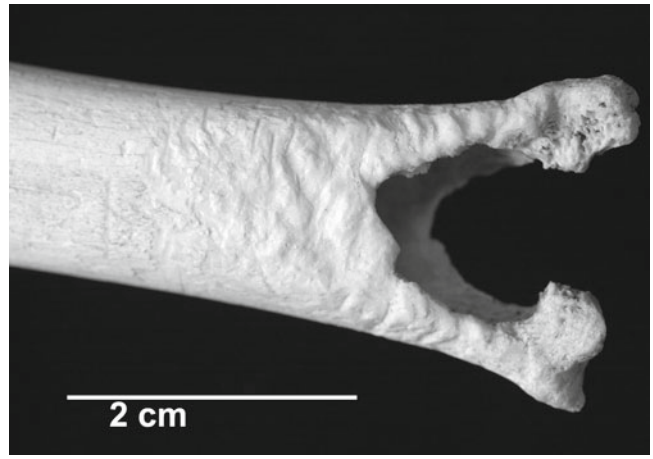

Fig. 34. Herbivore chewing on the end of a limb bone, removing the middle part of the articular end and shaft and leaving linear grooves on the edges of the bone. This forked appearance of the bone is very characteristic of chewing by herbivores. From Riofrio (Spain) Courtesy of I. Caceres.

Fig. 35. The end of a limb bone embedded in the floor of a brown hyaena den entrance, where constant trampling by hyaenas rounded the end of the bone. Photo courtesy of Graham Avery.

trampling over the surface (Fig. 35). In addition, water or wind produce rounding of both enamel and dentine at the salient angles, but digestion eats away first the enamel leaving the dentine exposed.

8. Four categories of digestion of postcranial bones are currently recognized. These categories are based on presence of digestion of the femur head, as this is one of the most commonly preserved elements in small mammal assemblages (17). Digestion on the distal humerus articulation, also commonly

preserved in the fossil record, is comparable to that of the femur. Digestion is categorized as light, moderate, heavy, and extreme. Digestion may also produce rounding of exposed ends of bones without penetration of tissues (see above), polishing of articular bone, cracking of limb bone shafts (see above), and breakage of bone (see below).

9. Five categories of digestion of small mammal molars are currently recognized (17,29,30). The first category of modification is extremely light digestion only seen as a slight pitting of the surface of the enamel but with no penetration of the salient angles and no rounding of the occlusal and root ends. Light digestion has some removal of surface enamel in addition to surface pitting, but this is limited to the top of the crown and little dentine is exposed. Moderate digestion extends along the lengths of the salient angles but only exposes dentine to a limited degree. Dentine starts having a wavy surface. Heavy digestion and extreme digestion show a greater degree of dentine exposure, with the dentine collapse and loss of the tooth structure in the extreme case.
10. Effects of molar morphology: Several distinct morphologies of tooth types must be distinguished when analyzing digestion, as they have different resistance to digestion: rodent incisors, arvicolid molars, murine molars, and insectivore molars. Arvicolid molars have projecting salient angles that are exposed to digestion on three sides of each angle as well as from both root and occlusal ends, and enamel is removed along the angles starting at both ends, exposing the dentine beneath. Murine and insectivore molars have less projecting cusps and ridges, and they are less affected by digestion. On average murid molars are 1–2 stages later than arvicolid molars in showing evidence of digestion, such that a predator producing moderate digestion on the latter would only produce very light digestion on the former. Rodent incisors have greater consistency in morphology, and even they may differ in enamel thickness or the presence of grooving along the crown, their patterns of digestion remain equivalent.
11. Mimicking carnivore action: soil corrosion. Several bones from monitored horse carcasses in Wales showed the effects of extensive surface corrosion where bone was resting on the ground (pH values near 4). They were monitored for periods of 10–14 years, and the modification was observed to increase slowly with time and to be due to the acidity of the soil on which the bones were resting. The absence of tooth marks and the observations of progressive increase in “scooping out” observed over a period of years, exclude the possibility of carnivore action. Carnivores chew all over the bone, but soil corrosion affects only salient angles and areas in direct contact with the ground.

12. Breakage patterns: fracture outline can be curved or pointed (angle oblique to the long axis of the bone and often ending in a sharp point); transverse (perpendicular to the long axis of the bone) or mixed. Curved or spiral breaks occur on fresh or green bone, and they can often be attributed to human action or carnivore chewing. Other agents cannot be ruled out; for example bones may be broken if an animal falls to its death, producing spiral breaks, but none of these agents is likely to produce the abundance of curved breaks seen in carnivore or human butchery assemblages. The angle between the break and the bone cortical surface is the fracture angle, and it may be oblique (either acute or obtuse), perpendicular, or both for fractures that have variable angles (i.e., intermediate). Oblique angles occur on green bone, mixed on dry and transverse on buried bone, and their presence parallels the fracture outline. The margin of the fracture may be smooth or jagged. Smooth fractures are usual on green bone, and again the indications of this aspect of broken bone are the same as that seen above for fracture outline. These three features (fracture outline, angle, and edge) can be combined to identify perimortem green bone fracture.
13. Peeling occurs on bones with low density (e.g., ribs, metapodials, radii, fibulae of small to medium sized large mammals) as result of disarticulation or marrow extraction.
14. Circumference categories are a measure of ravaging of limb bones. Three categories are complete circumference for at least a portion of the shaft, more than half complete, and less than half complete. The more extreme the splitting of the shafts and the greater the number of split bones, the greater the jaw strength of the carnivore causing the splitting. Hyaenas produce the most extreme degree of splitting of long bones, while broken bone assemblages with low frequency of splitting may be due to postdepositional damage. Splitting of limb bones also occurs as a result of human butchery to obtain access to the marrow, and a butchered bone assemblage may be revealed by consistent patterns of breakage. Some skeletal elements are more resistant to splitting than others and this needs to be taken into account.
15. Fragmentation indexes are used to illustrate degrees of fragmentation. One that we have used applies an ordinal rank from 1 to 10 for breakage of bones in a skeleton, with 1 signifying all bones in a single skeleton are broken and 10 that no bones are broken (16). An even simpler method of measuring fragmentation is to record the size distribution of bone fragments or specifically diaphysis fragments (34). The completeness

index records the proportion of identifiable specimens (NISP) that are complete (1, 17, 25). When NISP equals the minimum number of elements (MNE) fragmentation is zero, and the extent to which NISP is greater than MNE is another measure of fragmentation (1).

16. Disarticulation: First to separate from a mammal carcass is the scapula, quickly followed by separation of the mandible from the skull. Next is disarticulation of the shoulder joint and of the skull from the vertebral column. The hind limbs separate next, and once separate both forelimbs and hindlimbs disarticulate in similar fashion, from distal (metacarpals and phalanges) to proximal. The vertebral column remains intact for considerably longer than any other part of the skeleton in the order cervical, thoracic, lumbar, and sacrum.
17. Human chewing effects. Because human teeth are low and rounded, the characteristic of human chewing are distinct from that of most animals. The exception to this is chewing by chimpanzees (49). Figures 36, 37, 38, and 39 show some of the variation of deformation of cooked bones, the effects of gnawing and compression of bone, the presence of striations on bone, and the effects of incisor scraping by humans.

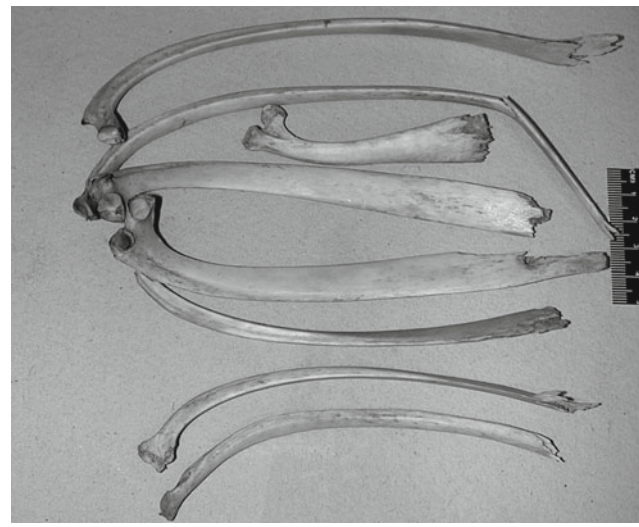

Fig. 36. Boiled sheep eaten by Koi people (South Africa) today (Brain's collection). The ends are bent and deformed, a feature produced when the bones are sucked or bent to get at the marrow.

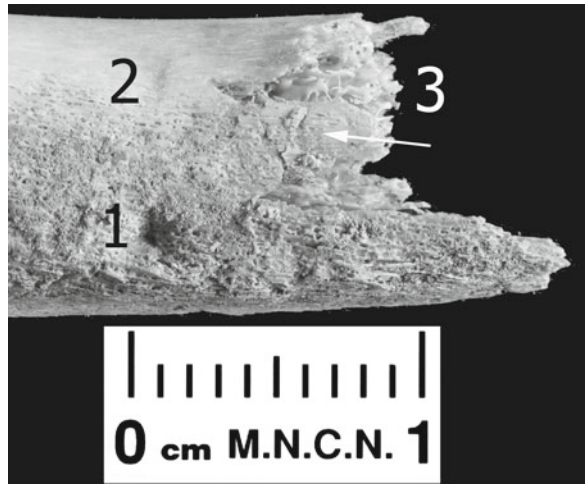

Fig. 37. Pig rib chewed raw by modern people showing a premolar puncture mark (1), a tooth gnawing linear mark (2) and compression at the fracture edge (3).

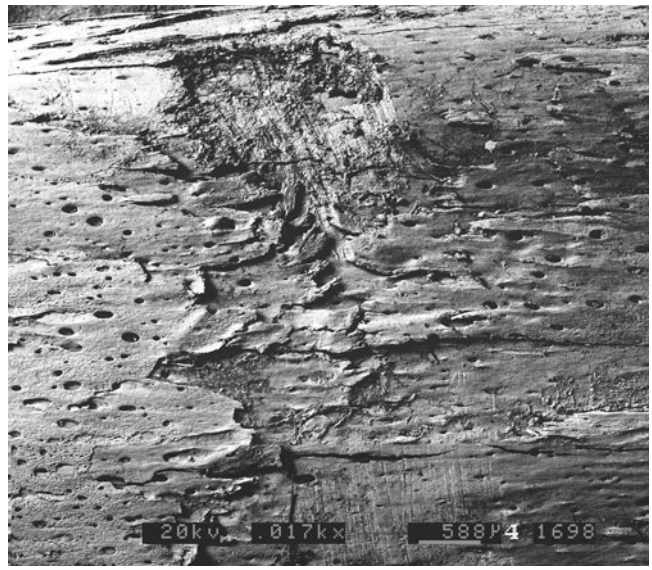

Fig. 38. SEM microphotograph of a sheep bone gnawed raw by humans today. The shape of this groove is distinct with internal striations produced by irregularities of the human incisor edge.

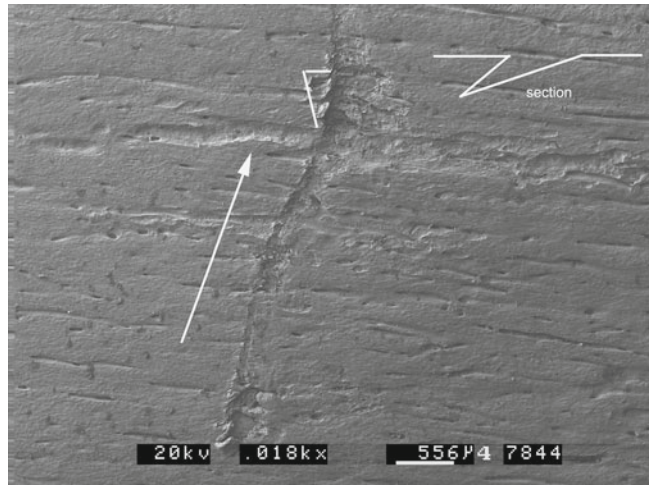

Fig. 39. SEM picture of a human gnawing mark showing characteristic traits, such as section of oblique V-shape and hertzian lateral cones that may provide the directionality of gnawing action. In this case, on the other side of the hertzian cone, lateral bone flakes can also be distinguished.

References

1. Lyman RL (1994) Vertebrate taphonomy. Cambridge University Press, Cambridge
2. Shipman P (1981) Applications of scanning electron microscopy to taphonomic problems. Ann N Y Acad Sci 376:357–386
3. Brain CK (1981) The hunters or the hunted? University of Chicago Press, Chicago
4. Binford LR (1981) Bones. Ancient men and modern myths. Academic Press, New York
5. Haglund WD, Sorg MH (eds) (1997) Forensic taphonomy: the postmortem fate of human remains. CRC Press LLC, Boca Raton
6. Haglund WD, Sorg MH (eds) (2002) Advances in forensic taphonomy: method, theory and archaeological perspectives. CRC Press LLC, Boca Raton
7. Bromage TG, Boyde A (1984) Microscopic criteria for the determination of directionality of cutmarks on bone. Am J Phys Anthropol 65:357–366
8. Bromage TG, Bermúdez de Castro JM, Fernández Jalvo Y (1991) The SEM in taphonomy research and its application to studies of cut-marks generally and the determination of handedness specifically. Anthropologie 19: 163–169
9. Shipman P, Rose J (1983) Early hominid hunting, butchering and carcass-processing behaviours: approaches to the fossil record. J Anthrop Archaeol 2:57–98
10. Olsen SL, Shipman P (1988) Surface modification on bone: trampling versus butchery. J Archaeol Sci 15:535–553
11. Fernandez-Jalvo Y, Caceres I (2010) Tafonomía e Industria Lítica: marcas de corte y materias primas. En: Rodríguez-Vidal J, Santiago A, y E. Mata (eds). Cuaternario y Arqueología. Homenaje a Francisco Giles Pacheco. Servicio de Publicaciones de Diputación de Cádiz y Servicio de Publicaciones. de Universidad de Cádiz, 169–177.
12. Andrews P, Fernández-Jalvo Y (1997) Surface modifications of the Sima de los Huesos fossil humans. J Hum Evol 33:191–217
13. Blumenschine RJ, Selvaggio MM (1988) Percussion marks on bone surfaces as a new diagnostic of hominid behavior. Nature 333: 763–765
14. Blumenschine RJ, Selvaggio MM (1991) On the marks of marrow bone processing by hammerstones and hyaenas: their anatomical patterning and archaeological implications. In: Clark JD (ed) Cultural beginings. Approaches to understanding early hominid life-ways in the African savanna. Bonn, pp 17–32
15. Cappaldo SD (1997) Experimental determinations of carcass processing by Plio-Pleistocene hominids and carnivores at FLK 22 (Zinjanthropus), Olduvai Gorge, Tanzania. J Hum Evol 33:555–597

16. Andrews P, Molleson T, Boz B (2005) The human burials at Çatalhöyük. In: Hodder I (ed) Inhabiting Çatalhöyük: reports from the 1995–1999 seasons. Çatalhöyük Research project Volume 4. McDonald Institute Monographs, British Institute of Archaeology at Ankara, Cambridge, pp 261–278
17. Andrews P (1990) Owls, cave and fossils. Natural History Museum, London
18. Brain CK (1967) Bone weathering and the problem of pseudo-tools. S Afr J Sci 63:97–99
19. Barham LS, Pinto A, Stringer C (2002) Bone tools from Broken Hill (Kabwe) cave, Zambia, and their evolutionary significance. Before Farming 2:1–16
20. Backwell LR, d'Errico F (2001) Evidence of termite foraging by Swartkrans early hominids. Proc Natl Acad Sci 98:1358–1363
21. Denys C, Fernández-Jalvo Y, Dauphin Y (1995) Experimental taphonomy: preliminary results of the digestion of micromammal bones in laboratory. CR Acad Sci 321, série II a (Paris):803–809
22. Fernández-Jalvo Y, Marín Monfort MD (2008) Experimental taphonomy in museums: preparation protocols for skeletons and fossil vertebrates under the scanning electron microscopy. Geobios 41:157–181
23. Grimm RJ, Whitehouse WM (1963) Pellet formation in a great horned owl. Auk 80:301–306
24. Raczynski J, Ruprecht AC (1974) The effects of digestion on the osteological composition of owl pellets. Acta Ornithol 14:1–12
25. Dodson P, Wexlar D (1979) Taphonomic investigation of owl pellets. Paleobiology 5:275–284
26. Lowe VPW (1980) Variation in digestion of prey by the tawny owl. J Zool 192:283–293
27. Yalden DW, Yalden PE (1985) An experimental investigation of examining kestrel diet by pellet analysis. Bird Study 32:50–55
28. Fisher DC (1981) Crocodilian scatology, microvertebrate concentrations and enamelless teeth. Paleobiology 7:262–275
29. Williams J (2002) Small mammal deposits in archaeology: a taphonomic investigation of *Tyto alba* (barn owl) nesting and roosting sites. PhD thesis, University of Sheffield
30. Fernández Jalvo Y, Andrews P (1992) Small mammal taphonomy of Gran Dolina, Atapuerca (Burgos), Spain. J Archaeol Sci 19:407–428
31. Sutcliffe AJ (1970) Spotted hyaena: crusher, gnawer, digester and collector of bones. Nature 227:1110–1113
32. Villa P, Mahieu E (1991) Breakage pattern of human long bones. J Hum Evol 21:27–48
33. Haynes G (1980) Evidence of carnivore gnawing on Pleistocene and recent mammalian bones. Paleobiology 6:341–351
34. Haynes G (1982) Utilization and skeletal disturbances of North American prey carcasses. Arctic 35:266–281
35. White TD (1992) Prehistoric cannibalism at Mancos 5MTUMR-2346. Univiversity Press, Princeton
36. Hoffman R (1988) The contribution of raptorial birds to patterning in small mammal assemblages. Paleobiology 14:81–90
37. Toots H (1965) Sequence of disarticulation in mammalian skeletons. Contrib Geol Univ Wyo 4:37–39
38. Hill A (1979) Butchery and natural disarticulation an investigatory technique. Am Antiq 44:739–744
39. Hill A, Behrensmeyer AK (1984) Disarticulation patterns of some modern East African mammals. Paleobiology 10:366–376
40. Speth JD (1983) Bison kills and bone counts. University of Chicago Press, Chicago
41. Frison GC, Todd LC (1986) The Colby mammoth site. University of New Mexico Press, Albuquerque
42. Andrews P, Cook J (1985) Natural modifications to bones in a temperate setting. Man 20:675–691
43. Behrensmeyer AK, Gordon K, Yanagi G (1986) Trampling as cause of bone durface damage and pseudo-cutmarks. Nature 319:768–771
44. Surcliffe AJ (1973) Similarity of bones and antlers gnawed by deer to human artefacts. Nature 246:428–430
45. Cáceres I, Esteban-Nadal M, Bennàsar ML, Fernández-Jalvo Y (2009) Disarticulation and dispersal processes of cervid carcass at the Bosque de Riofrío (Segovia, Spain). J Taphonomy 7:129–141
46. Turner CGII (1983) Cannibalism in Chaco Canyon: the channel pit excavated in 1926 at Small House Ruin by Frank H.H. Roberts, Jr. Am J Phys Anthrop 91:421–439
47. Pinto Llona AC, Andrews P (1999) Amphibian taphonomy and its application to the fossil record of Dolina (middle Pleistocene, Atapuerca, Spain). Palaeogeogr Palaeoclimatol Palaeoecol 149:411–429
48. Fernández-Jalvo Y, Andrews P (2003) Experimental effects of water abrasion on bone. J Taphonomy 3:147–163
49. Pobiner BL, DeSilva J, Sanders WJ, Mitani JC (2007) Taphonomic analysis of skeletal remains from chimpanzee hunts at Ngogo, Kibale National Park, Uganda. J Hum Evol 52:614–636

50. Toth N, Schick K (1993) Early stone industries and inferences regarding language cognition. In: Gibson KG, Ingold T (eds) Tools, language and cognition in human evolution. Cambridge University Press, Cambridge, pp 346–362
51. Andrews P, Fernández-Jalvo Y (2003) Cannibalism in Britain: taphonomy of the Creswelian (Pleistocene) faunal and human remains from Gough's Cave (Somerset, England). Bull Nat His Mus Lond (Geology/Palaeontology) 58:59–81
52. Fernández-Jalvo Y, Díez JC, Cáceres I, Rosell J (1999) Human cannibalism in the early Pleistocene of Southern Europe (Sierra de Atapuerca, Burgos, Spain). J Hum Evol 37:591–622

Chapter 13

Light Microscopy of Microfractures in Burned Bone

Christopher W. Schmidt and Rose Uhlig

Abstract

Bone color changes depending upon the taphonomic agents that affect it. Burning turns bone black, brown, blue, gray, and white as the bone's temperature increases and collagen is lost. It also creates diagnostic fractures that are visible at the gross level. Usually heat-altered bone is readily identified as such, but there are times when dark organic stains can mimic bone that is charred black. This paper provides a means to observe and quantify microfractures in burned bone for those instances when macroscopic observations fail to clarify if a bone fragment is actually burned; specifically, it distinguishes charred from organically stained bone. It is based upon a study of 50 calcined (burned to a bright white), charred, and organically stained bone fragments ($n = 150$) that were viewed with a standard stereomicroscope at ×30. Microfractures are readily discerned on charred and calcined bones, being more common on the latter; they are not present on organically stained bone. Charred bones may have their cortical surfaces obscured by a microlayer of adhering soft tissues as well as by microflaking of the external circumferential lamella. Overall, the methods described here allow the detection of microfractures on bone using a very simple approach and readily available technology.

Key words: Cremation, Taphonomy, Fire, Bone, Cracking, Microflaking

1. Introduction

Numerous taphonomic agents can alter the color of human bone; burning, in particular, creates significant changes. As temperature increases, burned bone departs from its normal color to a dark black and brown, then to blue and gray, and finally to a bright white—a condition known as calcined (1). Because of the diagnostic patterns of color it creates, the burning of bones is generally considered to be readily identifiable via standard visual inspection. However, there are times when the context or condition of bone can stymie the interpretation of its color and some nonthermally related taphonomic agents can render colors similar to what is seen in burned bone. Perhaps that which is most commonly encountered

Lynne S. Bell (ed.), *Forensic Microscopy for Skeletal Tissues: Methods and Protocols*, Methods in Molecular Biology, vol. 915,
DOI 10.1007/978-1-61779-977-8_13,

is solar bleaching, which turns bone white and leads to significant surface cracking that is reminiscent of calcined bone. Another agent is organic staining. This is particularly problematic in archaeological contexts where bones are buried near hearths or middens that are rich with organic material. Bones from organically rich sediments can appear dark black, such that at the gross level they look to have been charred. Additionally, this kind of staining comes from small plant and tree roots outside of anthropogenic features.

The current study provides a means of distinguishing burned and organically stained bones at the microscopic level. It focuses on fractures that form as bone is heated. At the macroscopic (i.e., gross) level, several distinctive fractures appear that are diagnostic of thermal alteration. These fractures, however, tend to be better expressed in bone that has been heated beyond the dark black or charred stage. The methods employed here use basic microscopy to view remains for the presence of microfractures (those which cannot be seen at the gross level). A sample of unburned, organically stained bones was studied to demonstrate the efficacy of the approach. The advantage to this manner of distinguishing burned from organically stained bone is its simplicity. Using a microscope to study burned bone is not new; the distinction between burned and nonburned bone has been made histologically (e.g., (2)). But, bioarchaeologists may not have the equipment, money, time, or expertise to create and study bone thin sections. By comparison, the method described here is quite easy to master and uses a standard dissecting stereomicroscope, a device that is inexpensive and commonly found in typical archaeology labs. It also speeds up the analysis; for those who work with thousands of cremated and possibly cremated fragments, expediting any part of the analytical process is of value.

1.1. Bone Fracturing at the Macroscopic Level

As bone heats up it expands, often rapidly. Because heat is not evenly spread across any bone, even in a crematorium, microvariations in temperature lead to certain aspects of bone expanding while other areas at lower temperatures do not expand or expand at slower rates. In long bones, this leads to the formation of longitudinal fractures early on in the burning process that form along the length of the shaft. Bones do not explode, but heating is a dynamic process and in experiments conducted by one of the authors (CWS) bones wobbled and audibly cracked open as oils and water rapidly emerged from deep inside. Unevenness in heating is exacerbated by soft tissues because they vary in thickness and, therefore, their ability to protect bones. Bones that are near the body surface, like cranial bones and the tibia may reach high temperatures early in the burning process while it may take some time for deeper bones to be affected. Therefore, depending upon when the burning process is interrupted, a skeleton may have bones in many stages of degradation, ranging from barely burned and charred to near complete calcination.

Fractures also form perpendicular to the long axis of bones. These are transverse fractures and they too occur early in the burning process. They can connect longitudinal fractures and lead to a checkerboard appearance or what is called checking. When flakes of cortex fall away because longitudinal and transverse fragments have intersected, very angular fractures are left behind called step fractures. They get this name because the fracture looks like a step or series of steps created by the nearly 90° intersection of the longitudinal and transverse fractures. They can be so sharp margined and symmetrical in appearance that step fractures can look like cut marks, especially when small fragments are found in isolation.

Sometimes, transverse fractures are curvilinear, meaning they arc across the bone rather than traversing in a perfectly straight line. These are thought to be caused by contractions of soft tissues as they desiccate and retreat from the heat; the soft tissues pull on the bone and affect the way the fracturing forces move transversely across the bone (3). In fact, transverse curvilinear fractures may be one of the better indicators that a bone was burned while soft tissues were present.

Rounded surfaces, like the ends of bones, tend to have reticulated fracture patterns that look like the fine cracks one sees in old paintings. For this reason, the heat-related fractures found there are termed patina. This kind of fracturing does not look like the checkerboard appearance seen on bone shafts. Patina fractures intersect at various angles and lead to a very complex web of fractures in bones that usually have burned to a gray or white color.

Thus, at the macroscopic level the ways in which bones break due to thermal exposure are well known and well documented. They can be distinguished from fractures caused by peri- and postmortem trauma and are used in conjunction with bone color to document the patterning of thermal damage on a body or particular bone (3). Therefore, it is anticipated that the study of microfractures will be most applicable when bones lack (or have obscured) the usual indicators of burning, are found in organically rich deposits, or simultaneously bear a number of confounding taphonomic alterations.

2. Materials

1. Cleaned bone fragments must be used; adhering dirt makes it difficult to see microfractures (see Note 1).
2. Fragments of any size can be studied; for the current study the fragments were 3 cm in length and at least 1 cm wide (thus, all observations were made on an area of bone that ranged between 1 and 3 cm^2).

3. All of the burned fragments used herein were human bones from archaeological and modern cremations (see Note 2).
4. The first group of bone consisted of 50 charred bone fragments. These fragments were primarily black, although the edges and endosteal surfaces sometimes were brown to gray in color.
5. The second group consisted of 50 fragments that were predominantly white in color. This group was included to see if microfracturing was more prevalent in heavily burned bone.
6. The third group consisted of 50 fragments that had a 1 cm or larger organic stain.
7. The organically stained bones had obvious plant staining including root marks (see Note 3).
8. It is recommended that only cortical areas be studied because cortical fracturing is better documented than that of trabecular bone (see Note 4).

3. Methods

1. Bone fragments were cleaned with tap water and a soft bristled brush.
2. Bone fragments are viewed with a standard stereomicroscope at ×30 magnification.
3. Most of the fragments viewed were completely burned or stained, but in cases where they were not, observations excluded normally colored areas of bone (see Note 5).
4. Microfractures are identified visually as distinct lines on cortical surfaces (see Note 6).
5. In quantitative study, microfracturing is scored as a discrete variable, being either present or absent. At least one fracture needs to be clearly visible on the cortex for fracturing to be considered present (Fig. 1 shows a large and prominent microfracture on the inner table of a calcined cranial fragment).
6. Verification is helpful with identification; in the current study, both authors scored each fragment (see Note 7).

3.1. Microfracture Patterning

Microfractures occur on charred and calcined bone, but they are more common on the latter (see Note 8). But, they are not found on every charred fragment. It appears that bone discolors and turns black before it starts to lose enough water and collagen for fractures to occur. In fact, charred fragments are more likely to have microfractures if some aspect is heated beyond a charred state. Unfortunately, that means a fragment that is starkly black in color and most likely to be confused with those having an organic stain may require other indicators of burning beyond microfracturing.

Fig. 1. Microfractures on the endosteal surface of a calcined cranial fragment. Original magnification, ×30.

3.2. Soft Tissues, Flaking

Sometimes microfractures are impossible to see on charred fragments because their surfaces are covered with a microscopic layer of burned soft tissues, which looks like a fine crust on the outer aspect of the cortex. When present, this condition makes it impossible to see the underlying bone (see Note 9). In fact, charred soft tissues appear more frequently on bones that are burned only to black than microfractures. Therefore, in many instances it may be that the presence of charred soft tissues is a better indicator of burning than are microfractures.

Another factor that affects the presence of distinct microfractures is flaking of the cortex at the microscopic level. External circumferential lamella can flake off, even in a charred state, leaving only the deeper cortex exposed. Presumably, this flaking is the result of microfracture formation and intersection. Thus, if it appears that some flaking has occurred, it likely resulted from shallow microfractures and indicates that the remains have been burned. Taphonomic agents other than burning can lead to cortical flaking. The diagnostic traits of heat-related flaking, however, are that the remaining surface from where the flaking took place will be as black as the outermost aspect of the remaining cortex, and the exposed margin will look jagged and angular under magnification marking where transverse and longitudinal fractures came together (much like the condition known as checking and step fracturing seen at the macroscopic level) (e.g., (3)).

Overall, microscopic study is recommended in those cases where the usual macroscopic indicators of burning are ambiguous or difficult to determine. If microfractures are not found, analysts are encouraged to look for charred soft tissues and/or microflaking. If these are not present and the fragments are black, they are likely that color for reasons other than burning, including organic staining.

4. Notes

1. The total sample size was 150 fragments that were not coated with any type of preservative.
2. The fragments were naturally fractured cremains from a Late Archaic site from southern Indiana (Jerger) and a modern commercial cremation donated to the lab. The study used charred and calcined fragments from both sites.
3. The organically stained remains came from a Late Archaic cemetery from southern Indiana that had no cremations and several instances of root etching and staining from plants and adjacent features.
4. The fragments that were chosen for the current study lacked trabeculae; most were midshaft fragments from long bones. Trabecular bone may have diagnostic fracture patterns and future work should look more into how trabeculae change at the microscopic level as a result of thermal exposure.
5. Partially burned bones can be studied. In fact, it is often the case that bones that are ambiguously stained are darkened incompletely.
6. Microfractures have similar morphologies to macrofractures. They may look like longitudinal, transverse, patina, step fractures, and checking.
7. Each bone fragment was initially scored by the second author (RU). The primary author (CWS) then scored the fragments independently. In instances where there was disagreement on how to score fragment color, the authors discussed the discrepancy until an agreement was reached. There were no discrepancies on the identification of microfractures; even though they are microscopic, microfractures are diagnostic and not readily confused with other types of fractures that may be present on bone.
8. A statistical analysis of the remains described herein found that 38% (19/50) of the charred fragments had microfracturing present. The microfractures were usually manifest as either longitudinal or transverse cracks (Fig. 2). In addition, thirty-one charred fragments (62%) had the cortical surface obscured, in whole or in part, by charred soft tissues. Eighty percent (40/50) of the calcined fragments showed microfracturing, while none (0/50) of the organically stained bone had microfracturing (Fig. 3). Chi-square results find a significant difference between charred and organically stained bone ($df = 1$, $\chi^2 = 23.46$) and charred and calcined bone ($df = 1$, $\chi^2 = 5.76$).
9. No attempt was made to scrape the burned soft tissue from the cortices to see if microfractures were present underneath. This may be something to consider in future studies.

Fig. 2. Charred bone with microfractures (*arrow* points out one of several on image). Original magnification, ×30.

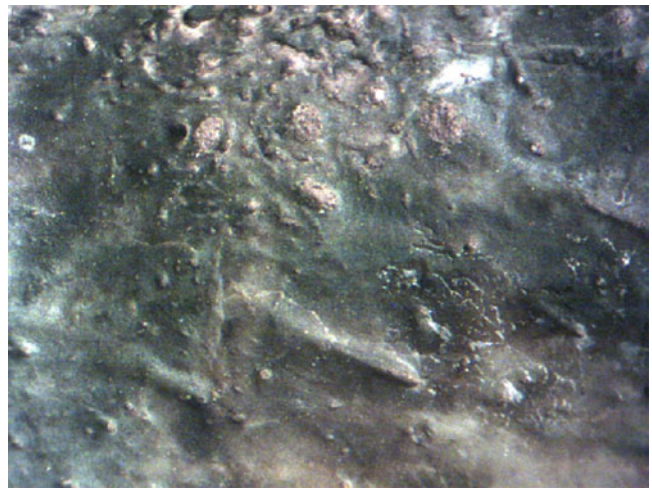

Fig 3. Organically stained bone lacking fracturing. Original magnification, ×30.

Acknowledgments

The authors wish to thank Curtis Tomak for access to some of the burned human remains used in this study and Molly Hill Schmidt for editorial comments.

References

1. Schmidt CW, Symes SA (2008) The analysis of burned human remains. Academic, Amsterdam
2. Hanson M, Chester RC (2007) Examining histology to identify burned bone. J Archaeol Sci 34:1902–1913
3. Symes SA, Rainwater CW, Chapman EN, Gipson DR, Piper AL (2008) Patterned thermal destruction of human remains in a forensic setting. In: Schmidt CW, Symes SA (eds) The analysis of burned human remains. Academic, Amsterdam, pp 15–54

Chapter 14

A Preliminary Assessment of Using a White Light Confocal Imaging Profiler for Cut Mark Analysis

Christopher W. Schmidt, Christopher R. Moore, and Randell Leifheit

Abstract

White light confocal microscopy creates detailed 3D representations of microsurfaces that can be qualitatively and quantitatively analyzed. The study describes its application to the analysis of cut marks on bone, particularly when discerning cuts made by steel tools from those made by stone. The process described comes from a study where cuts were manually made on a cow rib with seven cutting tools, four stone (an unmodified chert flake, a chert biface, a bifacially ground slate fragment, and an unsharpened piece of slate), and three steel (a Swiss Army Knife, a serrate steak knife, and a serrate saw). Kerfs were magnified ×20 and 3D data clouds were generated using a Sensofar® White Light Confocal Profiler (WLCP). Kerf profiles and surface areas, volumes, mean depths, and maximum depths were calculated with proprietary software (SensoScan® and SolarMap®). For the most part, the stone tools make shallower and wider cuts. Kerf floors can be studied at higher magnifications; they were viewed at ×100. When comparing the kerf floors of the unsharpened slate and the serrate steak knife it was found that the slate floor was more uneven, but the serrate steak knife generated more overall relief. Although preliminary, the approach described here successfully distinguishes stone and steel tools; the authors conclude that the WLCP is a promising technology for cut mark analysis because of the very detailed 3D representations it creates and the numerous avenues of analysis it provides.

Key words: Trauma, Profilometry, Topography, Pathology

1. Introduction

Determining the origin of cut marks on bone is of interest to a wide range of scientists, including paleoanthropologists, archaeologists, and forensic anthropologists (e.g., (1–13)). This study explores the potential use of a white light confocal profiler (WLCP) for cut mark analysis. The advantage of this technology is that it provides a detailed representation of microsurface morphology that can be analyzed both qualitatively and quantitatively; 3D representations are studied with metrological software employing standardized

Lynne S. Bell (ed.), *Forensic Microscopy for Skeletal Tissues: Methods and Protocols*, Methods in Molecular Biology, vol. 915, DOI 10.1007/978-1-61779-977-8_14,

computations of surface texture and profile roughness. The goal of this pilot study is to demonstrate the efficacy of the WLCP when determining the type of tool that made a particular cut mark. Overall, it is capable of generating detailed 3D representations that are analyzed with accompanying software and readily distinguishing cut marks made with steel tools from those made with stone.

The Sensofar® confocal microscope uses white light from a LED source that is focused through a minute slit over the specimen. The light is electronically manipulated to produce *x*, *y*, and *z* data as it scans the specimen in vertical planes. Data points are collected at submicron intervals with a vertical resolution of 0.005 μm. The sample is scanned vertically in steps so that every point on the surface passes through the focus window. The height of the surface at each pixel location is found by detecting the peak of the narrow axial response. Because only one or a few points of the surface are illuminated at the same time, in-plane raster scanning also is required in order to build up the axial response at each vertical step. This process builds the confocal image that is used for measurement processing.

Confocal profiling provides the highest lateral resolution that may be achieved by an optical profiler. This makes it possible to reduce the spatial sampling to 0.10 μm, which is ideal for critical dimension measurements. High numerical aperture (0.95) and magnification (×100 and ×150) objectives are available to measure smooth surfaces with steep local slopes (over 70°). The optical profiler has extremely high light efficiency and an unlimited intrinsic measurement range, and stages of almost any size may be used. Confocal algorithms provide vertical repeatability on the nanometer scale, which are proprietary for the Sensofar® model used here.

The materials and methods sections describe a recent study which helped to establish a protocol for WLCP-based cut mark analysis. This approach, while useful, marks only the beginning of this type of study. It is anticipated that, as more researchers engage in WLCP study, both cut mark data collection and analysis will improve.

2. Materials

1. Cut marks on the surface of a dry domestic cow (*Bos taurus*) rib were studied.
2. The tools used to make the cut marks included an unmodified chert flake, a bifacial chert knife, an unsharpened (dull) slate blade, a bifacially ground slate blade, a bifacial steel knife, a serrate steak knife, and a serrate steel saw blade.
3. The chert flake was a piece of medium grade chert from a chert type reference sample curated at the University of Indianapolis. It was not sharpened or retouched for the study.

4. The bifacial chert knife was a reproduction manufactured from high grade raw material (the authors did not wish to contaminate the blade of an ancient stone tool with modern bone); it was pressure flaked along its margin, which led to a serrate edge.
5. The slate fragment was a single piece that was a reproduction of an Inuit ulu. It had both unsharpened (dull) and sharpened areas along its margin; the sharpened aspect was uniformly bifacially beveled.
6. The bifacial steel knife was a standard 2.5 in. Swiss Army Knife®.
7. The serrate steel saw blade was from a Leatherman® tool. The serrations were 3 mm apart but were manufactured into the blade by honing only one side; thus, the saw blade was asymmetrical along the cutting surface.
8. The steak knife had very small serrations that were periodically interrupted by groups of larger (around 1 mm) serrations.
9. The data collecting and analytical software were SensoSCAN® 2300 version 2.45 and Sensofar's SolarMap® software, respectively.

3. Methods

1. Each implement was manually drawn across the cow rib, perpendicular to the long axis of the bone. Since the cuts were made by hand, the forces used to make them were similar but not identical.
2. Cuts were made by moving the implement in one direction; no sawing or back-and-forth cuts were made. Three cuts were made with each implement and they were labeled directly on the bone (see Note 1).
3. All profile and surface data were collected with a Sensofar WLCP housed in the Indiana Prehistory Laboratory at the University of Indianapolis.
4. The cow rib was placed on the stage and held in place with dental clay. Care was taken to position each cut mark as perpendicular to the objective lens as possible when being studied (see Note 2).
5. Observations were first made with a ×10 objective lens to locate each cut mark (see Note 3).
6. Magnification was increased to ×20 for data collection.
7. Profiles were made with SensoSCAN® software near the center of each cut mark.
8. Once the profile scan was made, the resulting profile image was restored and smoothed.

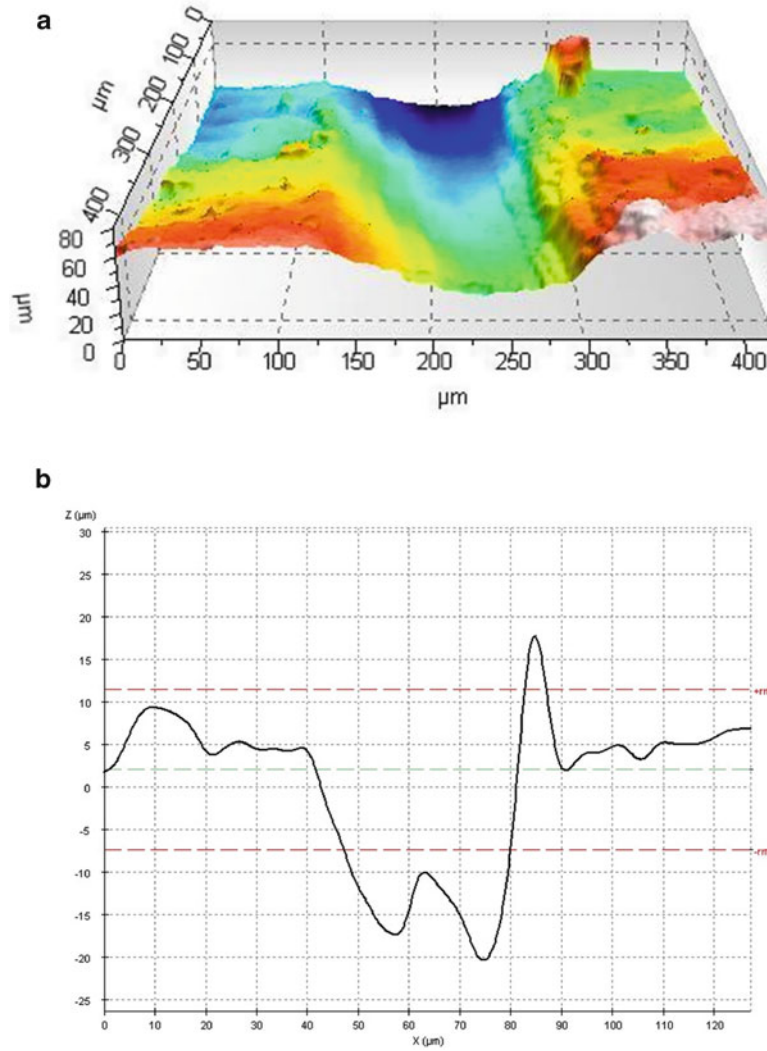

Fig. 1. (**a**) Topography of an unmodified chert flake cut, ×20. (**b**) Profile of unmodified chert flake near midpoint of cut, ×20.

9. For topography, the cut mark data clouds were processed using SolarMap® software with the following settings: Recipes: none; Operation Mode: default; Measurement: topography; Objective: ×20; and Z Scan: usually between 300 and 400 µm. Terms and Filter settings were default.
10. Data were leveled and missing data points were filled (see Note 4). 3D reconstructions were made for detailed visual inspection of each cut mark and these were compared to the profiles (Figs. 1, 2, 3, 4, 5, 6, and 7).
11. The margins of each cut mark were outlined with a mouse driven pointer and measurements were made under the "Hole/Peak" analysis option in the SolarMap® software (see Note 5).

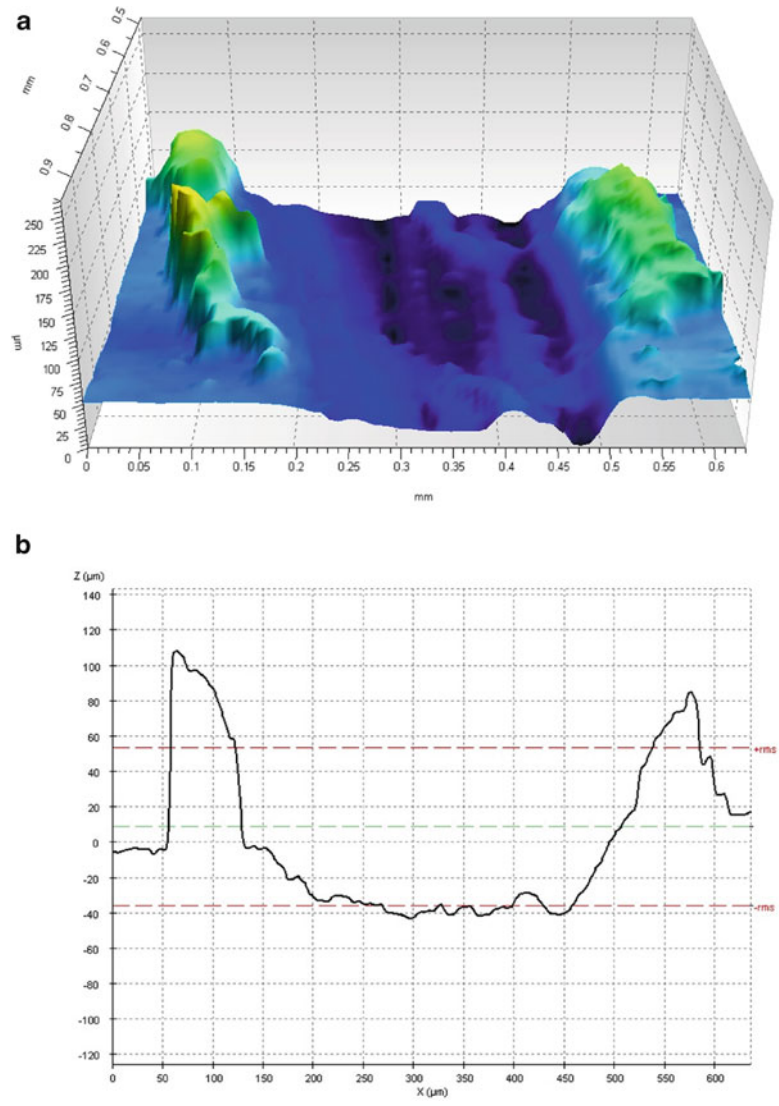

Fig. 2. (**a**) Topography of chert biface cut, ×20. (**b**) Profile of chert biface cut, ×20.

12. The measurements were: surface area, volume, maximum depth, and mean depth.
13. For surface area, the length of each cut mark was standardized to just under 500 µm (the maximum *y*-axis dimension at ×20), leaving the width to vary by implement.
14. Kerf floors of the dull slate and the serrate steak knife were magnified to ×100 and standard 2D and 3D profile and surface roughness parameters (under ISO 4287 and ISO25178, respectively) were computed (see Note 6).

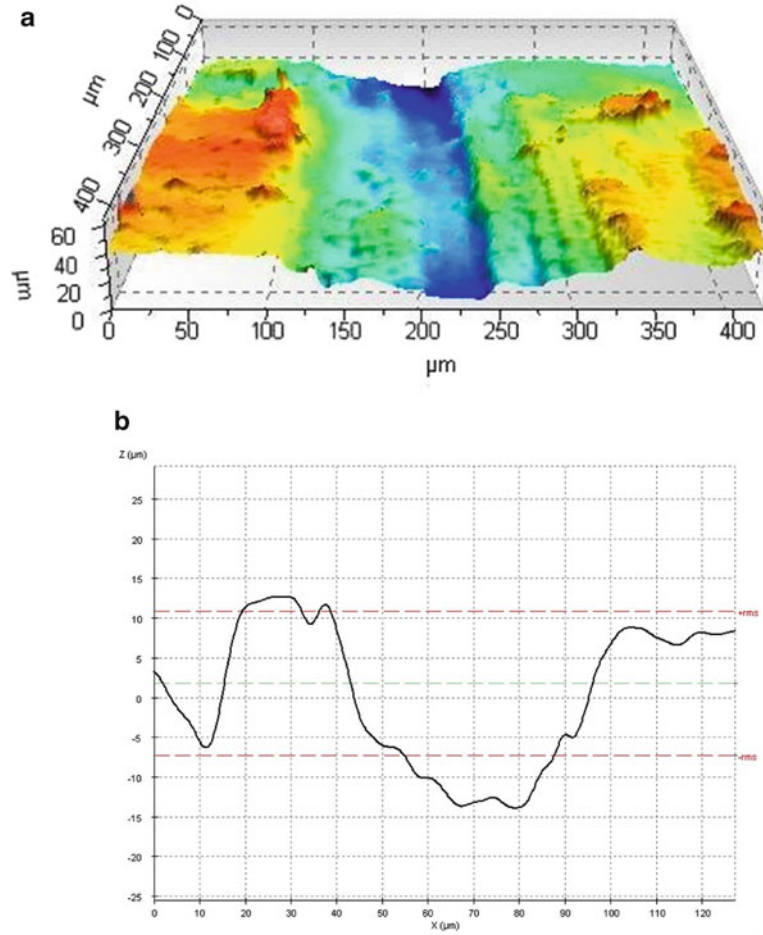

Fig. 3. (**a**) Topography of a dull slate blade cut, ×20. (**b**) Profile of dull slate blade cut near midpoint of cut, ×20.

15. For the kerf floor surface analysis, a 20 μm by 50 μm area that was free of debris was selected for study (the debris is material that falls from the kerf walls into main channel of the cut).
16. Profiles for the roughness parameters were taken at a point 75% "down" the cut mark in plan view (see Note 7).

3.1. Kerf Patterns

Surface area, maximum depth, and mean depth variables indicated differences between cut marks made by steel and stone tools. Steel tools tend to create deeper cuts relative to their surface areas while stone tools tend to make wider cuts (have larger surface areas) relative to their depths (Table 1). The surface area variable shows the width of the cutting surface as it enters the bone. The smallest surface area was the steel knife, the largest was the chert biface. Mean depth reflects the width of the tool relative to depth. This variable clearly distinguishes the stone and steel tools, as the steel tools tend to be narrower relative to their depths. In general, the

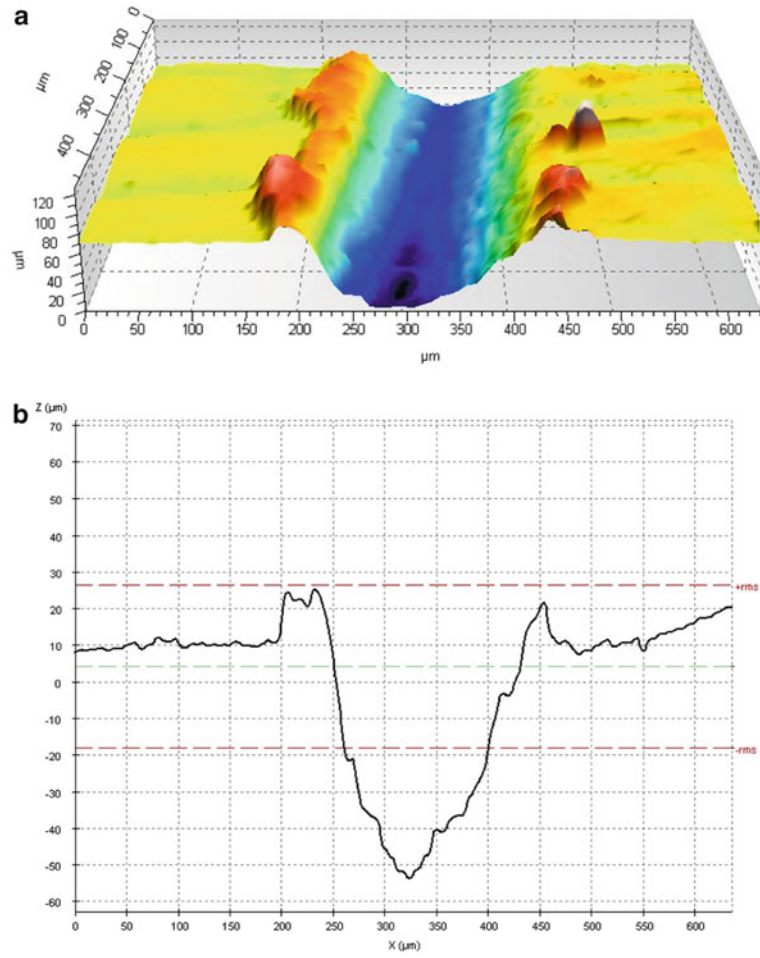

Fig. 4. (**a**) Topography of bifacially ground slate blade cut, ×20. (**b**) Profile of bifacially ground slate blade near midpoint of cut, ×20.

steel tools made deeper cuts, but recall that the cutting force was not standardized. Volume measures the amount of material removed from the bone by the cut. This variable is a poor discriminator between stone and steel tools. The smallest volume was for the chert flake and the largest volume was the serrate knife. The second smallest area was the steel knife and the second largest was the chert biface.

Specifically, the implements that created the widest cuts, as indicated by surface area, were the chert biface and the dull slate. By contrast, the steel knife created a very narrow cut mark and had a small surface area. Cut mark volumes indicate a strong association between surface area and volume. However, despite the fact that the chert flake created a wider cut, it also created a relatively shallow cut. The mean depth data indicate that the chert flake, dull slate, and chert biface produced comparatively shallow cuts relative

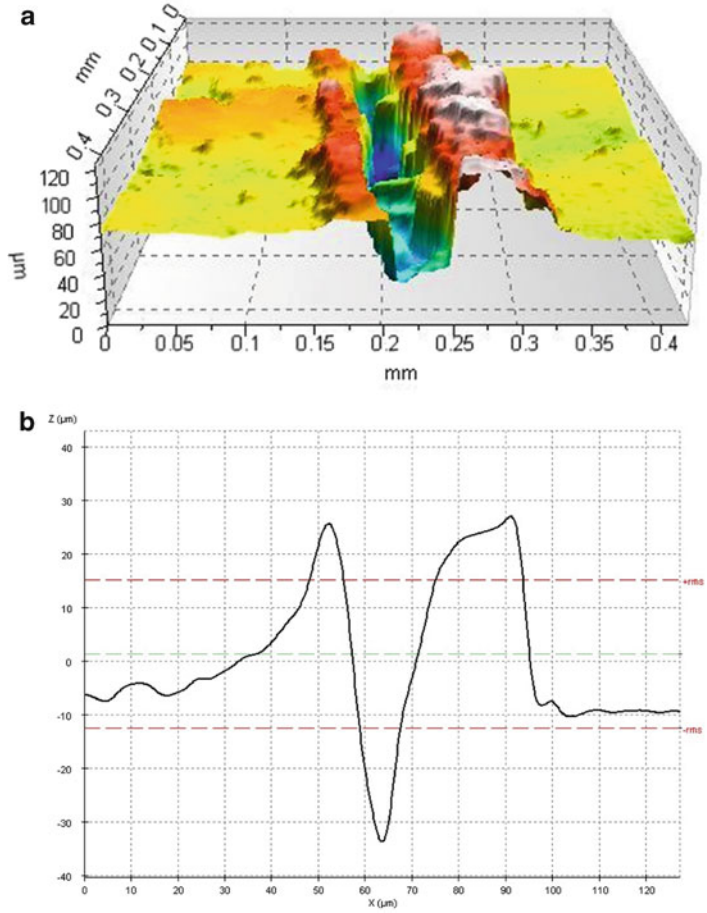

Fig. 5. (**a**) Topography of a bifacial steel knife cut, ×20. Notice the debris in the kerf that fell from the kerf walls during the cutting. (**b**) Profile of bifacial steel knife near midpoint of cut, ×20.

to their overall size. The steel implements produced cut marks that were deep compared to their overall size. Interestingly, the sharp slate had a profile that was intermediate to the other stone implements and the steel ones. The sharp slate had a very smooth cutting surface, so it created a profile similar to the steel tools. Its profile was not quite as narrow as the steel tools, however, because of its greater width when compared to the steel tools (compare Figs. 1b and 5b).

Implement symmetry was maintained in the kerfs. Bifacially beveled tools, like the sharpened slate (Fig. 5b) and the steel knife (Fig. 1b), each had kerf walls that increasingly tapered from the top of the cut mark to the floor. Likewise, asymmetric implements created assymetric cuts. This is best seen in the serrate saw (Fig. 2b), which had a vertical wall on one side and an angled side on the other, corresponding with the location of the serrations.

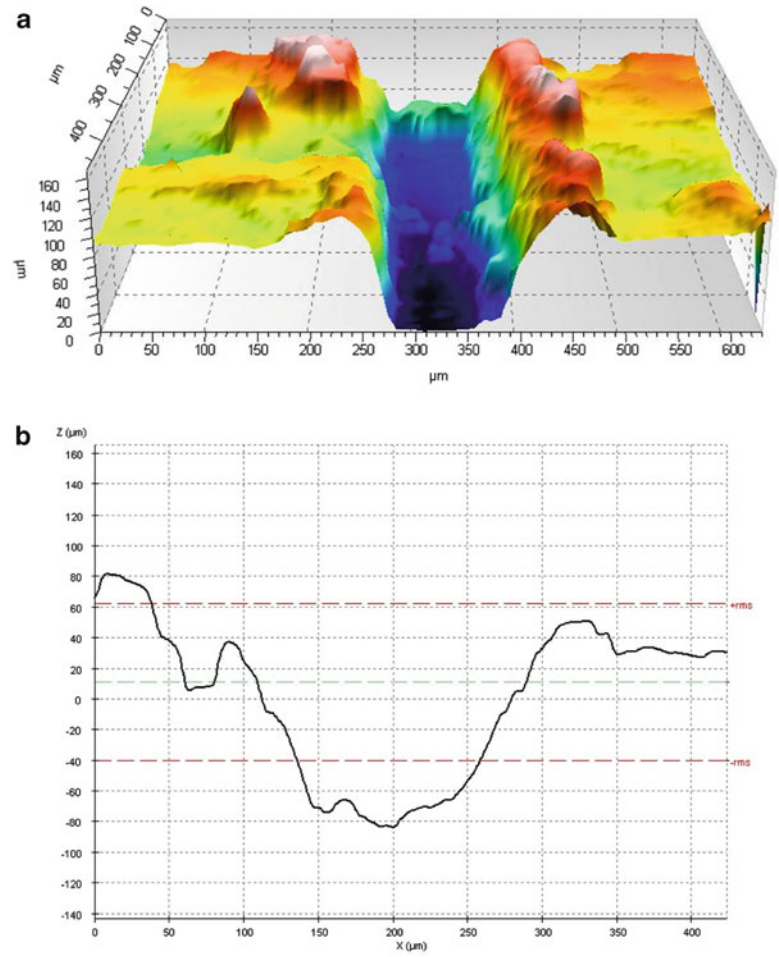

Fig. 6. (**a**) Topography of a serrate steak knife cut, ×20. (**b**) Profile of a serrate steak knife near midpoint of cut, ×20.

The ×100 kerf floor and profile data demonstrate additional differences between the dull slate and the serrate steak knife. The floor surface parameters indicate that the serrate saw removed more bone and had a greater overall depth of cut. The profile parameters, however, indicate that the floor of the dull slate was rougher. Figures 8 and 9 show the profiles and their distinctive differences. The dull slate floor is very rough in that there are many peaks and valleys evident in the profile. But, the overall height of the profile is greater for the serrate steak knife. The vertical scale shows that the highest and lowest points along the serrate knife profile exceed those of the dull chert. The raw surface and profile roughness parameters are not included here because the sample only includes two implements.

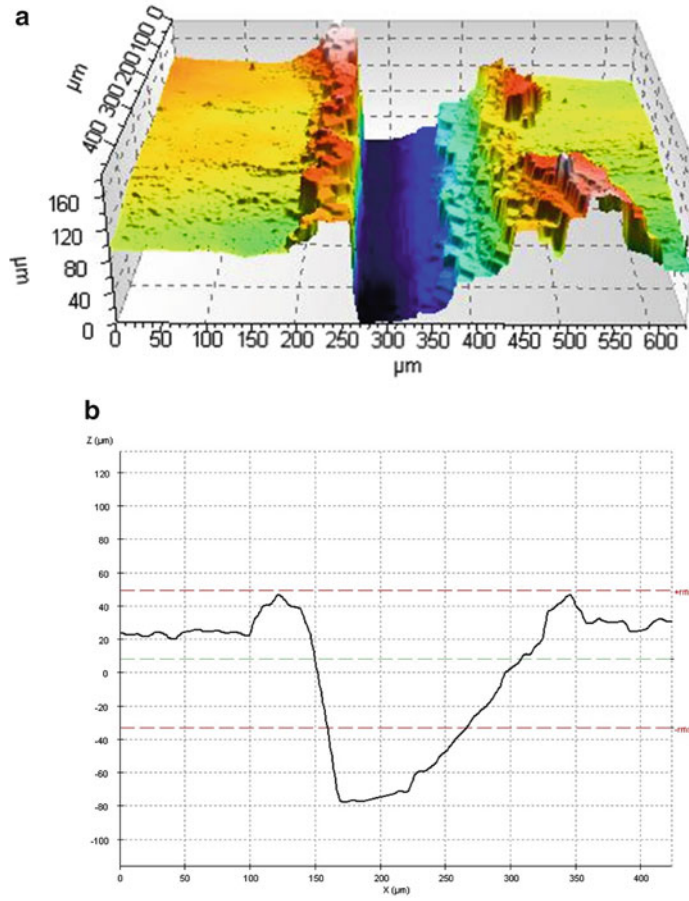

Fig. 7. (**a**) Topography of a serrate steel saw blade cut. Notice the asymmetry in the cut, which is consistent with the unifacial beveling of the saw, ×20. (**b**) Profile of serrate steel saw blade near midpoint of cut, ×20.

Table 1
Order of cutting implements for each cut mark variable, ranked from smallest to largest

Surface (µm²)	Volume (µm³)	Max depth (µm)	Mean depth
Steel knife	Chert flake	Chert flake	Chert flake
Chert flake	Steel knife	Dull slate	Dull slate
Steak knife	Dull slate	Chert biface	Chert biface
Sharp slate	Sharp slate	Sharp slate	Sharp slate
Serrate saw	Steak knife	Steak knife	Steel knife
Dull slate	Chert biface	Steal knife	Steak knife
Chert biface	Serrate saw	Serrate saw	Serrate saw

3.2. Considerations

The power of the WLCP to discriminate stone and steel tools is almost instantly obvious. Where determinations are more challenging are where similarly shaped and/or sharpened implements are compared (see Note 8). There are, however, a few overall trends that are worth noting. For the most part, steel tools tend to create kerfs that are narrower relative to their depths. Stone tools, by contrast, tend to make cuts that are wider, especially near the bone surface. Serrate steel tools create narrow cuts at the surface, but have wider floors than non-serrate knives. Differences between non-serrate and serrate and steel and stone tools have been documented before using the SEM (10). Symes et al. (10) found that serrate tools leave diagnostic striae on kerf walls, while Greenfield (4) found that stone tool marks were shallower and more variable than those created by steel, which created cuts that were steeper and better defined. He provided detailed descriptions of cut mark appearances and drew profiles based upon what he saw at magnifications ranging from ×30 to about ×200. His results were similar to what Walker and Long reported in 1977 and to what was observed in the current study. What the SEM based studies were not able to do was generate data to describe the cut marks; all of the interpretations were made from visual inspection of micrographs, which limited the information available to the analysts. By contrast, the WLCP generates both visual representations as well as surface and profile data that can be used together to make a determination. Certain cut marks are difficult to distinguish visually, especially when they are made by similar tools. Quantitative representations give analysts more to work with and may eventually serve to dependably discern numerous types of cutting implements.

A point worth repeating is that asymmetry in cutting devices is reflected in the kerfs. However, all of the cuts created for this study were made keeping the implement blade perpendicular to the cow bone. Cuts made in archaeological or forensic contexts may not be formed with the blade at such a right angle, which could lead to asymmetry that was not observed in the current analysis (i.e., (10)). Future testing could address this concern and diagnostic signs of obliquely oriented cuts may be identified.

Finally, the approach to cut mark analysis described here is based upon the study of several cutting implements but it only includes a small fraction of the total number of bladed instruments that could leave marks on bones. Cut marks from hundreds of implements, ranging from scissors to power tools, need to be studied and characterized. The hope is that future analysts will follow the guidelines provided here and construct a 3D kerf database comprised of profiles and floor surfaces that can be drawn upon to identify any particular implement. The effort necessary is sizable, but the payoff for those who study cut marks will be significant.

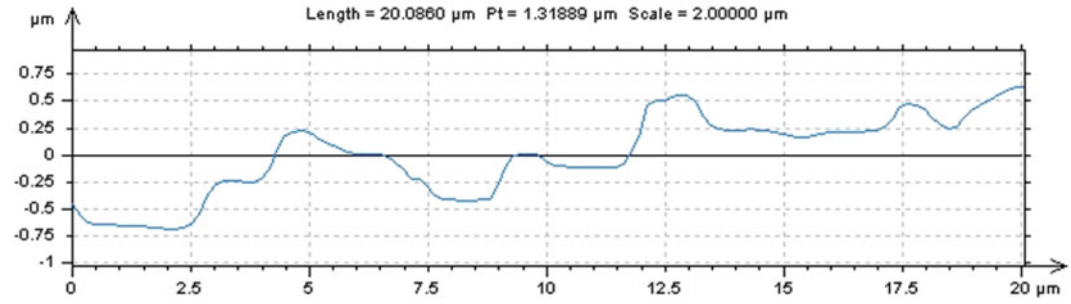

Fig. 8. Dull slate blade floor profile at a point 75% along cut mark, ×100.

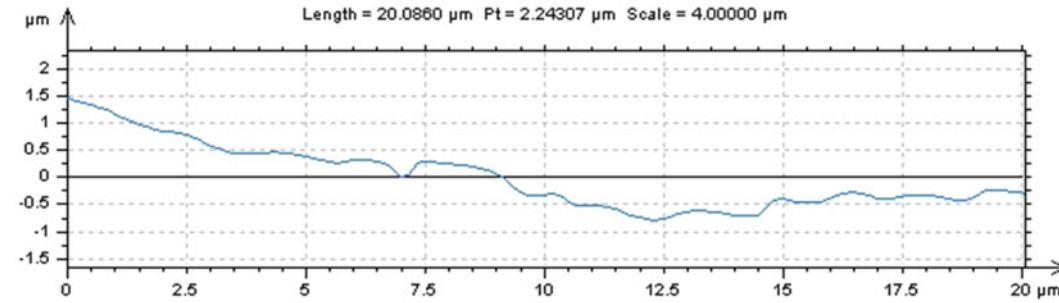

Fig. 9. Serrate steak knife floor profile at a point 75% along cut mark, ×100.

4. Notes

1. The forces used to create cut marks were not standardized; this gave the cuts natural variations, but standardizing forces may benefit future studies because it would better control for the depth an implement penetrates.
2. It is not necessary to make all cuts perpendicular to the bone surface, but, the cut angle needs to be documented so that the kerf data are appropriately collected and compared. For example, two cuts made with a single implement with identical force will generate different kerf shapes if one cut is made perpendicular to the bone surface and the other is made obliquely. Variations in the angle, force, and direction of cut marks (even those that are precisely made) may be caused by subtle changes in the integrity and shape of the bone being cut. Due to the heterogenous nature of cut marks, it is recommended that data be collected from at least three locations along the kerf. In all likelihood cuts found on archaeological bone or in forensic

cases will bear the microscopic imperfections and nuances in cut shape and size that were identified in this study.

3. Comparisons should be made at the same magnification. For the current study ×20 was the best compromise between the amount of each cut mark that was quantified and the level of detail. Higher magnifications may not include the entire kerf and lower magnifications may not generate enough detail.
4. The initial profile curves look incomplete when first generated by the software. It is necessary to use the "restore" option to complete the profile. All of the profile curves were smoothed. This should be done consistently so that smoothed and unsmoothed curves are not compared.
5. Topographic images require having empty data regions filled. This is necessary because the entire extent of an extremely vertical surface may not come into contact with the light from the microscope.
6. The ISO measurements are included in the SolarMap® software. There are other ISO options available, but these measurements seemed most applicable to the current study because they addressed volumes and areas of 3D spaces.
7. Measuring at a point 75% down the cut mark allowed for standardization. But, this point was chosen rather arbitrarily and does not denote a particularly significant landmark. Future studies may use specific landmarks (i.e., points where the cut changes in morphology) for making profiles.
8. A blind test was conducted to see if one author (Schmidt) could determine from the data a cut that was made by another author (Moore). Moore made three cuts; Schmidt was not present at the time of the cuts and had no knowledge of the implements that were used for each. Using visual inspection of the 3D surface models, the profiles, and the surface data, Schmidt was able to clearly distinguish the stone vs. steel tools. However, it proved more difficult to determine the specific stone or steel tool that was used. In general, the serrate biface and the dull slate created similarly wide and shallow cuts. Among the steel tools the serrate steak knife and the serrate saw made similar marks (in Table 1 dull slate and the serrate biface are ranked very similarly for three of the four variables as are the serrate steak knife and the serrate saw). Using the cut mark topographic and profile data, two of the three blind test cutting implements—the chert biface and the sharpened slate—could be specifically identified. However, the chert flake was not successfully identified because the cut that was made by Moore was shallower and wider than the previous cuts, resulting in kerf data that were similar to the dull slate.

Acknowledgments

Thank you to Molly Hill Schmidt for editorial comments and to Lynne Bell for her patience and support for this chapter. Funding was provided by the National Science Foundation (to CWS), BCS-0922930.

References

1. Blumenschine RJ, Marean CW, Capaldo SD (1996) Blind tests on inter-analyst correspondence and accuracy in the identification of cut marks, percussion marks, and carnivore tooth marks on bone surfaces. J Archaeol Sci 23:493–507
2. Lewis JE (2008) Identifying sword marks on bone: criteria for distinguishing between cut marks made by different classes of bladed weapons. J Archaeol Sci 35:2001–2008
3. D'Errico F, Backwell F (2009) Assessing the function of early hominin bone tools. J Archaeol Sci 36:1764–1773
4. Greenfield HJ (1999) The origins of metallurgy: distinguishing stone from metal cutmarks on bones from archaeological sites. J Archaeol Sci 26:797–808
5. Potts R, Shipman P (1981) Cut marks made by stone tools on bones from Olduvai Gorge, Tanzania. Nature 291:577–580
6. Sansoni G, Cattaneo C, Trebeschi M, Gibelli D, Porta D, Picozzi M (2009) Feasibility of contactless 3D optical measurement for the analysis of bone and soft tissue lesions: new technologies and perspectives in forensic sciences. J Forensic Sci 54:540–545
7. Seetah K (2008) Modern analogy, cultural theory and experimental replication: a merging point at the cutting edge of archaeology. World Archaeol 40:135–150
8. Shipman P, Rose JJ (1983) Evidence of butchery and hominid activities at Torralba and Ambrona: an evaluation using microscopic techniques. J Archaeol Sci 10: 465–474
9. Shipman P, Rose JJ (1988) Surface modification on bone: trampling versus butchery. J Archaeol Sci 15:535–553
10. Symes SA, Williams JA, Murray EA, Michael Hoffman J, Holland TD, Saul JM, Saul FP, Pope EJ (2002) Taphonomic context of sharp-force trauma in suspected cases of human mutilation and dismemberment. In: Haglund WD, Song MH (eds) Advances in forensic taphonomy: method, theory and archaeological persp ectives. CRC Press LLC, Boca Raton, FL, pp 403–433
11. Thali MJ, Taubenreuther U, Karolczak M, Braun M, Brueschweiler W, Kalender WA, Dirnhofer R (2003) Forensic microradiology: micro-computed tomography (Micro-CT) and analysis of patterned injuries inside of bone. J Forensic Sci 48:1336–1342
12. Walker PL, Long JC (1977) An experimental study of the morphological characteristics of tool marks. Am Antiq 42:605–616
13. White TD (1992) Prehistoric cannibalism at Mancos 5MTUMR-2346. Princeton University Press, Princeton, NJ

Chapter 15

Identification of Cooked Bone Using TEM Imaging of Bone Collagen

Hannah E.C. Koon

Abstract

Mild heating (≤100° C, 1 h)—typical of cooking—does not lead to detectable changes in any biochemical parameter yet measured; consequently bones that have been cooked, but which have not reached a temperature that will induce charring go undetected. We have used a microscopy based approach to investigate changes in the organization of the bone protein, collagen, as it is heated, using bone from heating experiments, short term burials, and archaeological sites. The work has revealed that the presence of a mineral matrix stabilizes the collagen enabling the damage to accumulate, but preventing it from causing immediate gelatinization. Once the mineral is removed, the damage can be observed using appropriate visualization methods. This chapter describes the transmission electron microscopy (TEM) technique that has been used to detect cooked bone by visualizing minor heat-induced damage at the level of the collagen fibril.

Key words: Transmission electron microscopy, Bone collagen, Collagen fibrils, Cooked bone, Heated bone, Gelatinisation, Positive staining

1. Introduction

A technique that can determine whether a bone has been cooked, but not heated to such an extent that it has become burnt, has both forensic and archaeological applications. The problem with detecting cooking is that the bone temperature remains relatively low (≤100° C) and there are currently no physical or wet chemical methods able to detect changes at this temperature. The reason probably lies in the fact that the dominant organic component of bone is mineralized collagen and our work has revealed that mineral provides a huge stabilizing affect to the collagen. As a consequence, bone must be heated in excess of 150° C (1) or boiled at 95° C for >9 h (2) before the collagen converts to gelatine and there is a detectable drop in concentration or change in composition.

Lynne S. Bell (ed.), *Forensic Microscopy for Skeletal Tissues: Methods and Protocols*, Methods in Molecular Biology, vol. 915, DOI 10.1007/978-1-61779-977-8_15,

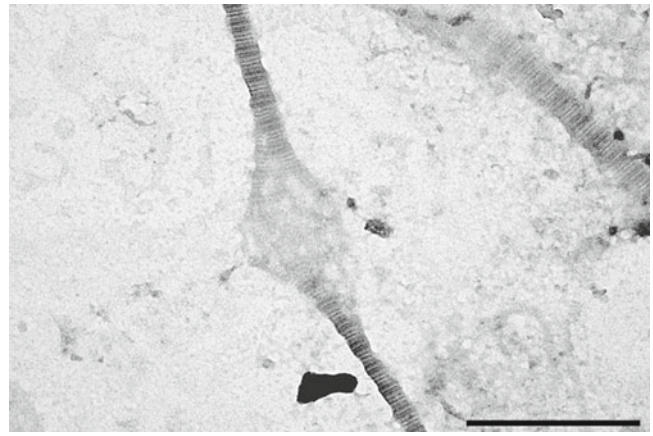

Fig. 1. A transmission electron microscopy (TEM) image showing a close up of a *Beaded* region on a heat damaged fibril. The *Beaded* region appears about to separate to form smaller fragments. The scale bar is 500 nm.

However, we have identified subtle structural changes within the collagen at milder temperatures.

The collagen molecules are packing into long robe-like structures called fibrils which are tens of nanometres in diameter and a few microns in length and therefore can only be observed under an electron microscope. As a bone is heated we have observed that the collagen accumulates regions of damage along the length of the fibrils and at the ends. These subtle heat-induced changes are not visible whilst the collagen is encased in mineral; however once the mineral is removed and the fibrils are stained and viewed under the microscope it is possible to detect this damage (Fig. 1).

A transmission electron microscopy (TEM) analysis of the integrity of collagen fibrils was first used to look at factors affecting the toughness of meat (3). Later the same approach was used to examine the effect of boiling on fish bone collagen (4). More recently we have refined the technique and applied it to cooked mammalian bone from heating experiments, experimental burials, and archaeological sites (5, 6). We have also quantified the degree of heat-induced damage by classifying the collagen fibrils as undamaged or exhibiting one of the two forms of alteration, *Beaded* and *Dumbbell* the latter of which appears to be a more advanced stage of damage. By recording the damage in this way it is possible to differentiate between uncooked material and bone heated at the mild temperatures which are associated with cooking (Fig. 2).

The method can be split into three main parts: the first involves extracting the collagen component from the bone. Common collagen extraction techniques such as boiling, drilling, or powdering are not applicable for this method because they will introduce heat to the bone or cause fragmentation of the collagen fibrils (Fig. 3). This method therefore employs a careful extraction of bone shards followed by a mild demineralization step. Two different demineralization

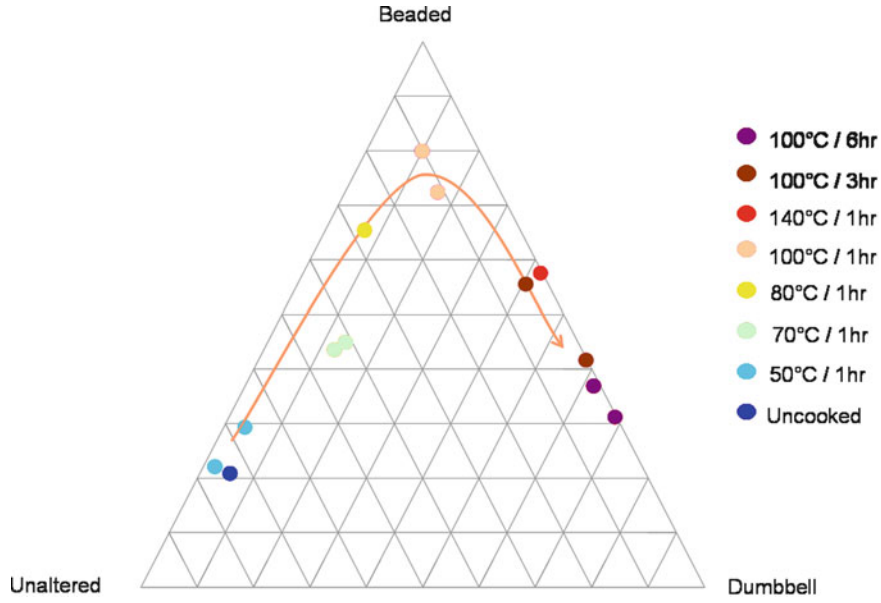

Fig. 2. A ternplot showing the results of heating experiments conducted on mid-shaft femur bovine bone. A ternplot is a way of showing the contributions of three components on a single graph; thus it is useful for showing the percentage of Unaltered, Beaded, or Dumbbell observed in each sample. It has been set up so that a point in the *left-hand* corner of the *triangle* would represent a sample containing only Unaltered fibrils, a point in the *upper* corner would contain 100% Beaded fibrils and a point in the *right-hand* corner would contain 100% Dumbbells. Each point represents the proportion of Unaltered, Beaded, and Dumbbell type fibrils recorded from each sample (mean values from two analyses of 100 fibrils). Different *colored* points represent different heating regimes. The *arrow* follows the trend in alteration from the least extreme through to the most extreme heating regime.

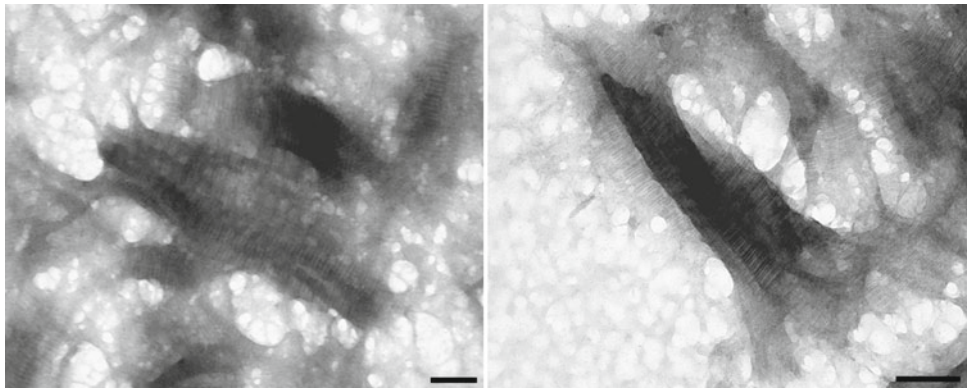

Fig. 3. TEM images of collagen from bovine bone which, prior to demineralization, has been powdered under liquid nitrogen using a spex-mill. The scale bars are 200 nm.

methods are described. In the majority of cases the cold acid method is advised because it is faster and also because it causes the fibrils to swell and in doing so accentuates the damaged regions. There are however a couple of exceptions including when dealing with poorly preserved archaeological bone which has a low collagen content or bone from young individuals (≤5 years). In both cases the acid treatment may cause the fibrils to swell to such an extent that they convert

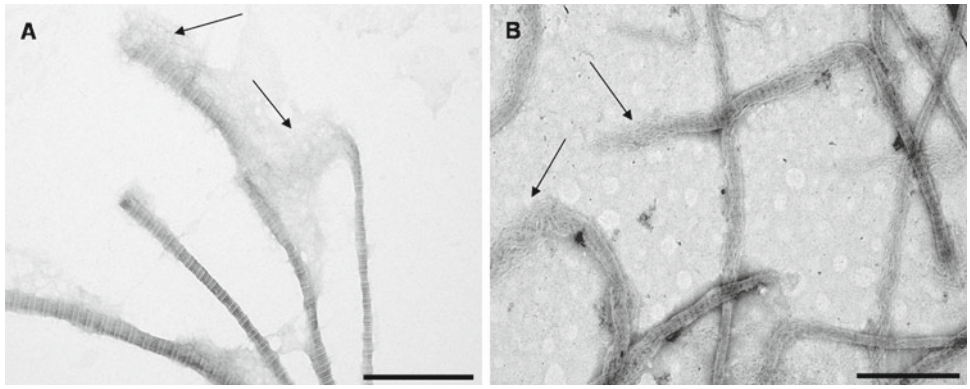

Fig. 4. Examples of collagen fibrils exhibiting frayed ends due to heat damage (indicated by the *arrows*). The alternating *dark* and *light* banding pattern along the fibrils are typical of collagen and is caused by the gap and overlap regions within the molecular packing of the fibril. The samples have been prepared using (**a**) positive stain (see Subheading 3 for preparation details) and (**b**) negative stain. The negatively stained sample was prepared using 5 mL of 3% w/v Phosphotungstic acid adjusted to neutral pH. A PBS solution containing the previously homogenized sample was mixed with the stain in the same pipette. The solution was then dropped onto a grid and left for 1 min before any excess liquid was wiped away. Note that damaged regions observed in heated samples are present after both negative and positive staining treatment and are therefore not due to a reaction of the specimen to the positive staining treatment. The scale bars are 500 nm.

to gelatine, therefore the milder ethylenediamine tetraacetic acid solution (EDTA) demineralization method is advised.

Once the collagen has been extracted from the bone mineral the next stage is to liberate the individual fibrils, stain them, and then apply them to a TEM grid. A collagen specimen is difficult to see under normal conditions in an electron image because the atomic masses of the elements which make up collagen (mainly oxygen, carbon, and nitrogen) are not high enough to produce powerful scattering of electrons. Thus in order to view collagen under the TEM, specimens must first be stained with heavy metals which will scatter the electron beam and enhance the contrast of the image.

Two common methods for visualizing collagen under the TEM are by negative or positive staining. In the former the object remains unstained but is embedded in a dried film of heavy metal salt. The stain surrounds the molecules and penetrates into any open irregularities on the surface, such as the gap regions along the collagen fibril. With this technique the specimen appears light on a dark background. Positive staining involves treatment of the specimen with a chemical that increases the mass density. The sample is immersed in a heavy metal salt stain, but unlike in the case of negative staining, this is later washed away. Some of the heavy metal ions remain attached to charged groups on the surface of the collagen fibril. For example, phosphotungstate ions are negatively charged and so will react with the positively charged groups on the collagen. Uranyl acetate will react with negatively charged groups such as the carboxyl side chains of aspartic acid and glutamic acid residues. When positively stained, the collagen fibrils appear dark against a light background (Fig. 4).

Negative staining has advantages over the positive staining technique in that the preparation method is simpler and quicker. However "edge detail" is obscured by the stain to a variable extent and it is often difficult to distinguish heat damaged regions along the fibrils from areas where dried stain has accumulated. Therefore for this method a double positive staining technique is employed. Phosphotungstic acid (PTA) staining alone proved insufficient to visualize the damaged collagen fibrils therefore double staining with PTA and uranyl acetate are used in this method as this has been shown to provide greater contrast (7).

2. Materials

2.1. Preparation of Bone Shards

1. Water-cooled diamond band saw (Exakt, Germany) or hack saw.
2. Hammer.
3. 3 mm mesh sieve.

2.2. Demineralization

1. Hydrochloric acid solution (HCl) (0.6 M) diluted with water from a 12 M stock solution (Aristar sp. gr. 1.18, BDH lab supplies, Poole). Store in a screw-topped glass bottle at 4° C for up to 6 months. (See Note 1).
2. EDTA (0.5 M, pH 7.4) prepared by dissolving 93.06 g EDTA disodium salt (GPR, BDH) in 500 mL water. The pH is adjusted to 7.4 using 0.5 N sodium hydroxide (NaOH) (Anala R, BDH) and the solution is stored in a screw topped plastic bottle at room temperature for up to 6 months. (See Note 2).
3. Phosphate buffer (PBS) (pH 7) prepared by dissolving 31.2 g of Sodium dihydrogen phosphate (NaH_2PO_4, $2H_2O$) (GPR, BDH) in 1 L water. A solution of disodium hydrogen phosphate (Na_2HPO_4, $12H_2O$) (analytical grade, VWR international) is also prepared by dissolving 28.39 g in 1 L of water. 19.5 cm^3 of NaH_2PO_4 solution was then added to 30.5 cm^3 of Na_2HPO_4 solution and made up to 100 cm^3 with water to bring the buffer to pH 7. The PBS is stored in a screw topped glass bottle until required.
4. Roller Mixer SRT1 (Stuart Scientific).

2.3. Separation of Collagen Fibrils and Staining with PTA

1. 1% w/v solution of Phosphotungstic acid (PTA) (Agar Scientific Ltd.) is prepared in water. The pH of the solution was raised to pH 7 with 0.5 N NaOH. Store in a screw-topped glass bottle at 4° C for up to 1 month.
2. Homogeniser (Yellowline, DI25 basic).
3. Ice bath.

2.4. Preparation of Sample Grids and Staining with Uranyl Acetate

1. 2% w/v solution of uranyl acetate (Agar Scientific Ltd., Essex) is prepared in a 50/50% solution of water and ethanol (absolute, analytical reagent grade, Fisher Scientific UK Ltd., Leicestershire). Uranyl acetate is light sensitive therefore store the solution at 4° C in a screw-topped glass bottle wrapped in foil and sealed with parafilm. Store for up to 6 months but filter the solution prior to use to remove precipitates.
2. 50:50 solutions of ethanol and water.
3. Formvar film grids (Agar Scientific Ltd., Essex) 300 mesh, 3 mm diameter copper grids with a formvar and carbon coating (see Notes 3 and 4).
4. Dental wax (Agar Scientific Ltd., Essex).
5. Grade 1 filter paper.
6. Curved fine tipped forceps and self-closing fine tipped cross-over forceps (see Note 5).

2.5. TEM Analysis

1. Lint-free Velin tissue (Agar Scientific Ltd., Essex).
2. Curved fine tipped forceps.

3. Methods

3.1. Preparation of Bone Shards

This technique requires approximately a 60 mg sample of small bone shards (60 mgs of fresh bone should contain 15–20 mgs of collagen, see Note 6 for further details on sampling archaeological bone).

1. A cross section of bone is removed using a water-cooled electric saw. If this is not available a hack saw can be used (see Note 7). Two cuts are made approximately 1 cm apart. A screwdriver is then wedged between one of the cuts in order to lever out the section. The cross sections are then broken into smaller shards using a hammer.
2. To ensure complete demineralization there should be a degree of uniformity and an upper limit to the size of the shards (≤3 mm largest dimension). This can be achieved by putting the shards through a 3 mm mesh sieve.

3.2. Demineralization

3.2.1. Acid

1. 60 mg of bone shards are placed in a 2 mL Eppindorf tube with 2 mL of cold 0.6 M HCl and the lid is sealed with parafilm.
2. Several of these tubes are then placed into a 25 mL Universal tube and this is transferred on to a roller mixer or other agitation device, this apparatus should be placed in a refrigerator or cool room at 4° C (see Note 8).

3. The HCl solution is changed after 4 h and again after 24 h and then left for a further 6 days.
4. After the period of demineralization, the acid is removed with a pipette and the demineralized shards are washed five times (1× PBS followed by 4× water), each time 2 mL of the washing solution is added, the tube is then briefly vortexed and the washing solution is removed with a pipette. (See Note 9).

3.2.2. EDTA

1. 60 mg of bone shards are placed in a 25 mL universal tube with 15 mL of 0.5 M EDTA and the lid of the tube is sealed with parafilm. The tube is then placed on a roller mixer at room temperature.
2. The EDTA solution is changed after 24 h and then every 2–3 days for 2 weeks.
3. After the period of demineralization, the EDTA is removed with a pipette and the demineralized shards are washed ten times with water, each time 10 mL of water is added, the tube is then briefly vortexed and the washing solution is removed with a pipette. After the last wash the shards are left in the PBS solution overnight and stirred on the roller mixer. (See Note 9).

3.3. Separation of Collagen Fibrils and Staining with PTA

1. The demineralized bone shards are placed in a 25 mL tube with 3 mL of PTA solution. In order to liberate the individual collagen fibrils the solution is homogenized for 3 min. To maintain a low temperature the tube is placed in an ice bath and homogenization is conducted in 30 s bursts with 30 s intervals. (The head of the homogenizer must be disassembled and cleaned thoroughly with water before processing each new sample, to minimize cross contamination.) (see Note 10).
2. The resulting cloudy solution is centrifuged at 3,000 × *g* and 4° C for 15 min. Afterwards the supernatant is discarded and the remaining pellet is resuspended in 1 mL of PTA and mixed using a desktop vortex.

3.4. Preparation of Sample Grids and Staining with Uranyl Acetate

1. Two formvar grids (per sample) are laid onto a petri dish, shiny side up, and a drop from the homogenized collagen solution is pipetted on top. The grids are then left for 5 min in order for the collagen fibrils, suspended in the drop of solution, to drift down onto the grid and adsorb onto a carbon-coated formvar film. (Figure 5a).
2. The grid is then picked up with cross-over forceps and the excess liquid is drawn away from the grid surface by placing a piece of filter paper at the very edge of the grid which produces a wicking action (Fig. 5b).
3. The forceps are then propped against the side of a petri dish and the grid is left until it completely dries off.

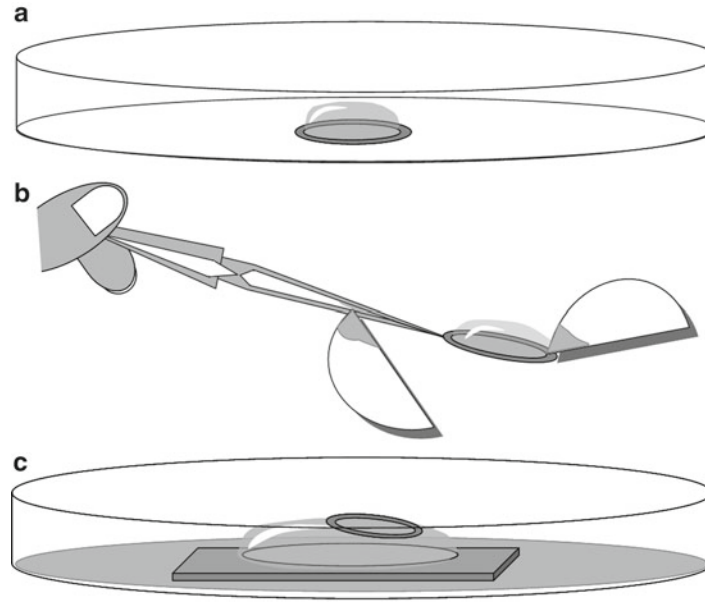

Fig. 5. A series of schematic diagrams showing different steps involved in staining and adsorbing the collagen fibrils onto a TEM grid. (**a**) A grid is placed within a petri dish and a drop of the homogenized collagen fibrils, suspended in PTA, is pipetted on top. (**b**) After 5 min the excess liquid is wicked away by carefully touching a tip of filter paper to the edge of the grid. During this step and especially later when washing the grids, liquid can collect between the prongs of the forceps, remove this with more filter paper before opening the forceps. (**c**) In another petri dish place a piece of filter paper dampened with the diluted ethanol solution. Pipette a drop of uranyl acetate onto a piece of dental wax on the filter paper (the dental wax helps the drop to keep its shape) then float the grid, specimen side down, onto the drop. If it sinks dry the grid off and try again. This whole system should be left for 30 min and covered as uranyl acetate is light sensitive.

4. A piece of filter paper is placed into another petri dish and dampened with the ethanol/water solution. A square of dental wax is then placed on top of the filter paper and a 0.5 mL drop of uranyl acetate is pipetted on top.
5. The dried grid is transferred from cross over to curved forceps and manipulated so that the grid can be floated on top of the drop of uranyl acetate, specimen side down (see Note 11 and Fig. 5c). The petri dish is then covered with an opaque lid and left for 30 min.
6. The grids are then picked up with crossover forceps and rinsed thoroughly with the ethanol/water solution and then with water. The excess liquid is removed with filter paper and then the grids are left to air-dry.
7. The sample grids can be analyzed straight away or else stored in a specimen grid box at room temperature.

3.5. TEM Analysis

The set up and operation procedure will vary slightly depending on the brand of TEM being used. The following information is

based on using a FEI Technai G2 Transmission Electron Microscope fitted with a CCD camera (see Note 12).

1. The typical operating settings are: beam setting 100 kV; aperture spot size 1; focus step 3 or 4.
2. Using curved forceps to hold the grid and velin tissue to steady the insertion rod fix the grid into the specimen holder and insert the rod into the TEM (see Note 13).
3. The sample grid is initially viewed at low magnification (×4,000). The grid is inspected to identify clean unbroken grid windows, using a tracker ball to roam over the grid surface.
4. When a clear window is identified the magnification is increased to ×10,000 to identify the stained fibrils within the grid window.
5. Once a fibril has been identified the magnification is increased to ×30,000–×40,000. The full length of the fibril is examined before it is classified as unaltered or altered (see Note 14). The altered fibrils are classed as exhibiting one of the two forms of damage; Beaded, where swollen areas appear at discrete positions along the fibril and at the ends; or Dumbbell, which consists of a short fragment of a fibril with swollen ends. The different forms of alteration as described and examples of each are shown in Fig. 6. Only discrete fibrils are included in the analysis; any fibrils which are obscured by other overlying fibrils or by grid bars are not included.
6. Once all of the fibrils within that grid window have been classified and recorded take the magnification back to 4,000 and move to the next grid window and continue recording in this manner until 100 fibrils have been identified (see Notes 15 and 16).
7. Continue with the same procedure on the second grid. The final proportion of Unaltered, Beaded, and Dumbbell recorded for each sample are given as a mean value. This value is the average from the two grids (100 fibrils per grid). (See Notes 17 and 18).

4. Notes

1. In all cases "water" refers to 18 MΩ deionized water.
2. EDTA is notoriously difficult to get into solution. It is more soluble at alkaline pH therefore add 400 mL of water to the salt and then add concentrated NaOH to the water to achieve a pH of approximately 8.5. With the addition of a magnetic stirrer and hot plate most of the EDTA salt should go into solution. As the salt solubilizes it will bring down the pH of

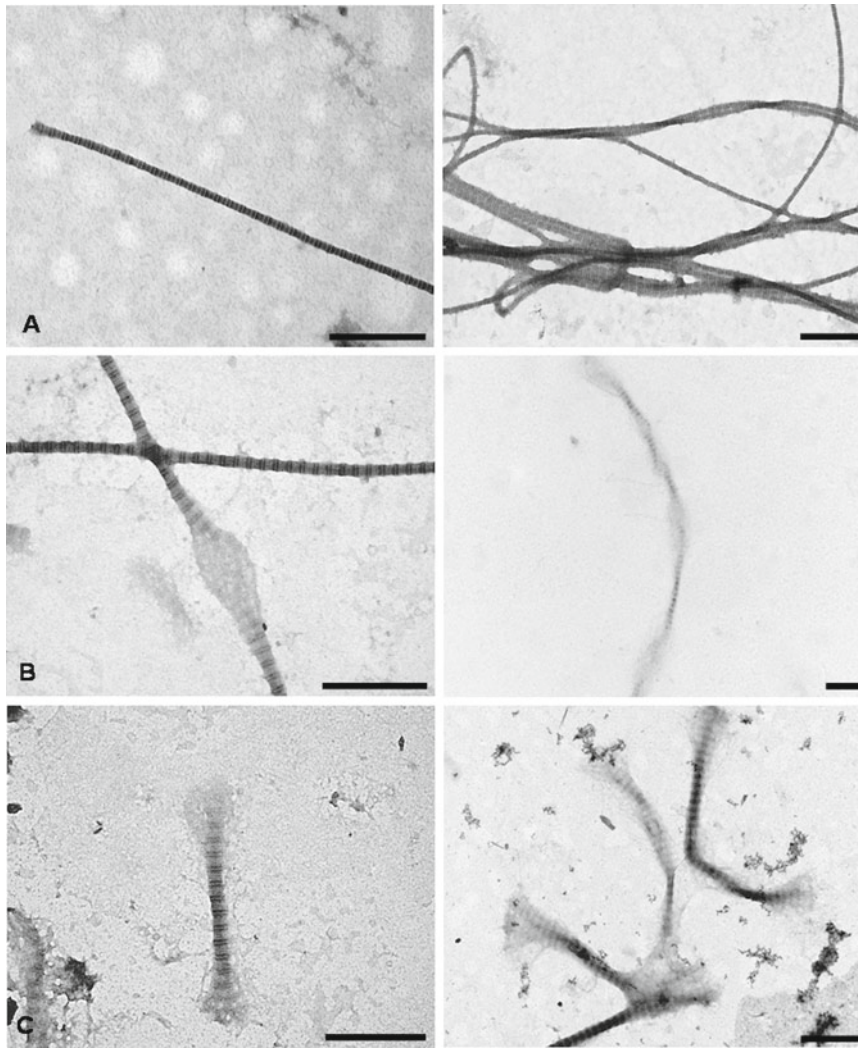

Fig. 6. Three pairs of TEM images which are typical of the different forms of alteration observed in collagen fibrils. (**a**) Shows examples of *Unaltered* collagen fibrils, they have an uniform diameter along the length of the fibril and show a continuous repeat pattern of banding, they are typically tens of microns in length. (**b**) Shows examples of *Beaded* fibrils, they have damaged *Beaded* regions along the length of the fibril where there has been a disruption to the banding pattern. In these regions there may be a faint remnant of banding, but usually the banding pattern has been completely lost; there is also an increased diameter in these disrupted regions. They can be as small as 5 μm but are generally greater than 10 μm in length and usually have frayed ends. (**c**) Shows examples of damaged collagen fibrils of a *Dumbbell* form. The banding is intact and clearly visible in the central fibrillar region which is between 500 nm and 3 μm in length but the ends are observed as grey swollen regions with no evidence of banding. The *Dumbbell* appears to be a more advanced form of alteration and probably occurs through a parting of a *Beaded* fibril at the sites of damage. The scale bars are 500 nm.

the solution therefore constantly monitor the pH and add NaOH accordingly to maintain a pH 7.4–7.8. Once all of the EDTA has dissolved top up the solution with water to reach a total volume of 500 mL.

3. 300 mesh size proved to be the best for this analysis, because it meant that, in the majority of cases, the grid windows are big

enough to visualize the full length of collagen fibrils without too much interference from the grid bars. At 200 mesh the windows are too large and the weight of the specimen on the grid often causes the windows to break.

4. The carbon surface of the grid becomes contaminated by organics when stored which makes it less hydrophilic. The grids are therefore given a high tension (HT) discharge (1.5 kV and 30 A at 1×10^{-1} mbar) prior to use to make them more hydrophilic. As well as removing contamination this also seems to help to disperse the collagen fibrils across the entire grid surface.
5. When manipulating the grid it is easiest and sometimes best to use curved forceps and this has been indicated in the method. However, the metal grid frame is very thin and the grid windows very fragile so the grids can easily become misshapen and damaged. Be careful therefore not to apply undue pressure, always grip the grid by the outer rim and on most occasions use self closing cross-over forceps.
6. Collagen can be lost in the burial environment due to leaching or microbial attack therefore when dealing with archaeological bones more material may be required to obtain sufficient collagen. Also diagenetic alteration in the burial environment can mimic changes caused by cooking, although cooking appears to predispose the collagen to more rapid degradation in the burial environment. As a consequence when analyzing archaeological bone it will be necessary to obtain a suspected uncooked bone sample with a similar burial history to use as a baseline for damage. Finally, when dealing with fragmented archaeological bone, samples should be taken away from the fracture site to minimize the risk of sampling diagenetically altered collagen.
7. A water cooled saw is ideal for removing bone sections as is does not produce heat. A hack saw can be used instead; however the sawing motion must be done very slowly and with regular breaks to prevent the bone from getting too hot.
8. Whilst the bone samples were being demineralized they were kept at 4° C to minimize any destruction to the collagen by acid hydrolysis (8). The demineralization solutions are also constantly agitated to increase the rate and efficiency of demineralization.
9. If the demineralized shards are not required straightaway for TEM they can be stored in 2 mL of the PBS solution at 4° C for up to 5 days.
10. Parts of the homogenizer can become worn with continued use and this could induce additional damage to the collagen fibrils. Therefore every few months prepare a modern unheated "control" sample to test for damage.

11. If the grid is not completely dry or not placed carefully on top of the uranyl drop, it will sink to the bottom and not stain properly.
12. This analysis has been conducted successfully on different models of electron microscopes. The main difference is that on older models most of the operation of the microscope has to be done manually rather than electronically and this can slow down the analysis.
13. It is usually necessary to steady the arm of the sample holder when inserting and removing the sample grid. However, take care not to touch the insertion rod of the sample holder as the grease from finger tips will affect the vacuum within the TEM. Also when inserting and removing the grids from the grid storage box and the sample holder always place a sheet of Lint-free Velin tissue underneath, that way if a grid is accidentally dropped it will not be ruined.
14. If the beam is at high intensity and is left on one area of the fibril for too long the image can become grainy also the formvar windows are very delicate and can easily melt, therefore, when using high magnification take care not to spend too long on any one area of the grid window. If the TEM is fitted with a video camera it is possible to negate this problem by turning down the intensity and inserting the CCD camera. Once the brightness and contrast have been turned up the image of the fibril can then be viewed on a monitor without introducing damage from the electron source and this will preserve the grid for longer.
15. When moving around the grid it can be difficult to keep track of which grid windows have already been viewed. It is advisable to move from left to right and when the edge of the grid is reached move one row up or down and continue back along the row moving right to left.
16. Each time the magnification is alternated between low and high it will be necessary to change the aperture and refocus the beam. On older microscopes this will have to be done manually.
17. Repeated analyses have shown that a recording of 100 fibrils provides an accurate representation of the state for collagen within a given sample. However if there is more than a 10% difference between the values obtained from the two grids a further 100 fibrils are counted and the mean was taken from the two closest values. If there is still more than a 10% difference between the two closest values the sample is rejected.
18. Once confident in identifying fibrils it should take approximately 1 h to analyze a sample. To avoid eye strain and lapses in concentration it is advisable not to analyze more than two samples without taking a break.

Acknowledgments

This method has been refined over a number of years and with the help and advice from TEM technicians at Newcastle, Bradford, and York Universities. Particular thanks must go to J. Fearnley and M. Stark. The majority of the method development was supported by a NERC CASE studentship (NER/S/A/2002/12028) with the BLC Leather Technology Centre.

References

1. Covington AD, Song L, Suparno O, Koon HEC, Collins MJ (2008) Link-lock: an explanation of the chemical stabilisation of collagen. J Soc Leath Tech Ch 92(1):1–7
2. Roberts SJ, Smith CI, Millard A, Collins MJ (2002) The taphonomy of cooked bone: characterizing boiling and its physico-chemical effects. Archaeometry 44(3): 485–494
3. Snowden JM, Weidemann JF (1978) A morphological and biochemical examination of the hydrothermal denaturation of collagen. Meat Sci 2:1–18
4. Richter J (1986) Experimental study of heat induced morphological changes in fish bone collagen. J Archaeol Sci 13(5):477–481
5. Koon HEC, Nicholson RA, Collins MJ (2003) A practical approach to the identification of low temperature heated bone using TEM. J Archaeol Sci 30(11):1393–1399
6. Koon HEC, O'Connor TP, Collins MJ (2010) Sorting the butchered from the boiled. J Archaeol Sci 37(1):62–69
7. Puchinger L, Leichtfried D, Stachelberger H (2002) Evaluation of old parchment collagen with the help of transmission electron microscopy. In: Larsen R (ed) Microanalysis of parchment. Archetype Publications Ltd, London
8. Collins MJ, Galley P (1998) Towards an optimal method of archaeological collagen extraction; the influence of PH and grinding. Anc Biomol 2:209–222

INDEX

Lynne S. Bell (ed.), *Forensic Microscopy for Skeletal Tissues: Methods and Protocols*, Methods in Molecular Biology, vol. 915, DOI 10.1007/978-1-61779-977-8, © Springer Science+Business Media, LLC 2012

C

M

N

O

P

R

S

T

V

W